# Design, simulation and optimization of shared mooring line configurations for floating wind farms

A thesis accepted by the Faculty of Aerospace Engineering and Geodesy of the University of Stuttgart in partial fulfillment of the requirements for the degree of Doctor of Engineering Sciences (Dr.-Ing.)

by

Qi Pan
born in Guangchang, China

| | |
|---|---|
| Main referee: | Prof. Dr. Po Wen Cheng |
| Co-referee: | Prof. Muk Chen Ong |
| | Prof. Dr.-Ing. Zamira Daw |

Date of defense: 03.12.2025

Stuttgart Wind Energy at the Institute of Aircraft Design
University of Stuttgart
2025

# Acknowledgments

There is an old saying that every banquet comes to an end. As I bring this PhD journey to a close, I reflect on the incredible experiences that made this achievement possible.

First and foremost, I am grateful to my family for their unconditional love and respect throughout this journey. Their belief in me has been a constant source of peace and strength during challenging times.

I would like to express sincere gratitude to my supervisor, Prof. Dr. Po Wen Cheng, for his guidance and expertise. His continuous support and feedback have been instrumental in shaping the direction of my research.

Special thanks go to my smart colleagues in SWE team for their collaboration and stimulating discussions, and to my lovely friends, whose encouragement and companionship have been indispensable throughout my doctoral studies.

To everyone who has accompanied me during this journey, thank you. This thesis would not have been possible without the collective support, love and help I have been fortunate to receive.

# Abstract

The growing demand for wind energy drives rapid expansion in the offshore wind sector, while high costs remain a significant barrier to the deep-sea deployment of floating wind farms. Shared moorings, which use either shared anchors or shared lines to reduce mooring-related costs, provide a promising alternative to conventional configurations. Although shared anchors have already been utilized in the real-world project, shared line designs that connect two floaters with a single line and could further reduce costs, remain in the early study phase.

Existing stiffness-linearized design methods for shared line configurations are constrained by small prescribed floater offsets, and their simplification of mooring lines as linear springs can lead to unrealistic chain diameters or mooring masses. At the same time, simulation tools that capture fluid-structure interactions in floating wind farms demand high computational resources, which limit their use for large number of simulations. As a result, the feasibility and cost-saving potentials of shared line designs remain largely unexplored.

This study establishes a comprehensive framework to address key challenges in the design, simulation, and optimization of shared line configurations, providing insights for their evaluation and implementation in floating wind farms. Firstly, a nonlinear design method is introduced for cost-effective shared line configurations. Unlike linearized methods that model mooring lines as linear springs and rely solely on small prescribed floater offsets, the proposed method incorporates configuration properties, mooring elasticity, and geometry features, which collectively govern load distribution and mooring stiffness,

enabling more reliable designs than linearized methods. It can also accommodate conventional configurations, offering flexibility in front-end mooring evaluation for floating wind farms.

Secondly, a simplified simulation tool is developed for efficient prediction of floating turbine dynamics. It integrates a low-order multi-body solver, a quasi-static mooring model, and a Gaussian wake model. Verification against a relatively higher-fidelity tool (FAST.Farm) shows that the simplified model significantly enhances computational efficiency by over 75-fold, and keeps prediction differences below 9% under various loading conditions. Results indicate that the simplified model effectively captures fundamental dynamics, and its flexible wind modeling supports wind-free simulations, such as decay tests, while FAST.Farm (v3.5.1) terminates due to its reliance on wind dynamics.

Thirdly, this study comprehensively evaluates shared line and conventional designs in terms of dynamic performance and mooring cost. Existing studies often neglect wake effects, mooring fatigue or examine only a narrow set of configurations. In contrast, this study explores a broader design space using the nonlinear design method, incorporates wake effects through the simplified modeling approach, and accounts for mooring fatigue in feasibility evaluations. Results show that two-turbine arrays with shared line moorings yield about 3% higher costs but achieve over 35% lower fatigue damage at cost extremes.

Finally, two optimization strategies are proposed for shared line configurations. Unlike previous studies that often focused on single turbines and frequency-domain analyses, this study applies the simplified modeling approach to capture floating array dynamics, and incorporates wake effects and mooring fatigue for more solid feasibility assessments. The cost-driven strategy employs Particle Swarm Optimization (PSO) algorithm to minimize mooring material cost, while the cost-fatigue trade-off strategy uses the Non-dominated Sorting Genetic Algorithm II (NSGA-II) to balance mooring material cost with fatigue resistance. Two optimal solutions are evaluated in terms of performance and mooring cost, and provide insights for mooring optimization in floating wind farms.

# Kurzfassung

Die steigende Nachfrage nach Windenergie treibt das Wachstum im Offshore-Windsektor voran, während hohe Kosten den Einsatz schwimmender Windparks in der Tiefsee noch begrenzen. Shared Line Verankerungen, bei denen Anker oder Leinen zwischen mehreren Turbinen geteilt werden, bieten eine vielversprechende Alternative zu herkömmlichen Konfigurationen. Während gemeinsame Anker bereits eingesetzt werden, befinden sich gemeinsam genutzte Leinen, die zwei Schwimmkörper verbinden, noch in der frühen Forschungsphase.

Linearisierte Entwurfsmethoden für Shared Line, die kleine Verschiebungen annehmen und Leinen als lineare Federn approximieren, können unrealistische Kettendurchmesser oder Ankergewichte erzeugen. Hochauflösende Simulationswerkzeuge sind zudem rechenintensiv, wodurch große Parameterräume schwer untersuchbar sind. Dies erschwert die Bewertung von Machbarkeit, Dynamik und Kosteneffizienz solcher Designs. Diese Studie entwickelt einen Rahmen für Entwurf, Simulation und Optimierung von Shared Line Konfigurationen. Zunächst wird eine nichtlineare Entwurfsmethode vorgestellt, die Verankerungseigenschaften, Leinenelastizität und Geometrie berücksichtigt, und zuverlässigere Designs als bei linearen Methoden erzielt werden.

Anschließend wird eine nichtlineare Entwurfsmethode für kosteneffiziente Shared Line Konfigurationen vorgestellt. Im Gegensatz zu linearen Methoden, die ausschließlich auf kleine Floater-Verschiebungen stützen, berücksichtigt die vorgeschlagene Methode Verankerungseigenschaften, Leinenelastizität und Geometrie, die gemeinsam die Lastverteilung und Verankerungssteifigkeit bestimmen. Dies ermöglicht zuverlässigeren Entwurf sowohl für Shared Line als auch

für herkömmliche Konfigurationen und bietet Flexibilität bei der Front-End-Analyse schwimmender Windparks.

Zweitens wurde ein vereinfachtes Simulationswerkzeug zur effizienten Vorhersage der Dynamik schwimmender Turbinen entwickelt. Es kombiniert einen Multi-Body-Solver niedriger Ordnung, ein quasistatisches Verankerungsmodell und ein Gaußsches Nachlaufmodell. Die Validierung gegen FAST.Farm zeigt, dass das vereinfachte Modell die Recheneffizienz um über das 75-fache steigert und die Vorhersageabweichungen unter verschiedenen Belastungsbedingungen unter 9% hält. Die Ergebnisse belegen, dass das Modell die grundlegende Dynamik zuverlässig erfasst und flexible Windfeldsimulationen, wie z.B. Abklingtests, unterstützt, während FAST.Farm aufgrund der Abhängigkeit von der Winddynamik abbricht.

Drittens bewertet die Studie Shared Line und herkömmliche Konfigurationen umfassend hinsichtlich dynamischer Leistung und Verankerungskosten. Im Gegensatz zu bisherigen Arbeiten, die Nachlaufeffekte und Mooring Ermüdung oft vernachlässigen oder nur wenige Konfigurationen untersuchen, analysiert diese Studie einen breiten Konstruktionsraum unter Nutzung der nichtlinearen Entwurfsmethode, berücksichtigt Nachlaufeffekte und integriert Mooring Ermüdung in Machbarkeitsbewertungen. Die Ergebnisse zeigen, dass Zwei-Turbinen Shared Line Designs etwa 3% höhere Kosten verursachen, aber über 35% weniger Ermüdungsschäden aufweisen.

Abschließend werden zwei Optimierungsstrategien vorgestellt. Frühere Studien beschränkten sich häufig auf einzelne Turbinen und Frequenzbereichsanalysen, nutzt diese Arbeit den vereinfachten Modellierungsansatz, um Turbinendynamik, Nachlaufeffekte und Mooring Ermüdung in Machbarkeitsbewertungen einzubeziehen. Die kostenorientierte Strategie minimiert die materialkosten mittels PSO, während die Kosten-Ermüdungs Kompromissstrategie NSGA-II verwendet, um Materialkosten mit Ermüdungsbeständigkeit in Einklang zu bringen. Zwei optimale Lösungen werden hinsichtlich Leistung und Kosten bewertet und liefern wertvolle Hinweise für die Mooringsoptimierung in schwimmenden Windparks.

# Contents

# Abbreviations and symbols

**Abbreviations**

BEM Blade Element Momentum

CAPEX Capital expenditure

CFD Computational Fluid Dynamics

DLC Design Load Case

DWM Dynamic Wake Meandering

FLS Fatigue Limit State

FOWT Floating Offshore Wind Turbine

LCOE Levelized Cost Of Energy

MBL Minimum Breaking Load

MODU Mobile Offshore Drilling Units

NSGA Non-dominated Sorting Genetic Algorithm

NTM Normal Turbulent Model

OPEX Operational expenditure

PM Pierson–Moskowitz

PSD Power Spectral Density

PSO Particle Swarm Optimization

QTF Quadratic Transfer Function

TLP Tension Leg Platform

ULS Ultimate Limit State

VLM Vortex Lattice Method

**Symbols**

| | | |
|---|---|---|
| $\mu_j$ | Penalty weighting factor (Equation 7.7) | [-] |
| $\beta$ | Wake area parameter (Equation 4.8) | [-] |
| $\Delta U$ | Velocity deficit (Equation 4.5) | [m/s] |
| $\epsilon$ | Velocity deficit parameter (Equation 4.6) | [-] |
| $\omega$ | Mooring line weight in water per unit length (Equation 4.1) | [N/m] |
| $\phi$ | Mooring line angle relative to the horizontal plane (Equation 4.1) | [°] |
| $\rho$ | Water density (Equation 4.1) | [kg/m$^3$] |
| $\rho_c$ | Mooring line mass per length in air (Equation 5.1) | [kg/m] |
| $\sigma$ | Standard deviation of the velocity deficit profiles (Equation 4.5) | [m/s] |
| $A$ | Chain equivalent cross-sectional area (Equation 4.1) | [m$^2$] |
| $a_D$ | Intercept parameter of the S-N curve (Equation 4.3) | [-] |

| | | |
|---|---|---|
| $C(r_x)$ | Maximum normalized velocity deficit (Equation 4.5) | [-] |
| $c_1$ | Cognitive factor in velocity model (Equation 7.1) | [-] |
| $c_2$ | Social factor in velocity model (Equation 7.1) | [-] |
| $C_A$ | Drag embedment anchor cost (Equation 5.3) | [$] |
| $C_L$ | Mooring steel line cost (Equation 5.3) | [$] |
| $C_m$ | Mooring material cost | [$] |
| $C_T$ | Thrust coefficient (Equation 4.6) | [-] |
| $D$ | Mooring fatigue damage (Equation 4.4) | [-] |
| $D_c$ | Mooring chain diameter (Equation 5.1) | [m] |
| $D_h$ | Tangential hydrodynamic force on line segment (Equation 4.1) | [N] |
| $D_m$ | Maximum mooring fatigue damage within the shared line design (Equation 7.5) | [-] |
| $D_r$ | Turbine rotor diameter (Equation 4.6) | [m] |
| $E$ | Mooring chain Young's modulus (Equation 4.1) | [kN/m$^2$] |
| $EA$ | Mooring line axial stiffness (Equation 4.1) | [kN] |
| $f(x)$ | General objective function (Equation 7.3) | [-] |
| $F_1$ | First front in NSGA-II | [-] |
| $f_g$ | Chain grade-dependent factor (Equation 5.2) | [kN/m$^3$] |
| $F_h$ | Normal hydrodynamic force on line segment (Equation 4.1) | [N] |

| | | |
|---|---|---|
| $F_l$ | Final front in NSGA-II | [-] |
| $f_{pen}(x)$ | General objective function with penalty (Equation 7.7) | [-] |
| $G$ | Global best position (Equation 7.1) | [-] |
| $g$ | Gravity acceleration | [kg·$m/s^2$] |
| $g(x)$ | Inequality constraint | [-] |
| $G_c$ | Mooring chain grade | [-] |
| $h(x)$ | Equality constraint | [-] |
| $H_s$ | Significant wave height | [m] |
| $K$ | Mooring stiffness at static equilibrium (Equation A.1) | [N/m] |
| $k$ | Wake growth rate (Equation 4.6) | [-] |
| $L_L$ | Mooring line lay-down length | [m] |
| $L_S$ | Mooring line suspended length | [m] |
| $L_T$ | Mooring line total length | [m] |
| $M$ | Mass matrix (Equation 4.9) | [-] |
| $m$ | Slope of the S-N curve (Equation 7.7) | [-] |
| $M_L$ | Mooring line mass in air | [kg] |
| $MF$ | Mooring line pretension at fairlead (Equation A.1) | [N] |
| $N$ | Force matrix (Equation 4.9) | [-] |
| $N_c$ | Cycle number to failure (Equation 4.4) | [-] |

| | | |
|---|---|---|
| $p$ | Applied force matrix (Equation 4.9) | [-] |
| $P_0$ | Initialized population in NSGA-II | [-] |
| $p_c$ | Crossover probability in NSGA-II | [-] |
| $P_i$ | Particle $i$ best position (Equation 7.1) | [-] |
| $p_m$ | Mutation probability in NSGA-II | [-] |
| $q$ | Generated coordinates representing the degrees of freedom (Equation 4.9) | [-] |
| $Q_0$ | Offspring population of $P_0$ in NSGA-II | [-] |
| $r$ | Radial distance from the wake center (Equation 4.5) | [m] |
| $R^2$ | Coefficient of determination | [-] |
| $r_1$ | Random number in velocity model (Equation 7.1) | [-] |
| $r_2$ | Random number in velocity model (Equation 7.1) | [-] |
| $R_t$ | Combined population of $P_t$ and $Q_t$ | [-] |
| $r_x$ | Downstream location (Equation 4.5) | [m] |
| $R_L$ | Static mooring line length ratio | [-] |
| $R_M$ | Mass ratio of the anchor line to the floater's displaced mass | [-] |
| $R_S$ | Mass ratio between each anchor line and the shared line | [-] |
| $R_T$ | Mooring line force ratio | [-] |
| $S$ | Stress range (Equation 7.7) | [MPa] |

| | | |
|---|---|---|
| $s$ | Line suspended length (Equation 4.1) | [m] |
| $T_L$ | Mooring tension force (Equation 4.1) | [N] |
| $T_p$ | Wave peak period | [s] |
| $U_\infty$ | Upstream undistributed velocity (Equation 4.5) | [m/s] |
| $U_i$ | Downstream disturbed velocity due to upstream turbine $i$ (Equation 6.1) | [-] |
| $v_i(t)$ | Velocity of particle $i$ at iteration $t$ (Equation 7.1) | [-] |
| $V_r$ | Turbine rated wind speed | [m/s] |
| $V_{50}$ | Extreme wind speed with 50-year return period | [m/s] |
| $w_x$ | Parameter controls velocity impact (Equation 7.1) | [-] |
| $WF$ | Steady wind force on the turbine (Equation A.1) | [N] |
| $X$ | Floater offset (Equation A.1) | [m] |
| $x$ | General design variable (Equation 7.3) | [-] |
| $x_i(t)$ | Current position of particle $i$ (Equation 7.1) | [-] |
| $z$ | Line vertical position (Equation 4.1) | [m] |

# 1 Introduction

Renewable resources, such as solar and wind, significantly reduce carbon emission and facilitate global energy transition to net-zero emission by 2050. However, current commitments to reducing greenhouse gas emission are insufficient to effectively mitigate global warming [1]. To limit warming to 1.5°C, the share of solar and wind energy in electricity generation, which grows at an annual average rate of 14%, must accelerate to 24% annually to achieve the targets by 2030 [2]. This ambitious demand for wind energy expects to add at least 320 GW of new capacity in 2030, a hike from the 117 GW of new global installations in 2023 [3].

The promising outlook for wind energy signals rapid expansions in both onshore and offshore wind sectors, although the current offshore wind market stays relatively small compared to the onshore sector. In 2023, the offshore wind capacity increased by 10.8 GW, which was less than 10% of the total new installations worldwide [3]. However, offshore turbines possess advantages over onshore turbines, by accessing stronger wind speeds with less interference from nearby human communities. The compound annual growth rate for offshore wind capacity is expected to be approximately 4 times that of the onshore wind sector over the next five years [3]. This optimistic growth rate highlights the long-term potential of the offshore wind market.

With the majority of offshore wind resources located in waters exceeding 60 m, floating wind technology offers the potential to meet future demands for offshore wind energy. However, currently, floating wind projects suffer from high costs and increased risks induced by harsh environmental conditions. Technological innovations, such as large scaled turbines and improved structural

designs, present opportunities to reduce both costs and risks. Studies indicate that floating wind energy can be cost-competitive. For instance, the averaged Levelized Cost Of Energy (LCOE) of a 125-MW floating wind farm in water depths exceeding 100 m, falls at the lower bound of the typical LCOE range of offshore bottom-fixed wind farms [4].

Floating Offshore Wind Turbines (FOWTs) rely on mooring systems to maintain stability and ensure safe operation. Beyond station-keeping, mooring systems influence the overall costs of FOWTs. [5] reported that mooring costs per turbine range from below 0.5 and over 3 million EUR per meter of water depth. Installed at a water depth of 200 m, a recent 15-MW FOWT project with a six-line mooring configuration incurred anchor and mooring line costs of 35000 and 174000 GBP per MW, respectively [6]. An exchange currency rate of 1.15 is used to convert the anchor and mooring line costs to an estimated total of 3.6 million EUR. This highlights the importance of developing feasible and cost-effective mooring solutions.

## 1.1 Motivation

In conventional mooring systems, each FOWT is independently supported by its own mooring lines, and each line is individually secured by an anchor to the seabed. These conventional designs have been employed in floating wind projects, such as Kincardine offshore wind farm [7] and Hywind Scotland [8]. While the floating wind sector has leveraged mooring design expertise from the offshore oil and gas industry, it accepts non-redundancy configurations that arrange three lines per FOWT, fewer than those used by the Mobile Offshore Drilling Units (MODUs), to achieve cost-effective mooring solutions for floating wind projects.

Shared moorings can be broadly categorized into shared anchor and shared line configurations. Shared anchor designs use a single anchor to secure multiple mooring lines, while shared line designs employ a single line to connect and

support two floaters. These designs provide a promising alternative to conventional moorings, with the potential to reduce mooring-related costs. The shared anchor design has been implemented in the Hywind Tampen floating wind project [9], where 11 FOWTs are stabilized using 19 anchors [10], significantly fewer than the 33 anchors that would be required for conventional three-line configurations. Compared to shared anchor designs, shared line configurations can further reduce mooring-related costs, by replacing two lines connected to a shared anchor with a single line, which eliminates the need for shared anchors.

However, studies on shared line configurations are still in the early stages. Compared to conventional mooring designs, they face increased challenges related to mooring forces and floater motions, due to altered load distributions and reduced mooring stiffness. Shared lines introduce coupling effects between connected FOWTs and increase mooring forces in the upwind lines, which counterbalance the cumulative environmental loads from multiple connected FOWTs. They also reduce overall mooring stiffness, which leads to increased floater motions of connected FOWTs. These challenges may collectively pose risks to the safe operation of FOWTs, which highlights the importance of comprehensive assessments for shared line configurations.

Existing performance and cost assessments often rely on simplified analyses or a narrow set of configurations. The lack of robust design methods and efficient frameworks for dynamic simulation and time-domain optimization prevents comprehensive evaluation of shared line configurations. As a result, their performance and cost-saving potential remain insufficiently explored. This study addresses these gaps by developing robust design methods, efficient simulation tools, and tailored optimization strategies. By enabling more reliable designs and comprehensive evaluations, this study investigates the performance and cost-saving potential of such innovative configurations to support their broader development and practical adoption.

## 1.2 Research questions

Chapter 2 reviews existing studies on shared line designs used for FOWTs and identifies three major research gaps. To address these gaps, three research questions are formulated accordingly, focusing on design method, simulation framework, and optimization analysis.

- How can a practical and cost-effective shared line configuration be determined for a floating wind farm?

  A reliable design method is critical for developing practical and cost-effective mooring configurations. Previous approaches linearize mooring stiffness under the assumption of small offsets, but there is a lack of design consensus on acceptable offset limits. Moreover, studies have shown that shared line designs tend to increase floater offsets. This raises concerns about the validity of the small-offset assumption, and the reliability of the stiffness-linearized method that uses small offsets as the only design constraint. Besides, previous studies demonstrate that this method can lead to unrealistic mooring lines with chain diameters or masses exceeding the feasible limits. This further raises questions on the applicability of this method for shared line configurations.

  Furthermore, mooring material cost is an important design criterion for evaluating shared line designs, as the primary motivation is to reduce mooring-related expenses. Although some studies have demonstrated the economic advantages of certain shared line designs over conventional baselines, they do not capture the overall potential or broader impact of shared line designs. Some studies rely on simplified analyses, such as static tests, which overlook the dynamic responses of connected FOWTs, raising questions about their cost-saving evaluations. Therefore, a wider design space and robust design constraints are essential to fully assess the performance and cost-saving potential of shared line configurations.

This research aims to improve the design reliability, by incorporating practical constraints and realistic mooring properties into a nonlinear design method. Design parameters neglected in existing stiffness-linearized methods are evaluated, and their impacts on floater motions and mooring forces are investigated through sensitivity analysis. A comparison with the stiffness-linearized method demonstrates the improved design reliability of shared line configurations using the proposed approach. To compare the performance of mooring configurations, both static and dynamic analyses are performed to provide a more robust evaluations. Details of the method and results are presented in Chapter 5.

- How can an efficient simulation tool be developed for evaluating shared line designs in floating wind farms?

  An efficient simulation tool is essential for evaluating the performance of a broad range of shared line designs in floating wind farms, particularly when accounting for their dynamic responses. Although existing studies have developed various tools to predict FOWT and mooring performance, they are often limited in scope. Some focus on static or frequency-domain analyses, which may fail to capture extreme floater motions and mooring forces, while some time-domain approaches overlook wake effects that can significantly affect wind thrust forces on downstream FOWTs. These limitations reduce prediction accuracy and prevent reliable evaluations of FOWTs using shared line designs.

  Moreover, simulation tools that capture fluid-structure interactions often require high computational resources. This challenge becomes more pronounced when large numbers of simulations are needed, such as in parametric studies and optimization of mooring configurations. As the wind-farm scale increases, the computational burden further grows, which limits existing studies to a narrow set of mooring configurations and provides insufficient attention to mooring fatigue. Experience from the oil and gas industry indicates that mooring fatigue is the primary failure mode for mooring systems. Therefore, it is important to improve the

computational efficiency of simulation tools, while still capturing both dynamic FOWT responses and wake effects, for reliable evaluations of floating wind farms employing shared line designs.

To address these challenges, this research develops a simplified simulation tool that balances computational efficiency with prediction accuracy for the early-stage analysis of shared line designs in floating wind farms. This tool is verified against a relatively higher-fidelity simulation tool (FAST.Farm), by comparing their computational time for the same test case and dynamic predictions of a two-turbine array under different environmental conditions. Its extension to four-turbine arrays further demonstrates its applicability to larger-scale floating wind farms. Details of the framework, code hierarchy, and verification are presented in Chapter 6.

- How can a tailored optimization strategy be developed for shared line designs in floating wind farms ?

  As research on shared line designs remains at an early stage, their optimization has received limited attention. Existing mooring optimization studies for individual FOWTs with conventional moorings often rely on frequency-domain analyses, which may overlook the extreme response of the turbine, floater and mooring lines. Time-domain analyses offer more accurate predictions, but they demand significant computational effort, which limits their application in optimization studies for both individual FOWTs and floating wind farms.

  Although some time-domain optimization studies have been conducted for other types of floating structures, they primarily focus on extreme loading conditions and pay limited attention to mooring fatigue. Since shared lines connect two FOWTs, failures can cause more severe consequences than those for the single FOWT with conventional configurations. Therefore, to mitigate fatigue-related mooring failures, it is important to incorporate mooring fatigue considerations into the optimization study.

In addition, unlike mooring optimization for individual FOWTs, shared line mooring optimization for floating wind farms should account for wake effects on downstream FOWTs for more accurate prediction of FOWT and mooring performance. Wake effects and the coupling between connected FOWTs through the shared line strongly influence the dynamics of the turbine, floater, and mooring system. These responses differ from those observed in individual FOWT scenarios and affect long-term mooring fatigue resistance. Such complexities emphasize the need for tailored optimization strategies for shared line designs in floating wind farms.

To address these gaps, this research develops two strategies for shared mooring optimization. Time-domain analyses are performed using the simplified modeling approach, incorporating wake effects in simulations and mooring fatigue in evaluations. The cost-driven strategy minimizes mooring material costs, while the cost-fatigue trade-off strategy balances mooring costs with long-term fatigue resistance. Two algorithms, PSO and NSGA-II, are applied for these single-objective and multi-objective problems, respectively. Optimal solutions are compared to support the comprehensive evaluation and the broad adoption of shared line configurations in floating wind farms. Further details of the optimization framework, implementation, and results are presented in Chapter 7.

## 1.3 Thesis structure

The thesis is divided into three main parts. The first part introduces the research questions (Chapter 1), reviews the state of the art on mooring designs, simulation tools, and FOWT optimization (Chapter 2), and presents the fundamental background for modeling FOWT arrays under various environmental conditions (Chapters 3 and 4).

The second part addresses the three core research questions, focusing on the nonlinear design method for shared line configurations (Chapter 5), simplified

modeling approach for simulating the floating wind farms with different mooring configurations (Chapter 6), and shared line mooring optimization (Chapter 7). These questions are interrelated, as shown in Figure 1.1. For example, the nonlinear design method introduced in Chapter 5 is used to generate shared line configurations for two-turbine arrays in Chapter 6, where the simplified modeling approach is verified against FAST.Farm to assess both prediction accuracy and computational efficiency. Furthermore, the simplified modeling framework developed in Chapter 6 is incorporated into the shared line mooring optimization in Chapter 7. The final part summarizes the conclusions and contributions to the community, and discusses future directions for the design, simulation, and optimization of shared line configurations in Chapter 8.

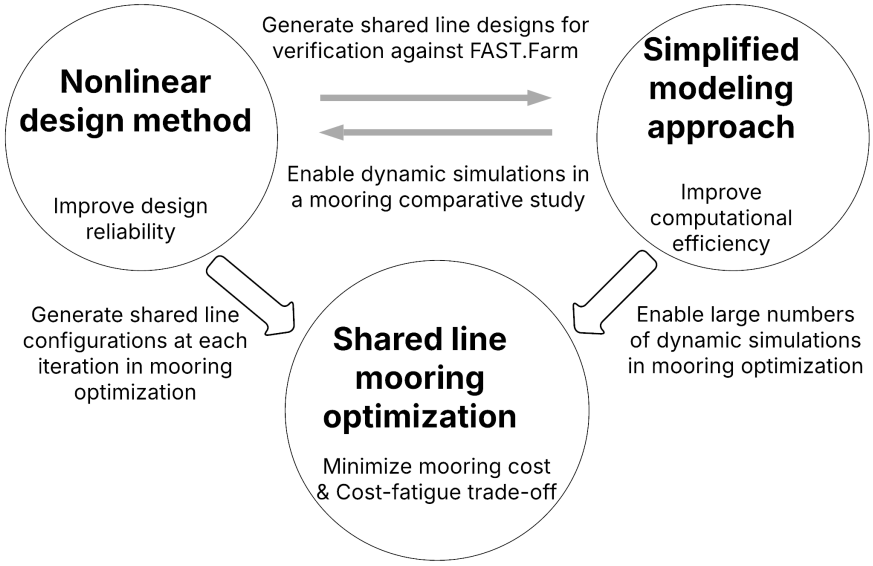


Figure 1.1: The interrelated research questions.

# 2 Literature review

This chapter briefly introduces previous work associated with mooring systems, including mooring design and analysis for FOWTs in Section 2.1, simulation tools developed for both individual and arrays of FOWTs in Section 2.2, and optimization strategies applied to the turbine, floater and mooring system in Section 2.3.

## 2.1 Mooring design and analysis for FOWTs

This section reviews mooring design for FOWTs, with a focus on the use of quasi-static and dynamic mooring analyses, the selection between steel chain links and synthetic fiber ropes for mooring lines, and the stiffness-linearized design method for shared line configurations. This review forms the basis for applying the quasi-static mooring analysis for shared line designs using steel chains in this study.

### 2.1.1 Quasi-static and dynamic mooring analyses

Mooring systems have been employed for Mobile Offshore Drilling Units (MODUs) in the oil and gas industry since 1954, when a submersible barge started drilling operations [11]. The expertise developed in mooring analysis within this sector has naturally transitioned to the floating wind industry. As noted by [12], mooring line response analyses can be generally categorized as either quasi-static or dynamic. The key difference is the inclusion of hydrodynamic forces

on mooring line components, as further discussed in Section 4.1.4. This transfer of knowledge in mooring analysis is relevant, because the four main types of platforms utilized for FOWTs, including semi-submersible, tension leg, spar and barge, have all been used in offshore oil and gas operations.

However, since MODUs rely more heavily on manned operations and face more severe consequences in the event of mooring failure, their mooring design philosophies differ from those of FOWTs. Generally, MODUs follow stricter strength criteria than FOWTs, and require redundancy checks under both intact and one-line damaged loading conditions. These checks evaluate the station-keeping capability of mooring systems. In contrast, FOWTs are not required to perform one-line damage redundancy tests, as they can adopt non-redundancy mooring configurations, typically consisting of three or four mooring lines per FOWT, fewer than those used by MODUs, to reduce cost and complexity. Examples of non-redundancy configurations can be found in floating wind projects such as Hywind Scotland [8] and Kincardine [13].

Despite different priorities in mooring design between these two industries, the quasi-static mooring analysis has been widely used in mooring designs of FOWTs. In this analysis, mooring line loads are calculated based on floater motions, while neglecting hydrodynamic forces on the line segments. For example, [14] applied the quasi-static mooring analysis to determine the mooring line length for a 5-MW semi-submersible FOWT. [15] analyzed the effect of adding clump weights to the mooring configuration for a 15-MW semi-submersible FOWT, with the configuration determined using the quasi-static mooring analysis. Similarly, [16] used quasi-static mooring analysis to determine the mooring pretension and anchor position for a 15-MW spar FOWT.

The quasi-static mooring analysis considers only the spatial positions of the anchor and fairlead as determined by floater motions, making it well-suited for early-stage design and analysis. In contrast, the dynamic mooring analysis accounts for additional hydrodynamic forces associated with damping, inertial effects, and the relative motion between the mooring line and the surrounding

fluid. Despite simplifications, the quasi-static analysis has demonstrated prediction accuracy in various studies. For instance, [17] developed a quasi-static mooring model for a 3-line configuration used in CFD simulations of a 5-MW spar FOWT, and validated this model against experimental results from free-decay tests. Similarly, [18] used the quasi-static mooring analysis to simulate mooring forces at fairleads, and validated the results against experimental data from free-decay tests of a 10-MW semi-submersible FOWT.

The exclusion of hydrodynamic forces such as inertia and drag on the mooring line, limits the use of the quasi-static mooring analysis under certain conditions. For instance, [19] compared simulations using both quasi-static and dynamic mooring analyses against experimental results for a 7-m mooring line made of steel chains. Linear harmonic motions with different natural periods were imposed to represent 2-D floater motions in surge, heave, and pitch. The quasi-static analysis accurately predicted mooring forces and floater motions for long-period excitations (7.9 s), but it underestimated the maximum forces and introduced phase shifts in floater motions for short-period (1.6 s) excitation. Similar observations were reported in a validation study, which compared both quasi-static and dynamic mooring analyses against experimental results of a semi-submersible platform [20].

Assuming a length scale of 100, given that typical mooring line lengths exceed 700 m in floating wind projects [7, 8], the corresponding time scale is 10. This implies the real motion periods scale to approximately 16 s and 79 s, respectively, for the short and long period excitations used in [19], which fall within the natural period ranges of floater heave and surge motions for semi-submersible FOWTs. Under normal operating conditions, surge typically dominates over heave, while heave is more significant during high-wave events or under extreme loading conditions. Therefore, the quasi-static mooring analysis can provide accurate predictions of mooring forces under normal operation scenarios.

Moreover, under extreme loading conditions, the damping and inertia coefficients used in the dynamic mooring analysis for hydrodynamic force calcula-

tions are highly sensitive to both environmental conditions and floater motions. These coefficient should be determined by experiments or high-fidelity simulations, making dynamic analysis less practical for early-phase mooring design studies. This understanding forms the basis for the mooring design and analysis of shared line configurations used in arrays of FOWTs. This understanding supports the use of quasi-static mooring analysis for the design and evaluation of shared line configurations in floating wind farms.

### 2.1.2 Selection of mooring line material

The choice of line material is not limited to steel chain in mooring designs for FOWTs. For example, [21] introduced a semi-taut mooring configuration, consisting of steel chains and polyester ropes for a 10-MW spar FOWT at a water depth of 180 m. Similarly, [22] studied 7 configurations considering both steel chains and synthetic fiber ropes for a 5-MW semi-submersible FOWT in shallow waters of 50 m. In addition, [23] compared the performance of nylon and polyester ropes in the single-point mooring configuration for a 10-MW twin-hull FOWT at a 120-m site, and found favorable use of nylon over polyester ropes in reducing mooring fatigue damage and extreme load.

A key feature of synthetic fiber ropes, compared to steel chains, is their viscoelastic properties, which lead to varying stiffness. This nonlinear stiffness is highly dependent on loading conditions, such as load amplitude, load frequency and load history. To account for these properties, several methods have been proposed in mooring design for FOWTs. [21] applied iteratively the elastic catenary and taut equations for steel chains and polyester ropes, respectively, to reach a smooth force-displacement relationship for the mooring line. [22] utilized the elastic catenary equation to examine the influence of water depth for steel chains, and employed a spring-dashpot model for synthetic fiber ropes. [23] determined the quasi-static and dynamic stiffness properties of nylon and polyester ropes through tension tests, and fitted the results to the Syrope model to generate the force-elongation relationship.

Polyester mooring has become the most common solution for deep-water production platforms in the offshore oil and gas industry, as it provided the most cost-effective choice under harsh environmental conditions [11]. In the floating wind project Floatgen, a mooring configuration consisting of 6 nylon lines was used for a 2-MW FOWT at a water depth of 33 m [24]. While expertise in using synthetic fiber ropes can be leveraged from offshore oil and gas applications, floating wind projects encounter unique challenges due to differences in water depths, environmental conditions, platform dimensions, and mooring design requirements. Studies have highlight these challenges in the application of fiber ropes in floating wind, related to cost, strength, and stiffness modeling.

For example, [22] evaluated the manufacture and installation costs of mooring configurations using steel chains and fiber ropes, and found that the reference design using only steel chains at a water depth of 200 m, was most cost-effective. Although synthetic fiber ropes provided potential cost advantages, the need for suction anchors increased overall expenses. In terms of strength, [25] conducted residual strength tests of polyester ropes and found a 2.9% reduction in strength after one year of sea trials. This raises questions about the long-term reliability when applying synthetic fiber ropes in floating wind projects and underscores the need for further validation and monitoring.

Furthermore, regarding stiffness models, [26] fitted the laboratory tension test results of fiber ropes to both the Syrope and bi-linear models, and observed different mooring ultimate forces and fatigue damage during the dynamic analysis of a 10-MW FOWT. This raises concerns about the appropriate selection and parameter tuning of stiffness models for synthetic fiber ropes under various loading conditions. Similarly to strength, this also casts uncertainty on the adoption of stiffness models derived from the offshore oil and gas applications for FOWTs, as there is a lack of publicly available data to validate these models in mooring force predictions against on-site measurements in floating wind projects.

Therefore, based on the literature review of the key challenges associated with using synthetic fiber ropes, particularly in terms of cost, strength, and stiffness

modeling, this study focuses on mooring lines made of steel chains. Steel chains have been suggested as a more cost-effective solution at water depths around 200 m, offering higher strength stability and simpler stiffness modeling compared to the synthetic fiber ropes.

### 2.1.3 Shared line design

Shared line design has been proposed for marine structures such as fishing cages and wave energy converters, and subsequently extended to floating wind farms. For instance, [27] analyzed a four-cage grid mooring system designed for ocean aquaculture operations, in which anchor lines were connected to grid lines through buoy elements. The mooring forces of anchor lines and the static shape of the grid were determined using quasi-static mooring analyses. Similarly, [28] studied a shared line configuration for 9 wave energy converters, and found that this design had a slight impact on heave and pitch motions under operational conditions but resulted in a large mooring force under survival conditions.

Studies on shared line designs in floating wind farms have explored various topics, including configuration design, cost-benefit estimation, and the use of stiffness-linearized design method. For example, [29] proposed three shared mooring layouts and evaluated the resulting floater motions for the 5-MW semi-submersible FOWTs. In their study, the mooring system was modeled as a set of springs with a linearized stiffness matrix for frequency-domain calculations, while the quasi-static mooring analysis was used for time-domain simulations. Results showed no motion resonance within the wave-frequency range, but surge displacements exceeded 100 m in shared mooring layouts, significantly larger than those with conventional configurations.

To reduce floater displacement, studies have incorporated buoys and clump weights into mooring designs to increase mooring stiffness. For instance, [30] investigated the effects of buoys and clump weights in shared mooring configurations for a $2 \times 2$ floating array, where each 5-MW barge FOWT was fastened by 8 lines. They employed the finite element method to account for mooring

dynamics, and the comparison highlighted the benefits of these elements in reducing floater motions. However, there is a lack of studies on the impact of buoys and clump weights on mooring costs and stress concentration at their connection points along the line.

In terms of cost-benefit estimation, [29] used data from a specific report and estimated a reduction of up to 60% in mooring costs with proposed shared mooring layouts. [31] applied a sizing tool to assess the minimum overall procurement costs for mooring chains and drag anchors. [32] analyzed a $2 \times 2$ floating array at different water depths, and developed a cost model for material and installation costs of mooring lines and drag anchors. Their findings showed significant cost savings with shared moorings compared to conventional configurations in water depths exceeding 400 m.

While shared line designs offer cost-saving potentials, they also alter load distribution in mooring lines by coupling multiple FOWTs, which affects their dynamic responses. Existing stiffness-linearized approaches often assume small floater offsets and employ a linear spring model to represent the mooring system [32, 33]. In these approaches, a small prescribed offset is chosen as the only design constraint. The static offset is calculated by dividing a constant wind force over the linearized stiffness matrix, and the mooring line mass per unit length is linearly scaled to meet this offset requirement. These approaches have been adopted in subsequent studies, such as [34, 35].

The stiffness-linearized design method is useful for conceptual designs of shared moorings due to its simplicity. However, it can lead to impractical mooring designs, because it overlooks the key characteristics of mooring lines. Specially, it neglects the nonlinear mooring stiffness that arises from line geometry and material elasticity, and inaccurately scales mooring mass based on linearized mooring stiffness rather than determining it from the chain diameter. For example, [32] calculated a mooring line mass density (mass per unit length) of 26 kg/m, while [33] reported 872 kg/m for shared lines. Both densities fall outside the typical range observed in mooring lines for existing floating wind projects.

Moreover, the reliability of shared line designs generated using the stiffness-linearized method, is highly dependent on the prescribed floater offset. This offset serves as the only design constraint and determines the line mass density by linearly scaling with the linearized stiffness. The offset limit, defined as the maximum allowable floater displacement, is important for dynamic cable design, as excessive displacements can increase cable curvature. However, while larger floater motions lead to greater curvature, studies suggest that this is not a critical factor in determining the fitness of dynamic cables. Instead, the cable's orientation relative to the floater plays a more significant role [36].

Supporting this, 1-year field observations of a 100-kW FOWT have shown that dynamic cables remained safe operation without failures, even as the floater moved up to 21 m during typhoon seasons, in water depths ranging from 80 m to 100 m [37]. In addition, simulations of a 2-MW FOWT at the same site indicated that dynamic cable could operate safely even when offsets reach up to 40 m [37]. These findings raise doubts about the validity of assuming small floater offset, as well as the reliability of the stiffness-linearized method that considers the floater offset as the only design constraint.

Furthermore, there is no consensus in current studies on the appropriate offset limit for mooring designs. For example, [38] set an admissible offset of 10 m for a 5-MW tri-floater FOWT using mooring configurations consisting of 6, 9, and 12 lines at various water depths between 50 m to 300 m. Similarly, [32] used a fixed offset of 20 m for shared mooring designs across four different water depths, ranging from 200 m to 800 m. In contrast, [39] optimized a conventional mooring design at a water depth of 330 m, where the optimized design resulted in the maximum dynamic displacements of 49 m in surge and 31 m in sway. In addition, [33] chose 10% of water depth as the offset limit to calculate the linearized shared mooring stiffness, and defined the offset limit as 12% of water depth to adjust the mooring line length.

Therefore, although the stiffness-linearized method is simple and useful for conceptual shared line designs, its reliance on small floater offsets and omission of detailed mooring line characteristic restrict its applicability for reliable shared

line designs. To advance the design and analysis of shared line configurations, a more comprehensive design framework is needed, which should take account for both line and chain parameters, and accommodates a wider range of practical design constraints, rather than relying only on an uncertain offset limit.

## 2.2 Simulation tool for FOWTs

This section reviews studies on simulation tools developed for FOWTs, including both uncoupled and fully coupled analyses. In addition, the current status of modeling floating wind farm is outlined, to highlight the research gap in developing a more efficient simulation approach for the floating wind farm with shared line designs.

### 2.2.1 For an individual FOWT

Numerous simulation tools have been developed to analyze individual FOWTs under various environmental conditions. Some of these are uncoupled simulations, which focused on specific aspects such as turbine performance, and often neglected the couplings among structural components. For instance, [40] simulated the power output of a TLP FOWT using three different aerodynamic models, which predicted higher variation than experimental results. In that study, the first-order derivative of measured floater surge motion was used to adjust the relative wind speed, while hydrodynamic forces on the floater and the structural dynamics were neglected. In contrast, fully coupled simulations can capture more dynamic responses of the entire FOWT system than those uncoupled analyses, by considering the fluid-structure interactions and couplings among the structural components. Common simulation tools used for fully coupled analyses of individual FOWTs range from high-fidelity Computational Fluid Dynamics (CFD) solvers to mid- and lower-fidelity engineering models.

High-fidelity tools are better suited for in-depth investigations of unsteady dynamics and fluid-structure interactions. They are often used for verification studies, with complicated simulation setup and high computational demands. For instance, [41] developed a coupled CFD tool to analyze a semi-submersible FOWT, with focuses on mutual interactions between the turbine performance and platform motions. Similarly, [42] investigated the impact of dynamic floater motions on unsteady aerodynamic power, and the effect of aerodynamic forces on hydrodynamic responses through fully coupled simulations of a 5-MW semi-submersible FOWT. These studies highlight the advantage of CFD tools in detailed aerodynamic phenomena, which cannot be accurately captured by mid- and lower-fidelity engineering models.

Compared to high-fidelity CFD simulations, mid-fidelity tools provide advantages in computational efficiency and often simplify aerodynamic, hydrodynamic, and structural elastic calculations. For instance, the aerodynamic module in OpenFAST [43] simplifies the complex 3-D flow around turbine blades by approximating it as local 2-D flow at blade cross sections. [44] validated a physics-based digital twin solution using OpenFAST simulations against measurements from the TetraSpar prototype. Results showed that the averaged errors in predicted tower damage equivalent loads ranged from 10% to 15%, which is acceptable for preliminary performance evaluation.

Lower-fidelity numerical tools, such as reduced-order models, are often more appropriate than high- and mid-fidelity tools in the early design stages, due to their computational efficiency. These tools are useful when fast simulations, broader parametric explorations, and large numbers of tests are required. While they simplify the physical modeling, they still capture the fundamental dynamics of FOWTs and provide acceptable accuracy. For instance, [45] applied a reduced-order model to simulate a scaled 10-MW FOWT equipped with tuned liquid multi-column dampers, and validated the simulation results against experimental data from wave tank tests.

### 2.2.2 For an array of FOWTs

Expanding the simulation from a single FOWT to an entire floating wind farm introduces several challenges, such as modeling the operating environment, including the farm-scale wind field, the wake dynamics, and the interactions between FOWTs, particularly in shared mooring designs. To predict the dynamic performance of floating wind farms with shared line designs, various simulation tools have been proposed in existing studies to meet different research objectives.

Some studies have neglected wake effects and focused on the influence of different mooring configurations. For example, a four-turbine floating array with shared line designs was analyzed using integrated simulations with FAST and ANSYS AQWA [30, 46]. Similarly, two semi-submersible FOWTs with a shared line design were simulated in Simpack [47], while dynamic simulations of two spar-type FOWTs were performed using HAWC2 [48] and SIMA [49]. In each of these studies, the wake effects from upstream turbines were not considered, as the research objective was to evaluate mooring configurations.

However, studies have proved that the wake effect is significant for the performance of the downstream turbine [50, 51], and for the overall wind power production of the entire wind farm [52, 53]. Therefore, to accurately predict the dynamic performance of the floating turbine array with shared line designs, it is essential to take wake effect into considerations. In FAST.Farm, the dynamic wake model is utilized to capture the wake-deficit evolution, the wake meandering and wake-added turbulence, all of which are crucial for the predictions of loads and performance [54]. Examples of FAST.Farm applications for dynamic analysis of a floating wind farm include the investigations into the influence of shared mooring designs on a ten-turbine floating array [34, 35].

As a mid-fidelity simulation tool [54], FAST.Farm requires considerable computational effort to account for wake interactions during the dynamic analysis of floating wind farms. This issue becomes more pronounced when large-scale wind farms are analyzed or parametric studies of system-level investigations

are conducted, as dynamic simulations can be both computationally intensive and time-consuming. Therefore, an efficient simulation tool that significantly reduces computational effort while maintaining sufficient prediction accuracy is highly beneficial for early-stage analysis of floating wind farms.

## 2.3 Optimization strategy for FOWTs

This section reviews the optimization strategies applied to the wind turbine, floater, and mooring system for FOWTs. A focus is placed on the mooring optimization, aiming to identify current research objectives and methodologies. The review also highlights a critical research gap: a limited investigation of long-term mooring integrity through time-domain analyses of FOWTs that account for both the wake effects and the dynamic interactions among connected FOWTs.

### 2.3.1 Turbine optimization

The optimization strategies for wind turbines have been thoroughly reviewed by [55]. According to this review, in turbine performance optimization, the objective function has evolved from maximizing the power coefficient in earlier studies, to enhancing annual energy production and minimizing the cost of energy, with the goal to improve cost-competitiveness. The cost of energy refers to the cost per kWh, taking into account the total expenses incurred over the lifetime of the wind turbine. In addition to the single-objective optimization that minimizes the cost of energy, multi-objective optimization approaches have also been explored, which typically integrates cost minimization with objectives related to airfoil shape design and blade performance refinement.

### 2.3.2 Floater optimization

The evolution of platform designs employed in FOWTs has been reviewed by [56], with a focus on the floater configurations across wind farm, prototype and demonstrate scales. According to this review, two dominant goals of platform designs are maintaining stability and minimizing costs. For the first objective, hydrostatic analysis is useful for stability evaluation, while controlling platform motions under extreme environmental conditions remains a primary design focus. Since the four main floater types exhibit different dynamic responses, their motion-reduction strategies differ accordingly. For instance, semi-submersible platforms exhibit larger heave motions than other types. To address this, heave plates are used in WindFloat platform, which is a typical semi-submersible floater, to mitigate heave motions.

The second design objective focuses on reducing material costs and enhancing turbine performance to lower the Levelized Cost Of Energy (LCOE). The review highlights that FOWT designs tend to be more cost-driven than those in the offshore oil and gas industry. An example is the Hywind Tampen project, which utilizes a concrete-based floater from a local supply chain to reduce capital expenditure per MW.

### 2.3.3 Mooring optimization

Mooring optimization in the offshore oil and gas industry typically aims to reduce the number of mooring lines and adjust their dimensions to minimize material and installation costs, as well as platform offsets. Design variables such as anchor radius, chain length, and pretension are considered in the optimization process [11, 57]. While these design principles are carried over to the floating wind sector, the focus shifts from reducing the number of lines to optimizing line orientation and length.

For example, [58] applied a gradient search method to optimize the spar, mooring lines, and cables. The mooring design variables included line direction, pre-

tension and anchor radius, while their constraints accounted for mooring load limit and minimum fatigue life. The FOWT was analyzed in frequency domain, with the mooring forces calculated by the quasi-static model, the aerodynamic forces proportional to relative velocity, and the hydrodynamic coefficients obtained from an external tool. During the spar and mooring optimization, power cables were not included. Their findings highlight the importance of considering mooring fatigue in optimization process.

Similarly, [39] optimized catenary mooring lines for a semi-submersible FOWT using Nelder-Mead simplex algorithm. Design parameters included horizontal distance between fairlead and anchor, as well as mooring line length and orientation. Design constraints included ultimate mooring load, platform offset and the safety requirement of drag embedded anchors, which can only withstand horizontal loading. Mooring forces were calculated by the quasi-static catenary equations, and the mooring stiffness was linearized at the equilibrium position. Their study suggests that the linearized mooring stiffness leads to overestimated floater motion, and recommends to perform time-domain simulations for more accurate mooring optimization.

While frequency-domain analysis is computationally efficient and commonly used, time-domain analysis provides a more detailed representation of dynamic responses. Despite this advantage, the high computational demand of time-domain analysis has limited its application in mooring optimization for FOWTs. This challenge is further amplified when it comes to optimizing shared line systems. Few studies have conducted FOWT mooring optimization in time domain. Simplified models have been employed in existing studies, for instance, a simplified mooring model has been combined with a low-order simulation tool to support FOWT substructure optimization in time domain [59]. Although some studies have applied time-domain analysis to other types of floating structures, these optimization studies have focused on extreme loading conditions rather than long-term fatigue performance.

For instance, [60] optimized a single-point mooring system for a vessel-shaped fish farm using time-domain analysis. Design variables included horizontal dis-

tance between fairlead and anchor, segment length and size, and design constraints were similar to those in [39], with additional requirements on floater excursion and wire rope clearance from the seabed. To reduce the computational effort, a quasi-static mooring model was used for screening analysis, which reduced the sample number by 40%. A gradient-based optimization algorithm, Sequential Quadratic Programming, was employed in conjunction with the Kriging metamodels to search for the optimal design.

In addition, [61] integrated mooring-riser designs for a deep-water floating production system in the oil and gas industry, and optimized the platform offsets to match the safe operation zone for risers through time-domain analyses. Design variables for the mooring system include the line orientation, line radius, pretension and polyester cable diameter. Design constraints involve the maximum offset, the maximum and minimum line tension, and touch-down point clearance. Particle Swarm Optimization (PSO) is employed with the $\epsilon$ -constraint method to search for the feasible solution of mooring configurations.

# 3 FOWT systems and performance factors

This chapter provides a fundamental background on FOWTs in Section 3.1 and explores several key factors influencing FOWT performance. These include mooring systems in Section 3.2 and environmental conditions in Section 3.3. A solid understanding of these factors is essential for evaluating the performance of FOWTs, as introduced in Section 3.4.

## 3.1 Offshore wind turbines

A wind turbine is a power generation device that converts the wind kinetic energy into the rotor mechanical energy, then transforms this rotational energy into the electrical energy. As the demand for renewable energy continues to grow, FOWTs presents a promising solution to harness wind power in deep waters, where fixed-bottom turbines are not economically feasible.

A typical FOWT mounts a single turbine on top of a tower, while a new FOWT concept with dual turbines has been installed [62]. The turbine and tower are supported by a floating platform, and their station-keeping forces are provided by the mooring system, to ensure floater motions within allowable limits. The primary structural components, such as the nacelle, rotor and tower, remain similar to those used in bottom-fixed turbines.

Unlike offshore bottom-fixed turbines, which are limited to shallow waters, FOWTs can operate in deep-sea environments, with their substructures anchored to the seabed using mooring systems, allowing deep-sea deployments to harvest stronger and more consistent wind resources. Typical examples of offshore wind turbines are illustrated in Figure 3.1.

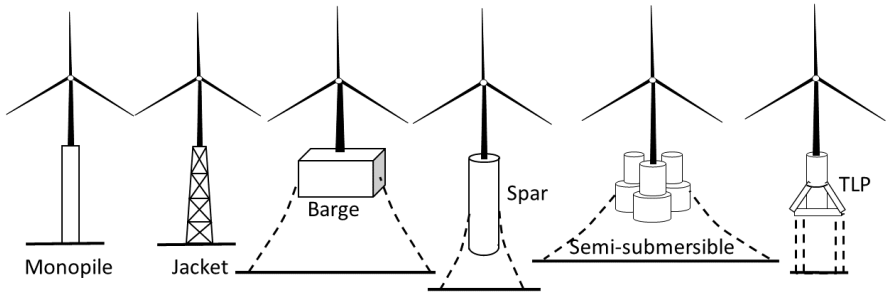


Figure 3.1: Examples of offshore wind turbine concepts, from left to right: bottom-fixed wind turbines using a monopile and a jacket, and FOWTs using a barge, a spar, a semi-submersible, and a Tension Leg Platform (TLP).

As the majority of offshore wind resources are located in deep waters, the advancement of FOWTs presents a promising opportunity to meet future wind energy demands. Prototypes such as Hywind Demo (later renamed "Unitech Zefyros" [63]) paved the way for commercial-scale projects. Since then, various FOWT concepts have been introduced. Examples include Hywind Demo [64], WindFloat 1 [65], Floatgen [24], and TetraSpar [66]. These designs focus on improving power production and reducing the high costs associated with the deep-sea deployment.

Several floating wind projects have demonstrated the technical feasibility of FOWTs, such as Hywind Scotland [8], Kincardine Offshore Wind Farm [7], and WindFloat Atlantic [67]. Large wind turbines have been developed to reduce the LCOE, which is strongly influenced by capital cost factors, such as the manufacture costs of the wind turbine, platform, and mooring system [68]. The rated capacity of individual FOWTs has increased from 2.3 MW in Hywind Demo [63] to upgraded 8.6 MW in Hywind Tampen [9]. Recently, a 20-MW FOWT prototype has been installed [69].

To accommodate the growing size of wind turbines, supporting platforms have been designed to improve their stability and reduce costs. Four main types of supporting platforms, as shown in Figure 3.1, including barge, spar, semi-submersible, and Tension Leg Platform (TLP), have been employed in existing floating wind projects from 2007 to 2023 [56]. Barges have a wide water-plane area with a shallow draft, while spars use a ballasted cylinder with a deep draft. TLPs use taut mooring systems, while semi-submersibles often use catenary mooring designs. Among these four types, semi-submersibles are the most widely deployed in floating wind farms, followed by spars. Semi-submersibles offer advantages during tow-out and installation, and often require less material than spars. However, they have drawbacks, such as a large seabed footprint and a large heave motion. TLPs have only been demonstrated in the Blue H project [70], which install a two-bladed turbine. They remain at a low technical readiness level and are not yet considered as a proven solutions for FOWTs [56].

## 3.2 Mooring systems

Mooring systems are essential for the stability and safe operation of floating wind farms, providing station-keeping forces to counteract harsh environmental loads and maintain floater motions within allowable limits. Figure 3.2 shows the basic conventional mooring systems for FOWTs. Both taut and catenary mooring configurations include fairleads that connect mooring lines to the platform, and anchors fasten the lines to the seabed.

Compared to taut mooring systems, catenary mooring systems possess larger seabed footprints, with part of the line resting on the seabed. This design has been adopted in semi-submersible FOWTs, such as in the floating wind projects Hywind Scotland [8] and Kincardine [13]. In contrast, taut mooring systems often depend on line tensile stretch and have no lay-down length at static equilibrium, as demonstrated in the TLP FOWT of Blue H project [70].

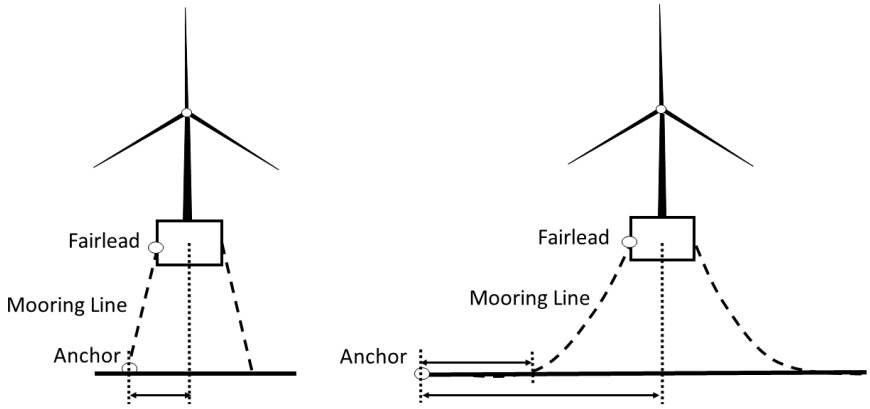


Figure 3.2: Basic conventional mooring systems for FOWTs, from left to right: taut mooring without a lay-down length on the seabed, and catenary mooring with a footprint on the seabed.

### 3.2.1 Fairlead

The fairlead can be either fixed or rotational, with the latter allowing pitch and yaw rotations around its bearing axis. Fixed fairleads may cause chain wear in the short term, whereas rotational fairleads can reduce loads and mitigate fatigue damage. Figure 3.3 illustrates an example of an eccentric chain fairlead that can be used in the drilling and production structures.

Figure 3.3: An eccentric chain fairlead [71].

### 3.2.2 Anchor

Among the anchor types used in offshore oil and gas projects, drag embedment anchors are most commonly applied for drilling units, because of their ease of deployment and retrieval without specialized assistance [11]. In the floating wind sector, both drag embedment anchors and suction anchors, as shown in Figure 3.4, are widely deployed. For example, drag embedment anchors have been used in the projects of Floatgen [72] and WindFloat Atlantic [73], while suction anchors have been employed in the Hywind Scotland Pilot Park [8] and Tampen [10] projects.

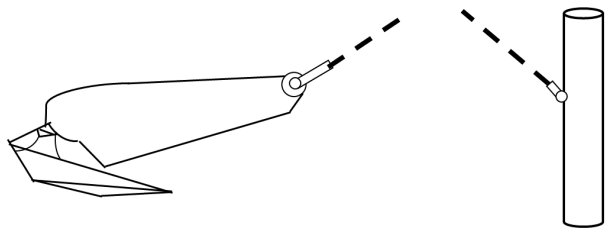

Figure 3.4: Examples of drag embedment anchors (left, adapted from [74]) and suction anchors (right, adapted from [75]). The dashed line indicates the mooring line fastened by the anchor.

Two primary considerations for anchor designs are the structural maximum load and the geo-technical holding capacity associated with soil-structure interaction. Drag embedment anchors are not designed to withstand vertical loads, while suction anchors are limited to soft clay soil and require a longer installation time [11]. Beyond structural and geo-technical considerations, cost also plays a role in anchor selection, as both the material and installation costs of suction anchors are higher than those of drag embedment anchors [76].

### 3.2.3 Line material

Similar to anchor designs, the choice of mooring line materials, such as steel chains, wire ropes and synthetic ropes (nylon, polyester and high-modulus polyethylene), is also influenced by the environmental condition, such as water depth. Examples of mooring line materials [77] are shown in Figure 3.5.

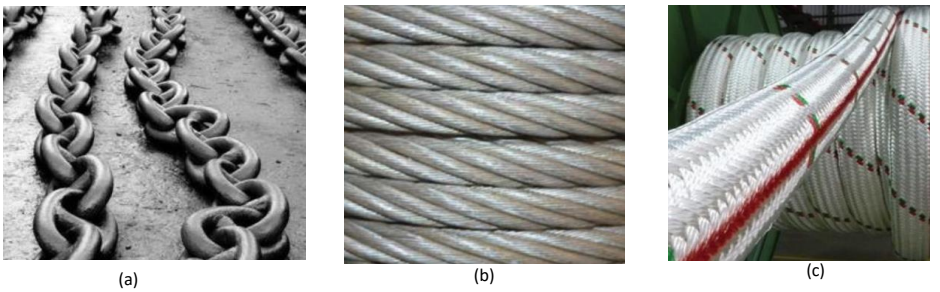


Figure 3.5: Mooring line materials [77]: (a) steel chain links; (b) wire ropes; (c) synthetic ropes.

The mooring line materials employed in the floating wind projects [78] are summarized in Table 3.1, with increasing water depths. Steel chains, wires, and synthetic ropes have been used in the mooring configurations at water depths of up to 300 m. In contrast, for offshore oil and gas structures at similar depths, the all-chain catenary mooring design is the most cost-effective solution [11].

Wire rope is lighter than steel chain and is often used as the suspended portion of the mooring configuration. But it could suffer from excessive bending when it is placed at the touch-down point on seabed. Synthetic ropes can reduce mooring weight, but some materials, such as polyester ropes, experience permanent elongation due to bedding-in and creep, which affects the rope length and stiffness [11].

Table 3.1: Mooring designs for floating wind projects (adapted from [78]).

| Project | Depth | Floater | Mooring system |
|---|---|---|---|
| Three Gorges | 30 m | Spar | 9 lines: wire, chain |
| Floatgen | 33 m | Barge | 6 lines: synthetic fiber |
| Eolink demonstrator | 36 m | Semi* | Single point: polyester |
| WindFloat I | 49 m | Semi | 4 lines: wire, chain |
| Hibiki | 50 m | Barge | 4 lines: chain |
| Fuyao | 65 m | Semi | 9 lines: R3 chain, M2 chain |
| Kincardine | 80 m | Semi | 4 lines: polyester |
| DemoSATH | 85 m | Barge | Single point, 6 lines: fiber, chain |
| WindFloat Atlantic | 100 m | Semi | 3 lines: HMPE, chain |
| Hywind Scotland | 105 m | Spar | 3 lines: R4s-chain |
| Fukushima Mirai | 120 m | Semi | 6 lines: chain |
| Hywind Demo | 220 m | Spar | 3 lines: wire, R4-chain |
| TetraSpar | 220 m | Spar | 3 lines: synthetic rope, chain |
| Hywind Tampen | 300 m | Spar | 3 lines: wire, R3-chain |

**"Semi" is an abbreviation for semi-submersible floater.*

### 3.2.4 Chain link type

For mooring lines made of steel chains, their links can be either stud or studless types. A stud chain link is shown in Figure 3.6, where the term "Stud" refers to the component welded to the chain link. The cross-sectional diameter corresponds to the chain nominal diameter $D_c$, while the equivalent diameter, derived from the volume per unit length of the line, is $1.8 \times D_c$ for studless links and $1.89 \times D_c$ for stud links [79].

The design and manufacturing requirements for stud and studless mooring chains are detailed in offshore standards. The presence of stud increases the submerged mass per unit length and axial stiffness compared to those studless links of similar chain diameters [80, 79, 11]. As a result, adding a stud can help mitigate the stress concentrations in the stud links. However, after prolonged use, the frequent loosening of the stud may result in high stress concentration at the connection point, reducing the fatigue performance of the chain link [11].

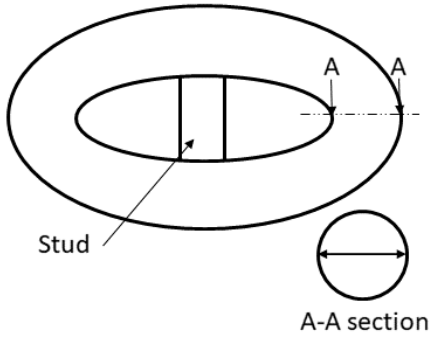


Figure 3.6: A stud chain link (adapted from [80]).

### 3.2.5 Mooring in oil & gas and floating wind sectors

Compared to floating wind projects, offshore oil and gas applications typically use more robust mooring designs governed by stricter safety requirements. These designs often feature more lines to withstand harsher environmental conditions in deeper waters. Table 3.2 compares mooring configurations of a deep-water drilling and production project, Hoover-Diana spar, and of a floating wind project, Hywind Scotland, to highlight key design differences between these two sectors. Both projects utilize spar-type platforms.

Table 3.2: Project and mooring differences between the Hoover-Diana spar [81, 82] and the Hywind Scotland projects [83, 75, 8].

| Variable | Hoover-Diana spar | Hywind Scotland |
|---|---|---|
| Project cost | 1.1 billion USD | 2.0 billion NoK |
| Production start-up | in 2000 | in 2017 |
| Site water depth [m] | 1463 | from 98 to 117 |
| Spar hull weight [t] | 35000 | 10000 |
| Mooring line number | 12 | 3 |
| Mooring line length [m] | 2164 | from 691 to 875 |
| Mooring line material | chain + wire rope | chain |

Table 3.2 indicates the distinct mooring design requirements of the offshore oil & gas industry compared to the floating wind sector. Assuming a currency exchange rate of 10, the project cost of the Hoover-Diana spar is approximately

5.5 times that of the Hywind Scotland project. With its heavier structure and operation in water depths exceeding 1000 m, the consequences of mooring failure are far more critical for the Hoover-Diana, compared to those of FOWTs in the Hywind Scotland project, which are located in water depths shallower than 200 m. As a result, to ensure safe operation under harsher environmental conditions, the Hoover-Diana spar employs a more robust mooring system comprising 12 lines made of both chain and wire rope. In contrast, the lighter FOWTs in the Hywind Scotland project are anchored by three mooring lines made up of steel chains.

### 3.2.6 Shared mooring designs

The shared mooring concept has been developed in two forms: using either a shared anchor for multiple mooring lines or a shared line for multiple FOWTs. The shared anchor design, where a single anchor secures multiple lines, has been implemented in the floating wind project Hywind Tampen [9], where 11 FOWTs were fastened by 19 anchors [84, 85], compared to the 33 anchors that would be required using conventional three-line configurations for each FOWT. Part of the shared anchor layout [85] is shown in Figure 3.7.

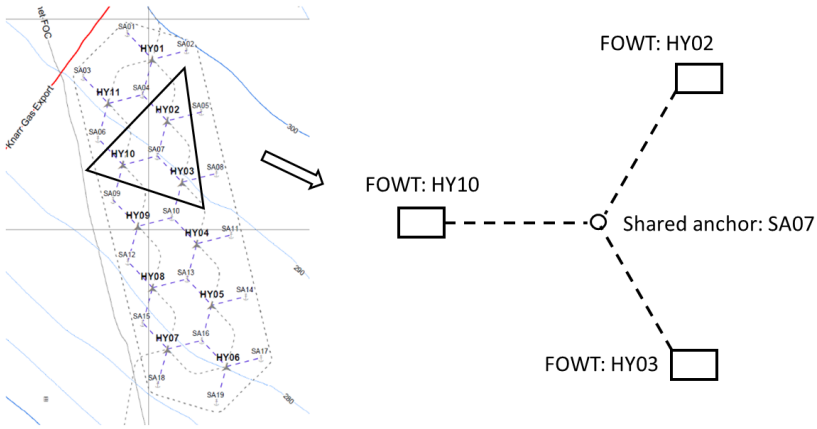


Figure 3.7: Shared anchor layout for the Hywind Tampen project (adapted from [85]), illustrated with an example array of three FOWTs using a shared anchor. The dashed lines represent mooring lines.

The shared line design is still in the research stage. Compared to conventional configurations, a shared line design has the potential to reduce both the number of anchors and the length of mooring lines.

Figure 3.8 shows a two-FOWT array using a shared line and 4 anchor lines. In this configuration, the shared line connects fairlead 1 on FOWT1 to fairlead 2 on FOWT2, eliminating the need for an anchor. This shared line configuration has been investigated through both numerical simulations [47, 86, 48] and experimental studies [87] to assess FOWT performance. The shared line may be partially in contact with the seabed [47] or entirely suspended in seawater [47, 86].

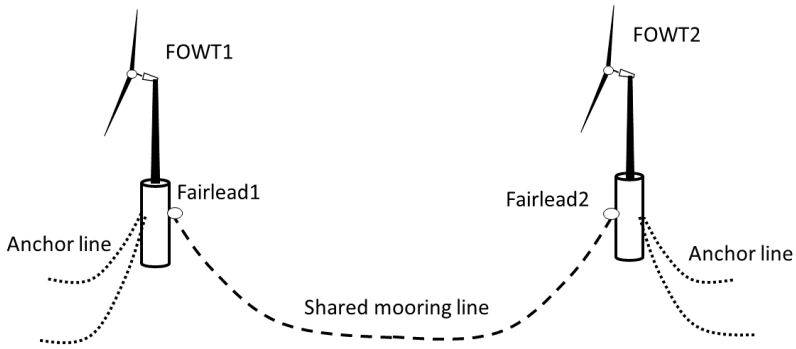


Figure 3.8: Shared line layout for a two-turbine array using a shared line and 4 anchor lines.

## 3.3 Environmental conditions for FOWTs

A floating wind farm operates in the open sea and is continuously subjected to environmental loads from wind and waves. As a power generation device, the turbine converts wind energy into electricity, while these environmental forces act on the turbine, tower, platform and mooring system, and excite motions that affect power output and cause fatigue damage to the structural

components over time. Therefore, it is essential to understand the nature and influence of these environmental factors in order to maintain safe and efficient operation of FOWTs.

### 3.3.1 Wind

Wind is the movement of air, with a wide range of scales in time and space. For example, a spring breeze in a park may last for a few minutes, while a catastrophic typhoon can persist for several hours. Turbulence of wind describes speed variations and results from friction with the Earth's surface and thermal effects. On a large scale, the spatial variability of wind reflects the diversity of global climate regions, while within a specific region, geography affects solar radiation, which in turn influences surface temperatures and humidity. For a given site of interest, the long-term variability makes it difficult for accurate wind prediction, but within a shorter time frame, such as shorter than 1 year, the seasonal variations become more predictable [88].

Wind plays a critical role in FOWT performance, as the primary function of a FOWT is to harvest wind energy and generate electricity. The produced power changes cubically with wind speed. To maximum power production while preventing mechanical overload, it is important to control the FOWT, for instance by adjusting the rotor speed and blade pitch of the turbine. In addition, as the wind direction changes, the turbine's yaw system aligns the rotor, since a yaw misalignment can lead to unbalanced loads on the blades and reduce power production. Wind also induces cyclic loadings on structural components such as blades, which can result in fatigue damage and compromise structural safety over time. Therefore, accurate wind reconstruction is essential for assessing FOWT performance and ensuring FOWT safe operation.

### 3.3.2 Wake

Within the wind field of a floating wind farm, the presence of a turbine slows the upstream inflow, causing the wind to propagate downstream with reduced speed and decreased static pressure. This region of the distributed flow is known as wake. Between the far-upstream and far-wake regions, static pressure maintains approximately constant, but kinetic energy drops. Wake characteristics are collectively determined by the upstream inflow conditions and FOWT performance, and are typically featured reduced wind speed and increased turbulence [88].

Due to the limited spacing between FOWTs, downstream turbines are often located within the near-to-far wake regions of upstream turbines. These wakes significantly reduce the power production of downstream turbines. Measurements from the offshore wind farm Middelgrunden [89] indicate that the second turbine, located within the wake region of the first turbine, produces only 20% of the power generated by the upstream turbine under two main wind directions. For floating wind farms, it has been observed that the wake of a 6-MW FOWT remains detectable at a distance of $9Dr$ downstream [90]. Therefore, it is important to account for wake effects when evaluating the performance of floating wind farms.

### 3.3.3 Wave

Ocean waves are undulations of the sea surface, primarily generated by winds blowing across it. Sea waves are created by local winds, while swells denote the waves produced from distant sources. Earthquakes can create tsunamis or seismic waves, while the gravitational pull of moon and sun produces tides. Waves are characterized by their periods, wavelengths, heights, and propagation directions. A wave classification [91] is presented in Table 3.3.

In general, wind-induced waves have a period of less than 25 s, and gravity is important to wave propagation. In deep seas, the wave traveling speed depends

Table 3.3: Waves classified by their periods ranging from seconds to days (adapted from [91]).

| Wave | Period | Cause |
|---|---|---|
| Chop | 1-10 s | Local winds |
| Swell | 10-30 s | Distant storm |
| Seiche | 10 min - 10 hr | Wind, tsunami, tidal resonance |
| Tsunami | 10 min - 1 hr | Underwater disturbance |
| Tide | 0.5-1 day | Gravitational attraction of Sun and Moon |

on its period, and the wave particles beneath the surface move in circular orbits. However, in shallow waters, the wave orbital movements interacts with the seabed, which creates friction, and consequently wave propagation depends on the water depth [92].

Waves can continue to grow in size until they reach a maximum limit determined by the wind speed and its fetch, which represents the sea area where the wind blows. At this growing stage, the sea is considered fully developed [91]. The sea state codes for marine crafts [93] are summarized in Table 3.4.

Table 3.4: Definition of sea state codes with worldwide occurrence probability for marine crafts (adapted from [93]).

| Code | Sea condition | Wave height | Probability |
|---|---|---|---|
| 0,1,2 | Calm, smooth | up to 0.50 m | 11.2486 |
| 3 | Slight | 0.50-1.25 m | 31.6851 |
| 4 | Moderate | 1.25-2.50 m | 40.1944 |
| 5 | Rough | 2.50-4.00 m | 12.8005 |
| 6 | Very rough | 4.00-6.00 m | 3.0253 |
| 7 | High | 6.00-9.00 m | 0.9263 |
| 8 | Very high | 9.00-14.00 m | 0.1190 |
| 9 | Phenomenal | over 14.00 m | 0.0009 |

Waves excite floater motions and influence the stability of the turbine. Excessive floater motions can reduce power production and even lead to structural

failure. For example, floater pitch motion affects the relative wind speed and directly impacts turbine performance. In addition, excessive floater surge can increase cable curvature and the risk of cable failure. Furthermore, waves affect mooring dynamics and generate cyclic loading on mooring lines, which induces fatigue damage over time.

### 3.3.4 Current

Currents describe the continuous movement of seawater, varying in strength and scale across different regions. The current connectivity is important for marine ecosystems. Currents are driven by wind, Earth's gravity, and Earth's interactions between the Moon and the Sun. In addition, spatial differences in seawater, such as temperature and salinity, as well as interactions with eddies and internal friction, can generate currents. Earth's rotation further causes the turning of currents on time scales beyond a few hours [94]. In coastal regions and fjords, the speed of tidal currents can reach 2–3 m/s or higher [93].

Three types of currents affect the operation of floating structures, including ocean, tidal, and storm surge currents. Ocean currents refer to the movement of both surface and deep ocean waters, driven by gravity and variations in seawater properties. Tidal currents are strongest in straits and deep waters. Similarly, storm surge currents reach their peak strength in confined areas and deep waters, generated by wind shear and barometric pressure gradients over storm-affected regions [11]. These currents generate drag forces on both the floating platform and its mooring system, proportional to the square of the current velocity. The current force increases the mean static load, produces low-frequency excitation and damping, and contributes to the slow-drift motion of the floater. In addition, currents can cause vortex-induced motion of the cylinder columns, which is relevant to spar and TLP platforms [11].

## 3.4 FOWT performance evaluation

This section provides a brief overview of the measurements, experiments, and simulations carried out on FOWTs. Since only a few floating wind projects publicly share real-time performance data on the turbine, tower, floater, and mooring system, the available information is limited. Model tests have been conducted for various FOWT concepts, with real-time hybrid models used to address the mismatch scaling issue. Numerical simulations are categorized by different fidelity levels to meet design targets at various design phases.

### 3.4.1 Measurement-based evaluation

Lidar measurements have provided reliable wind speed estimates and produced a power curve comparable to that obtained from sonic measurements. For example, [95] utilized a nacelle-based lidar to measure the power curve of a 2-MW FOWT. During the five-month measurement campaign, wind data collected by the lidar was used to reconstruct the wind field. Similarly, [90] investigated the wake of a 6-MW FOWT using lidar measurements.

In addition to lidar-based wind speed measurements, temperature has also been used as an indicator to study wake influences on the dynamic performance of downstream FOWTs. For instance, measurements from the Hywind Scotland floating wind farm showed clear wake effects on the standard deviations of floater motions. They further revealed that wake impacts vary under different atmospheric stability conditions, as indicated by temperature differences between the measurements at the nacelle and the wave buoy [51].

Finally, to maintain FOWT structural integrity is crucial for safe operation, making it important to monitor the loading conditions of key components. For example, [44] investigated the tower structural health of the TetraSpar prototype by monitoring the tower bending moment using load cells installed at the top, middle, and bottom of the tower, along with nacelle wind speed measurements.

### 3.4.2 Experimental investigation

FOWTs endure multi-disciplinary loads, including aerodynamic forces from wind on the turbine and tower, hydrodynamic forces from waves and currents on the floater and mooring system, and elastic forces between their structural components. This multi-disciplinary nature poses challenges in model tests, since the aerodynamic and hydrodynamic loads follow the Reynolds and Froude scaling laws, respectively, which cannot be satisfied simultaneously.

For model tests that adhere to the Froude scaling law, the primary challenge is accurately modeling aerodynamic loads. This scaling mismatch can be addressed either by a physical model in a wave basin with equivalent treatment for aerodynamic loads under the Froude scaling law, or by a real-time hybrid model that uses simulation results to replace actual loads [96]. Physical models include a thrust disk, geometry-match blades, and performance-match blades. They have been used in the model tests for floating wind projects, such as the thrust disk in WindFloat [97], geometry-match blades in OC3-Hywind [98], and performance-match blades in GICON [99].

Two types of real-time hybrid models have been used in FOWTs experiments [96]. The first type replaces the turbine model with a system that computes equivalent aerodynamic forces, and applies these forces to the scaled substructures in the wave tank for real-time measurements. For instance, [100] computed the aerodynamic thrust by running simulations in FAST, based on the measured floater motions from the wave tank tests. And the calculated thrust was applied to the fan controller to adjust the fan status.

The second type models the substructures (platform and mooring system), and conducts tests on the scaled turbine and tower in the wind tunnel, with the floater motions controlled by actuators. An example is the wind tunnel test of a scaled 10-MW turbine [101]. In their tests, the aerodynamic forces were measured from the wind tunnel tests of the scaled turbine, while the forces measured at the tower-base together with the hydrodynamic loads, served as

inputs for numerical simulations of platform and mooring line. The resulting floater motions were then imposed to the turbine model.

### 3.4.3 Numerical simulation

Compared to measurements and experiments on FOWTs, most studies have focused on numerical simulations. Fully coupled analyses have been conducted to investigate the performance of different FOWT concepts under various environmental conditions. These simulations capture the fluid–structure interactions by solving equations, providing an initial assessment of the FOWT design. They encompass a broad range of research topics and serve as an important complement to experimental tests and prototype operations.

Research topics include design refinement of FOWT structural components, such as airfoils [102], towers [103], platforms [104], mooring lines [16], and anchors [105]. Other studies focus on structural response prediction, for instance, tower-base fatigue [106], floater motion [47], and mooring performance [15]. In addition, research has also addressed control design, including active blade pitch control [107], generator torque control [108], and tuned dampers [45].

Simulation tools can be classified by fidelity level, ranging from low to high. High-fidelity tools have the highest prediction accuracy in capturing fluid–structure interactions but require the highest computational resources. They are typically employed in the final verification stage, where detailed modeling of the FOWT is essential. Examples of high-fidelity approaches include coupled CFD simulations and real-time hybrid experimental models [96, 109].

Middle-fidelity tools are often applied in the validation and refinement design phases, as they can account for structural flexibility, analyze system dynamics, and capture aero-hydro-servo-elastic coupling. Compared to high-fidelity tools, they offer a balance between prediction accuracy and computational efficiency. Examples of middle-fidelity tools include OpenFAST [43] and HACW2 [110].

Low-fidelity tools are commonly used in the preliminary design stages to provide quick assessments, making them suitable for parametric study or analyses that require iterative or computationally intensive runs. These tools often rely on quasi-static or steady-state analyses, empirical methods, or reduced-order state-space models [109]. Examples include SLOW [111] for modeling individual FOWTs and FLORIS [112] for wind farm control.

# 4 FOWT modeling and simulation

Wind turbines convert wind kinetic energy into mechanical energy through blade rotation. The mechanical energy drives the rotor and generator to produce electrical power. To ensure stability in deep waters, FOWTs are connected to mooring systems that provide station-keeping forces under varying environmental conditions. As a result, the modeling and simulation of FOWTs involve multiple disciplines. This chapter focuses on FOWT modeling and simulation, covering system dynamics in Section 4.1, environmental modeling in Section 4.2, and simulation tools in Section 4.3.

## 4.1 System dynamics of FOWTs

The multi-disciplinary nature of FOWTs results in complex fluid-structure interactions and dynamic responses, primarily involving the turbine, tower, floater, and mooring lines under varying wind and wave conditions. To accurately capture these phenomena, it is essential to understand the main dynamics of the FOWT system, including aerodynamics, hydrodynamics, structural elasticity, and mooring dynamics.

### 4.1.1 Aerodynamics of wind turbines

To formulate aerodynamic loads on turbine blades, three dominant theories implemented in simulations of FOWTs are Blade Element Momentum (BEM)

theory, Vortex Lattice Method (VLM), and Computational Fluid Dynamics (CFD) [109].

Details on BEM theory can be found in [88]. In BEM theory, the blade is discretized into small elements, each acting as an independent 2D airfoil, without radial interaction between the flow and annuli. The aerodynamic thrust and torque on the blade elements depend on the lift and drag coefficients of each airfoil. Various correction models have been proposed to refine BEM theory, such as dynamic stall for yawed rotors at low tip speed ratios, and tip/root loss factors to account for the effect of a finite number of blades.

Detailed descriptions of VLM are available in [113]. VLM models the wing as a surface with a series of superimposed horseshoe vortices, each inducing velocities at a specific control point. The vortex strengths at all these points satisfy the boundary condition of no-flow through the wing, and they are related to the wing circulation and the pressure differences between the wing surfaces. The integral of these pressure differences determines total aerodynamic loads. Moreover, VLM has been extended to capture the turbulent wake vortex [109].

CFD is a numerical approach that solves the Navier–Stokes equations and computes pressure and velocity at each point within a computational domain. Both direct numerical and large eddy simulations resolve the smallest flow eddies using fine meshes. To reduce computational effort, two simplified rotor modeling methods have been implemented in CFD simulations of wind turbines: the actuator disc model and the actuator line model [109].

### 4.1.2 Hydrodynamics of platforms

Three dominant methods have been developed to compute hydrodynamic loads on the platform, including potential flow theory, Morison equation method, and CFD method [109]. Descriptions of free-surface flow based on potential theory, Morison equation, and wave-induced loads on the platform are detailed in [114].

Potential flow theory assumes that sea water is incompressible and inviscid, with irrotational fluid motion. The velocity of fluid motion is determined by the gradient of a scalar velocity potential. Mass conservation requires a zero-divergence of the velocity, ensuring the velocity potential satisfies Laplace's equation. It must also satisfy the boundary conditions within the fluid domain. Bernoulli's equation establishes the relationship between the hydrodynamic pressure and the velocity potential, so that the wave-induced hydrodynamic forces depend on the fluid motion and the wet surface of the structure.

Potential flow theory neglects viscous effects, which are important for pressure forces due to flow separation, particularly in slender cylindrical structures under extreme wave conditions. The Morison equation is used to account for these viscous effects, with the corresponding hydrodynamic forces determined by the mass and drag coefficients of the structure, as well as the relative velocity and acceleration to the fluid. The empirical mass and drag coefficients depend on both the characteristics of the structure and fluid, such as body form, roughness number, fluid Reynolds number, and the Keulegan-Carpenter number.

Similar to the modeling of aerodynamic loads, CFD method is used to compute the hydrodynamic loads on platforms by solving the Navier–Stokes equations. In contrast to potential flow theory that considers the mean surface, CFD can capture instantaneous free-surface effects, for instance, by the volume of fluid method. In addition, the Reynolds Averaged Navier-Stokes Equations are commonly employed to solve the wave-structure interaction problem [109].

### 4.1.3 Structural elasticity

Details of beam theory for wind turbine blades can be found in [115]. Turbine blades are constructed from multiple layers of different materials, and exhibit elastic deformation (twist and bending) under aerodynamic loads. Beam theory can be applied to compute this structural deformation and capture its eigenmodes in absent of external loads. In turn, blade deformation influences

the aerodynamic forces acting on it, highlighting the aero-elastic interactions for the wind turbine.

Similarly, tower structural flexibility is influenced by both material properties and geometrical design. Further details on tower design can be found in [88]. Tower stresses are dominated by bending stress. Similar to elastic blade analysis, beam theory can be used to model tower elastic deformation. In addition, aero-elastic coupling is important for the tower response. For instance, tower-top displacement affects blade orientation and induces a local velocity, which in turn influence the aerodynamic forces on the blades. Consequently, the varying aerodynamic forces change floater motions, which ultimately affect the tower-base stresses and overall tower deformation.

### 4.1.4 Mooring dynamics

Figure 4.1 illustrates the coordinate system and spatial positioning used for mooring line analysis, including a detailed inset showing the mooring tension force ($T_L$) on a line segment of unstretched length ($ds$). The spatial angle between the line segment and the horizontal plane is denoted as $\varphi$, with $\varphi = 0$ at the touch-down point. The distance from the anchor position to the floater center is defined as the anchor radius, while the distance from the fairlead position to the floater center is defined as the fairlead radius.

The governing equations for calculating mooring line tension forces are given in Equation 4.1. For lines made of steel chains, it is reasonable to neglect bending and torsional stiffness [114].

$$\begin{aligned} dT_L - \rho g A dz &= [\omega \sin\varphi - F_h(1 + T_L/EA)]ds, \\ T_L d\varphi - \rho g A z d\varphi &= [\omega \cos\varphi + D_h(1 + T_L/EA)]ds. \end{aligned} \tag{4.1}$$

where $T_L$ is the mooring line tension force, and its variation due to the unstretched line length $ds$ is denoted as $dT_L$. The variables $dz$ and $ds$ represent

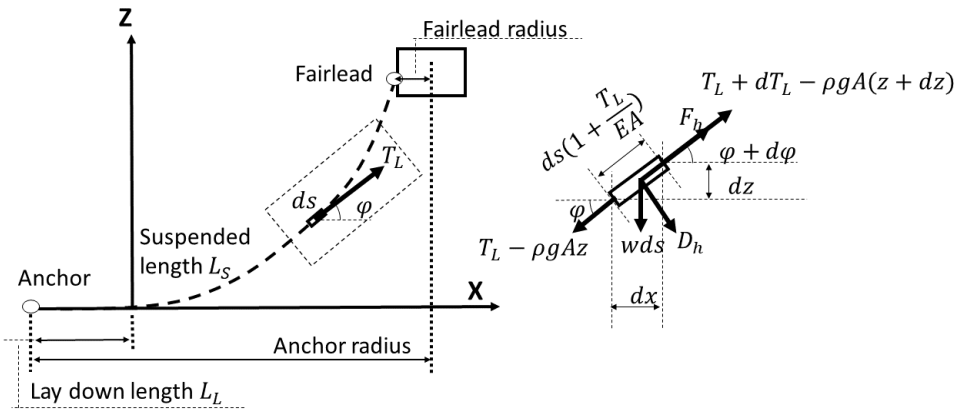


Figure 4.1: Spatial positioning for mooring line analysis, with detailed mooring force components shown on a line segment (adapted from [114, 11]).

the vertical and suspended lengths of the mooring line segment, respectively. The terms $\rho gAdz$ and $\omega ds$ are the change in buoyancy and mooring line weight in water, respectively, due to the segment variables $dz$ and $ds$. The mean hydrodynamic forces per unit segment length, $F_h$ and $D_h$ are disregarded in the quasi-static mooring analysis but are included in dynamic mooring analysis.

Mooring elasticity, which accounts for the elongation of mooring lines under mooring tension forces, plays an important role in mooring performance, but is neglected in the stiffness-linearized design method [32, 33]. The axial stiffness of mooring lines ($EA$, in kN), accounts for this elastic effect, and can be used to estimate the elongation of mooring lines under tension forces ($T_L/EA \times ds$). The axial stiffness is the product of the Young's modulus of the chain ($E$) and the equivalent cross-sectional area of chain link ($A$), as defined in Equation 4.2 [79], where $D_c$ represents the chain diameter.

$$EA = \begin{cases} 0.854 \times 10^8 \times D_c^2, & \text{for studless chain} \\ 1.010 \times 10^8 \times D_c^2, & \text{for stud chain} \end{cases} \tag{4.2}$$

where constant coefficients incorporate the necessary unit conversion so that

$EA$ is directly related to $D_c$. The Young's modulus of the chain is $5.44 \times 10^7$ $kN/m^2$ for studless chains, and $6.40 \times 10^7$ $kN/m^2$ for stud chains, respectively, with the equivalent cross-sectional area equals to $0.5\pi \times D_c^2$ (in $m^2$).

To incorporate $F_h$ and $D_h$, a common numerical approach applies the Morison equations while treating the mooring line as a slender body. [20] introduced a lumped-mass method for modeling lines, where $F_h$ and $D_h$ are computed for line segments using the Morison equations. This lumped-mass model serves as the theoretical basis for MoorDyn, the mooring module of OpenFAST and FAST.Farm, enabling the prediction of dynamic mooring forces [116].

Under turbulent wind and irregular wave conditions, cyclic mooring tension forces can induce significant fatigue damage in mooring lines in the long term. Experiences from offshore oil and gas applications indicate that mooring fatigue is one of the primary sources of failure [11]. Therefore, estimating mooring fatigue damage is essential for ensuring FOWT system integrity and reliability. In this study, fatigue damage is evaluated using an S–N curve, where the stress cycles are identified through the Rainflow-counting method. The relationship between stress and the number of cycles is expressed in Equation 4.3.

$$N_c = \frac{a_D}{S^m} \tag{4.3}$$

where $N_c$ represents the number of stress cycles to failure, and $S$ is the stress range expressed in MPa, calculated as the mooring line force divided by the cross-sectional area of the steel chain links. For studless chains, the S–N curve slope ($m$) is 3, and the intercept ($a_D$) is $6 \times 10^{10}\,\mathrm{MPa}^3$, where the units of $a_D$ follow from the relationship in Equation 4.3. Both the S–N curve formulation and its parameters are based on the offshore industry standard [12].

The cumulative fatigue damage from all stress cycles is then calculated using Miner's rule, as shown in Equation 4.4.

$$D = \sum_{i=1}^{n} \frac{n_i}{N_i} \tag{4.4}$$

where $D$ represents the total mooring fatigue damage calculated as the sum of the individual damage. Each individual damage is obtained by dividing the number of stress cycles $n_i$, corresponding to the stress range $S_i$, by the number of cycles to failure $N_i$, which is derived from the S-N curve for the given stress range $S_i$.

## 4.2 Environmental modeling

A FOWT harnesses wind energy in deep waters and is typically subjected to combined forces from wind, waves and currents. To capture dynamic responses of FOWTs, it is essential to accurately model these environmental conditions. This section presents the models used to represent wind, waves, and currents affecting FOWT performance.

### 4.2.1 Wind model

In analysis of turbines, wind models represent the wind speed variation over time and space. The descriptions of turbulence intensity are based on [88]. Turbulence intensity is defined to quantify the overall turbulence level, as a ratio of the standard deviation of wind speed to the mean wind speed, typically calculated over ten minutes or an hour. This variable is influenced by the ground surface roughness and height above the surface. It also depends on topographical features and thermal effects. Under neutral conditions, wind shear that describes the increase in wind speed with height can be expressed by either a logarithmic or a power law wind profile.

Time series of wind speeds at a specific location can be decomposed using a discrete Fourier transformation, so that the variance of the time history

equals to the spectral power across all frequency samples. Conversely, a time history can be reconstructed for a given power spectral density function, using the inverse discrete Fourier transform. Further descriptions of wind statistical properties can be found in [115].

The descriptions of turbulence spectra and coherence functions are based on [88]. The Kaimal and von Karman spectra are commonly used to characterize the distribution of longitudinal component of wind turbulence, capturing wind speed variations across different frequencies. The Kaimal spectrum features a lower, wider peak compared to the von Karman spectrum. In addition, the Kaimal spectra share the same expression for the lateral and vertical components as the longitudinal component but with different length scales.

Both the Kaimal and von Karman spectra describes the wind variation on one specific point. The cross-correlations between turbulent fluctuations at two specific points can be described by coherence functions, in terms of frequency and separation. An analytical expression for the coherence of speed fluctuations can be derived from the von Karman spectrum, while for the Kaimal spectrum, a simpler and purely empirical exponential model of coherence is often used.

In contrast to the Kaimal and von Karman spectra, the Mann model is derived from a three-dimensional spectral tensor representation of the turbulence, and considers the correlation between the longitudinal and vertical components due to Reynolds stresses. Three-dimensional Fourier transform is used to produce all three components of turbulence simultaneously. Further descriptions of the Mann model can be found in [88].

### 4.2.2 Wake model

The wake effect from an upstream turbine reduces wind speed and increases turbulence for downstream turbines, which results in power losses and higher structural loading on turbines within the wake. In addition, the wake effects of multiple upstream turbines are superimposed within a floating wind farm,

collectively influencing downstream turbines. Therefore, it is significant to model wake effects for simulations of a floating wind farm.

Descriptions about turbulence in wakes are based on [88]. Shear-generated turbulence arises from the velocity gradient between the reduced-speed wind flow in the wake and free flow outside the wake. This speed difference induces mixing between the wake and free flow, which expands the wake region. As the mixed flow propagates downstream, it spreads in a broader but shallower manner until it fully recovers. In addition, turbine-generated turbulence results from tip vortices, characterized by high frequency and rapid decay.

Wake can be broadly classified into near wake and far wake, with further details available in [117, 88]. The near wake region, located close to the upstream turbine, is characterized by complex 3-D unsteady flow behavior. The BEM theory fails to capture these unsteady aerodynamics, while CFD methods that solves the Reynolds-averaged Navier-Stokes equations, are better suited for modeling these dynamic behaviors at a higher computational cost.

Analytical wake models have been proposed for power prediction and the layout design of wind farms. Jensen model is the most widely used [52], and it defines the wind speed deficit as a function of a constant wake decay factor, with the assumption of a linear wake expansion. However, the wake dynamics are not considered in the Jensen model, and require higher fidelity calculations for accurate description of wake.

The Dynamic Wake Meandering (DWM) model [118] has been proposed for predicting both loads and power, incorporating the modeling of quasi-steady wake deficits, wake meandering, and wake turbulence effects. In this model, the wake is treated as a passive tracer, driven by the large-scale turbulence structures within the atmospheric boundary layer. The principles of DWM have been implemented in the reference simulation tool FAST.Farm [54].

Since wind farm layouts are designed to minimize wake losses, downstream turbines are typically located in the far wake, where the velocity deficit follows an approximately Gaussian axisymmetric shape [119]. An analytical wake model

has been proposed to predict the average velocity deficit in turbine wakes, with further details available in [119]. In this model, an exponential function is used to describe the normalized velocity deficit $\frac{\Delta U}{U_\infty}$ as:

$$\frac{\Delta U}{U_\infty} = C(r_x)e^{\frac{-r^2}{2\sigma^2}} \tag{4.5}$$

where $\Delta U$ is the velocity deficit, $U_\infty$ is the upstream undistributed inflow. $C(r_x)$ denotes the maximum normalized velocity deficit at the downstream wake center, $r$ is the radial distance from the wake center, $\sigma$ refers to the standard deviation of the Gaussian-based velocity deficit profiles at each downstream location of $r_x$.

By applying the principles of mass and momentum conservation, $C(r_x)$ is derived as a function of the thrust coefficient $C_T$ and the wake region expansion $\frac{\sigma}{D_r}$. Here, $D_r$ represents the diameter of the wind turbine. A linear wake expansion is assumed to describe $\frac{\sigma}{D_r}$ in terms of downstream location $r_x$, so that $C(r_x)$ is written as:

$$C(r_x) = 1 - \sqrt{1 - \frac{C_T}{8(kr_x/D_r + \epsilon)^2}} \tag{4.6}$$

where the wake growth rate is defined as $k = \frac{\partial \sigma}{\partial r_x}$, and $\epsilon$ denotes the velocity deficit just behind the rotor, which approaches $\frac{\sigma}{D_r}$ as $r_x$ equals zero. $\epsilon$ is a function of the wake area parameter $\beta$, expressed as:

$$\epsilon = 0.25 \times \sqrt{\beta} \tag{4.7}$$

where $\beta$ represents the ratio of the wake cross-sectional area at $r_x = 0$ to the turbine swept area. It depends on the thrust coefficient $C_T$ as:

$$\beta = 0.5 \times \frac{1 + \sqrt{1 - C_T}}{\sqrt{1 - C_T}} \tag{4.8}$$

### 4.2.3 Wave model

Time series of wave elevation can be decomposed into multiple regular wave components, each with an wave amplitude described by a specific wave spectrum. The instantaneous wave elevation follows a Gaussian distribution with a zero mean, and its variance corresponds to the wave spectrum integrated across all frequencies. Wave height is assumed to follow a Rayleigh distribution, so that the significant wave height ($H_s$) and peak period ($T_p$) properties can be determined by the wave spectrum. Further details on statistical descriptions of waves can be found in [114, 93].

Waves can continue to grow in size until they break. Various wave spectra have been proposed to model waves at both developing and fully developed stages, as well as those generated by different sources, such as storms or tides. Commonly used wave spectra include the Pierson–Moskowitz (PM) spectrum and JONSWAP spectrum. Descriptions of these two wave spectra are provided in [114, 93].

The PM spectrum is a two-variable wave spectral function that describes fully developed wind-generated waves. It is derived from wave analyses in the North Atlantic Ocean. In contrast, the JONSWAP spectrum is based on the measurements from the Joint North Sea Wave Project, and used to model non-fully developed seas, where waves are generated by wind over the region with finite water depth and limited fetch. The PM spectrum serves as the basis for several spectral expressions, including the JONSWAP spectrum, with modifications to its two spectral variables. The JONSWAP spectrum features a sharper peak in its spectral density function compared to the PM spectrum.

### 4.2.4 Current model

The surface current velocity is contributed by various factors, including tidal influence, local wind, ocean circulation, and water density differences. Of these components, the velocity components associated with tide and local wind vary

with the water depth. Additional details on current velocity components and their variations with water depths can be found in [114].

To simulate the impact of ocean currents on floating structures, the current velocity is incorporated into the motion equation by considering the relative fluid velocity, which is defined as the velocity difference between the floater and the current. Further details on calculating the relative fluid velocity, considering current velocity and direction using 3-D and 2-D current components, can be found in [93].

In this study, the current model is not included in the dynamic simulations, because the specific design load cases considered for evaluating FOWT performance do not require it. The simulation of a single FOWT using OpenFAST shows that the most critical floater surge occurs at the rated wind speed, rather than at the highest wind speed, under comparable wave height and period conditions [120]. At the highest wind speed with a 50-year return period, the corresponding wind-induced current velocity is 0.57 m/s, while the tidal current with the same return period reaches 0.49 m/s [121]. At the rated wind speed, the current velocity is considerably smaller, and its influence on the relative fluid velocity is therefore limited.

## 4.3 FOWT simulation

To simulate the multi-body system of FOWTs, different simulation tools have been developed to capture the dynamic response of the turbine, tower, floater, and mooring lines. This section first reviews two simulation models for FOWTs, including a low-order modeling approach and a relatively higher-fidelity tool, both of which integrate the nonlinear aero-hydro-servo-elastic characteristics of FOWTs. The reference FOWT model and the design load cases considered for simulation, analysis and optimization in this study are then introduced. Finally, the optimization algorithm applied for FOWT performance and mooring cost evaluation is presented.

### 4.3.1 Low-order modeling approach

The low-order modeling approach captures the essential dynamics that govern the performance of the FOWT to reduce the system complexity and computational effort. This tool solves the motion equations of the FOWT subjected to the environmental and mooring line forces, and predicts dynamic responses of the FOWT with a reduced set of degrees of freedom. It was initially developed from a structural model in the 2-D plane, which only considers surge, heave and pitch motions of the floater, the rotor azimuth and the fore-aft motion of the tower top [111]. This reduced-order modeling approach was validated against the wind-wave tank experiments of a 10-MW semi-submersible FOWT [122]. It was later updated by including sway and roll motions of the floater, along with the pitch angle of the rotor blade for control design purposes [45].

In the structural model, each FOWT is represented as a flexible multi-body system comprising a rigid rotor disk, a flexible tower, and a rigid floater. This model is based on the assumption of a large rigid body motion and a small elastic deformation. Newton's second law is applied to translational motion, while Euler's law governs rotational motion of each structural component, with the momentum equations formulated directly.[111] provided detailed descriptions of the kinematic quantities, including translational and rotational velocities and accelerations, as well as the Newton-Euler equations for each rigid body. The global Newton-Euler equations for the rigid bodies can be expressed as:

$$M(\boldsymbol{q})\ddot{\boldsymbol{q}} + N(\boldsymbol{q}, \dot{\boldsymbol{q}}) = p(\boldsymbol{q}, \dot{\boldsymbol{q}}) \tag{4.9}$$

where $\boldsymbol{q}$ denotes the generalized coordinates representing the degrees of freedom of each FOWT, $M$ is the mass matrix, $N$ represents the Coriolis, centrifugal and gyroscopic forces, and $p$ corresponds to the applied forces including translational forces and torques, such as the aerodynamic and hydrodynamic forces. For efficient numerical calculations, Equation 4.9 can be transformed into state space by solving for the second derivative of the generalized coordinates $\ddot{\boldsymbol{q}}$.

The tower is modeled as a flexible beam, with its elastic deformation estimated using a characteristic shape function. Only the motion of the tower top in the fore-aft direction is considered as a degree of freedom. This module defines a translational spring-damper element at the tower top, and calculates the overall stiffness of the tower by integrating each sectional stiffness, assuming a static shape with prescribed structural damping. [111] provided detailed descriptions of the shape function and the kinetics for a linear Bernoulli beam with only one degree of freedom. Including the flexible beam, $\boldsymbol{q}$ in Equation 4.9 represents a combination of rigid body motion and small elastic deformations of the structural components.

For the aerodynamic modeling of the turbine, the rotor is treated as a rigid disk, without explicitly modeling each blade. The thrust force and shaft torque are calculated based on the rotor effective wind speed, rotor diameter, and the thrust and power coefficients, which are derived from the mid- or high- fidelity tools such as AeroDyn used in OpenFAST, for specific tip speed ratios and blade pitch angles. The rotor effective wind speed is defined as the averaged speed across the rotor swept area.

In the hydrodynamic modeling of the FOWT, Cummins' equation is used to transform the motion equations from the frequency domain to the time domain. To reduce the computational effort associated with the direct convolution of the radiation memory effect, a linear transfer function is employed to fit a state-space model. In the time-domain motion equation, the frequency-dependent added mass is neglected. Instead, a constant added mass interpolated at its eigenfrequency of the floater motion is used, and the frequency-dependent radiation damping is disregarded. The Morison equations are used to account for viscous forces that are neglected in potential flow theory. In addition, second-order slow-drift forces are included using Newman's approximation, avoiding the complexity calculations of full Quadratic Transfer Function (QTF).

Mooring forces are computed either by linear interpolation of fairlead positions using a look-up table that is pre-generated from external quasi-static mooring software with considering a wide range of fairlead positions [111], or through

direct coupling with external mooring software [45]. These mooring forces, combined with the linearized stiffness derived from the force-displacement relationship database, are incorporated into the global Newton-Euler equations in Equation 4.9.

This low-order simulation model captures the fundamental interactions between FOWT components and external forces from the environment and the mooring system. The benefits of using such a low-order model for FOWT analysis include high computational efficiency and ease of tuning and modification. In the early research stages of shared line designs, this low-order model is further integrated into a broader workflow for wind farm analysis, which is described in detail in Chapter 6.

### 4.3.2 Reference simulation tool

This study uses FAST.Farm (v3.5.1), a relatively higher-fidelity simulation tool compared to the simplified model, for analyzing floating wind farms. FAST.Farm uses OpenFAST to calculate the system dynamics of each FOWT and incorporates the Dynamic Wake Meandering model (DWM) to account for wake dynamics [54]. The DWM model captures the wake-deficit evolution, wake meandering, and wake-added turbulence, which are important for predicting loads and performance. Full-field turbulent wind velocities are generated by TurbSim [123], and incorporated into FAST.Farm as ambient inflow data. As this study focuses on assessing shared line designs rather than wake modeling, consistent wake parameters are applied across simulations of the FOWT array with different mooring configurations.

OpenFAST is an open-source simulation tool designed for modeling individual FOWTs with conventional mooring configurations. It provides a modular framework that couples Aerodyn, ElastoDyn, HydroDyn, ServoDyn, and MoorDyn, enabling nonlinear aero-hydro-servo-elastic simulations of FOWTs in the time domain. Descriptions about each OpenFAST module are based on [43, 116, 54]. AeroDyn computes aerodynamic loads on both the blades and

the tower using the actuator line method. Each blade and the tower are discretized into nodes, where 2D lift and drag forces, as well as pitching moments, are calculated at each node. The 3D aerodynamic loads are then obtained by integrating these 2D distributed forces along the structure. ElastoDyn defines the structural properties of the tower, nacelle, drivetrain, blades, and floater, as well as the initial conditions of each structural component. Beam theory is applied to both the blades and the tower to calculate elastic forces and deformations.

HydroDyn calculates the hydrodynamic loads on the floater using potential flow theory or strip theory, depending on the structural dimensions relative to the wavelength. The radiation memory effect is computed either through direct time-domain convolution or using a state-space model for a more efficient linear representation. Second-order drift forces are derived using either full QTFs or the modified Newman approximation. The Morison equation is applied to determine distributed inertia, added mass, and viscous drag forces. ServoDyn defines the controller characteristics of the FOWT. MoorDyn computes mooring forces using a lumped-mass approach to discretize the mooring line dynamics. The mooring model accounts for internal axial stiffness and damping, weight and buoyancy, hydrodynamic forces, and seabed contact forces.

### 4.3.3 Reference FOWT model

The FOWT is based on a preliminary model developed in the EU Horizon Project COREWIND, targeted for a site with a water depth of 200 m. It incorporates the IEA 15-MW wind turbine [124], a semi-submersible platform, and a conventional three-line mooring configuration [120]. The reference semi-submersible platform with the coordinate system is illustrated in Figure 4.2.

In the conventional mooring layout, three lines are arranged with a 120° angle between two adjacent lines. Principal parameters of the structural components, including the turbine, tower, floater and mooring lines, are summarized in Table 4.1.

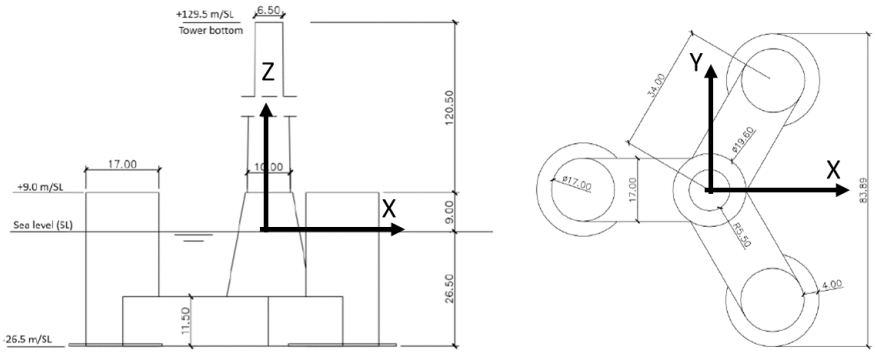


Figure 4.2: The reference semi-submersible platform (adapted from [120]).

Table 4.1: Principal parameters of the reference FOWT model.

| | Principle parameter | Unit | Value |
|---|---|---|---|
| Turbine | Rated power | MW | 15 |
| | Rotor diameter ($D_r$) | m | 240 |
| | Cut-in/ cut-out wind speed | m/s | 3/ 25 |
| | Rated wind speed ($V_r$) | m/s | 10.6 |
| | Minimum/ maximum rotor speed | rpm | 5.0/ 7.6 |
| Tower | Hub height above sea level | m | 135 |
| | Length | m | 120.5 |
| | Base height | m | 9 |
| Floater | Center of gravity from keel | m | 15.4 |
| | Displaced volume of water | $m^3$ | 36431 |
| | Center of buoyancy from keel | m | 10.7 |
| | Metacentric height | m | 6.4 |
| | Operational draught | m | 26.5 |
| Mooring system | Fairlead radius | m | 42.5 |
| | Anchor radius | m | 600 |
| | Line mass | kg/m | 561.2 |
| | Line length | m | 614 |

The 15-MW FOWT model has been analyzed using OpenFAST under different environmental conditions to assess its performance, including eigenfrequencies,

floater motions, and power output, as part of the COREWIND project. The selection of load cases follows the IEC standard, using a reduced set of Design Load Cases (DLCs). Details on the OpenFAST simulations for the 15-MW FOWT are available in [120].

Mooring design evaluation have selected DLCs 6.1 and 6.2 to assess station-keeping capability under extreme events. These load cases represent idling turbines with yaw misalignment under extreme sea states, and correspond to the Ultimate Limit State (ULS). In addition, DLCs 1.3 and 1.6 cover turbine operational scenarios, while DLCs 2.1 and 6.1 account for shut-down and parked turbine conditions. These DLCs are used to evaluate the global performance of the FOWTs.

Simulation results from OpenFAST show that in DLC 1.6, under rated wind speed and extreme wave conditions, the floater experiences a maximum surge of 20 m. In contrast, for the idling turbine scenario in DLC 6.1 with a 50-year return period wind speed, the maximum surge is approximately 17 m, lower than the peak value observed in DLC 6.1. Therefore, this study adopts the operational scenario at rated wind speed for mooring design, as it produces the most critical floater surge, which serves as a key design constraint and influences the safe operation of dynamic cables.

The FOWT model is employed in the wind-farm analysis, with each FOWT sharing similar structural properties for the turbine, tower, and platform as outlined in Table 4.1. The initial three-line mooring configuration did not specify the anchor type. However, it fails to maintain the safety of the drag embedment anchors, when the floater experiences surge exceeding 18 m, causing a negative lay-down length of the upwind anchor line on the seabed. This indicates that the drag embedment anchor is subject to a vertical lift force, which it is not designed to withstand. Therefore, new configurations using the drag embedment anchors are designed for the FOWT model in Chapter 5.

### 4.3.4 FOWT mooring optimization

The multi-discipline nature of FOWTs poses challenges in their optimization design, due to the large number of design parameters, the nonlinear system responses, and the high computational effort of time-domain simulations. The substructure optimization in the floating wind sector is driven by cost considerations [125, 5, 78, 56]. This process typically involves a geometric parameterization of the FOWT with a cost-reduction objective. The balance between optimization quality and computational effort is addressed by using various fidelity simulation models [125].

Both frequency-domain and time-domain simulations have been performed for FOWT substructure optimization. The frequency-domain method is widely used in the offshore oil and gas sector, and relies on the response spectrum derived from the environmental spectrum and the response amplitude operator of the floating structure. This method is also employed in mooring optimization for FOWTs [58, 39]. However, frequency domain analysis is limited in capturing the dynamic performance of FOWTs under extreme environmental conditions, as it assumes linear systems of FOWTs. Time-domain FOWT mooring optimization remains relatively scarce, mainly due to the nonlinear fluid-structure interactions that demand high computational effort. In contrast, mid-fidelity time-domain analyses have been applied to mooring optimization of other marine structures under irregular wave conditions [60, 61].

Mooring optimization consists of three main steps: formulation of the objective function, definition of key environmental and system variables, and establishment of constraints [58, 39, 60, 61]. The objective function defines the goal, such as minimizing mooring cost. Key variables influence both mooring performance and cost, such as the number and orientation of mooring lines. Design constraints specify the requirements that mooring solutions should satisfy, for example, mooring forces must remain within allowable limits. All these can be expressed mathematically, allowing optimization algorithms to identify the optimal solution.

Optimization algorithms can be broadly categorized into gradient-based and gradient-free methods. The gradient-based method is guided by gradients of the objective function and iteratively searches for an optimal solution. This method is efficient to identify local minima but requires the objective function to be continuous and differentiable. It has been used in frequency-domain mooring optimization for a FOWT [58] and in time-domain mooring optimization for fish farms using surrogate models [60]. In contrast, the gradient-free method is more flexible and robust when handling complex nonlinear objective functions [125]. Common gradient-free methods include Nelder-Mead method, Particle Swarm Optimization (PSO) algorithm, and Evolutionary Algorithms.

The Nelder–Mead method is a local search algorithm suited for simple and smooth objective functions. For example, it has been applied in frequency-domain FOWT mooring optimization to minimize line length with a constant chain diameter [39]. The PSO algorithm is a global, stochastic, population-based approach. It has been used in time-domain mooring optimization of a floating production platform in the oil and gas sector to minimize floater offset [61]. Evolutionary Algorithms, such as the Non-dominated Sorting Genetic Algorithm II (NSGA-II), are nature-inspired methods that can handle multi-objective problems with a high computational cost. For instance, NSGA-II has been employed in FOWT mooring optimization using a low-order simulation tool [59]. In that study, the objective function balanced tower-top displacement, mooring fatigue damage, and material cost.

# 5 Shared line design for floating wind farms

As discussed in Chapter 2, stiffness-linearized design methods have several limitations when they were applied to early-stage design and static analysis of FOWTs with shared line configurations. These methods assume small floater movements, linearize mooring stiffness, neglect mooring elasticity, and consider the prescribed floater offset as the only design constraint. All these parameters are important to govern load distribution, and such simplifications can lead to impractical mooring designs. To address these challenges, this chapter introduces a nonlinear design method that incorporates practical design considerations, realistic configuration properties, and multiple design constraints, providing a more robust and reliable framework for shared line designs.

The design considerations, parameters, constraints, and the overall process are discussed in Section 5.1. Section 5.2 investigates the sensitivity of different variables related to shared line designs and their influence on the performance of the FOWT array. The generated shared line configurations from static analysis are presented in Section 5.3, and some of them are compared with those obtained using the stiffness-linearized method in Section 5.3.3. Finally, comparative studies between conventional and shared line designs are presented in Section 5.4, based on dynamic simulations of a two-FOWT array using a simplified modeling approach (detailed in Chapter 4).

## 5.1 Nonlinear design method

Conventional mooring design is an iterative process that typically starts with a preliminary mooring configuration. Based on the initial configuration, the detailed mooring profile is defined through static analysis, which determines the material and size of line components, the arrangement of line orientations, the selection of anchor type, and the anchor radius to define the anchor position. Dynamic analyses are then performed to examine key parameters, such as floater motions and mooring forces under different environmental conditions. This process is also applied to shared line designs for floating wind farms.

### 5.1.1 Difference from stiffness-linearized methods

The key differences between the proposed nonlinear and the existing stiffness-linearized design methods for shared line configurations used in floating wind farms are summarized in Table 5.1.

Table 5.1: Differences between the nonlinear and stiffness-linearized design methods.

| Feature | Stiffness-linearized | Nonlinear |
|---|---|---|
| Assume small floater offset | yes | no |
| Linearize mooring stiffness | yes | no |
| Apply only offset constraint | yes | no |
| Scale line mass linearly | yes | no |
| Neglect mooring elasticity | yes | no |
| Neglect anchor radius | yes | no |
| Neglect floater pitch | yes | no |
| Neglect wake deficit | yes | no |

### 5.1.2 Mooring design considerations

In offshore oil and gas applications, mooring design typically begins with a reference configuration. The number and dimensions of mooring lines are then

adjusted to optimize four key factors: vessel offset, line forces, fatigue damage, and clash avoidance [11]. However, since shared line concepts are still in the early design phase, few feasible reference designs are available. As a result, the static design process begins with anchor lines, while properties of the shared lines are determined based on static force equilibrium with these anchor lines.

Static analysis serves as an initial screening tool to reduce the computational effort required for subsequent dynamic evaluations. This combined approach of static analysis and dynamic simulation is widely adopted. Previous studies have applied static analysis to generate conventional mooring designs [14, 15, 16] and have performed dynamic simulations to evaluate the performance of floating structures with specific configurations [30, 46, 49, 48]. However, an integrated design approach that addresses the unique challenges associated with shared line configurations is still lacking.

Compared to conventional moorings for individual FOWTs, shared line designs modify the mooring load distribution within the floating array, and introduce coupling between connected FOWTs. This results in higher loads on upstream anchor lines, and different floater motions due to the altered mooring stiffness and coupling effects. Consequently, shared line designs require thorough feasibility checks to ensure mooring integrity.

In static analyses, the most critical load case at rated wind speed produces the maximum wind thrust and induces the largest static floater offset. This approach has been employed in stiffness-linearized methods [32, 33]. In dynamic simulations, most existing studies focus on extreme loading conditions and pay insufficient attention to mooring fatigue. Mooring fatigue is important for the integrity of shared line designs, as upstream anchor lines experience heavier loads, while downstream turbines are subject to different wind field with increased turbulence intensity due to wake effects, and rely on shared lines to resist environmental forces.

Finally, since the primary motivation for developing shared moorings is cost reduction, cost evaluation is integrated into the nonlinear design approach to effectively demonstrate the potential for cost savings. In contrast, existing

cost estimates consider only a limited number of shared line and conventional mooring designs, and do not provide a comprehensive cost assessment.

### 5.1.3 Mooring design parameters

The mooring design parameters are summarized in Table 5.2. Since mooring design is site-specific, water depth is a key consideration. A water depth of 200 m is selected in this study, consistent with the TetraSpar floating wind project [66] and slightly shallower than that of the Hywind Tampen project [9]. To emphasize cost-effective solutions, all mooring lines are made of steel chain links with the lowest grade R3, and drag embedment anchors are used across all configurations.

Table 5.2: Mooring design parameters.

| Parameter | Input value |
|---|---|
| Water depth | 200 m |
| Line material | Steel chain links |
| Anchor type | Drag embedment anchor |
| Fairlead number | 3 per FOWT |
| FOWT spacing | $6D_r$ |
| Static length ratio $R_L$ | [0.3: 0.1: 1.5] |
| Chain diameter $D_c$ | [70: 1: 220] mm |
| Chain grade $G_c$ | [R3, R3S, R4, R4S] |
| Mass ratio $R_M$ | [1/3: 1/60: 3.5/3]% |

A two-turbine array represents the smallest floating array unit capable of implementing shared line designs, as illustrated in Figure 5.1. Each FOWT is equipped with three fairleads: two are connected to anchor lines fastened to the seabed, and the third supports a shared line that links two FOWTs.

The initial spread angle between any two adjacent lines is set to 120°. The horizontal spacing between the centers of the upstream and downstream platforms is defined relative to the rotor diameter ($D_r$). The distance of $6D_r$ is adapted

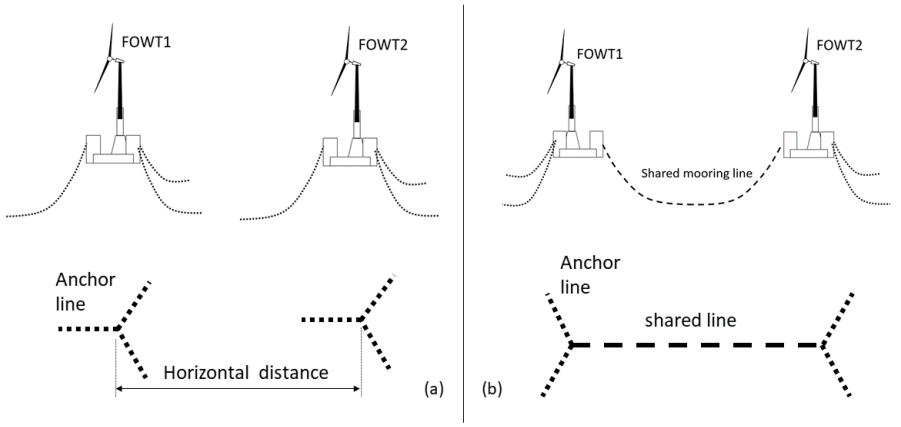


Figure 5.1: Mooring layouts for a two-FOWT array: (a) conventional configurations; (b) a shared line configuration.

from the layout of the Kincardine Offshore Wind Farm [7]. Two FOWTs have similar dimensions, except that the downstream platform is rotated 180° relative to the upstream floater in the shared line layout. The fairlead positions on the platform remain fixed, while anchor positions at seabed are determined by the anchor radius, which can vary across different mooring configurations. A flat seabed is assumed to ensure uniform vertical positions of all anchors.

To ensure the safety of drag embedment anchors, a portion of the mooring line must remain in contact with the seabed. Anchor lines refer to those non-shared lines and have similar chain and length properties in each configuration. The static length ratio $R_L$, is defined as the suspended length $L_S$ divided by the lay-down length $L_L$ on the seabed, without wind forces, as shown in Figure 4.1. Since no specific guidelines exist for $R_L$, the range used in this study are based on experiences from the individual FOWT scenarios [15].

Unlike anchor lines, $R_L$ is not prescribed for the shared line, as its total line length is determined by the spacing between two FOWTs and pretension. Given a pretension and the chain diameter or line mass, the suspended length and thus $R_L$ are obtained by solving Equation 4.1. Instead, a design constraint related to $R_L$ is imposed on the shared line to ensure that an adequate portion

remains in contact with the seabed, as discussed in Section 5.1.4. The range of chain diameter ($D_c$) and chain grade ($G_c$) for both anchor lines and shared lines are based on existing floating wind projects.

The mooring mass ratio ($R_M$) defines the mass of one anchor line relative to the displaced mass of the floater. Vertical mooring forces pull the floater downward, changing its displacement. Although active ballast or dynamic positioning systems can compensate for this change, no guidelines exist to define allowable limits in mooring design. In this study, a 5% change in displaced floater mass is set as the upper bound for the added weight imposed by three anchor lines. Since no line attachments, such as buoys and clump weights, are included in configurations, the mooring mass of each anchor line ($M_L$) is determined by the chain mass per unit length ($\rho_c$), total length ($L_T$), and number of lines. The mass of the shared line is not prescribed, instead, a design constraint addresses its mass within a specific range relative to the anchor line mass.

### 5.1.4 Mooring design constraints

The mooring design constraints are summarized in Table 5.3. Constraints 1–4 are applied during static analysis without wind forces, while Constraints 5–7 are used under steady wind loading conditions. The first constraint is related to the anchor line length $L_T$, which is set to a range between 600 m and 1000 m. This range is equivalent to 3 to 5 times the water depth of 200 m, which aligns with practices in the offshore oil and gas industry [11], and keeps consistent with existing floating wind projects. For instance, the anchor line is approximately 900 m in Hywind Scotland [8]. In Kincardine Offshore Wind Farm, the line lengths are 9 times the water depth of 60 m to 80 m [13].

The second constraint is pretension limit. Pretension ($MF$) is the initial mooring force at static equilibrium in the absence of environmental forces. Its acceptable range is defined relative to the chain's Minimum Breaking Load ($MBL$), between 10% to 20%, in alignment with practical installation concerns in the oil and gas industry [11].

Table 5.3: Design constraints.

| Test | Constraint Description | Range |
|---|---|---|
| no wind | 1: Anchor line length $L_T$ | 600–1000 m |
| | 2: Pretension $MF$ | 10%-20% $MBL$ |
| | 3: Shared line mass ratio $R_S$ | 0.5–1.5 |
| | 4: Shared line length ratio $R_L$ | $\geq 0.3$ |
| rated wind | 5: Maximum force $T_L$ | $\leq 50\% MBL$ |
| | 6: Minimum lay-down length $L_L$ | $\geq 0.1 L_T$ |
| | 7: Maximum offset $X$ | $\leq 60$ m |
| extreme | 8: Maximum force $T_L$ | $\leq 50\% MBL$ |
| | 9: Minimum lay-down length $L_L$ | $\geq 0$ |
| | 10: Maximum horizontal $X$ | $\leq 60$ m |
| operation | 11: Maximum force $T_L$ | $\leq 50\% MBL$ |
| | 12: Minimum lay-down length $L_L$ | $\geq 0$ |
| | 13: Maximum horizontal $X$ | $\leq 60$ m |
| | 14: Mooring fatigue damage | $\leq 0.1$* |

**A damage of 0.1 corresponds to a safety factor of 10.*

The third and fourth constraints address the shared line length and mass properties. A limit of 30% of the total length ($L_T$) is imposed on the static lay-down length ($L_L$) on the seabed. The horizontal $MF$ on the shared line is balanced by those on the anchor lines. Given $MF$, the suspended length ($L_S$) of the shared line can be derived from Equation 4.1, with knowledge of its chain diameter. The shared line may differ from anchor lines, causing weight imbalance and induce additional floater rotation. To mitigate this effect, the shared line mass is limited to 150% of the combined mass of two anchor lines. This mass ratio is denoted as $R_S$. Under this upper mass limit, the shared line configuration results in a maximum change of 5.8% in the displaced floater mass.

Under both steady wind and dynamic loading conditions, the maximum mooring force must remain below 50% of the chain's $MBL$. This force limit is consistent with partial safety factors used in ULS checks for quasi-static mooring analysis [12]. In addition, the lay-down length ($L_L$) is introduced to ensure the safety of drag embedment anchors and to validate the use of the catenary equation for shared lines. When a shared line lifts off the seabed, the catenary

assumption is invalid, and the cable equation proposed by [126] should be employed, as demonstrated in [86]. Since no specific guidelines define an allowable limit for $L_L$, this study adopts 10% of the total line length as a lower bound under under steady wind conditions, while under dynamic loading conditions a positive $L_L$ is required to allow for a wider range of potential configurations.

The horizontal floater offset ($X$) is defined as the Euclidean distance that captures both surge and sway motions from the initial equilibrium position. Its allowable limit is mainly governed by dynamic cable design requirements, as excessive floater offset can increase cable curvature. However, studies indicate that this increased curvature is not a critical factor, instead, the cable orientations relative to the floater bring a more significant impact [36]. Due to the lack of consensus on allowable limits, this study adopts 30% of the water depth as the upper bound. This 60-m limit is informed by simulations of a 2-MW FOWT, which showed safe cable performance when the floater moved up to 40 m in water depths between 80 m to 100 m [37].

The fatigue constraint addresses the long-term shared mooring integrity. The cumulative fatigue damage over the service life must remain below 0.1, corresponding to a safety factor of 10. According to [12], a fatigue safety factor of 5 is acceptable when the adjacent fatigue damage ratio is below 0.8, while for damage ratios between 0.8 and 1, the safety factor is linearly increased up to 8. In this study, a more conservative safety factor of 10 is adopted to account for two key considerations: (1) the simplified modeling approach neglects mooring and wake dynamics, which tends to underestimate fatigue damage, and (2) the use of non-redundant shared line configurations requires an additional margin to ensure the mooring reliability.

### 5.1.5 Mooring design process

The workflow consists of three main steps to generate a shared line configuration using static analysis, as illustrated in Figure 5.2. Steps 1 and 2 determine the anchor line and shared line profiles, respectively, without considering wind

forces. In Step 3, a constant wind force is applied, and the resulting static floater offset, mooring line forces, and lay-down lengths are calculated. After mooring static analysis, the mooring cost of each configuration is estimated, and dynamic simulation are conducted using the simplified modeling approach to evaluate the performance of the floating array.

In step 1, the anchor line length ($L_T$) is calculated by dividing the line mass ($M_L$) by its mass per unit length ($\rho_c$). Given the chain diameter ($D_c$, measured in mm), $\rho_c$ for chain links in air (in kg/m) is defined in Equation 5.1 [79], where the constant coefficients account for unit conversions, allowing $\rho_c$ to be directly related to $D_c$. In contrast, the stiffness-linearized design method [32, 33] linearly scales the line mass by its stiffness, rather than by the chain properties.

$$\rho_c = \begin{cases} 0.0199 \times D_c^2, & \text{for studless chain} \\ 0.0219 \times D_c^2, & \text{for stud chain} \end{cases} \tag{5.1}$$

The mass ratio ($R_M$) is quantifies the relationship between the mass of one anchor line relative to the displaced mass of the floater, accounting for the downward force from the mooring lines that changes the floater displacement. The resulting total length ($L_T$) is then evaluated against the first constraint, to ensure that it meets the design requirement of 3 to 5 times the water depth. Once $L_T$ is calculated, the static line length ratio ($R_L$), defined as the ratio of the lay-down length on the seabed ($L_L$) to the suspended length in water ($L_S$), is applied to determine $L_S$. Given $L_T$, $L_S$ is calculated as $L_T/\ (1 + R_L)$. With $L_S$, $\rho_c$, water depth, and fairlead positions known, the anchor radius and pretension are calculated using the elastic catenary equation (Equation 4.1), neglecting the hydrodynamic forces on the line segment. The pretension is further evaluated against the chain's $MBL$ (measured in kN), as expressed in Equation 5.2 [80].

$$MBL = f_g \times D_c^2 \times (44 - 0.08 \times D_c) \tag{5.2}$$

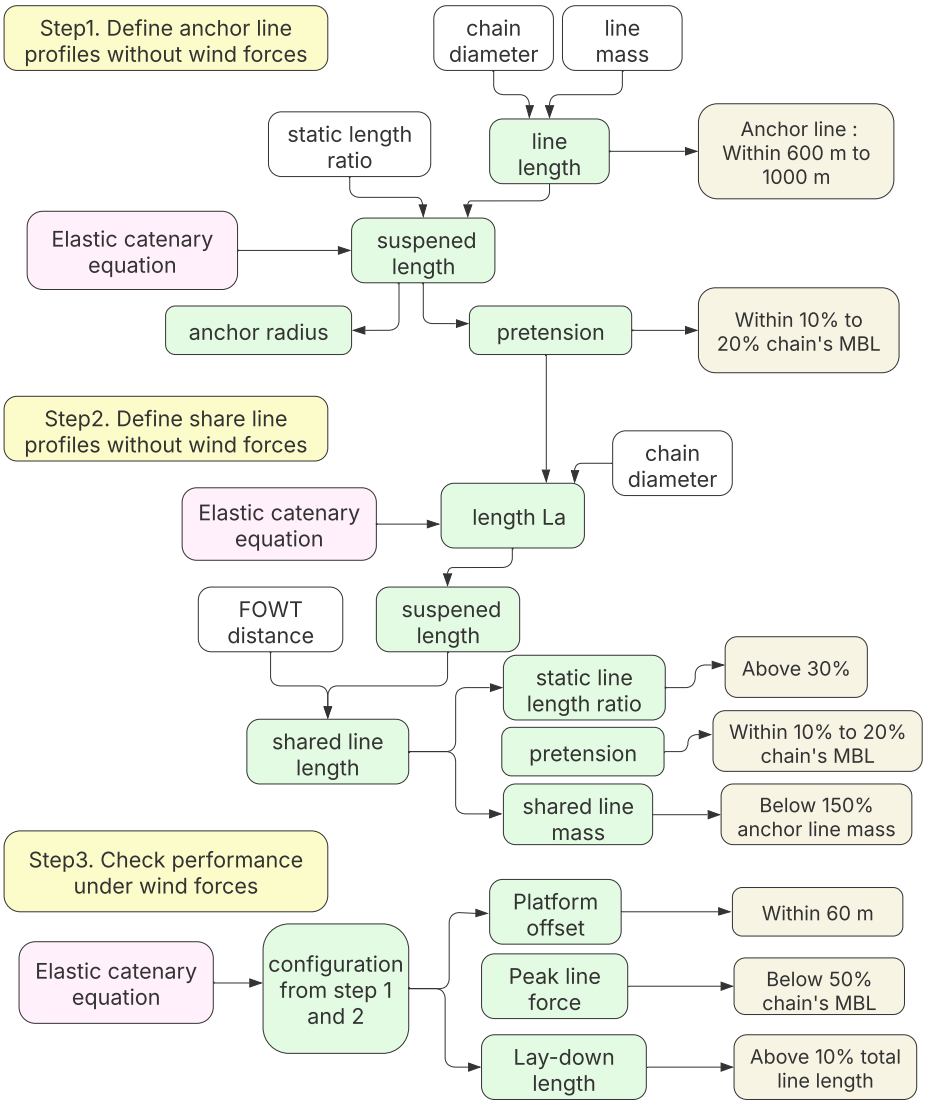


Figure 5.2: The design workflow using static analysis.

where $f_g$ is a factor dependent on chain grade and equals to 0.0223, 0.0249, 0.0274, and 0.0304 kN/m$^3$ for R3, R3S, R4 and R4S chains, respectively [80].

Step 2 begins by establishing static force equilibrium between the anchor lines

and the shared line. Given the shared line chain diameter and horizontal pretensions on anchor lins, the characteristic length ($L_a$) of the shared line is calculated by dividing the total horizontal force by its weight per unit length in water. With $L_a$, water depth, and fairlead positions known, the shared line suspended length and the horizontal distance from the touch-down point to the fairlead are then derived from Equation 4.1. The spacing between two FOWTs is used to determine the lay-down length of the shared line by subtracting the horizontal touch-down-to-fairlead distance and the fairlead radius.

A constant wind force of 2.2 MN, derived from OpenFAST simulations of the 15-MW FOWT under steady rated wind conditions, is applied in step 3, to calculate the static offset, line force, and lay-down length. After the static analysis, an empirical cost model for mooring material costs ($C_m$) is employed to estimate the minimum costs (in USD) of mooring lines and anchors. The cost of each mooring line ($C_L$) depends on the total line length ($L_T$) and the minimum break load ($MBL$) of the mooring chains, while the cost of each anchor ($C_A$) is expressed as a linear function of $MBL$ in Equation 5.3 [31].

$$\begin{aligned} C_L &= (0.0591 \times MBL - 87.6) \times L_T, \\ C_A &= 10.198 \times MBL. \end{aligned} \tag{5.3}$$

where the constant coefficients are empirically derived from an in-house tool for different FOWT concepts across various water depths [31]. These coefficients account for the necessary unit conversions of input parameters, including $MBL$ (in kN) and $L_T$ (in m), so that the resulting cost values for both mooring lines and anchors are directly given in USD. This cost model is applied only to mooring lines of steel chain links and drag embedment anchors. For a three-line configuration, the total mooring material cost ($C_m$) is calculated as three times the sum of $C_L$ and $C_A$. A real-world floating wind project benchmark, which features the 15-MW turbine and a six-line mooring configuration [6], is used to illustrate the uncertainty of this cost model under evolving price conditions, as discussed in Section 5.5.3.

## 5.2 Parameter sensitivity test

Following static tests without wind forces, conventional configurations with the smallest chain diameters are selected for parameter sensitivity tests, with their properties listed in Table 5.4. A small chain diameter typically corresponds to lower mooring stiffness, making the system more responsive to external forces. Their static length ratios range from 0.7 to 1.5, in increments of 0.1, representing different pretensions at the fairleads.

In addition, Table 5.4 presents the shared baseline designs, of which their anchor line profiles use the smallest chain diameter that meets requirements under both extreme and operational conditions. To investigate the critical shared line mass ratio, 59 designs covering a wide range of chain diameters and mass ratios are analyzed. For the direction, pitch, wake, and stiffness tests, five representative samples from these 59 designs, which have uniformly distributed mass ratios, are evaluated. All mooring lines use the lowest chain grade (R3).

Table 5.4: Properties of the baseline designs for sensitivity tests.

| Shared line mass ratio | - | Shared line |
|---|---|---|
| Chain diameter $D_{c1}$ [mm] | - | 144 |
| Length ratio $R_L$ | - | 0.7 |
| Mass ratio $R_M$ [%] | - | 0.92 |
| Chain diameter $D_{c2}$ [mm] | - | [128:1:186] |
| Shared line mass ratio | - | [0.69:1.48] |
| Other variable | Conventional | Shared line |
| Chain diameter $D_{c1}$ [mm] | 80 | 144 |
| Length ratio $R_L$ | [0.7:0.1:1.5] | 0.7 |
| Mass ratio $R_M$ [%] | 0.33 | 0.92 |
| Chain diameter $D_{c2}$ [mm] | - | [128, 143, 157, 172, 186] |
| Shared line mass ratio | - | [0.69, 0.86, 1.04, 1.26, 1.48] |

### 5.2.1 Shared line mass ratio

In a shared mooring layout, the shared line may differ from the anchor lines in chain diameter, chain grade, and line mass. The shared line mass ratio is defined as the mass of the shared line relative to the combined mass of two anchor lines. The selection of an appropriate mass ratio is critical, as it determines the mooring mass distribution and stiffness of the shared line configuration, which ultimately influence the global performance of the floating turbine array. This study investigates the critical mass ratios of shared lines, and the effect of this ratio on FOWT dynamic responses is illustrated in Figure 5.3 for the upwind anchor line (L2S) and the shared line (LS), at a wind direction of 30° under extreme loading conditions. This wind direction, defined in Figure 5.4, is considered critical because it induces both the maximum horizontal offset and the highest mooring line force ratios, as shown in Figure 5.5.

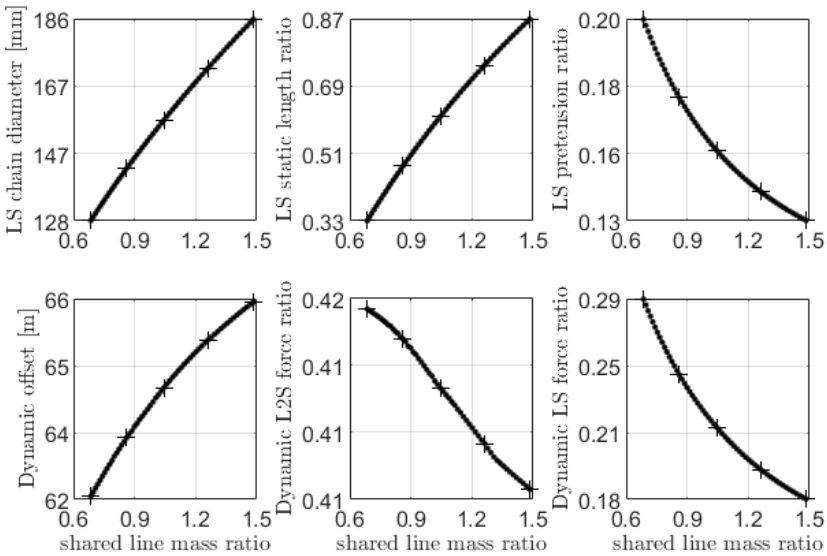


Figure 5.3: Static and dynamic responses across the 59 shared baseline configurations. Dynamic results are averaged across six seeds. Five representative samples with uniformly distributed mass ratios are highlighted. Force ratios are rounded to two decimals, so close values may appear identical.

In the 59 baseline configurations, the chain diameter of LS increases from 128 mm to 186 mm, resulting in a corresponding rise in the mass ratio of LS from 0.69 to 1.48. Despite the slight change in LS total length, which is constrained by the fixed spacing distance between FOWTs, its static length ratio increases significantly from 0.33 to 0.87. This is because, under constant pretensions from given anchor lines, a large chain diameter leads to a higher line mass density, which reduces LS suspended length required to maintain force equilibrium, and consequently increases its static length ratio.

However, as its chain diameter increases, the pretension ratio in LS decreases, as this ratio is defined relative to chain $MBL$, which also significantly rises with increasing chain diameter. The reduced pretension ratio indicates lower shared mooring stiffness, resulting in a larger floater offset of the downstream FOWT that consequently reduces mooring forces in the downwind anchor lines connecting the downstream FOWT. As a result, the force in LS also reduces to maintain equilibrium with these reduced anchor line forces. Similarly, the mooring forces in the upwind anchor line (L2S) decline in response to the reduced LS force.

In addition, Figure 5.3 clearly demonstrates a monotonic relationship between the shared line mass ratio and FOWT dynamic responses, including both the maximum floater offset and the highest mooring force ratios. Therefore, by selecting 5 representative mass ratios, which are uniformly distributed across the full range from the lowest to the highest, it can effectively capture the influence of various shared line mass ratios for a given anchor line profile.

### 5.2.2 Wind direction

The tested wind direction ($\theta$) varies from 0° to 90°, in increments of 15°. To ensure that the wind always blows toward the turbine along the positive X-axis, the mooring layout is rotated by $\theta$ accordingly, as shown in Figure 5.4.

Figure 5.5 shows the effect of wind direction on floater offsets and mooring force ratios of the most heavily loaded anchor lines (L1 and L2) for the individual

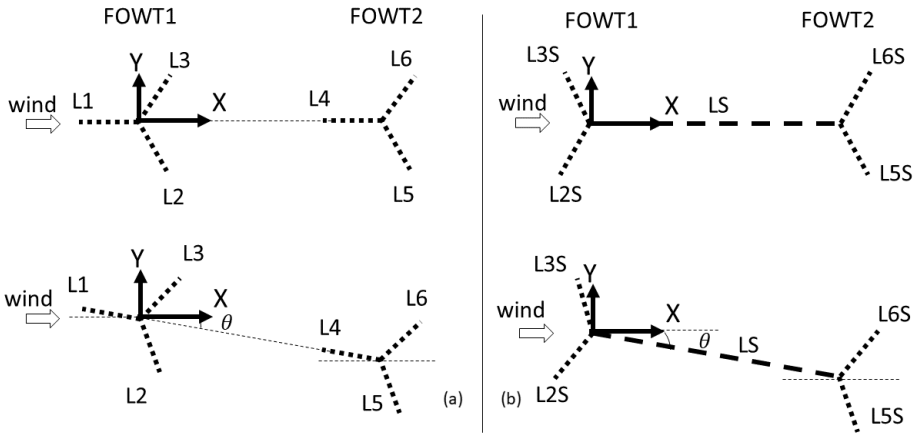


Figure 5.4: Mooring layout rotated clockwise by 30° to align the wind direction to 0°: (a) Conventional mooring layout; (b) Shared mooring layout.

FOWTs across nine conventional baseline designs. In addition, Figure 5.6 illustrates the effect of wind direction on floater offsets and force ratios of the three most heavily loaded lines (L3S, L2S, and LS) in the floating array using the shared baseline design.

In the static analysis, a constant floater pitch of 5° is imposed on the two FOWTs, and the static wake deficit is considered at 0° wind direction, by applying a 40% reduction to both the wind force and floater pitch for the downstream FOWT. For the floating array with conventional baseline configurations, although the floater offsets exceed the 60-m limit, the results still provide insight into wind direction sensitivity. At 60°, both static and dynamic analyses indicate a maximum floater offset. Meanwhile, the static analysis identifies the maximum force ratio at 15°, but the dynamic results indicate it occurs at 0°.

For the floating array with five shared baseline configurations, the static offset remains within the 60-m limit, while the dynamic offset exceeds this limit. This highlights the limitation of relying solely on static analysis, which may underestimate floater offsets and produce designs that are not fully reliable, as is the case with the stiffness-linearized method. Furthermore, the static analysis identifies the maximum offset at 15°, while dynamic responses indicate it occurs

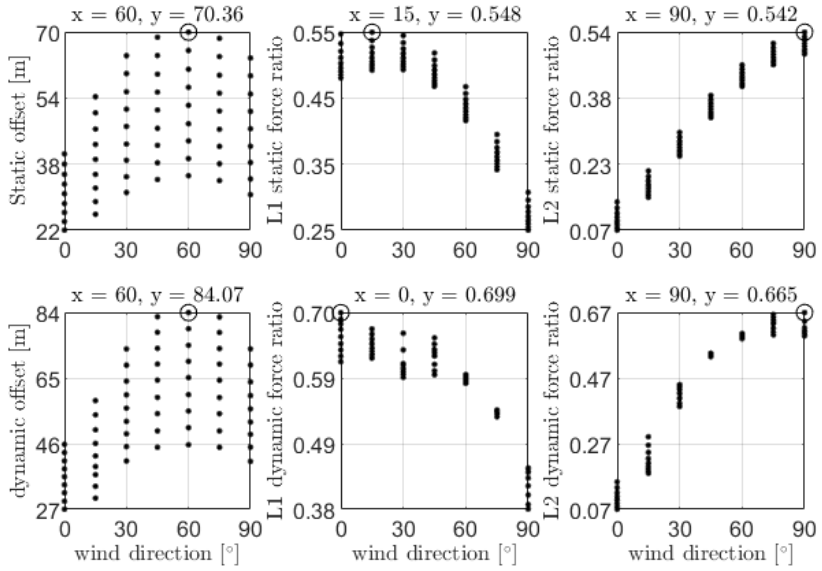


Figure 5.5: Floater offsets and line force ratios as a function of wind directions across nine conventional baseline configurations, with maximum values labeled and highlighted in each subplot. Dynamic results are averaged across six seeds.

at 30°. The highest mooring force ratios on anchor line L2S is observed at 30°. In contrast, for the highest shared mooring force ratio, the static analysis predicts it at 15°, while the dynamic responses indicate it occurs at 0°.

This wind direction test shows the effectiveness of static analysis as a lower-bound screening tool, but also indicates that solely relying on static analysis can underestimate system responses and misidentify critical wind directions. Dynamic simulations demonstrate that the most critical wind directions are 0° and 60° for conventional baseline moorings, while for the shared line baseline design, they are 0° and 30°. These directions are subsequently used to evaluate mooring configurations through both static and dynamic analyses.

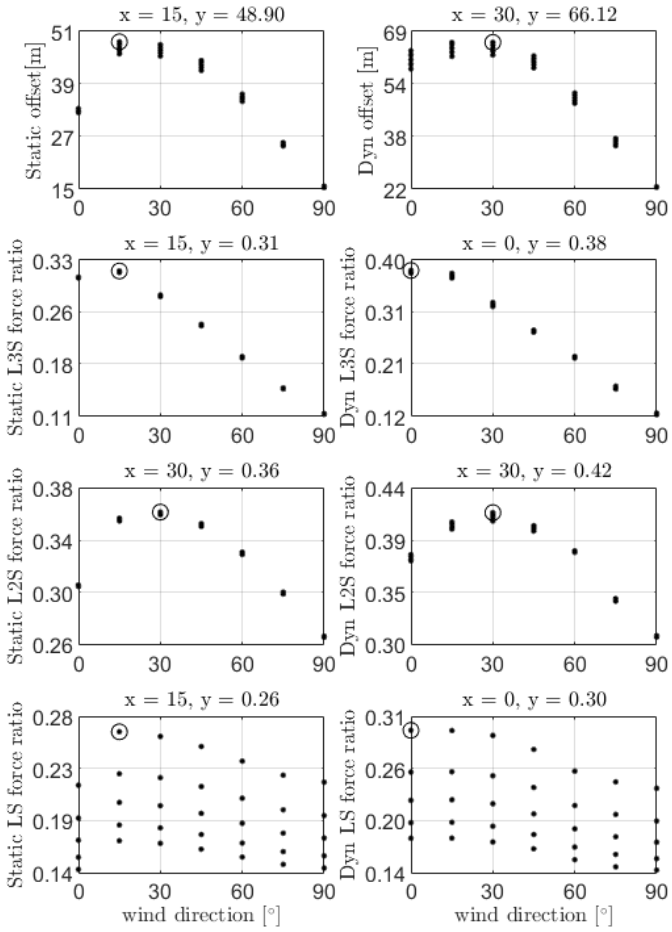


Figure 5.6: Floater offsets and line force ratios as a function of wind directions across five shared baseline configurations, with maximum values labeled and highlighted in each subplot. Dynamic results ("Dyn" for short) are averaged across six seeds.

### 5.2.3 Floater pitch motion

To investigate the influence of floater pitch, three pitch angles (from 0° to 6°) are examined for the floating array. Wind directions of 60° and 30° are applied to the nine conventional and five shared line configurations, respectively, with

their corresponding static offsets illustrated in Figures 5.7 and Figure 5.8.

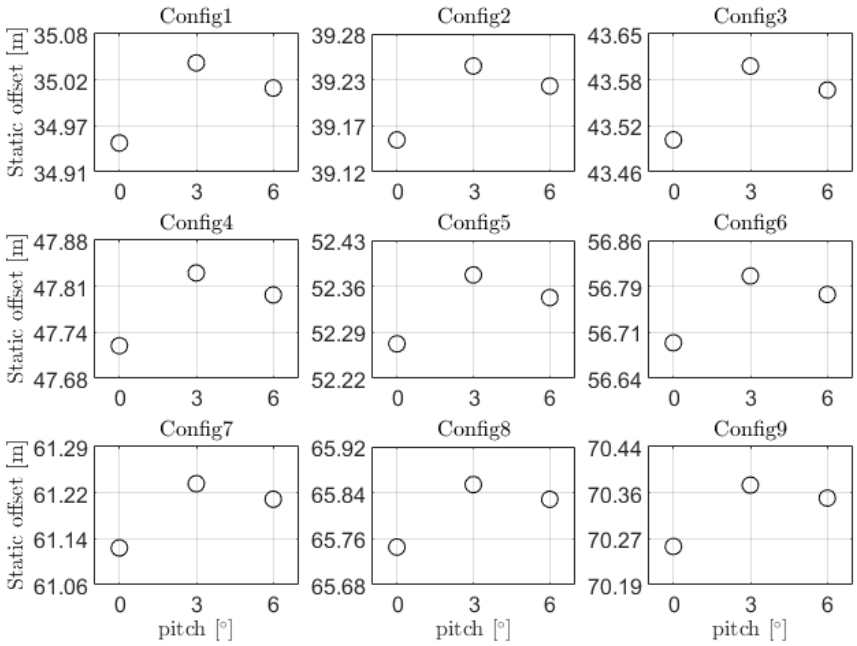


Figure 5.7: Static offsets as a function of floater pitch across nine conventional baseline configurations ("Config" for short) at the wind direction of 60°.

The stiffness-linearized method considers only horizontal translations and neglects floater pitch. However, floater pitch affects fairlead positions, and consequently influences static mooring forces The static analysis shows that including floater pitch has only a limited impact on the static FOWT offset of the floating array using the nine conventional baseline configurations, with a maximum deviation of 0.2 m. In contrast, the floating array with the five shared baseline configurations exhibits a larger offset variation as floater pitch increases, with offset differences of up to 0.6 m for the downstream FOWT.

However, including floater pitch does not always increase the static offset, since floater pitch affects both vertical and horizontal positions of fairleads that govern the mooring forces and influence floater offsets. A positive pitch decreases the horizontal distance but increases the vertical distance between the fair-

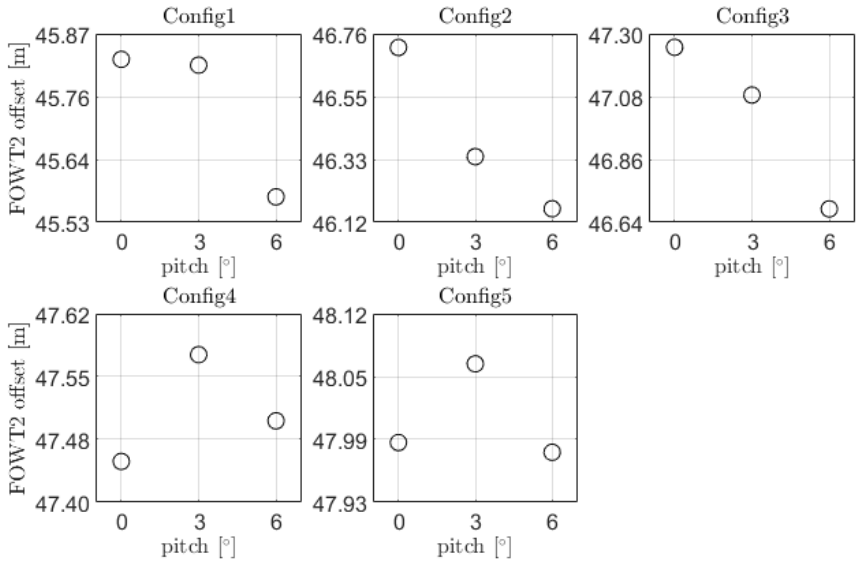


Figure 5.8: Static FOWT2 offsets as a function of floater pitch across five shared line baseline configurations at the wind direction of 30°.

lead and the anchor for the upwind lines, while having the opposite effect on the downwind line. These position changes affect the mooring pretension and stiffness at static equilibrium, which ultimately determines the rise or drop in static offset. Including floater motion tends to increase the static offset of FOWTs with conventional configurations, but decrease the offset of downstream FOWTs with shared line configurations.

The investigation on static floater pitch effects confirms the importance of including them in shared line designs. These effects are often neglected in existing design methods. Unless otherwise stated, a constant floater pitch of 5° is applied in the static analysis of the FOWTs. This pitch angle is based on OpenFAST simulations of a single FOWT at rated wind speed.

### 5.2.4 Wake effect

For conventional configurations, wake effects have little influence on the maximum floater offset and mooring force ratio of the floating turbine array, since both upstream and downstream FOWTs employ similar mooring configurations. In contrast, for shared line moorings at a wind direction of 0°, the reduction in wind thrust force caused by wake effects has a pronounced impact on the static performance of the downstream FOWT2, as shown in Figure 5.9.

At a wind direction of 0°, the downstream FOWT2 is entirely within the wake region of the upstream FOWT1, causing a decreased wind speed at the hub height of FOWT2 that consequently reduces the wind thrust force. The magnitude of this force reduction is determined by the spacing between the two FOWTs, the wind conditions, and the performance of the upstream turbine. In the static analysis, three reduction ratios are considered for comparison purposes. FAST.Farm simulations of the same floating turbine array with a similar spacing ($6D_r$) between FOWTs under steady rated wind conditions indicate that the wind thrust on the downstream turbine is reduced by approximately 21%.

Accounting for wake effects significantly reduces the static offsets across the five shared baseline configurations. The maximum deviation reaches over 7 m at the thrust reduction of 20%, and 15 m at 40%. Changes in the downstream offset also influence the load distribution and the upstream offset, leading to deviations over 4 m at a thrust reduction of 40%. In contrast, the mooring force ratios of anchor line L3S, which is the most heavily loaded line in the shared line configuration at 0°, exhibit only limited reductions across the five configurations, dropping by less than 2% at a 20% thrust reduction, and 4% at 40%. This minor change occurs because the mooring force ratio is defined relative to the chain's $MBL$, which exceeds twice the rated wind thrust force, as the force ratio limit is set below 50% under extreme loading conditions.

This investigation highlights the importance of including wake effects in shared line FOWT designs, which are often neglected in design methods. In the non-

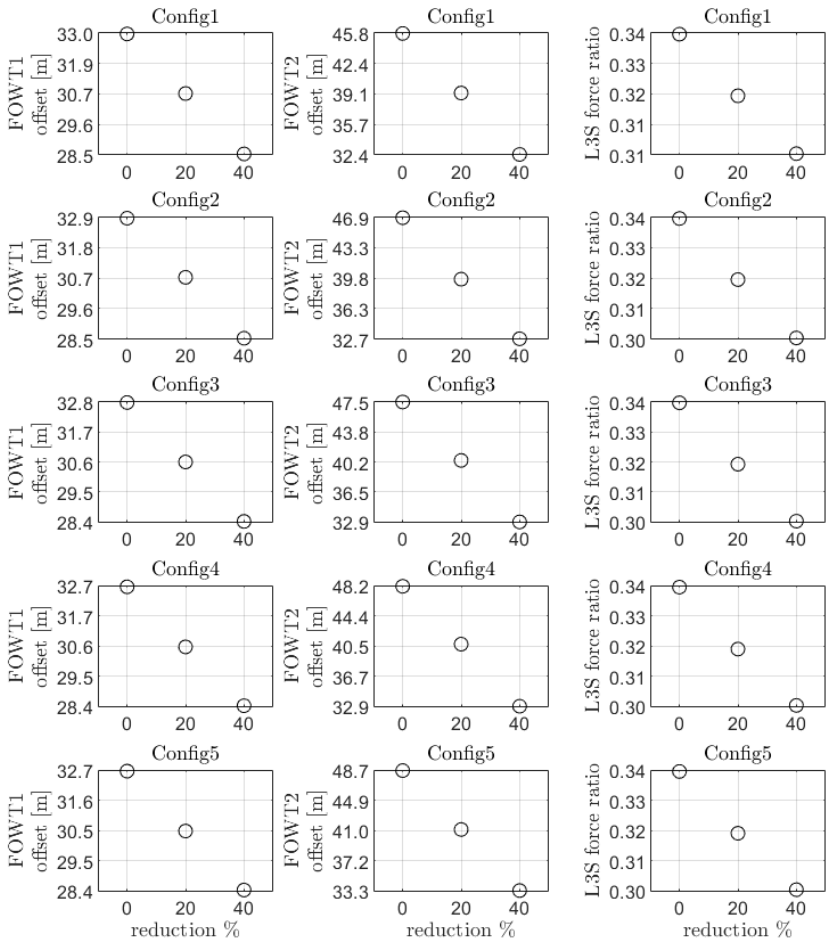


Figure 5.9: Static offsets of the upstream FOWT1 and downstream FOWT2, as well as the mooring force ratios of anchor line L3S as functions of thrust force reduction caused by wake effects at 0° for the five shared baseline configurations.

linear design approach, a 20% thrust reduction is adopted for static analyses of the downstream FOWTs with shared line configurations at a wind direction of 0°, based on FAST.Farm simulations of two-turbine arrays with shared line configurations under steady rated wind conditions.

### 5.2.5 Mooring axial stiffness

The stiffness-linearized method [33] neglects the axial stiffness ($EA$) of mooring lines in shared line designs. In contrast, the nonlinear design method considers $EA$ in both conventional and shared mooring configurations. Including $EA$ captures the elongations of mooring lines, which decreases mooring stiffness and directly increases static offsets. To examine the influence, static analyses of the floating turbine array using mooring configurations with and without $EA$ are compared in Figure 5.10 and Figure 5.11, for the nine conventional and five shared baseline configurations, respectively.

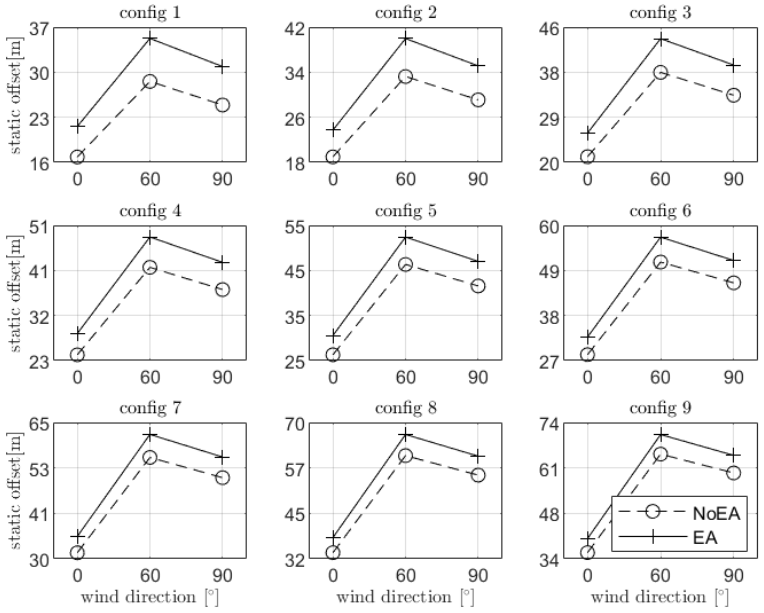


Figure 5.10: Influence of $EA$ on the static FOWT offsets of the floating turbine array across the nine conventional baseline configurations at three wind directions.

The static analysis applies a constant wind force of 2.2 MN and a floater pitch of 5° to the floating turbine array. At a wind direction of 0°, the thrust force is reduced to 1.7 MN (drop by 21%) to account for wake effects. Three directions of 0°, 60°, and 90° are examined for FOWTs with conventional moorings, while

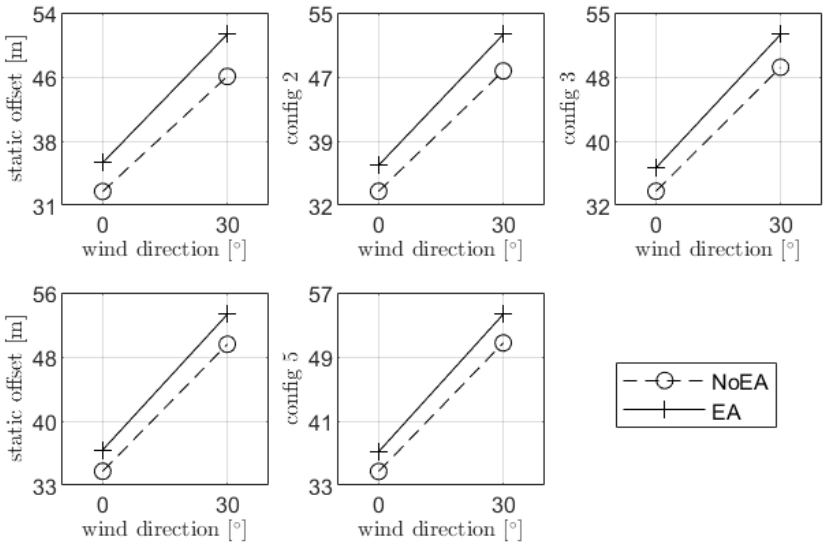


Figure 5.11: Influence of $EA$ on the static offsets of the downstream FOWT across the five shared baseline configurations at two critical wind directions.

two wind directions of 0° and 30° are analyzed for FOWTs with shared line moorings.

For FOWTs with the nine conventional configurations, including $EA$ increases the static offset under all three wind directions. For example, in configuration 7 (Figure 5.10), neglecting $EA$ results in an offset below the 60-m limit, while including $EA$ produces a offset of 62 m, exceeding the design limit. This highlights the importance to include $EA$ in the conventional mooring configurations for FOWTs to ensure a more reliable mooring design. A similar impact of $EA$ on static offsets is observed for FOWTs with the five shared line configurations. Including $EA$ significantly increases the static offset of the downstream FOWT across all five configurations, which underscores the necessity of including $EA$ in shared line designs.

## 5.3 Static analysis in mooring design

### 5.3.1 Conventional configurations

The nonlinear design method initially generates 29600 anchor line designs that meet the static test constraints under no-wind conditions, which are then further examined under three wind directions (0°, 60°, and 90°) to filter down to 17532 designs. Exceeding the offset and lay-down length limits are two main reasons to discard designs. Figure 5.12 shows the density distributions of 17352 configurations across line properties and static performance metrics. Line properties include chain diameters, line lengths, chain grades, and length ratios. Static results include pretension ratios, maximum offsets, maximum mooring force ratios, and minimum lay-down length ratios across three lines and three directions under steady wind conditions. Darker shading bins indicate higher occurrence, while white areas indicate no such design.

As the anchor line mass ratio increases, the 17352 configurations accommodate a wider range of chain diameters. Large diameters with low mass ratios and small diameters with high mass ratios are infeasible due to line length constraints. Line length generally decreases with increasing mass ratio, though designs with higher mass ratios show a wider spread. Long lines with low mass ratios or short lines with mass ratios above 1.0 are absent. Most design use the lowest chain grade (R3) and have a length ratio below 0.95. Pretension ratios concentrate between 0.1 to 0.15, and increase slightly with higher mass ratios. High pretension ratios with small mass ratios are less common.

Static offsets decrease as mass ratio increases, with major designs clustered at moderate mass ratios (from 0.6 to 1.0) and offsets below 48 m. Very low offsets at low mass ratios and very high offsets at high mass ratios are not observed. Similarly, maximum force ratio decreases with increasing mass ratio, concentrating between 0.18 to 0.32. When mass ratio exceeds 1.0, additional anchor line mass brings a minor effect to further reduce the upper bounds of

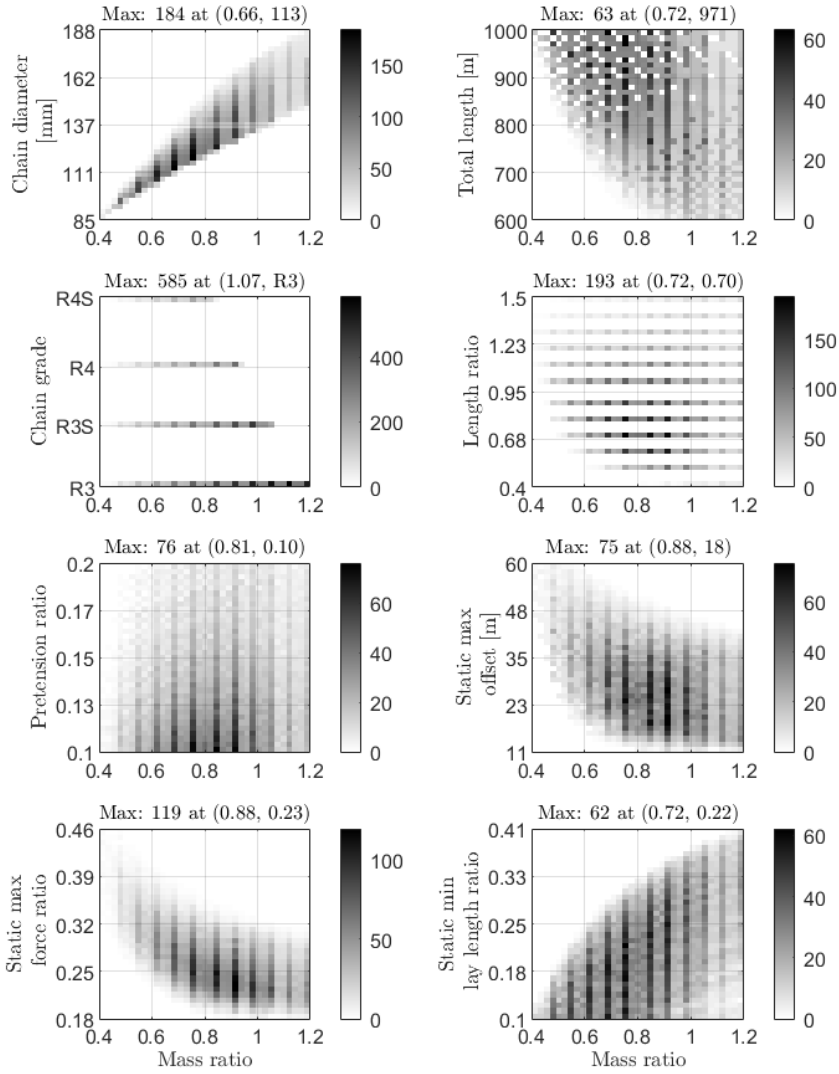


Figure 5.12: Grayscale 2D histograms of the anchor line properties and static performance as functions of anchor line mass ratio for 17352 conventional configurations. Shading indicates the count in each bin, with 36 bins along both X and Y axes. Each subplot reports the maximum bin count and its location of bin centers.

offset and force ratio. In contrast, the minimum lay-down length ratio increases with mass ratio, showing longer lay lengths at heavier masses.

The distribution indicates that heavier masses allow for larger chain diameters, longer lay-down lengths, lower maximum force ratios, and smaller static offsets. Most feasible designs are concentrated within anchor line mass ratios from 0.6 to 1.0. For steel chains, mooring stiffness is strongly affected by line mass, with heavier lines producing smaller offsets. As a result, static offsets and line force ratios of heavier mooring designs are near the lower bound, while their lay-down length ratios are near the upper bound.

### 5.3.2 Shared line configurations

Figure 5.5 shows that static analysis underestimates both offsets and mooring forces compared to dynamic simulations. As a result, designs that meet static criteria may still fail dynamic tests. This issue is pronounced for upwind lines in shared moorings, which experience the highest loads that static analysis underestimates. To address this, 5604 anchor lines that meet dynamic criteria under extreme loading conditions (Section 5.4.2) are used for shared line designs. For each anchor line, five shared line mass ratios are uniformly sampled across the full range, producing 28020 initial designs. Subsequent static wind tests (0°, 15°, and 30°) reduce this set to 4268 qualified designs, whose properties and static performance are shown in Figure 5.13.

The configuration properties illustrated include chain diameters and pretension ratios for both the anchor lines and the shared line, as well as anchor line length, anchor line chain grade, and shared line mass ratio. Static performance metrics comprise maximum offset, maximum force ratio, and minimum lay-down length ratio, each evaluated across all lines and three wind directions. Since the anchor line mass interval of 1/60 is slightly larger than the bin width along the X-axis (20 bins), an apparent stepping effect is observed, and the distribution appears divided into five blocks.

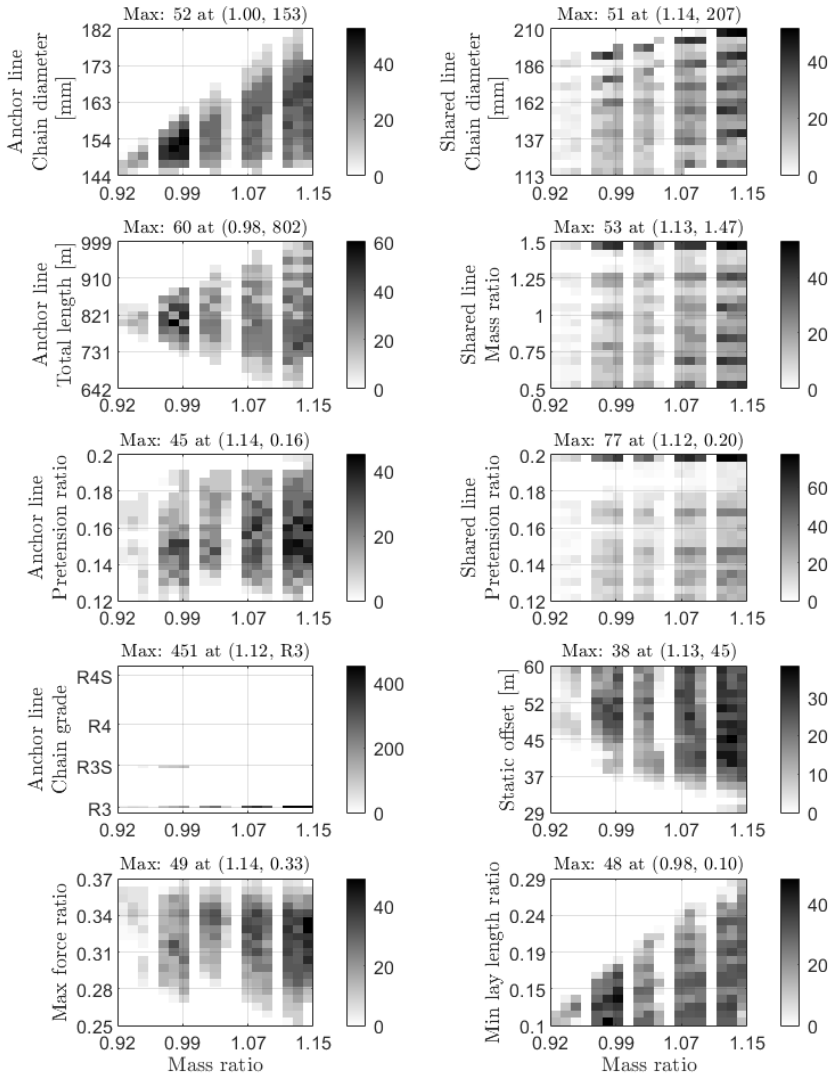


Figure 5.13: Grayscale 2D histograms of the line properties and static performance as functions of anchor line mass ratio for 4268 shared line configurations. Shading indicates the count in each bin, with 20 bins along both X and Y axes. Each subplot reports the maximum bin count and its location of bin centers.

As the anchor line mass ratio increases, the 4268 shared line designs accommodate a broader range of chain diameters with higher upper bounds. Anchor lines peak at a mass ratio of 1.00 with a diameter of 153 mm, while shared lines reach their peak at a higher mass ratio of 1.14 with a larger diameter of 207 mm. At the same mass ratio, the spread of anchor line diameters falls within that of the shared line, since the shared line adopts a wider range of mooring mass relative to the anchor line mass.

A K-shape region is observed in anchor line length as a function of mass ratio, with no feasible designs at small mass ratios for lengths above 910 m or below 731 m. Line lengths span a wider range with increasing mass ratio, and peak at a mass ratio of 0.98 and a length of 802 m. The shared line mass ratio is uniformly distributed, with a peak at an anchor line mass ratio of 1.13 and a shared line mass ratio of 1.47. Lower shared line mass ratios (from 0.5 to 0.75) at higher anchor line mass ratios (from 1.07 to 1.15) are also apparent, reflecting the diverse mass distribution within shared line designs.

Anchor line pretension ratios are concentrated between 0.14 and 0.18, peaking at a mass ratio of 1.14 and a pretension ratio of 0.16. In contrast, shared line pretension ratios cluster around 0.20 across the entire mass ratio range, with the highest occurrence at a mass ratio of 1.12. Most anchor line use the lowest chain grade, a choice that is consistent across all shared lines.

Static offsets decrease as the anchor line mass ratio increases, with most designs clustered at high mass ratios and peaking at a mass ratio of 1.13 with an offset of 45 m. Offsets below 37 m are absent at mass ratios lower than 0.99, but offsets above 45 m can still occur at mass ratios above 1.07. This occurs because the shared line governs the maximum offset, so a lighter shared line can produce a large offset even with a relatively heavy anchor line. The maximum force ratio follows a trend similar to that of the offset. In contrast, the minimum lay-down length ratio increases with mass ratio, with a peak of 0.10 at a mass ratio of 0.98.

The distribution shows that while heavier anchor lines can accommodate larger chain diameters for both the anchor lines and shared lines, as well as longer

anchor line lengths, static performance such as offsets and mooring force ratios, is strongly influenced by the shared line mass relative to the anchor line mass. Because the shared line mass ratio spans a wide range from 0.5 to 1.5, the resulting mass distribution within the shared line designs is highly diverse. As a result, combinations of heavier anchor lines with lighter shared lines can produce larger offsets and higher mooring force ratios.

### 5.3.3 Mooring design by the stiffness-linearized method

To highlight the differences from the nonlinear design method, the stiffness-linearized method [32, 33] is employed to generate shared line configurations for the two-turbine array. In their approach, the floater offset is assumed to be small, allowing each mooring line to be modeled as a linear spring with a linearized stiffness matrix. A constant wind force is applied to each floater to determine its horizontal offset.

A case study is conducted on the shared line layout shown in Figure 5.4(b), where anchor lines L2S and L3S connect the upstream FOWT1, and L5S and L6S connect the downstream FOWT2. The distance between the two turbines remains $6D$, with a steady wind force of 2.2 MN applied to both FOWTs. The line properties of L2S, L3S, and the shared line LS are initially unknown, while L5S and L6S are assigned properties similar to the anchor lines in the shared line configurations, as listed in Table 5.4. The stiffness-linearized method is then applied to determine the line properties for L2S, L3S, and LS.

The prescribed offsets are obtained from the static analysis of the two-turbine array with shared line configurations, as shown in Figure 5.9. The steady wind condition without wake effect results in $X_1$ of 32 m and $X_2$ of 45.8 m. Considering the static offset limit of 60 m for a water depth of 600 m [33], these offsets generally comply with the assumption of small displacements.

To calculate the mooring stiffness for the unknown lines, static force equilibrium is considered under both no-wind conditions, where pretensions balance each other, and steady wind conditions, where mooring forces counteract the wind

force. As a result, the mooring stiffness of each line depends on the prescribed offsets ($X_1$ and $X_2$), the wind force ($WF_1$), and the known stiffness of the downwind lines, which can be derived from the force–displacement relationship based on line characteristics. Details of the force equations are provided in Appendix A. Finally, the line mass densities are linearly scaled according to their respective mooring stiffness.

The mooring stiffness for the downwind lines (L5S and L6S) are derived through the linearized force-displacement relationship, as expressed in Equation 4.1, excluding mooring axial stiffness ($EA$). Since the stiffness linearized neglects the radii of both the anchor and fairlead, but the mooring stiffness is highly sensitive to the displacement range, three displacement ranges are considered, as displayed in Figure 5.14, starting at three surge displacements ($X_0$) of 0 m, 20 m, and 40 m, respectively.

A linear fit is first performed to determine the slope in Figure 5.14, which represents the mooring stiffness of the downwind anchor lines (L5S and L6S). This linearized stiffness is then used in Equation A.1 to compute the mooring stiffness of the upwind lines (L2S and L3S) and the shared line (LS). Finally, the mass density ($\rho_c$) is scaled linearly based on the mooring stiffness, and the chain diameter ($D_c$) is calculated using Equation 5.1. The resulting stiffness and chain properties for the upwind lines and shared line, determined by the stiffness linearized design method, are presented in Table 5.5.

The stiffness linearized design method generates three chain diameters for the upwind anchor lines and shared line that exceed the upper limit of available chain diameters on the market. This outcome highlights the limitation of the existing stiffness linearized design method. Although straightforward and simple for preliminary mooring designs, the stiffness linearized design method neglects mooring elasticity, fairlead and anchor radii, and relies solely on the small floater offset assumption, which can lead to unrealistic shared line designs.

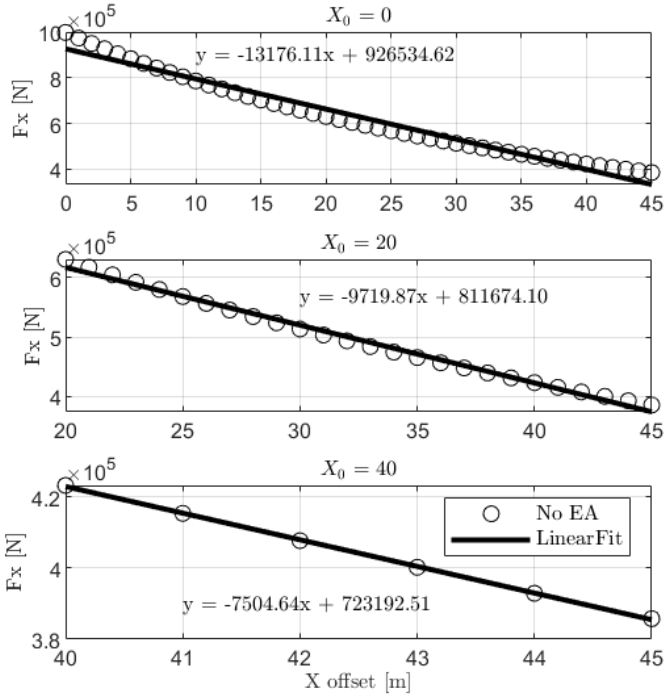


Figure 5.14: The force-displacement relationship for the downwind line without mooring axial stiffness ($EA$). $X_0$ represents the start point to linearize $K$.

Table 5.5: The calculated mooring stiffness ($K$) and chain diameter ($D_c$) for upwind line L2s and shared line Ls using the linear design method.

| $X_0$ [m] | $K$ [$10^4$ N/m] | | | $D_c$ [mm] | |
|---|---|---|---|---|---|
| | L5S | L2S | LS | L2S | LS |
| 0 | -1.3 | 5.0 | 7.2 | 261.1 | 313.5 |
| 20 | -1.0 | 5.5 | 9.5 | 318.7 | 419.2 |
| 40 | -0.8 | 5.8 | 11.0 | 373.0 | 512.7 |
| Nonlinear design method | | | | 144.0 | 128.0 |

## 5.4 Dynamic simulation in mooring design

As discussed in Section 5.3, the nonlinear design method generates 17352 conventional and 4268 shared line designs through static analysis. To evaluate their dynamic responses, simulations are conducted for the two-turbine floating array with these designs under turbulent wind and irregular wave conditions. The simplified modeling approach, detailed in Chapter 6, is used for these dynamic simulations. The goal is to assess the peak floater offset, maximum line force ratios, minimum lay-down length ratios, and mooring fatigue resistance.

### 5.4.1 Load cases and environmental conditions

The tested load cases consider both extreme and operational conditions, as summarized in Table 5.6, with corresponding environmental parameters including mean upstream wind speed ($V_m$), wind direction ($\theta$), significant wave height ($H_s$), and peak wave period ($T_p$). The wind direction $\theta$ is measured from the positive X-axis, and the array layout is rotated so that the inflow is aligned with 0°, as illustrated in Figure 5.4.

Table 5.6: Environmental conditions.

| Load case | mooring | $V_m$ [m/s] | $\theta$ [°] | $H_s$ [m] | $T_p$ [s] |
|---|---|---|---|---|---|
| Extreme | conventional | 11 | [0,60,90] | 5.1 | 9 |
| | shared line | 11 | [0,15,30] | 5.1 | 9 |
| Operation | conventional | 11 | [0,60,90] | 1.5 | 7 |
| | shared line | 11 | [0,15,30] | 1.5 | 7 |

Extreme loading conditions are selected based on OpenFAST simulations of an individual FOWT [120]. The results indicate that the most critical floater surge occurs at the rated wind speed (11 m/s) combined with extreme wave conditions corresponding to a 50-year return period under Design Load Case (DLC) 1.6. This surge exceeds that found at the highest wind speed (41 m/s) with a parked turbine status under DLC 6.1.

Normal operation conditions correspond to DLC 1.2, with an approximate 20% probability of the sea states near the rated wind speed [121] (Figure 6.2). Figure 5.15 illustrates the mooring fatigue damage for mean wind speeds ranging from 3 m/s (cut-in) to 25 m/s (cut-out), based on 1-hour simulations of a single FOWT with a conventional configuration. In OpenFAST simulations, three yaw misalignment angles and three random wind seeds were considered for each wind speed. Mooring fatigue damage (Equations 4.3 and 4.4) is calculated following the procedure described in Section 4.1.4.

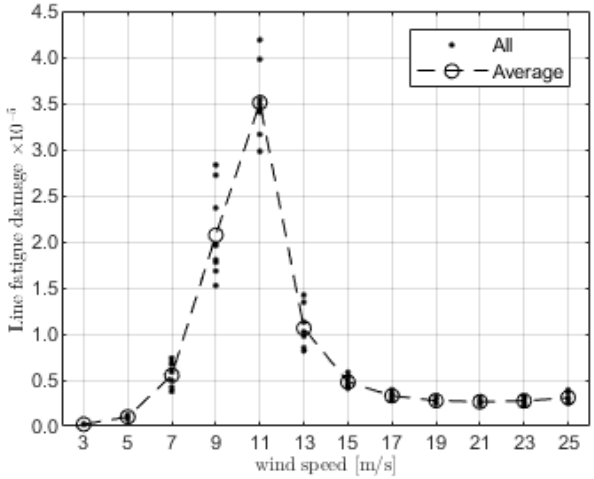


Figure 5.15: Mooring fatigue damage under DLC 1.2 for a single FOWT with a conventional configuration, for mean wind speeds ranging from 3 to 25 m/s.

Figure 5.15 shows that the highest mooring fatigue occurs at the mean upstream wind speed of 11 m/s, while fatigue remains relatively low at mean speeds below 7 m/s and above 13 m/s. The total normalized fatigue considering the occurrence probability of each mean speed reaches $1.3\times10^{-}5$, while the contribution from 11 m/s, given its occurrence of 18%, is approximately $0.7\times10^{-}5$. This indicates that the 11 m/s wind speed dominates the mooring fatigue of the single FOWT.

In addition, Figures 6.14 and 6.15 show that, for the floating turbine array with shared line designs, a mean upstream wind speed of 11 m/s produces the

highest mooring fatigue. Using a single sea state underestimates the normalized fatigue by approximately 50% for the three shared baseline designs with the smallest chain diameters (Tables 6.2 and 6.3), however, it provides a practical and efficient approach for large-scale simulations. Such underestimation is less pronounced for heavier mooring designs with larger chain diameters (Figure 5.19). Applying a higher fatigue safety factor of 10 (double the standard factor of 5 [12]) further compensates for the underestimation to ensure a reliable assessment.

Consistent with the static analysis, three wind directions are considered in the dynamic simulation, with the mooring layout rotated clockwise accordingly, as shown in Figure 5.4. The IEC Kaimal turbulence model, Class C, is used to represent moderate wind turbulence, with a mean upstream wind speed equal to 11 m/s. TurbSim V2 is employed to generate the synthetic turbulent inflow for the floating turbine array. The grid discretization for the TurbSim input file follows the guidelines of [54], while the distributed scripts [127] are used to specify the inflow generation parameters for each wind farm layout. Irregular waves are modeled using the Pierson-Moskowitz spectrum. Each dynamic simulation runs for 4800 s, with final 3600 s of simulation results are post-processed to extract variables for comparison. Six wind seeds are considered for each wind speed, and the results are averaged across all random seeds.

### 5.4.2 Conventional designs without wake or fatigue

The 17352 conventional configurations that meet the static design criteria are assessed under extreme loading conditions for three directions (60°, 90°, and 0°). Wake effects are excluded from dynamic simulations, and mooring fatigue is not considered under these extreme load cases. The number of qualified designs decreases to 14148, 8401, and 5604, respectively, for the three directions. Line properties of these 5604 designs, along with simulation results for the floating turbine array, are shown in Figure 5.16. These designs are also used for shared line designs described in Section 5.3.2. Results are averaged across

six seeds and represent extreme values across all lines and directions rather than any specific case.

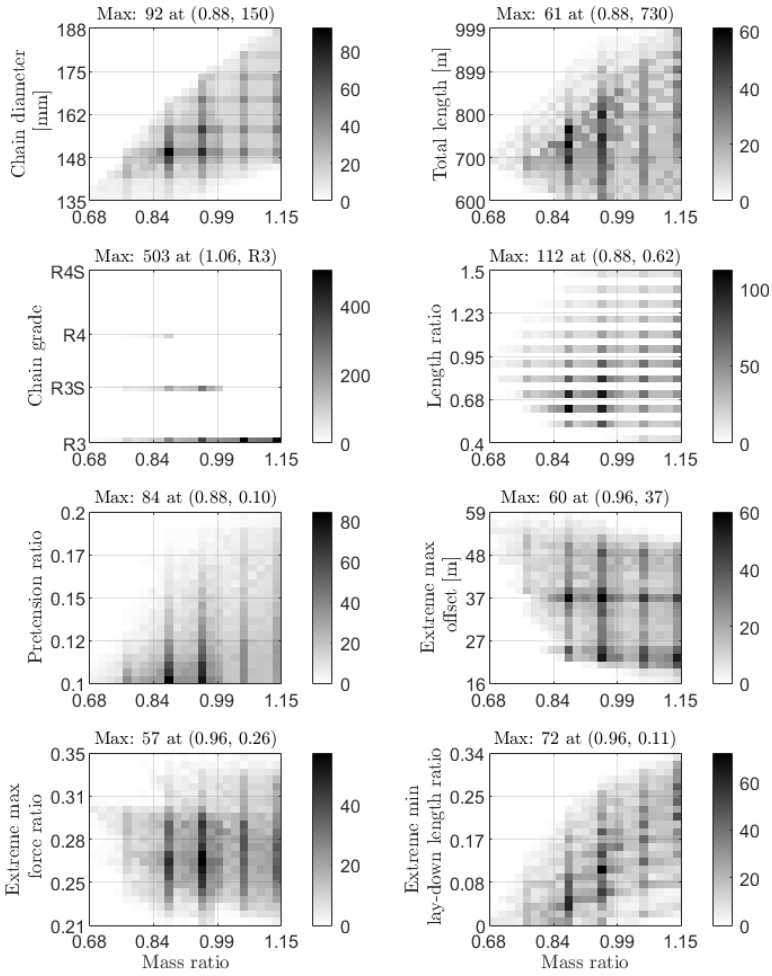


Figure 5.16: Grayscale 2D histograms of the 5604 anchor line properties and simulation results without wake or fatigue as functions of anchor line mass ratio. Shading indicates the count in each bin, with 24 bins along both X and Y axes. Each subplot reports the maximum bin count and its location of bin centers.

In general, the line properties and FOWT performance follow trends similar to

those observed in the static analysis (Figure 5.12) as functions of anchor line mass ratio. As the mass ratio increases, anchor lines accommodate larger chain diameters, smaller offsets, lower force ratios, and longer lay-down length ratios under extreme loading conditions. However, compared to static results, the starting point for both line properties and dynamic performance shift toward heavier designs. For example, feasible designs in static analysis begin at a mass ratio of 0.4 with a chain diameter of 85 mm, while in the dynamic simulations, they start at a heavier mass ratio of 0.7 with a larger chain diameter of 135 mm. The trends for length ratios increase with mass ratio in dynamic simulations, in contrast to the decreasing trend in static analysis, and the lower bounds for offsets and force ratios are higher, highlighting the limitations of relying solely on static analysis for determining feasible mooring designs.

### 5.4.3 Wake-free conventional designs including fatigue

The 5604 conventional designs that meet extreme design criteria are subsequently evaluated under operational conditions for three directions. Dynamic simulations exclude wake effects, but mooring fatigue damage is calculated following the procedure described in Section 4.1.4. After the fatigue analysis, the design set is reduced to 5016, of which line properties, together with simulation results for the floating turbine array, are shown in Figure 5.17. Results are averaged over six seeds and represent the extreme values across all lines and directions, rather than individual cases.

The distribution of the 5016 anchor line profiles remains generally consistent with that of the 5604 designs (Figure 5.16), which were previously evaluated without considering wake effects or mooring fatigue. However, shifts are observed in the locations of peak occurrences for line properties. In particular, both length and pretension ratios move toward higher mass ratios in the 5016 designs, reflecting the need for adequate fatigue resistance under operational conditions. The reduction in qualified designs and the observed shifts in line properties underscore that mooring fatigue is a critical factor in configuration

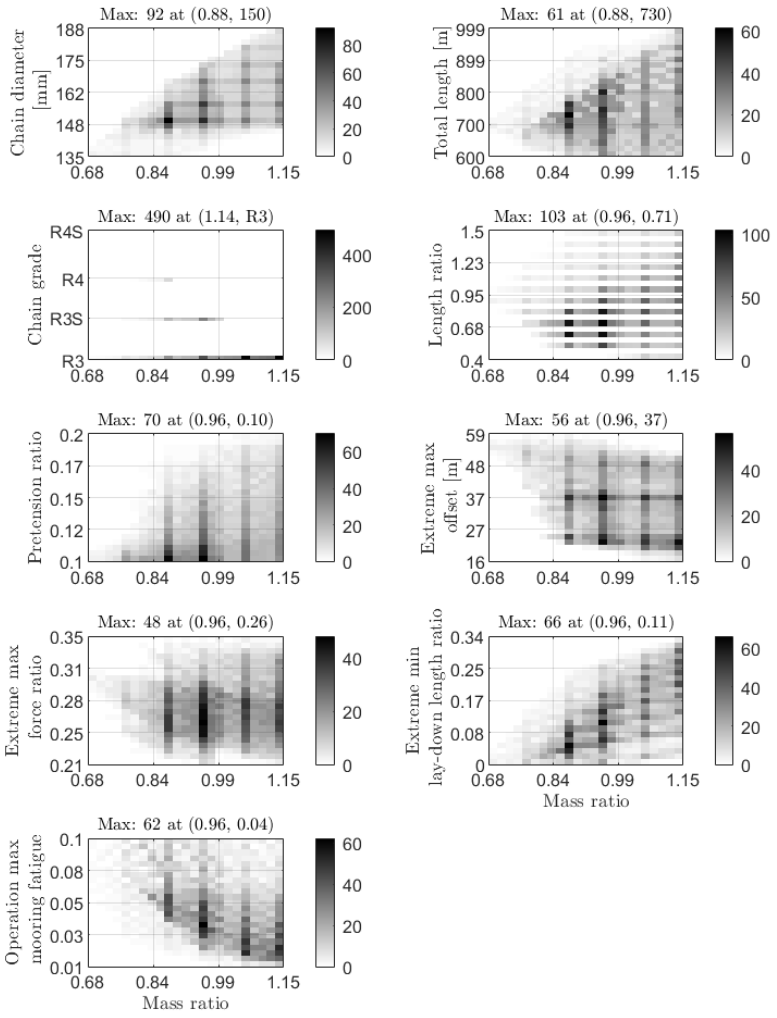


Figure 5.17: Grayscale 2D histograms of the 5016 anchor line properties and simulation results without wake effects as functions of anchor line mass ratio. Shading indicates the count in each bin, with 24 bins along both X and Y axes. Each subplot reports the maximum bin count and its location of bin centers.

assessment. Therefore, mooring fatigue should be incorporated into the design evaluation to ensure reliable mooring performance.

### 5.4.4 Conventional designs with both wake and fatigue

Including wake effects in dynamic simulations reduces the 5016 conventional configurations to 2206 designs that maintain sufficient fatigue resistance across three wind directions. Figure 5.18 presents their line properties and dynamic performance, which are averaged over six seeds and represent extreme values across all lines and directions.

The 2206 anchor line profiles cluster around mass ratios of 0.98, 1.06, and 1.14 across all subplots, and their line properties and dynamic responses generally remain consistent with those of the 5016 configurations shown in Figure 5.17. However, including wake effects shifts the line properties toward higher mass ratios with increased parameter values. The starting mass ratio rises to 0.80, compared to 0.68 for the 5016 lines. The most frequent chain diameter increases from 150 mm to 162 mm, with the lower bound rising from 135 mm to 155 mm. These increases in anchor line diameter and mass significantly improve mooring fatigue resistance, particularly for upwind lines supporting downstream FOWTs, which experience higher wind turbulence due to wake effects, resulting in greater load fluctuations and increased fatigue damage. This increased fatigue damage is the primary reason some of the 5016 configurations fail to meet the design criteria.

The increased chain diameter also influences the length distribution. The upper bound for anchor line length decreases from 1000 m in the 5016 configurations to 887 in the 2206 profiles, with the peak shifting downward from 730 m at a mass ratio of 0.88 to 710 m at a mass ratio of 0.98. Similarly, the length ratio drops from 0.71 to 0.63. While the pretension ratio generally keeps consistent with that of the 5016 configurations.

The upper bound for extreme offset reduces from 59 m in the 5016 configurations to 53 m in the 2206 profiles, with the peak dropping from 37 m to 20 m. Similarly, the upper bound for maximum mooring fatigue under normal operation conditions decreases slightly from 0.1 to 0.09, with the peak falling from 0.04 to 0.03. These reductions reflect improved station-keeping capability

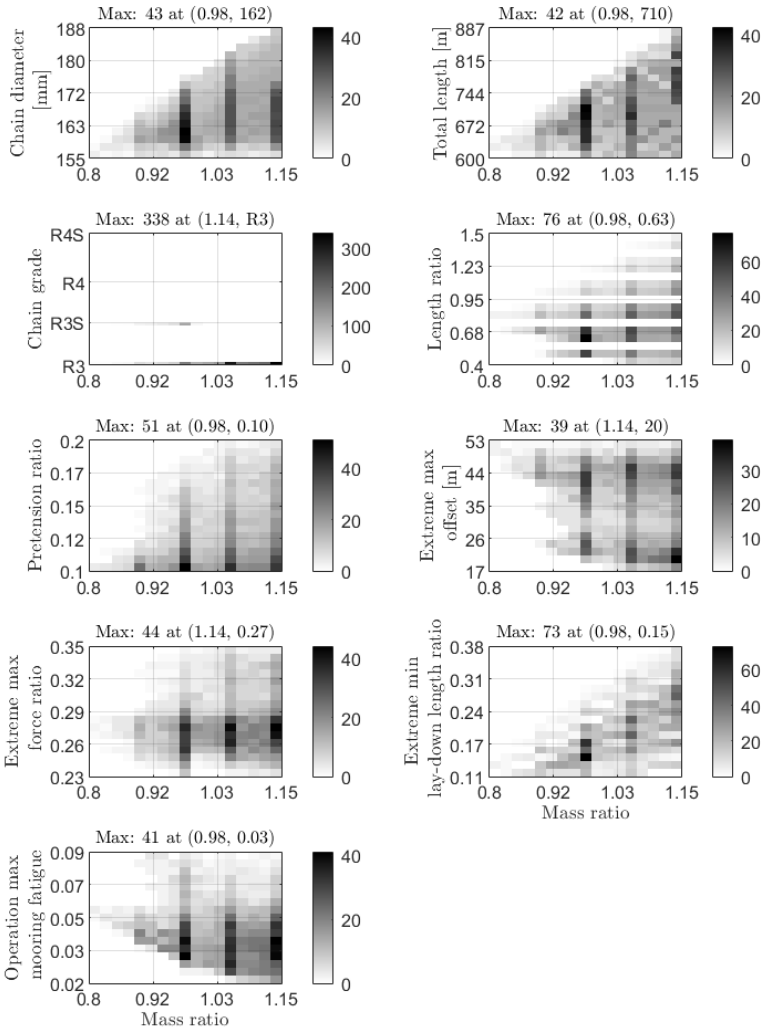


Figure 5.18: Grayscale 2D histograms of the 2206 anchor line properties and simulation results including wake and fatigue as functions of anchor line mass ratio. Shading indicates the count in each bin, with 18 bins along both X and Y axes. Each subplot reports the maximum bin count and its location of bin centers.

due to the higher mooring stiffness and fatigue resistance of these profiles. In contrast, compared to the 5016 configurations, the extreme mooring force ratio

displays an increased lower bound from 0.21 to 0.23, and a slight growth in the peak force ratio from 0.26 to 0.27 in the 2206 profiles. Changes in lay-down length ratio are more pronounced, with the lower bound rising from 0 to 0.11 and the peaks from 0.11 to 0.15.

### 5.4.5 Shared line designs with both wake and fatigue

The 5604 anchor line profiles that satisfy the extreme criteria and exclude fatigue assessment, rather than the 5106 profiles that pass both extreme and fatigue checks, are used to explore a broader range of potential shared line profiles. This approach is based on the understanding that shared line designs can change mooring stiffness and load distribution, which ultimately influence mooring fatigue performance.

For each of the 5604 anchor line profiles, five shared line mass ratios are uniformly sampled across the full range, producing 28020 initial shared line designs. Static wind tests reduce this set to 4268 qualified designs (Section 5.3.2). Dynamic simulations, including wake effects and mooring fatigue at three directions (0°, 15°, and 30°), further narrow the set to 510 designs. Their configuration properties and corresponding simulation results are presented in Figure 5.19. Results are averaged over six seeds and represent the extreme values across all lines and directions, rather than from any specific case. All lines use the lowest chain grade (R3).

Compared to the 4268 designs derived from static analysis (Figures 5.13), the 510 shared line designs evaluated by dynamic simulations show generally similar trends in line property distribution. Heavier anchor lines allow for larger chain diameters in both anchor lines and the shared line. Designs with anchor line lengths below 782 m or above 908 m at low mass ratios are less common. Pretension ratios in both anchor lines and the shared line cluster at higher mass ratios, with shared line pretension ratios reaching 0.20 across the full mass ratio range.

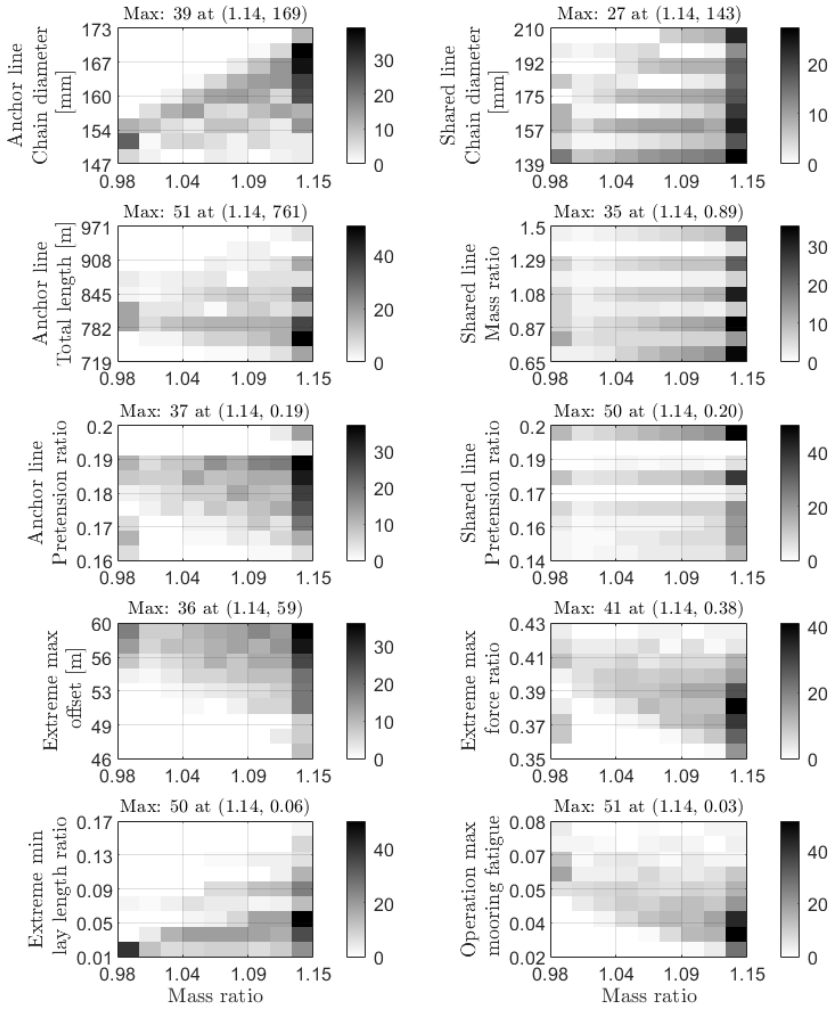


Figure 5.19: Grayscale 2D histograms of the 510 shared line designs, showing line properties and simulation results (with wake effects and mooring fatigue) as functions of anchor line mass ratio. Shading indicates the count in each bin, with 10 bins along both X and Y axes. Each subplot reports the maximum bin count and its location of bin centers.

The line properties and dynamic responses of the 510 designs consistently peak at a mass ratio of 1.14, with the minimum anchor line mass ratio shifting upward from 0.92 in static analysis to 0.98. The 510 designs also exhibit a

narrower spread of anchor line chain diameters, with the peak diameter rising from 153 mm in static analysis to 169 mm. Conversely, the most frequent shared line chain diameter decreases from 207 mm to 143 mm, although the minimum diameter grows from 113 mm to 139 mm.

The narrow diameter range of anchor lines in the 510 designs leads to a narrower range of anchor line lengths compared to the 4268 designs in static analysis, with the upper bound decreasing from 999 m to 971 m and the lower bound increasing from 642 m to 719 m. The minimum shared line mass ratio rises from 0.5 to 0.65, while the peak anchor line pretension ratio shifts from 0.16 to 0.19. The peak shared line pretension ratio remains unchanged at 0.20.

The minimum offset for the 510 designs reaches 46 m, significantly higher than the 29 m observed in static analysis. The extreme offset peaks at 59 m, compared with a peak static offset of 45 m. This difference highlights the limitation of using static analysis for shared line designs, which tends to significantly underestimate offset. The stiffness-linearized method uses the static offset as the only design constraint, leading to unrealistic shared line designs. The pronounced increase in offset for the 510 designs result in a noticeable rise in the extreme mooring force ratio and a reduction in the minimum lay-down length ratio. However, mooring fatigue under normal operation conditions peaks at only 0.03 at the highest mass ratio, indicating that fatigue is not a critical concern for most 510 shared line designs.

## 5.5 Conventional vs. shared line designs

### 5.5.1 Configuration characteristics

Figure 5.20 compares chain diameters, line lengths, and pretension forces of anchor lines, as well as mooring masses per FOWT across 2206 conventional and 510 shared line designs. Shared line designs tend to use smaller chain diameters and longer anchor lines, with higher and more narrowly distributed

pretension forces. They also tend to have heavier mooring masses per FOWT, while conventional designs exhibit a wider range of pretension ratios.

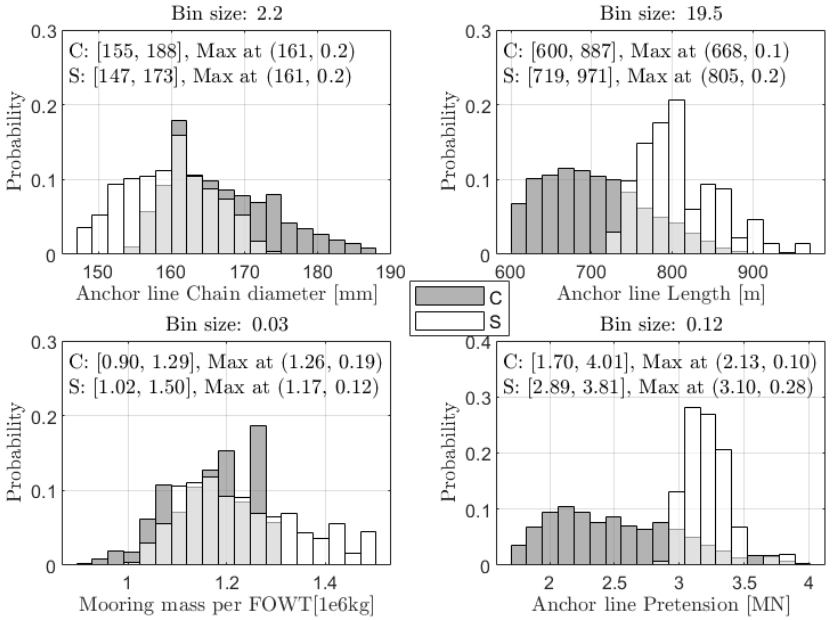


Figure 5.20: Comparison of configuration characteristics between the 2206 conventional ("C") and 510 shared line ("S") designs. Each subplot shows the bin size, data range, and the X-axis bin center at the maximum probability for both designs. Histograms use 20 bins along the X-axis.

Shared line designs show a leftward shift in chain diameter distribution, with peaks at 161 mm. Anchor line lengths in shared line configurations shift rightward, clustering around 805 m, while conventional designs are more evenly distributed up to 730 m, with a peak at 668 m. Shared line configurations also exhibit a rightward shift in mooring mass per FOWT, ranging from $1.02\times10^6$ kg to $1.50 \times 10^6$ kg, with a peak at $1.17 \times 10^6$ kg. In contrast, conventional configurations span a narrower range, starting at $0.9 \times 10^6$ kg, with increasing occurrence toward heavier mass and peaking at $1.26 \times 10^6$ kg. Anchor line pretensions in shared line configurations are more tightly distributed between 2.89 MN and 3.81 MN, with a peak at 3.10 MN, while conventional configurations cover a broader range from 1.70 MN to 4.01 MN, with a peak at 2.13 MN.

### 5.5.2 FOWT dynamic performance

Figure 5.21 compares the dynamic performance of the two-turbine floating array using 2206 conventional and 510 shared line designs under normal operation conditions at a wind direction of 0°. This wind direction has been used for performance evaluations [49, 47], and is applied across both conventional and shared mooring designs in this study. The simulations account for wake effects, and the performance evaluation includes mooring fatigue. Reported results are averaged over six random seeds.

The conventional mooring configurations produce maximum floater offsets ranging from 13 m to 33 m. Due to stronger wake-induced turbulence, the downstream FOWT2 reaches a higher peak offset (28 m) than the upstream FOWT1 (20 m). In contrast, the 510 shared line designs shift the offset ranges upward, with minimum offsets of 30 m and 46 m, and peak offsets of 34 m and 56 m for FOWT1 and FOWT2, respectively. While offsets for FOWT1 slightly overlap between the two design sets, FOWT2 exhibits significantly larger offsets using shared line designs.

The increase in floater offsets leads to higher mooring force ratios for the upwind lines connected to FOWT1, rising from a starting ratio of 0.22 (conventional) to 0.32 (shared) and a peak ratio from 0.26 (conventional) to 0.36 (shared). In contrast, the maximum force ratio on the downstream FOWT2 shifts leftward, indicating lower force ratios using the 510 shared line designs. This behavior results from the altered load distribution in the shared line configuration, which reduces the load on the mooring lines supporting the downstream FOWT, as the upwind anchor lines connected to the upstream FOWT experience the highest environmental loading.

Despite the larger offsets and higher mooring force ratios in the upwind anchor lines, the 510 shared line designs maintain sufficient mooring fatigue resistance, comparable to the 2206 conventional designs. The upwind lines show a slight increase in the lower bound of fatigue, from 0.01 (conventional) to 0.02 (shared),

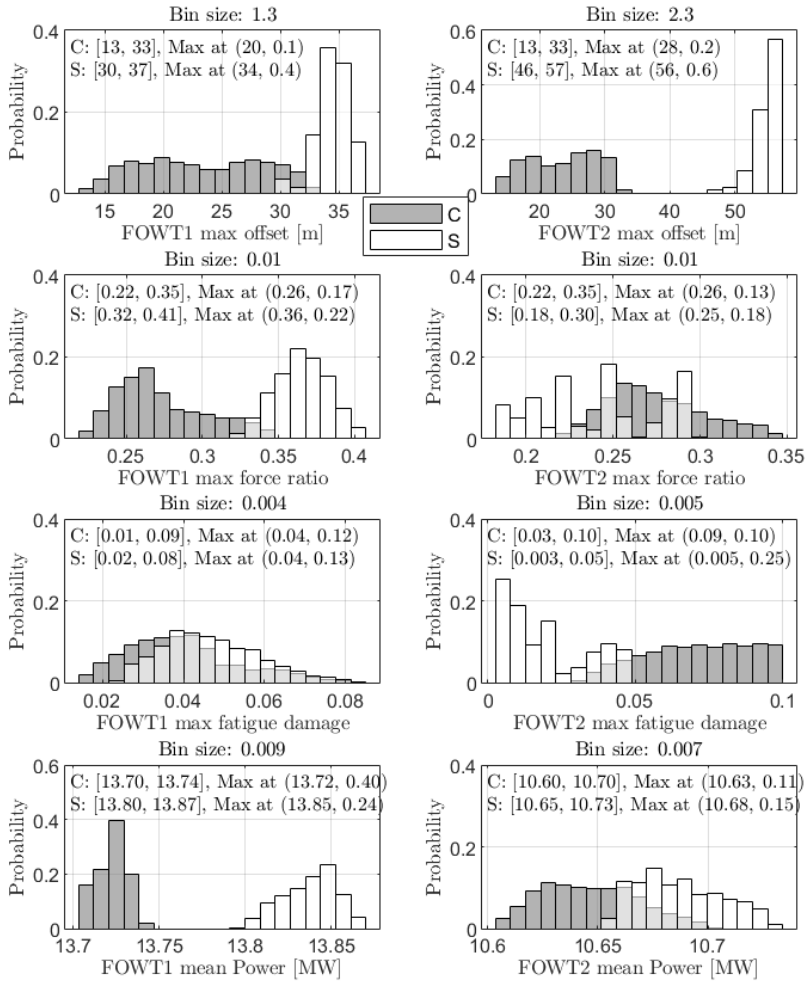


Figure 5.21: Comparison of dynamic performance across 2206 conventional ("C") and 510 shared line ("S") designs under operation conditions at a wind direction of 0°. Each subplot shows the bin size, data range, and the X-axis bin center at the maximum probability for both designs. Histograms use 20 bins along the X-axis.

while the mooring lines supporting downstream FOWT2 exhibit notably improved fatigue performance, with a reduced peak of 0.005 compared to 0.09 in the conventional configurations.

Finally, the mooring influence on power output is minor, with differences below 0.2 MW between conventional and shared line designs, and generally less than 0.1 MW within each type for both FOWT1 and FOWT2. The 510 shared line designs exhibit slightly higher power, with approximately 1% rise in the upper bound for FOWT1, and a rightward shift in FOWT2 power, raising its upper bound from 10.70 MW (conventional) to 10.73 MW (shared).

### 5.5.3 Mooring cost evaluation

The mooring material cost is estimated using an empirical model (Equation 5.3) from [31]. In this model, the cost of mooring lines depends on both the chain $MBL$ and total length $L_T$, while the anchor cost depends solely on the chain $MBL$. The model was developed based on the structural mass of three FOWT models, which were estimated using an in-house sizing tool, and it predicts the minimum cost for mooring systems composed of chain lines and drag-embedment anchors for semi-submersible FOWTs in water depths ranging from 40 m to 1000 m [31].

A real-world floating wind project benchmark, which features the 15-MW turbine and a six-line mooring configuration [6], is used to illustrate the uncertainty of this cost model under evolving price conditions. Due to limited benchmark details, a conventional layout is assumed. An exchange currency rate of 1.34 is used to convert the anchor and mooring line costs of $3.5 \times 10^4$ GBP and $17.4 \times 10^4$ GBP per MW, respectively, to approximately $3.5 \times 10^5$ USD and $17.5 \times 10^5$ USD for a single 15-MW FOWT with a three-line configuration.

Figure 5.22 illustrates the relevance of the cost model to real prices. The model predicts a minimum total cost of $22.3 \times 10^5$ USD for conventional designs, approximately 6 % higher than the benchmark cost of $21.0 \times 10^5$ USD. Both the anchor and mooring line costs for the real-world project fall within the predicted range, validating the model. The difference between the real prices and model estimates may be attributed to site-specific factors, as the benchmark assumes

a water depth of 100 m, while this study considers 200 m, influencing the mooring configuration and associated costs.

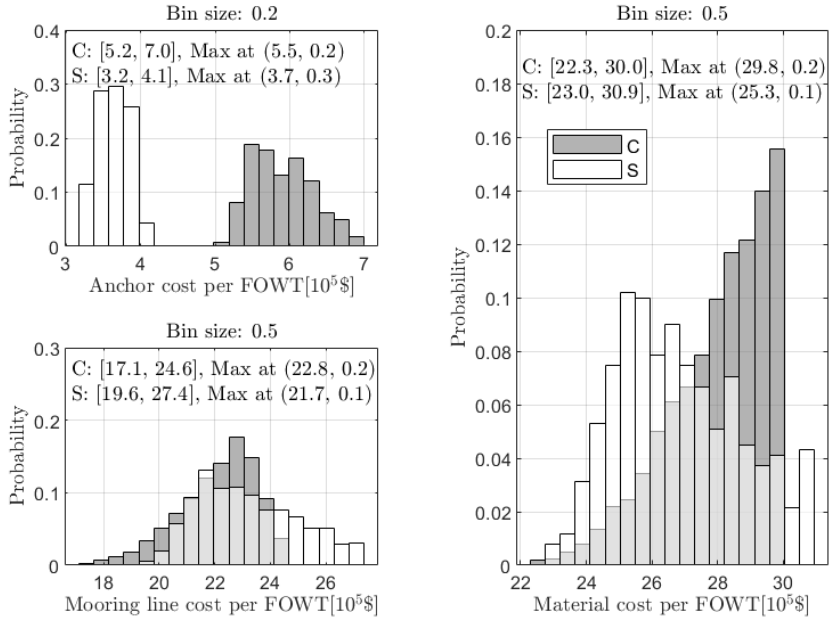


Figure 5.22: Mooring material cost per FOWT between 2206 conventional ("C") and 510 shared line ("S") configurations. (a) Top-left: anchor cost; (b) Bottom-left: mooring line cost; (c) Right: total mooring material cost. Each subplot shows the bin size, data range, and the X-axis bin center at the maximum probability. Histograms use 20 bins along the X-axis.

The shared line design connects two FOWTs with a single line, reducing the required number of anchors and lowering anchor costs compared to conventional designs. However, the increased offsets induced by shared lines require heavier anchor lines to withstand increased upwind mooring forces due to coupling effects, which raises the mooring line cost. For the 510 shared line designs, anchor costs range from 3.2 to $4.1 \times 10^5$ USD, narrower and lower than those of the 2206 conventional configurations, which range from 5.2 to $7.0 \times 10^5$ USD. In contrast, mooring line costs for shared line designs shift rightward, with higher minimum (about 13 %) and maximum (about 10 %) costs but a lower peak cost (about 5 %) compared to conventional configurations.

The increased mooring line cost raises the minimum mooring cost of the shared line designs to $23.0 \times 10^5$ USD, about 3 % higher than the lowest cost of the conventional configurations ($22.3 \times 10^5$ USD). However, the overlap in the cost distributions suggests that the 510 shared line designs can achieve a similarly broad range as the 2206 conventional configurations. Most shared line designs cluster around $25.3 \times 10^5$ USD, while conventional designs concentrate near $29.8 \times 10^5$ USD, about 15 % higher than the most frequent shared line cost. This finding refines previous static analyses by [32], which suggested that conventional designs are more cost-effective at a 200-m water depth.

At both ends of the mooring cost spectrum, the 510 shared line designs exhibit approximately 3 % higher costs than the 2206 conventional configurations. A detailed comparison of the lowest and highest mooring costs as well the configuration properties and dynamic responses is presented in Table 5.7.

Table 5.7: Configurations and dynamic responses for conventional and shared line designs with the lowest and highest mooring material costs per FOWT.

| | Conventional | | Shared Line | |
|---|---|---|---|---|
| Parameter | lowest | highest | lowest | highest |
| Mooring cost $C_m$ [$10^5$ USD] | 22.30 | 30.00 | 22.99 | 30.94 |
| Chain diameter $D_{c1}$ [mm] | 155 | 173 | 152 | 169 |
| Length ratio $R_L$ | 0.80 | [0.5:0.1:1.1] | 0.6 | 0.5 |
| Mass ratio $R_M$ [%] | 0.80 | 1.15 | 0.98 | 1.15 |
| Chain diameter $D_{c2}$ [mm] | - | - | 141 | 210 |
| *Mean power for FOWT1 [MW] | 13.70 | [13.72 13.74] | 13.85 | 13.81 |
| Mean power for FOWT2 [MW] | 10.60 | [10.63 10.69] | 10.67 | 10.73 |
| Maximum offset [m] | 32.80 | [14.79 30.03] | 55.61 | 49.11 |
| Maximum force ratio | 0.26 | [0.24 0.32] | 0.39 | 0.36 |
| Maximum fatigue damage | 0.098 | [0.050 0.060] | 0.064 | 0.035 |

**Dynamic results for normal operation load cases.*

At the lowest cost, the shared line designs employ heavier anchor lines with smaller chain diameters than the conventional configuration. At the highest cost, both conventional and shared line designs use similar anchor line masses, but the shared line adopt larger chain diameters than the anchor lines to reduce

the maximum offset. While conventional designs achieve slightly lower costs at both bounds, these savings come at the expense of dynamic performance: designs at the cost extremes experience over 30 % higher mooring fatigue and deliver about 1 % less power output compared with shared line designs. The enhanced fatigue resistance of shared line configurations may, in turn, enable more cost-effective operation and maintenance over the array's lifetime.

## 5.6 Summary

This chapter presents a nonlinear design method for shared line configurations to address the limitations of stiffness-linearized approaches. The proposed method integrates realistic line characteristics and practical design constraints, ensuring more robust configurations by considering mooring forces and geometry rather than relying solely on small prescribed offsets. While the stiffness-linearized method produces chain diameters that exceed the limits of chains available on the market, highlighting its shortcomings.

This chapter also investigates the influence of design parameters on shared mooring designs, including shared line mass ratio, wind direction, floater pitch, wake effects, and mooring axial stiffness. Sensitivity analyses indicate that all these factors should be considered in the static design. For conventional mooring designs, heavier line masses allow larger chain diameters, longer lay-down lengths, lower maximum force ratios, and smaller static offsets. In shared line designs, heavier anchor lines similarly support larger chain diameters and longer lines, but static offsets and mooring force ratios are strongly influenced by the shared line mass relative to the anchor line mass.

Using the simplified modeling approach, dynamic simulations of the two-turbine array are performed across large sets of shared line and conventional mooring designs. Accounting for mooring fatigue reduced the number of feasible conventional designs from 5604 to 5016, while including wake effects further reduced this to 2206, accompanied by shifts toward larger chain diameters, higher mass ratios, and greater extreme offsets. These results demonstrate the significant

influence of wake effects and fatigue on mooring design and performance evaluation.

Comparisons between static and dynamic analyses show that, while applying a constant wind force in static analysis can effectively estimate offsets and mooring forces, it significantly underestimates extreme responses. Consequently, the stiffness-linearized method for shared line design, which relies on static offsets, can produce unrealistic configurations that fail under dynamic simulations.

Despite larger offsets and higher mooring force ratios, the 510 shared line designs maintain sufficient mooring fatigue resistance comparable to the 2206 conventional designs. Their cost-saving potential is evaluated using an empirical material cost model, which is validated against a benchmark real price. While shared line designs exhibit 3% higher costs at the minimum, due to heavier mooring lines needed to withstand larger floater offsets, their most frequent cost achieves a 15% saving. Moreover, at both the lowest and highest costs, shared line designs demonstrate over 30% higher fatigue resistance, highlighting their advantages over conventional moorings for floating wind farms.

# 6 Simplified modeling approach for floating wind farms

This chapter introduces a simplified modeling approach for predicting the dynamic performance of floating wind farms with shared line designs. It addresses research gaps identified in the literature (Chapter 2). To balance computational efficiency and prediction accuracy, the simplified model employs a validated low-order solver to compute structural dynamics, as well as the aerodynamic and hydrodynamic forces on each FOWT, while mooring forces are calculated using analytical catenary equations.

The modeling framework is outlined in Section 6.1. Its computational efficiency and prediction accuracy are verified against a higher-fidelity simulation tool in Section 6.2. Section 6.3 presents the simulation results for a two-turbine floating array with both shared line and conventional mooring designs under different environmental conditions. Section 6.4 demonstrates an application of the proposed approach to improve the performance of shared line designs.

## 6.1 Framework of the simplified modeling approach

The simplified modeling method for the floating wind farm comprises three main modules: a low-order multi-body simulation module that solves the motion equations for each FOWT; a quasi-static mooring model that accommodates various configurations and computes mooring forces; and a Gaussian wake

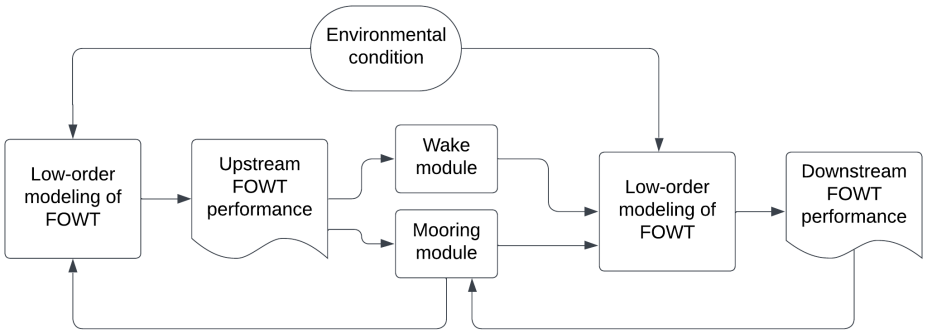


Figure 6.1: The framework of the simplified modeling approach (adapted from [128]).

model that calculates the mean wake deficits experienced by the downstream turbines. The modeling framework is illustrated in Figure 6.1.

The environmental module processes time series of wind, waves, and ocean currents, supplying input environmental variables to the low-order module to compute the system dynamics of each FOWT. For downstream turbines, the disturbed wind speed that accounts for the mean wake deficit, is used for aerodynamic force calculations. Given the sufficient spacing between turbines, wave conditions are assumed to remain unaffected by the floater motions. Further details about the low-order module are available in Section 4.3.1. This module calculates the aerodynamic and hydrodynamic forces, as well as the elastic deformation of the tower for each individual turbine.

Unlike the stand-alone implementations of the low-order simulation module [111, 45], which compute mooring forces either by linearly interpolation from a database or through coupling with external software, the simplified modeling approach delegates the calculations of mooring forces and moments to a separate mooring module. The mooring module applies the elastic catenary equations and provide the resulting mooring loads to the low-order simulation module for each FOWTs.

The performance modules manage the post-processing of simulation results, such as the body position and velocity vectors. They also support data analysis,

such as a fatigue damage calculation (Section 4.1.4). In addition, these modules provide essential spatial parameters to the wake and mooring modules. For example, they compute the distances between the hub center of the upstream turbine and each point on the downstream rotor grid for wake deficit estimation. They also output fairlead positions for mooring force calculations. The entire simplified modeling approach is implemented in MATLAB Simulink, and is compatible with controller integration for individual FOWTs.

### 6.1.1 Quasi-static mooring module

This module calculates mooring forces using a quasi-static approach based on floater positions (Section 4.1.4), making it well-suited for early-stage FOWT studies. Unlike dynamic mooring analysis (Section 2.1.1), which accounts for hydrodynamic forces such as inertia and drag on the mooring line, the quasi-static mooring analysis does not require damping or inertia coefficients that are highly sensitive to environmental conditions and floater motions. As a result, it avoids the need for dedicated experiments or high-fidelity simulations.

The quasi-static mooring analysis has demonstrated reliable prediction, validated through physical experiments and verified against MoorDyn simulations that account for mooring dynamics. [18] used MAP++ (version 1.10.0rc) to model mooring forces for the validation of a scaled 10-MW FOWT model against the wind-wave tank experiments. MAP++ employs a quasi-static mooring model that excludes fluid drag and inertia forces. In addition, this quasi-static modeling was verified against dynamic simulations in OpenFAST, which employed MoorDyn to compute dynamic mooring forces for a 15-MW semi-submersible FOWT. The results showed a maximum deviation of 3.6% in mooring pretensions [15] and less than a 1% difference in mean mooring forces [47] during steady wind and regular wave tests.

The mooring module can accommodate mooring lines that are either partially in contact with the seabed or fully suspended in seawater, as discussed in Section 3.2.6 for shared lines examined in the literature. The governing equations

for these lines are provided by [114] and [126], respectively. For fully suspended lines, the clearance from the seabed depends on their loading conditions, which may require additional buoys or clump weights to adjust their configurations, as studied by [34]. This requirement would increase the mooring system complexity compared to shared lines with sufficient seabed contact.

Currently, the module can model only steel chain lines for both conventional and shared line configurations. For synthetic fiber ropes, which feature viscoelastic properties, the nonlinear stiffness depends strongly on loading conditions such as load amplitude, frequency, and history. This stiffness must be determined through tension tests or fitted to specific models, which may not be practical for early-stage investigations of mooring configurations, as discussed in Section 2.1.2.

### 6.1.2 Gaussian wake module

The reconstruction of the wind field is crucial for assessing the power production of the floating wind farm. When the inflow passes through the rotating blades, the wind speed is reduced at the rotor plane and in the wake behind the rotor. The rotation of the blades adds turbulence to the disturbed downstream airflow, leading to complex lateral and vertical expansion, as well as meandering and dissipation of the wake.

The wake generated by the upstream turbines can affect the performances of downstream turbines [50, 51], and consequently reduce the wind power production of the wind farm [129, 52, 53]. From a power perspective, the analytical wake model developed by [119] is implemented in the wake module to account for the mean wake deficit on downstream turbine.

The Gaussian wake model (Equation 4.5, discussed in Section 4.2.2), which employs an exponential function with a wake expansion factor, effectively captures mean wake profiles on downstream turbines while maintaining computational efficiency [130]. It shows good agreement with LES simulations and wind tunnel measurements [119], and is flexible to integrate with the low-order solvers

for turbine dynamics when flow details are less critical than the overall velocity deficit. It has been employed for wind farm layout optimization [130]. Details of the deficit computation are provided in Section 4.2.2.

### 6.1.3 Comparison with FAST.Farm

FAST.Farm (version v3.5.1) is selected as the reference benchmark to evaluate the computational efficiency and prediction accuracy of the simplified modeling approach. FAST.Farm provides a higher-fidelity simulation of the floating wind farm than the proposed simplified approach, by employing OpenFAST to compute the dynamics of each turbine and incorporating the Dynamic Wake Meandering (DWM) model to capture wake dynamics within the farm [54]. Detailed descriptions of OpenFAST and FAST.Farm can be found in Section 4.3.2. Table 6.1 compares the simplified modeling approach and FAST.Farm in terms of their modules.

Table 6.1: Comparison of modeling approaches.

| Module | Simplified modeling | FAST.Farm (v3.5.1) |
|---|---|---|
| Structural | rigid blade<br>rigid shaft<br>1 tower top movement<br>5 floater motions | flexible blade<br>flexible shaft<br>4 tower top movements<br>6 floater motions |
| Aerodynamic | thrust & power coefficients<br>rotor averaged wind speed | Blade Element Momentum<br>full 3D wind field |
| Hydrodynamic | a linear transfer function<br>constant added mass<br>no radiation damping | convolution integral<br>dynamic added mass<br>radiation damping |
| Mooring | no seabed friction<br>no dynamic forces | seabed friction<br>Morison equations |
| Wake | Gaussian-based wake<br>mean wake profile | Dynamic Wake Meandering<br>wake dynamics |

## 6.2 Verification against FAST.Farm simulations

This section analyzes a floating array of two semi-submersible FOWTs using both the simplified modeling approach and FAST.Farm under various wind and wave conditions. The two-turbine array serves as a case study, representing the smallest unit for shared line designs used in floating wind farms. While this analysis focuses on this minimal array, the simplified modeling approach is not limited to two turbines and can accommodate larger arrays with more turbines, making it applicable to a range of floating wind farm layouts. The objective is to evaluate the computational efficiency and prediction accuracy of the simplified modeling approach.

### 6.2.1 Two-FOWT array: smallest unit for shared line designs

The two-FOWT array, representing the smallest unit for shared line designs, consists of two FOWT models described in Section 4.3.3, with their principal dimensions summarized in Table 4.1. Since the initial conventional mooring design exhibits a negative lay-down length when the floater offset exceeds 18 m (Section 4.3.3), new mooring configurations are adopted (Section 6.2.2). Figure 5.1 illustrates the array with both conventional and shared line moorings. The two FOWTs have similar structural dimensions, with the upstream floater oriented 180° relative to the downstream floater. The fairlead radius is 42.5 m, and the initial angle between each pair of mooring lines is 120°. Four anchor lines, all with similar characteristics, are secured to the seabed, while the shared line connects the two floaters without anchors.

### 6.2.2 New mooring configurations for the floating array

The nonlinear design method proposed in Chapter 5 is used to generate new mooring configurations. Rather than minimizing mooring costs, the design target is to identify the configuration with the smallest chain diameter and lowest mooring mass. As observed in Section 5.3, such a configuration results

in the highest floater offsets and mooring force ratios, making it easier to evaluate the differences between the simplified modeling approach and FAST.Farm. Since the focus of this chapter is on modeling the floating array rather than optimizing mooring design, this objective is considered appropriate.

Table 6.2 and Table 6.3 present the design parameters, constraints, and mooring properties for the new anchor lines and the new shared line, respectively. The site of interest has a water depth of 200 m, consistent with typical depths for current floating wind projects, such as TetraSpar demonstration project [66]. The variables are defined under static conditions, excluding wind and wave forces. The mooring line is made of steel, and the fairlead radius remains at 42.5 m. The vertical distance between fairleads and anchors is 185 m.

Table 6.2: Design parameters, constraints, and properties for new anchor lines.

| | Variable | Range, unit | Design 1 |
|---|---|---|---|
| Parameter | Length ratio | [0.3:0.05:0.7] | 0.3 |
| | Chain diameter | [68:1:205] mm | 124 |
| | Chain grade | [R3, R3S, R4, R4S] | R4S |
| Constraint | Mooring mass | 2e5 kg | 2e5 |
| | Total unstretched length | [600 1000] m | 987 |
| | Pretension ratio | [0.1 0.3] | 0.27 |
| Property | Mass per unit length in air | kg/m | 306 |
| | Mooring axial stiffness | GN | 2.5 |
| | Anchor radius | m | 1000 |
| | Mooring pretension | MN | 4.3 |

The length ratio is defined as the static ratio of the lay-down length to the suspended length (Figure 4.1) and is used to calculate the total unstretched length. The chain diameter determines the line mass per unit length (Equation 5.1), and along with the chain grade, decides the chain's $MBL$ (Equation 5.2). The mooring mass refers to the suspended line mass, with a fixed mass of 2e5 kg based on the initial mooring design (Table 4.1).

Pretension refers to the initial mooring force without wind and wave loads, and pretension ratio is the force ratio of pretension relative to the chain's $MBL$. The total unstretched length of the shared line is determined by the static

length ratio and the spatial distance between FOWTs, which is measured in terms of rotor diameter $Dr$.

Table 6.3: Design parameters, constraints, and properties for the shared line.

| | Variable and range | Design 1 | | |
|---|---|---|---|---|
| Parameter | FOWT distance [6, 7, 8] $Dr$ | 6 | 7 | 8 |
| | Length ratio [0.3:0.05:0.7] | 0.3 | 0.3 | 0.45 |
| | Chain diameter [60:1:200] mm | 145 | 135 | 133 |
| | Chain grade [R3, R3S, R4, R4S] | | R3 | |
| Constraints | Mooring mass per turbine 2e5 kg | | 2e5 | |
| | Pretension ratio [0.1 0.3] | 0.22 | 0.28 | 0.29 |
| Property | Total unstretched length m | 1443 | 1664 | 1914 |
| | Mass per unit length in air kg/m | 418 | 363 | 352 |
| | Mooring axial stiffness GN | 3.4 | 3.0 | 2.9 |
| | Mooring pretension MN | 3.30 | 3.71 | 3.81 |

### 6.2.3 Load cases and environmental conditions

Table 6.4 summarizes the load cases and environmental conditions, including wind speed ($V$), wave height ($H$), and wave period ($T$), along the simulation details for each test. For the static, decay, and steady wind tests, $V$ refers to steady wind speed, while for turbulent wind tests, it denotes the mean upstream undisturbed wind speed. Similarly, $H$ and $T$ represent the regular wave height and period in steady wind and regular wave tests, but correspond to the significant wave height and peak wave period in irregular wave tests.

In both the static and decay tests, a single FOWT with the new conventional configuration is first analyzed in OpenFAST, excluding wind and wave loads. The floating array with the shared line configuration is then simulated using FAST.Farm under a low wind speed of 2 m/s. This low-wind scenario ensures error-free simulations in FAST.Farm, which is not designed for simulations without wind, and avoids high wind forces that could affect the static performance or decay responses in these tests. In contrast, the simplified modeling

Table 6.4: Load cases in the verification study.

| Test | $V$ [m/s] | $H$ [m] | $T$ [s] | Shared | Tool[1] | Ratio[2] |
|---|---|---|---|---|---|---|
| Static | - | - | - | no | Simp | 15.4 |
| | - | - | - | no | Open | 1.5 |
| | 2 | - | - | yes | Simp | 15.4 |
| | 2 | - | - | yes | FAST | 0.15 |
| Decay | - | - | - | no | Simp | 15.3 |
| | - | - | - | no | Open | 1.6 |
| | 2 | - | - | yes | Simp | 15.3 |
| | 2 | - | - | yes | FAST | 0.16 |
| Steady wind | [3:2:13] | - | - | yes | Simp | 15.4 |
| | [3:2:13] | - | - | yes | FAST | 0.16 |
| Steady wind | 7 | [1.5:1:6.5] | 7 | yes | Simp | 15.2 |
| regular wave | 7 | [1.5:1:6.5] | 7 | yes | FAST | 0.16 |
| Turbulent wind | [7, 9, 11] | 1.5 | 7 | yes | Simp | 15.0 |
| | [7, 9, 11] | 1.5 | 7 | yes | FAST | 0.15 |
| irregular wave | 11 | [1.5:1:6.5] | 7 | yes | Simp | 15.0 |
| | 11 | [1.5:1:6.5] | 7 | yes | FAST | 0.15 |

[1] *"Simp" denotes the simplified modeling method, "Open" refers to OpenFAST v3.5.0 , and "FAST" represents FAST.Farm version v3.5.1.* [2] *Time ratio is the averaged ratio between the simulation time of each test case and its actual computational time.*

approach does not have this no-wind limitation, and the analytical Gaussian wake model is deactivated in the absence of wind to allow no-wind simulations.

The steady wind conditions range from 3 m/s (cut-in) to 13 m/s (above-rated), covering over 90% of the wind distribution in Gran Canaria [121], as shown in Figure 6.2 for the upper-bound wind speeds. Within this range, the combined occurrence probabilities of upstream mean wind speeds at 7 m/s, 9 m/s, and 11 m/s are approximately 19%, 21%, and 18%, respectively. Based on the single FOWT fatigue results (Figure 5.15), the fatigue contributions from these three wind speeds are the highest, while those from wind speeds below 7 m/s and above 13 m/s are relatively small. Therefore, turbulent wind tests focus on these three wind speeds to efficiently assess turbine performance.

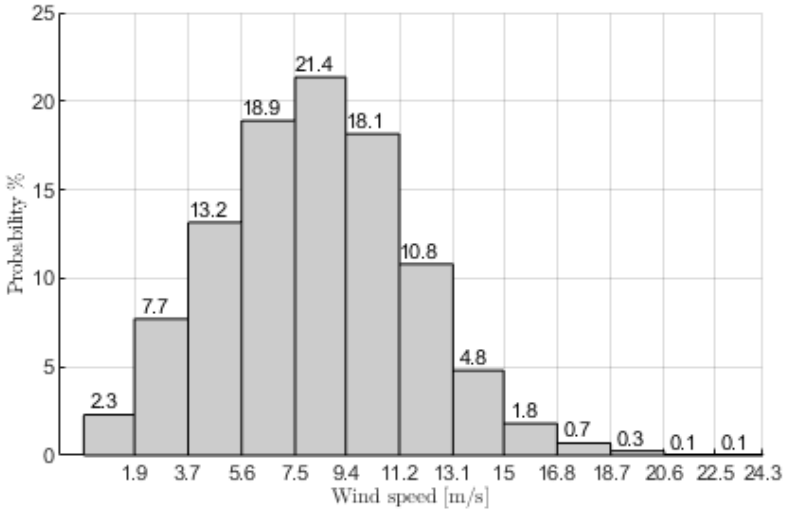


Figure 6.2: Wind speed distribution at the site of Gran Canaria, adapted from the 10-m reference distribution [121], using the logarithmic law to scale to hub-height. The occurrence probability is reported for each bin.

Regular wave heights span a broad range from 1.5 m to 6.5 m, covering both the normal operational and extreme wave conditions. Irregular waves are modeled using the Pierson–Moskowitz spectrum, consistent with the study on a single FOWT [120]. To model turbulent wind, a Class C turbulence level is assigned in the IEC Kaimal model, due to the lack of public turbulence intensity data for this site, representing the moderate wind turbulence conditions [121].

Two sets of turbulent wind and irregular wave tests are conducted. The first set keeps irregular wave conditions constant while changes the mean upstream wind speed to investigate turbine performance. Three mean wind speeds possess the highest occurrence in Gran Canaria (Figure 6.2). While the second set keeps the upstream turbulent wind fixed, but increases the significant wave height to examine FOWT performance.

### 6.2.4 Simulation setup and computational efficiency

FAST.Farm (v3.5.1) does not support no-wind simulations, as the coupling between turbine and wake relies on wind dynamics. Therefore, no-wind and decay tests are performed for a single FOWT in OpenFAST. For the floating array, a low wind speed of 2 m/s is applied during the static and decay tests, and the number of wake planes is set to 2, to minimize wake effects in FAST.Farm. A wake plane represents a cross-section of the turbine wake where the velocity deficit is calculated and is essential for analyzing wake interactions [54].

In addition, FAST.Farm encounters errors when wave heights exceed 4.5 m at wind speeds below 7 m/s. These errors arise from limitations in the near-wake correction, which becomes invalid when lower wind speeds result in a high thrust coefficient. The near-wake correction calculates velocity deficits using Blade Element Momentum (BEM) theory for thrust coefficient below 24/25. For higher thrust coefficients, the solution becomes unstable as the rotor influence become more significant.

In contrast, the simplified modeling approach is not subject to these limitations associated with the wind modeling and the wake model. The analytical Gaussian-based wake model is deactivated in the absence of wind and remains valid as long as the thrust coefficient is smaller than both $8(kx/D + \epsilon)^2$ and 1, as shown in Equations 4.6 and 4.8, respectively. As a result, the simplified model supports no-wind simulations for static or free-decay tests, and also allows for scenarios combining low wind speeds with high wave conditions for wave-dominated simulations.

TurbSim V2 is applied to generate the synthetic turbulence ambient flow for the floating array. The grid discretization for the low and high resolution domain in FAST.Farm followed the guidelines [54], and the distributed scripts [127] were conducted to define the parameters for the inflow generation for each wind speed and wind-farm layout.

The simulation-to-CPU time ratio is defined as the average ratio between the simulation time and the actual computational time, for evaluating the compu-

tational efficiency (Table 6.4). For example, the non-wind simulation of the individual FOWT with a conventional configuration runs for 20 min, with a total CPU time of 13.4 min in OpenFAST and 1.3 min using the simplified model in Simulink. Consequently, the simulation-to-CPU time ratios are 1.5 for OpenFAST and 15.4 for the simplified method. The higher time ratio achieved by the simplified modeling approach indicates a reduction of more than 75-fold in computational effort.

The computational effort for simulations in OpenFAST and FAST.Farm is strongly influenced by the number of output channels in the result files and the minimum time step defined across all modules. To reduce the computational demands, output channels are limited to turbine power, floater motion, and mooring line force, and visualization files of disturbed winds are excluded in FAST.Farm.

The module time step in FAST.Farm is set to 0.02 s, consistent with the global time step defined in the simplified modeling approach. However, the module time steps in the MoorDyn input files are set to 0.001 s and 0.0001 s, respectively, for conventional moorings in OpenFAST and shared moorings in FAST.Farm. These time steps ensure that MoorDyn conducts error-free calculations, since sensitivity tests show that using a time step of 0.0002 s causes errors during Moordyn dynamic relaxation.

The simplified modeling approach neglects mooring dynamics and enables a time step of 0.02 s for error-free simulations. As a result, its computational demand for simulating the floating turbine array with shared line configurations is significantly reduced. Comparison of simulation-to-CPU time ratios in Table 6.4 demonstrates the superior computational efficiency of the simplified model relative to the higher-fidelity FAST.Farm (v3.5.1). This efficiency enables faster analysis, simulation, and evaluation of floating wind farms with shared line configurations, making the simplified model a more practical choice for large-scale simulations.

## 6.3 Simulation results and performance comparisons

### 6.3.1 Static tests of a single FOWT and the floating array

First, the FOWT with a new conventional configuration is analyzed using both OpenFAST and the simplified modeling approach, excluding wind and wave loads. Each simulation runs for 20 min, and the static floater motions are recorded over the final 10 min, as summarized in Table 6.5.

Table 6.5: Comparison of static floater motions and mooring forces on lines L3 and L1 for a single FOWT using OpenFAST ("Open") and the simplified modeling approach ("Simp").

| model * | Tool | surge [m] | heave [m] | pitch [°] | $T_{L3}$ [MN] | $T_{L1}$ [MN] |
|---|---|---|---|---|---|---|
| FOWT1 | Simp | -0.14 | 0.10 | -1.73 | 4.24 | 4.23 |
| | Open | -0.13 | 0.11 | -1.70 | 4.24 | 4.23 |
| | Tool | surge [m] | heave [m] | pitch [°] | $T_{L4}$ [MN] | $T_{L6}$ [MN] |
| FOWT2 | Simp | -0.16 | 0.10 | -1.73 | 4.24 | 4.23 |
| | Open | -0.15 | 0.11 | -1.70 | 4.24 | 4.23 |

* *"FOWT1" and "FOWT2" denote the upstream and downstream FOWTs, respectively.*

Due to the symmetric mooring layout, the static sway, roll, and yaw motions remains zero, while the differences between these two tools are minimal, surge and heave motions differ by 0.01 m, pitch motion by 0.03°, and mooring forces at fairleads by 0.01 MN. This good agreement shows that the simplified model can accurately reproduce the response of a single FOWT with a conventional configuration, validating its reliability for static condition tests.

Next, the two-turbine array with shared line configurations is simulated using FAST.Farm and the simplified modeling approach at a wind speed of 2 m/s. This low-wind scenario ensures error-free simulations in FAST.Farm, which is not designed for no-wind conditions, and avoids the influence of high wind thrust forces on floater motions and mooring forces. Each test runs for 30 min, and the mean motions are recorded over the final 10 min, as listed in Table 6.6.

Table 6.6: Comparison of static floater motions and mooring forces on lines L3S, LS, and L6S for the floating array with shared line designs at 2 m/s, using FAST.Farm ("FAST") and the simplified modeling approach ("Simp").

| | | Tool | surge [m] | heave [m] | pitch [°] | $T_{L3S}$ [MN] | $T_{LS}$ [MN] |
|---|---|---|---|---|---|---|---|
| FOWT1 | $6Dr$ | Simp | -4.32 | 0.10 | -0.93 | 3.78 | 3.80 |
| | | FAST | -4.36 | 0.12 | -0.89 | 3.78 | 3.80 |
| | $7Dr$ | Simp | -0.20 | 0.08 | -1.05 | 4.22 | 4.17 |
| | | FAST | -0.26 | 0.09 | -1.02 | 4.21 | 4.15 |
| | $8Dr$ | Simp | -3.56 | 0.12 | -1.11 | 3.86 | 3.78 |
| | | FAST | -3.71 | 0.13 | -1.08 | 3.85 | 3.76 |
| | | Tool | surge [m] | heave [m] | pitch [°] | $T_{LS}$ [MN] | $T_{L6S}$ [MN] |
| FOWT2 | $6Dr$ | Simp | 7.24 | 0.12 | -1.62 | 3.80 | 3.50 |
| | | FAST | 7.29 | 0.13 | -1.55 | 3.79 | 3.51 |
| | $7Dr$ | Simp | 2.57 | 0.10 | -1.46 | 4.17 | 3.94 |
| | | FAST | 2.63 | 0.11 | -1.38 | 4.15 | 3.94 |
| | $8Dr$ | Simp | 6.35 | 0.13 | -1.43 | 3.78 | 3.58 |
| | | FAST | 6.56 | 0.15 | -1.35 | 3.75 | 3.57 |

For static tests of the floating array under low-wind conditions, the symmetric shared mooring configuration results in zero mean sway and roll motions. The mean yaw motion predicted by FAST.Farm is 0.03°. Both simulation tools produce similar static floater motions, with the maximum differences of 0.21 m in surge, 0.02 m in heave, and 0.08° in pitch. The mean mooring forces exhibit a maximum difference of 0.03 MN. This close agreement demonstrates that the simplified model can accurately reproduce the static response of the floating turbine array with shared line configurations.

Although the mean mooring forces show good agreement, significant differences are observed during the first 600 s of the simulations. Figures 6.3 and 6.4 compares the mooring forces predicted by the two simulation tools for the conventional and shared line mooring configurations, respectively. Strong agreement between OpenFAST and the simplified modeling approach in predicting mooring forces for a single FOWT with the conventional configuration. At the

start of the simulation, the predicted forces are close to the pretension value of 4.3 MN reported in Table 6.2. The OpenFAST results exhibit high-frequency fluctuations during the first 100 s. Following this ramp-up period, the mooring force converges to a stable value that closely aligns with the predictions of the simplified model.

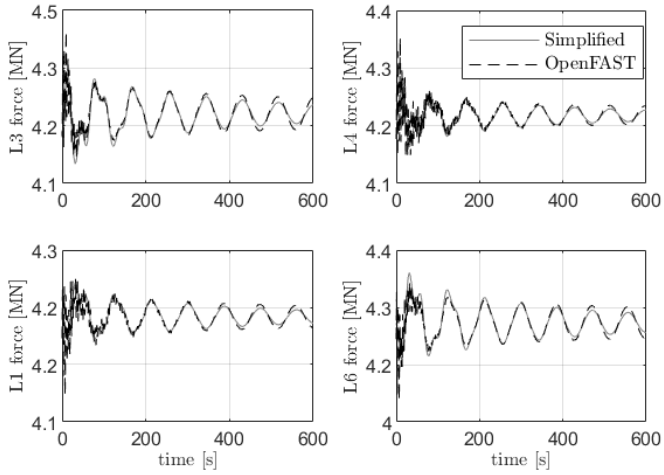


Figure 6.3: Comparison of mooring forces for a single FOWT with the new conventional configuration during the first 600 s of static no-wind tests, using OpenFAST and the simplified modeling ("Simplified").

However, as shown in Figure 6.4, at the start of the simulation, FAST.Farm predicts mooring forces below 4 MN in anchor lines L3S and L6S, despite their pretensions reaching 4.2 MN, while the simplified modeling approach predicts forces closely matching that pretension. A larger discrepancy is observed in the shared line, where FAST.Farm estimates forces below 1 MN, significantly below the pretension of 3.7 MN at a $7D_r$ spacing (Table 6.3), while the simplified model provides a much closer match.

The shared line has over 500 m of its length suspended in water under static conditions, generating a vertical mooring force exceeding 2 MN. The underestimated shared mooring force during initialization in MoorDyn (the mooring module for OpenFAST and FAST.Farm) may result from an inaccurate quasi-static calculation of node positions along the line.

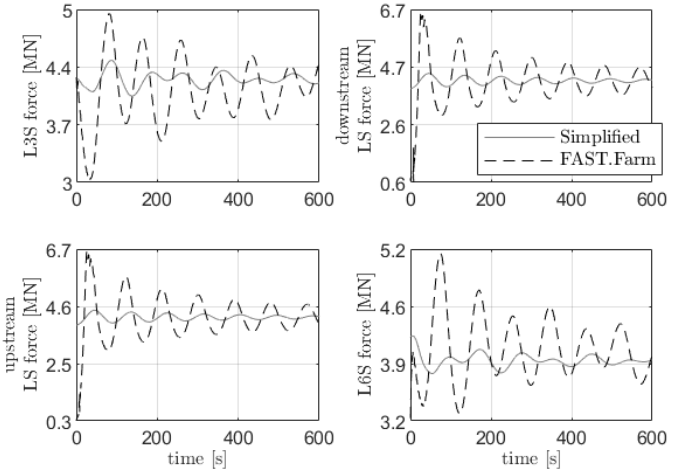


Figure 6.4: Comparison of mooring forces for the floating array with a shared line configuration at $7D_r$ spacing during the first 600 s of static low-wind tests, using FAST.Farm and the simplified model ("Simplified").

In MoorDyn input files, line ends are defined by the coordinates of fairleads and anchors. The close agreement observed for the single FOWT with the conventional mooring configuration (Figure 6.3) confirms the accuracy of the fairlead and anchor coordinates for the anchor lines. In contrast, the shared line has no anchors, and both ends share the same vertical coordinates. This likely causes misinterpretation of the fairlead and anchor positions, and the resulting zero vertical difference between the two ends leads to the small initial mooring force predicted by FAST.Farm.

Compared to FAST.Farm, the simplified model predicts an initial force of 3.9 MN in the shared line, closely matching the pretension. While the different initial forces have only a minor effect on the mean mooring force under low-wind conditions, they cause a significant influence on the free-decay tests, as discussed in Section 6.3.2. The mooring force comparison highlights the prediction accuracy of the simplified model and its advantages over FAST.Farm in terms of initial force estimation in the shared line.

### 6.3.2 Decay tests of a single FOWT and the floating array

A single FOWT with a conventional configuration is simulated in OpenFAST and the simplified modeling approach during the decay test, excluding wind and wave loads. Initial displacements of 5 m in surge, sway, and heave motions, and 5° in roll and pitch motions are applied. The floater motions, shown in Figure 6.5, are compared over 20 min of free decay, with magnified time and frequency axes to highlight differences between simulation tools.

Figure 6.5 shows strong agreement between OpenFAST and the simplified model in the free-decay test for the single FOWT with the conventional configuration. While the simplified model predicts slightly larger motion displacements than OpenFAST, it maintains the same motion frequencies, as summarized in Table 6.7. The displacement differences arise because the simplified model neglects the wave radiation damping in its hydrodynamic modeling, which increases motion amplitudes. Overall, the comparison demonstrates that the simplified model accurately captures the fundamental dynamics of the FOWT, providing responses comparable to OpenFAST.

Table 6.7: Comparison of motion eigenfrequencies (in Hz) for a single FOWT with a conventional configuration, predicted by OpenFAST and the simplified modeling approach ("Simplified").

| Tool | surge | sway | heave | roll | pitch |
|---|---|---|---|---|---|
| Simplified | 0.011 | 0.011 | 0.055 | 0.034 | 0.034 |
| OpenFAST | 0.011 | 0.011 | 0.055 | 0.034 | 0.034 |

During the free decay tests of the floating array with shared line configurations, a low wind speed of 2 m/s is applied to ensure error-free simulations in FAST.Farm. Figure 6.6 compares the decay response of the floating turbine array with a shared mooring line using FAST.Farm and the simplified modeling approach. An initial 5 m displacement is applied to translational motions and 55° to rotational motions. Since motion differences between the two simulation tools appear across all three shared mooring designs, the floating array with $7D_r$ spacing is chosen as the representative case.

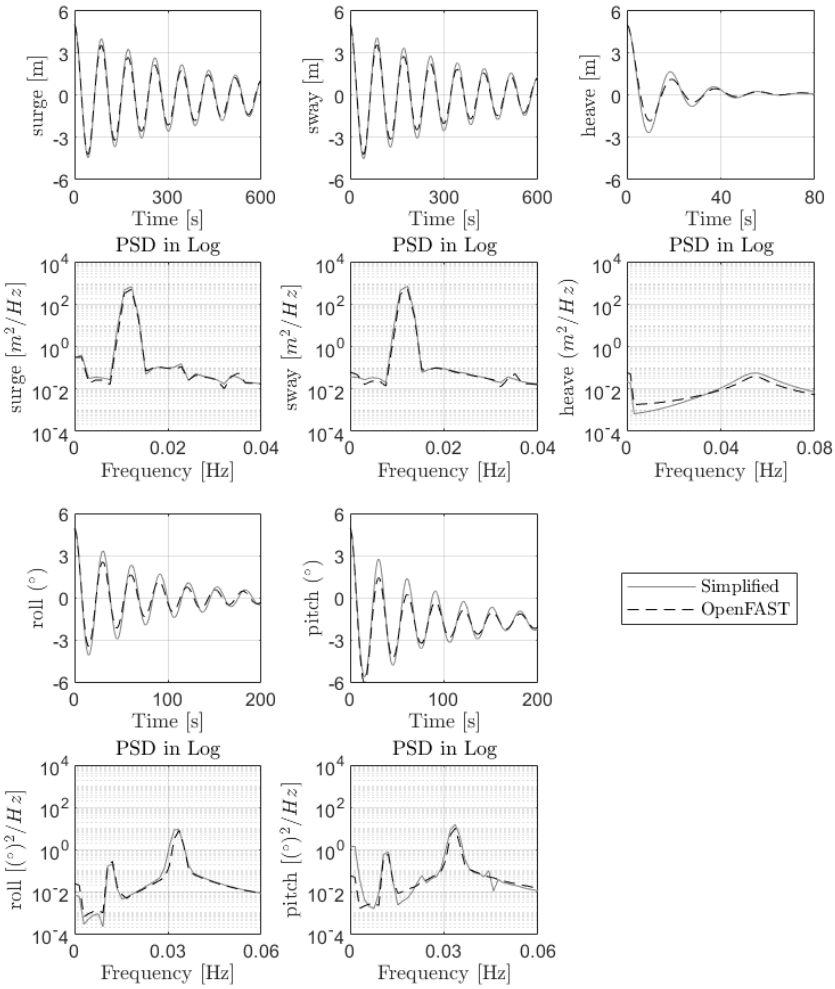


Figure 6.5: Comparison of motion decay tests for a FOWT with a conventional configuration using OpenFAST and the simplified modeling approach.

Notable surge and pitch differences are observed in the floating turbine array between FAST.Farm and the simplified model. Within the first 200 s, FAST.Farm produces larger displacements than the initial values and exhibits greater fluctuations. While FAST.Farm uses OpenFAST for individual FOWT

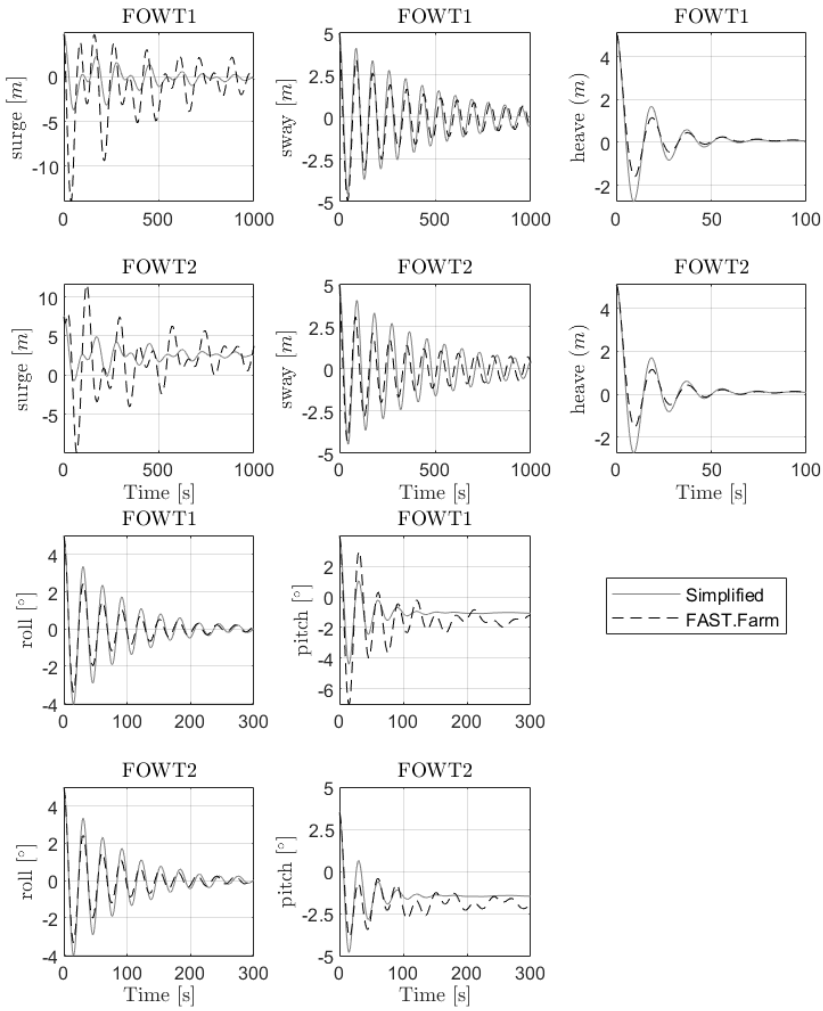


Figure 6.6: Comparison of motion decay tests for the floating turbine array with a shared line design at $7D_r$ spacing using FAST.Farm and the simplified modeling approach.

dynamics, the single-FOWT decay test (Figure 6.4) showed close agreement between OpenFAST and the simplified model, suggesting that the differences in the array decay tests arise from the shared mooring configuration and low-wind forces. At 2 m/s, the wind thrust force is below 0.2 MN and has minimal im-

pact on floater motion, indicating that the larger displacements in FAST.Farm are primarily induced by the shared line.

Figure 6.7 compares mooring forces at the fairleads for anchor line L3S and shared line LS during the first 200 s of the array decay tests at $7D_r$ turbine spacing. FAST.Farm predicts an initial shared mooring force below 2 MN in all four decay tests, significantly lower than the pretension of 3.7 MN at this spacing. As discussed in Section 6.3.1, over 500 m of the shared line remains suspended under static conditions, producing a vertical mooring force exceeding 2 MN. The underestimated initial force in MoorDyn (the mooring module of OpenFAST and FAST.Farm) likely results from inaccuracies in quasi-static node-position calculations. The misinterpretation of the fairlead and anchor positions of the shared line eliminates vertical difference between these two ends. In contrast, the simplified model predicts an initial shared mooring force that closely matches the pretension.

The correct interpretation of fairlead and anchor positions is also reflected in anchor lines of the shared line configuration, where both FAST.Farm and the simplified model predict an initial force of 4 MN, closely matching the pretension. However, in FAST.Farm, this creates a horizontal force imbalance between the anchor lines and the shared line, which is not seen in the simplified model. This force imbalance causes a larger negative surge of the upstream floater and increases the surge of the downstream floater during the first 20 s, exceeding its initial displacement. The higher mooring forces in the anchor lines also generate a bending moment on the floaters, resulting in a greater negative pitch for the upstream floater and a reduced positive pitch for the downstream floater during the first 15 s, compared to the simplified model.

Although larger motion differences appear during the first 200 s of the array decay tests, the motion eigenfrequencies, analyzed through power spectral densities (Figure 6.8) for $7D_r$ spacing at 2 m/s, show strong agreement between FAST.Farm and the simplified model. Table 6.8 summarizes these eigenfrequencies, confirming a good match.

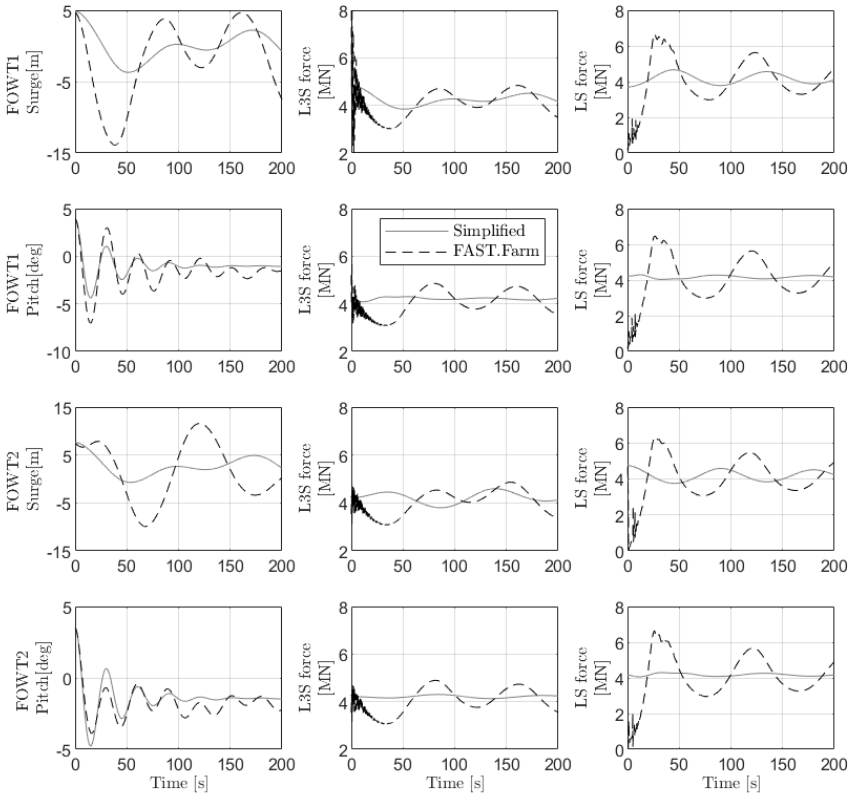


Figure 6.7: Comparison of mooring forces in anchor line L3S and shared line LS for the floating array with a shared line design at $7D_r$ spacing during the first 200 s, predicted by FAST.Farm and the simplified modeling approach. Each row shows the motion decay and corresponding mooring forces.

Table 6.8: Comparison of motion eigenfrequencies (in Hz) for the floating array with a shared line design at $7D_r$ spacing, predicted by FAST.Farm and the simplified modeling approach.

| Tool | surge 1 | surge 2 | sway | heave | roll | pitch |
|---|---|---|---|---|---|---|
| Simplified | 0.007 | 0.011 | 0.011 | 0.055 | 0.034 | 0.034 |
| FAST.Farm | 0.007 | 0.011 | 0.011 | 0.055 | 0.034 | 0.034 |

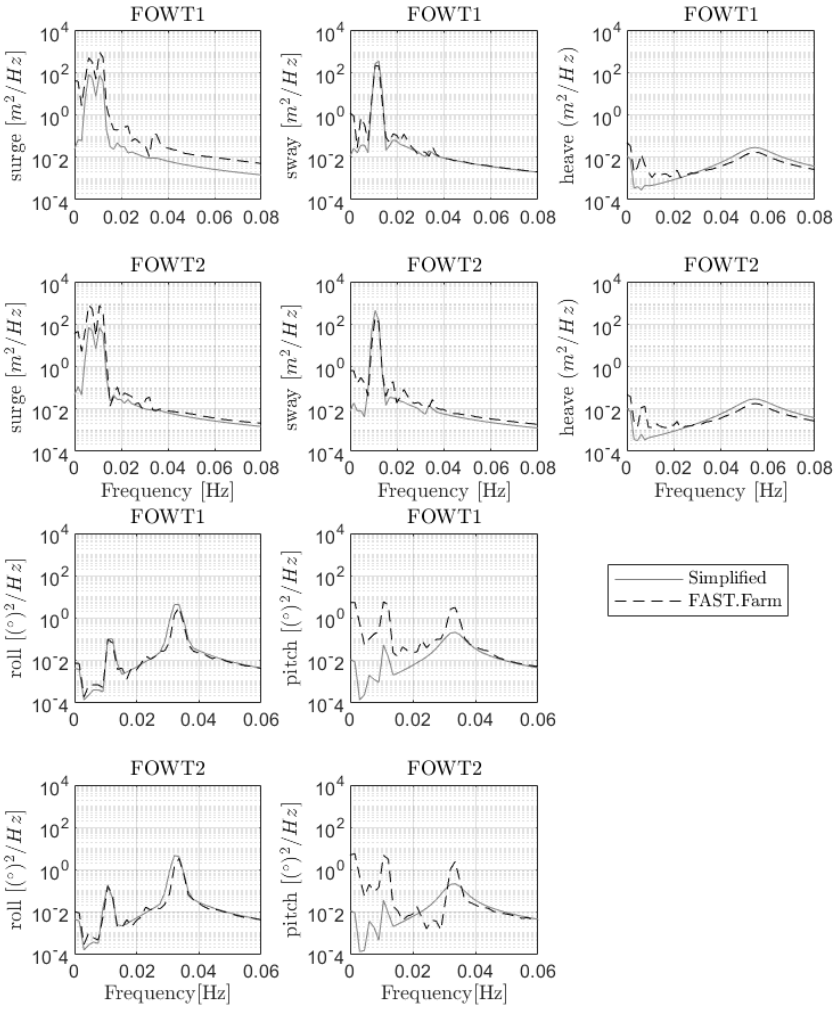


Figure 6.8: Comparison of Power Spectral Density (PSD) of floater motions on a logarithmic scale during free decay tests of FOWTs with a shared line design at $7D_r$ spacing, predicted by FAST.Farm and the simplified modeling approach.

The conventional mooring design produces an eigenfrequency of 0.011 Hz for both surge and sway motions. In contrast, the shared line configuration with $7D_r$ spacing introduces an additional surge frequency at 0.007 Hz, due to cou-

pling with the downstream FOWT through the shared line. Overall, the agreement observed in both single-FOWT and array decay tests shows that the simplified model accurately reproduces the decay response and captures the fundamental dynamics of the floating array, with the added advantage of more accurate initial shared mooring force predictions compared to FAST.Farm.

### 6.3.3 Steady wind tests of the floating array

The floating array with shared line configurations is evaluated under steady inflow conditions, with upstream wind speeds from 3 m/s to 13 m/s, to assess turbine power performance. The velocity deficits due to wake effects cause different downstream wind speeds and power outputs. Each test runs for 30 min, excluding wave loads, and the mean speed and power are recorded over the final 10 min. Figure 6.9 compares power outputs for upstream FOWT1 and downstream FOWT2, as well as the downstream mean wind speed, predicted by FAST.Farm and the simplified modeling approach, while Table 6.9 summarizes the corresponding mean power.

In the simplified model, the Gaussian wake model (Equation 4.5) uses three wake growth rates (Equation 4.6), 0.03, 0.04, and 0.05, denoted $K3$, $K4$, and $K5$, to assess the effect of wake expansion on downstream wind speed and turbine power. These rates are derived from the linear slopes of the normalized standard deviations of the Gaussian curves fitted to velocity deficit profiles in onshore turbine wakes. Experimental and LES studies have accounted for different terrain roughness, with $K3$, $K4$, and $K5$ corresponding to roughness of 0.005 m, 0.05 m, and 0.5 m, respectively [119]. A roughness of 0.006 m has also been suggested as representative of the Nantucket Sound wind farm site [131]. Due to the lack of publicly available site-specific data, future research is recommended to investigate the influence of upstream wind conditions and surface roughness on the wake expansion parameter for floating wind turbines.

Upstream turbine power, governed by the upstream wind speed, is independent of shared line configurations, showing differences between the two simulation

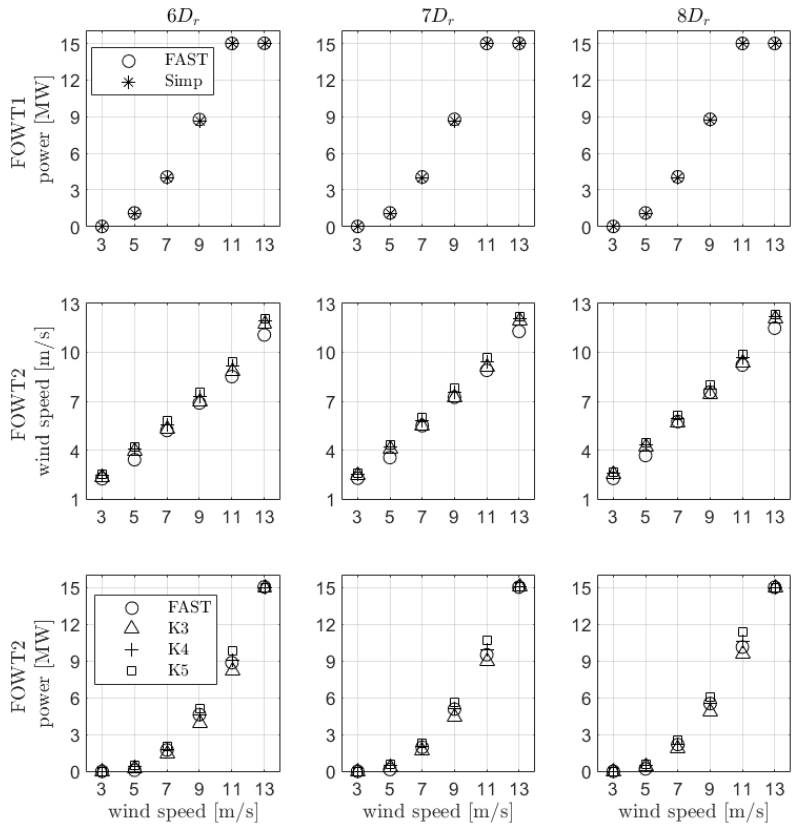


Figure 6.9: Comparison of mean power outputs and downstream wind speeds for the floating turbine array with shared line designs under steady inflow conditions, predicted by FAST.Farm ("FAST") and the simplified modeling approach ("Simp") with three wake growth rates ($K3$, $K4$, and $K5$).

tools within 0.1 MW. This small power difference indicates that the simplified model predicts comparable turbine power to FAST.Farm at the similar wind speed. Downstream wind speed and power, however, are strongly influenced by wake effects. Among the three wake parameters, $K4$ provides the closest agreement with FAST.Farm for downstream turbine power when upstream wind speed exceeds 5 m/s. Across three turbine spacings, the maximum downstream power difference occurs at rated wind speed of 11 m/s, ranging from 0.3 MW (3%) to 0.5 MW (5%) higher than FAST.Farm predictions.

Table 6.9: Comparison of mean power outputs (in MW) for the floating array with shared line designs under steady inflow conditions, predicted by FAST.Farm ("FAST") and the simplified modeling approach ("Simp") with three wake growth rates ($K3$, $K4$, and $K5$).

| | | Speed [m/s] | 3 | 5 | 7 | 9 | 11 | 13 |
|---|---|---|---|---|---|---|---|---|
| FOWT1 | - | Simp | 0.0 | 1.1 | 4.0 | 8.7 | 15.0 | 15.0 |
| | | FAST | 0.0 | 1.1 | 4.1 | 8.8 | 15.0 | 15.0 |
| FOWT2 | $6D_r$ | $K3$ | 0.0 | 0.3 | 1.4 | 3.9 | 8.2 | 15.0 |
| | | $K4$ | 0.0 | 0.4 | 1.7 | 4.6 | 9.1 | 15.0 |
| | | $K5$ | 0.0 | 0.4 | 2.0 | 5.1 | 9.8 | 15.0 |
| | | FAST | 0.0 | 0.1 | 1.7 | 4.6 | 8.8 | 15.0 |
| | $7D_r$ | $K3$ | 0.0 | 0.3 | 1.6 | 4.4 | 8.9 | 15.0 |
| | | $K4$ | 0.0 | 0.4 | 2.0 | 5.1 | 9.9 | 15.0 |
| | | $K5$ | 0.0 | 0.5 | 2.3 | 5.6 | 10.7 | 15.0 |
| | | FAST | 0.0 | 0.1 | 2.0 | 5.1 | 9.5 | 15.0 |
| | $8D_r$ | $K3$ | 0.0 | 0.4 | 1.9 | 4.9 | 9.6 | 15.0 |
| | | $K4$ | 0.0 | 0.5 | 2.2 | 5.5 | 10.6 | 15.0 |
| | | $K5$ | 0.0 | 0.6 | 2.5 | 6.0 | 11.3 | 15.0 |
| | | FAST | 0.0 | 0.2 | 2.2 | 5.5 | 10.1 | 15.0 |

The steady inflow analysis demonstrates that the simplified modeling approach accurately predicts upstream turbine power, with differences from FAST.Farm within 0.1 MW, while accounting for wake effects, the maximum downstream power difference remains within 5%, indicating that the simplified model provides accurate predictions of turbine performance in a floating array with shared line configurations.

### 6.3.4 Steady wind and regular wave tests of the floating array

The steady wind and regular wave tests are conducted at a constant upstream wind speed of 7 m/s, while wave heights range from 1.5 m to 6.5 m to evaluate wave effects on the floating turbine array. The analysis focuses on mooring forces in anchor line L3S and shared line LS, as these experience the largest loads on each floater. Each test lasts 40 minutes, with maximum and mean

forces extracted from the final 10 minutes of data. Figure 6.10 presents a comparison between the mooring forces predicted by FAST.Farm and those obtained from the simplified modeling approach using the $K4$ parameter in the Gaussian-based wake model.

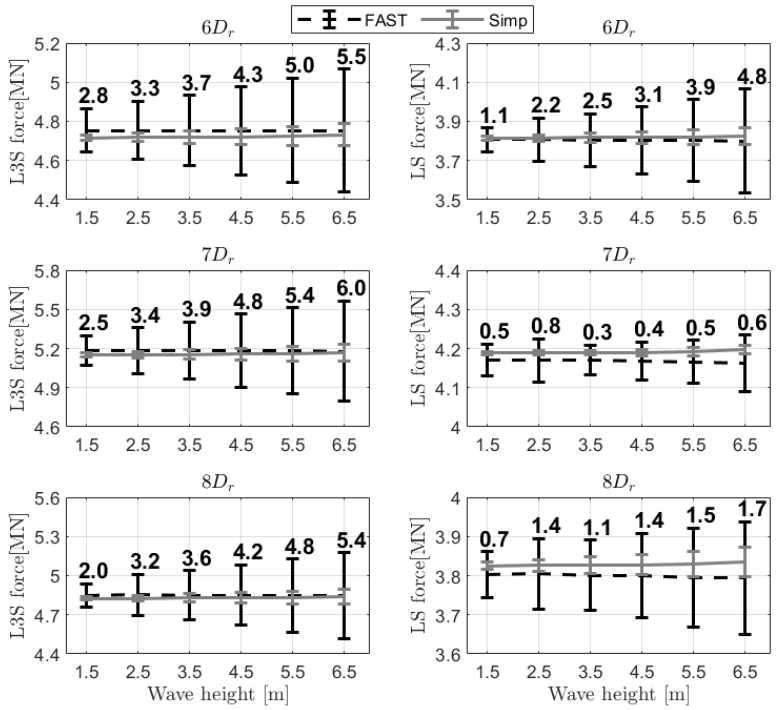


Figure 6.10: Comparison of the maximum and mean mooring forces for the floating array with shared line designs during steady wind and regular wave tests using FAST.Farm ("FAST") and the simplified modeling approach ("Simp"). Differences in maximum forces are displayed as percentages of the FAST.Farm results.

Figure 6.10 shows that the mooring forces predicted by the two simulation tools are in good agreement across all wave heights, confirming the accuracy of the quasi-static mooring model. The difference in mean mooring forces is within 0.1 MN. For the maximum mooring forces, the largest deviations for the most heavily loaded anchor line L3S are 5.5%, 6.0%, and 5.4% across the three turbine spacings, while for the shared mooring line LS, the corresponding

deviations are 4.8%, 0.6%, and 1.7%, all occurring at the highest wave height of 6.5 m. In general, the differences in mooring forces between the two tools increase with wave height.

Among the three turbine spacings, the $6D_r$ spacing shows deviations exceeding 4% in the shared line mooring forces under the highest wave conditions. To further present these force differences, Figure 6.11 illustrates forces in line L3S and LS for the floating array with a shared line design at a $6D_r$ distance, under both the lowest and highest regular wave conditions. Forces from the final 10 min of each test are used to calculate the power spectral density on a logarithmic scale.

Figure 6.11 shows that FAST.Farm exhibits larger mooring force fluctuations than the simplified model. As wave height increases from 1.5 m to 6.5 m, the dynamic range in line L3S grows from 0.2 MN to 0.6 MN due to mooring dynamics captured by the Morison equation in MoorDyn. The simplified model, using quasi-static mooring, neglects these dynamics and produces lower peak forces. Within the wave frequency range (0.1 to 0.45 Hz), FAST.Farm shows three peaks in the L3S force PSD at 0.14 Hz, 0.29 Hz, and 0.43 Hz. The simplified model, in contrast, exhibits a pronounced peak at 0.14 Hz and a weaker peak at 0.29 Hz, with much smaller magnitudes. Because it neglects mooring dynamics, the simplified model underestimates the contributions of fluid velocity and acceleration to mooring forces, corresponding to the PSD at 0.29 Hz and 0.43 Hz. At higher wave heights, increased fluid velocity and acceleration amplify the differences in L3S forces between the two models.

In FAST.Farm results, the shared line mooring forces show broadband energy with multiple local maxima, rather than distinct peaks like the anchor line forces. This reflects the influence of wake-induced turbulent wind loads on the downstream FOWT. However, these effects are not captured by the simplified model, because the Gaussian wake model predicts only the mean wake deficit using a constant wake parameter. In contrast, FAST.Farm accounts for wake advection, deflection, and meandering [54]. And higher wave conditions amplify

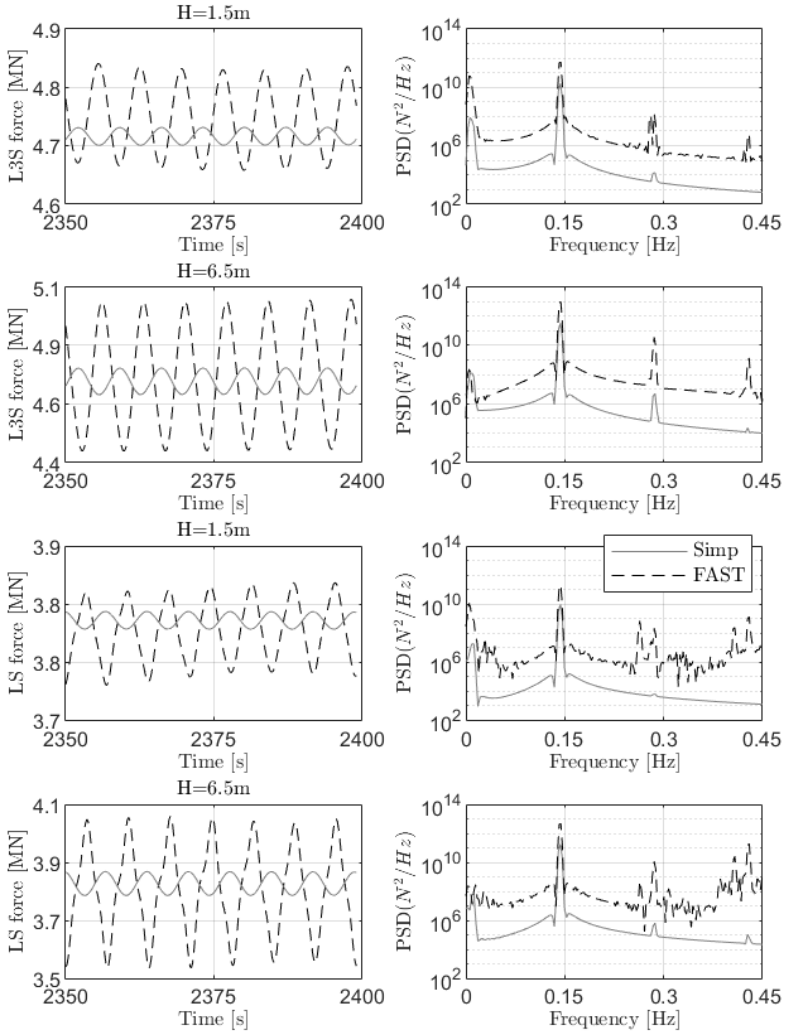


Figure 6.11: Comparison of mooring forces in lines L3S and LS for the floating turbine array with a shared line design at a $6D_r$ distance under steady wind and regular wave conditions, predicted by FAST.Farm ("FAST") and the simplified modeling approach ("Simp") with $K4$ in the wake model. Power spectral density is presented on a logarithmic scale.

the difference in wake models, increasing force deviation in the shared line between the two tools.

Overall, the steady wind and regular wave tests show that the simplified model provides mooring force predictions comparable to FAST.Farm. Lower peak forces in the anchor lines arise from the quasi-static mooring model, which neglects inertia and damping effects, while the Gaussian wake model inability to capture wake dynamics contributes to reduced peak forces in the shared line. Deviations between the two models remain below 5% for wave heights under 5.5 m, and have a maximum deviation of 6% for the highest wave of 6.5 m.

### 6.3.5 Turbulent wind and irregular wave tests of the floating array

Two sets of turbulent wind and irregular wave simulations (Table 6.4) are performed in FAST.Farm and using the simplified model with a wake growth rate of 0.04 ($K4$), since $K4$ provides the closest agreement in power output in steady wind tests. The first set maintains constant irregular wave conditions while varies the mean upstream wind speed. The second set keeps the upstream mean wind constant, but varies the significant wave heights. For each turbulent wind condition, six random seeds are used, and each simulation runs for 70 min. Data on turbine power output, floater surge displacement, and mooring line forces are collected from the final 20 min of each simulation, and then averaged across six seeds. Figures 6.12 and 6.13 compares the dynamic response of the floating array under two representative test conditions, predicted by FAST.Farm and using the simplified model with $K4$.

The comparisons demonstrate that the simplified model effectively reproduces the dynamic performance of the floating array with shared line configurations under turbulent wind and irregular wave conditions, showing close agreement with the results from FAST.Farm. Although the Gaussian wake model captures only the mean velocity deficit, leading to differences in downstream rotor-averaged wind speeds, and the quasi-static mooring model neglects inertia and damping effects, reducing peak mooring forces, the overall consistency between the two simulation tools supports the validity of the numerical implementation and the underlying modeling assumptions of the simplified approach.

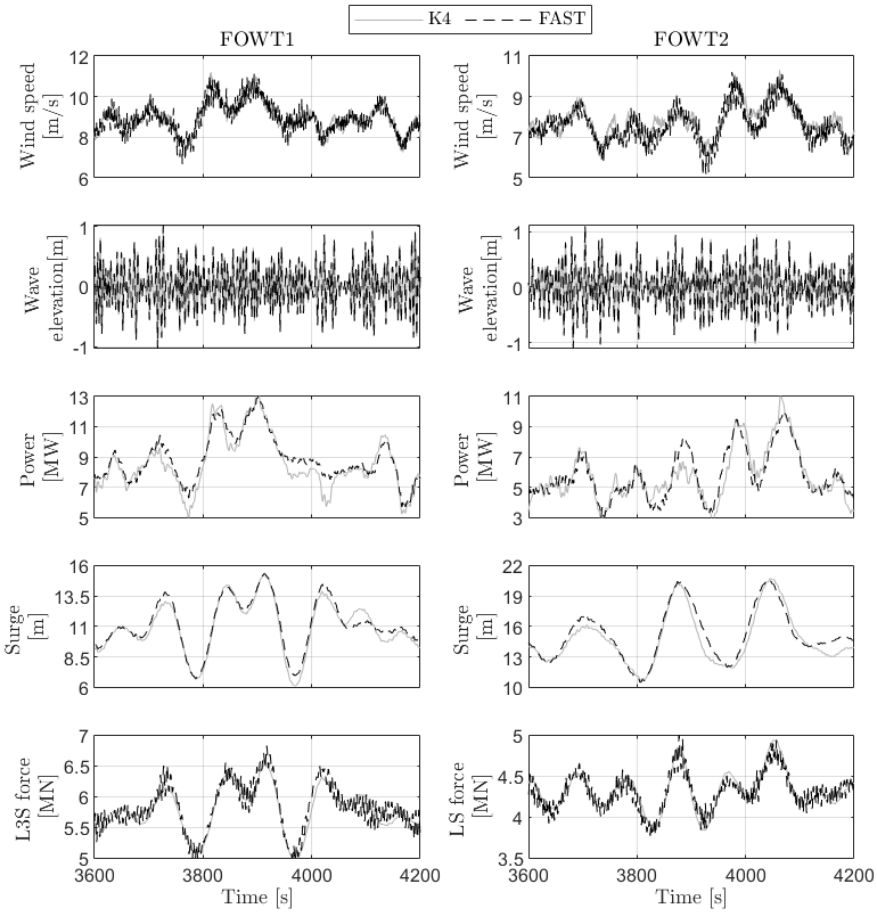


Figure 6.12: Comparison of the dynamic performance of the floating array with $7D_r$ spacing under the turbulent wind conditions with the upstream mean speed of 9 m/s, and irregular waves with a significant wave height of 1.5 m, using FAST.Farm ("FAST") and the simplified model with $K4$ ("K4").

Table 6.10 summarizes the mean power output of the floating turbine array as predicted by FAST.Farm and the simplified model with $K4$. The simplified model consistently underestimates the mean power of the upstream turbine by about 0.3 MW across the three upstream mean wind speeds. For the downstream turbine, it predicts roughly 0.2 MW lower at lower wind speeds and 0.2 MW higher at an upstream mean wind speed of 11 m/s compared to

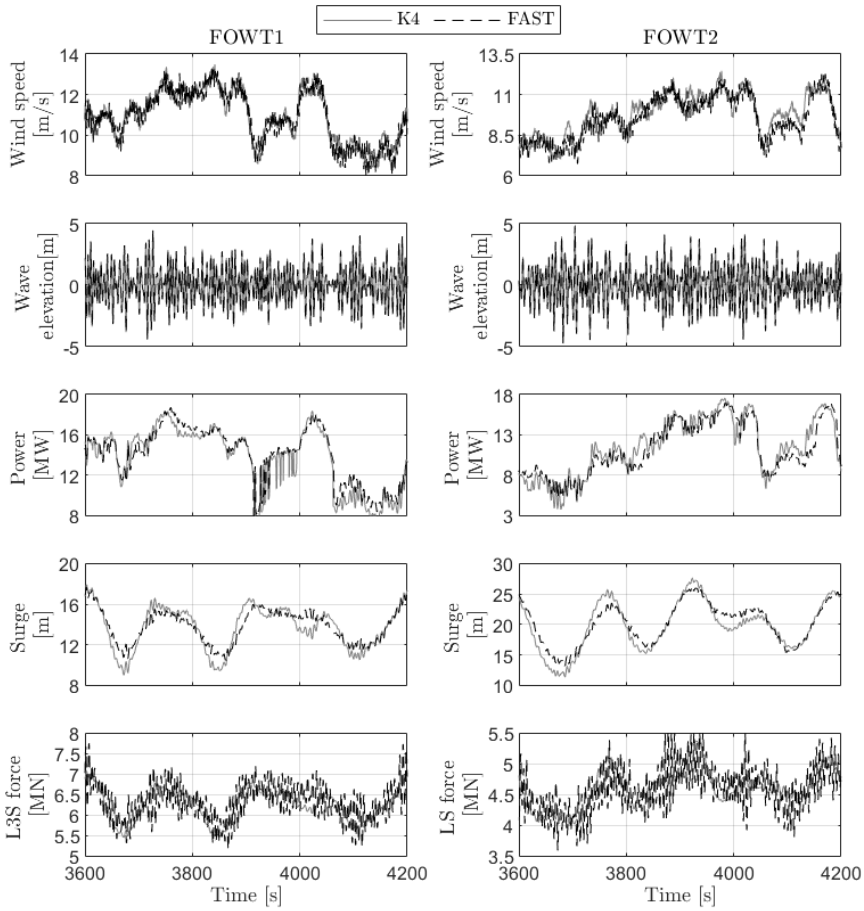


Figure 6.13: Comparison of the dynamic performance of the floating array with $7D_r$ spacing under the turbulent wind conditions with the upstream mean speed of 11 m/s, and irregular waves with a significant wave height of 6.5 m, using FAST.Farm ("FAST") and the simplified model with $K4$ ("K4").

FAST.Farm. Overall, the results show that the simplified model reproduces power production in close agreement with FAST.Farm.

Figure 6.14 compares the 20-minute mooring fatigue of anchor line L3S under turbulent wind tests for three mean upstream wind speeds, as predicted by FAST.Farm and the simplified model with $K4$. At a mean wind speed

Table 6.10: Comparison of the mean power (in MW) of the floating array with shared mooring configurations during the first set of turbulent wind and irregular wave tests, predicted by FAST.Farm and the simplified model with $K4$ ("K4").

| | | Speed [m/s] | 7 | 9 | 11 |
|---|---|---|---|---|---|
| FOWT1 | - | $K4$ | 4.0 | 8.6 | 13.9 |
| | | FAST.Farm | 4.3 | 8.9 | 14.2 |
| FOWT2 | $6D_r$ | $K4$ | 2.2 | 5.4 | 10.7 |
| | | FAST.Farm | 2.4 | 5.6 | 10.5 |
| | $7D_r$ | $K4$ | 2.4 | 5.8 | 11.2 |
| | | FAST.Farm | 2.6 | 6.0 | 11.0 |
| | $8D$ | $K4$ | 2.6 | 6.1 | 11.6 |
| | | FAST.Farm | 2.8 | 6.4 | 11.5 |

of 11 m/s, the mooring fatigue is highest across all three shared line designs. FAST.Farm predictions exceed those from the simplified model that can not capture the high-frequency fluctuations in mooring forces induced by dynamic wake effect and mooring dynamic forces. For the floating array at three spacings, the differences at 11 m/s reach 26 %, 17 %, and 43 %. These cases correspond to designs with the smallest chain diameters, whose feasibility has not been fully examined. Thus, the observed differences highlight the potential underestimation of fatigue by the simplified model, although such large difference are not expected for all designs.

Figure 6.15 compares the normalized mooring fatigue calculated using the occurrence probabilities of three mean upstream wind speeds (approximately 19%, 21%, and 18%, Figure 6.2), with the fatigue contribution from only the 11 m/s mean wind speed, as predicted by FAST.Farm and the simplified model with $K4$.

The results indicate that fatigue estimates are sensitive to the choice of sea states, with the 11 m/s mean wind speed dominating the contribution. Because only three mean wind speeds are considered, additional lower-damage and less frequent cases (Figures 5.15 and 6.2) from the remaining wind speeds

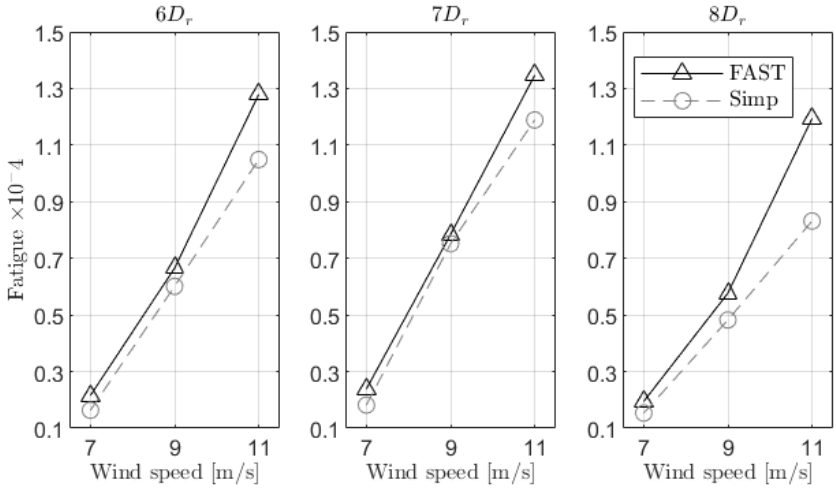


Figure 6.14: Comparison of the 20-minute mooring fatigue of line L3S under turbulent wind conditions, as predicted by FAST.Farm ("FAST") and the simplified model with $K4$ ("Simp").

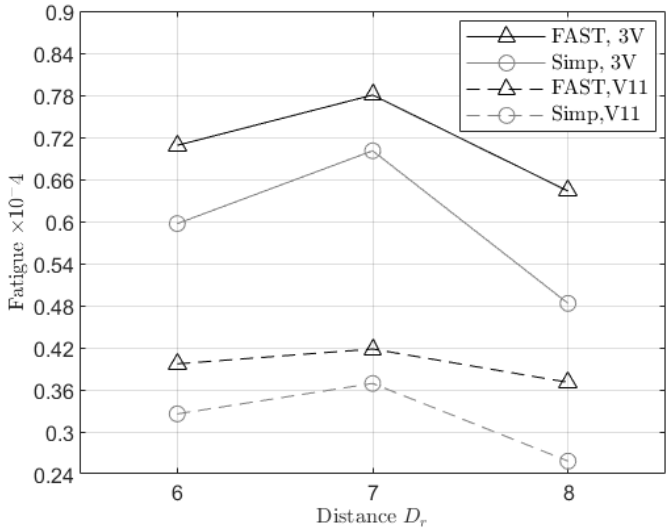


Figure 6.15: Comparison of the 20-minute mooring fatigue of line L3S under turbulent wind conditions and for the single mean speed at 11 m/s, predicted by FAST.Farm ("FAST") and the simplified model with $K4$ ("Simp").

would further reduce the total normalized fatigue. While using a single sea state underestimates fatigue by up to 46 % for both FAST.Farm and the simplified model, this remains a practical and efficient approach for large-scale simulations. The fatigue differences are most pronounced in these shared baseline designs with the smallest chain diameters, of which feasibility is uncertain, while heavier designs with larger chains are less affected (Figure 5.19). Applying a higher fatigue safety factor of 10 (twice the standard factor of 5 [12]) further compensates for the underestimation, supporting the reliability of the assessment.

For the second set of turbulent wind tests with different irregular wave conditions, Figure 6.16 compares the mean power output, maximum floater surge displacement, and maximum mooring line forces between the two tools for the floating array with shared line configurations. The deviations in power, surge, and mooring forces are presented as percentages relative to the FAST.Farm results, analyzed at significant wave heights ($H_s$) of 1.5 m, 3.5 m, and 6.5 m.

Different $H_s$ have only a minor effect on the mean power output of the floating array. The power differences between the two tools remain consistent with those observed in the first set of turbulent wind tests. The simplified model with $K4$ slightly underestimates the mean power of the upstream turbine by up to 2.2% (0.3 MW) and overestimates the power of the downstream turbine by up to 2.5% (0.3 MW) compared to FAST.Farm. However, different $H_s$ have a strong impact on the maximum floater surge and maximum mooring forces. At the lowest $H_s$, the simplified model predicts a slightly higher surge of the upstream FOWT (up to 2.9%) and a lower mooring force (less than 4.7%). These deviations increase with rising $H_s$, but remain within 5% for $H_s$ up to 3.5 m. While at the highest $H_s$, the surge difference reaches 8.3% for the downstream FOWT, corresponding to an increase of 2.2 m predicted by the simplified model. Similarly, the mooring force deviation rises to 7% for the shared line, with the simplified model underestimating the force by 0.4 MN.

Under turbulent wind tests with a constant upstream mean wind speed and irregular waves of six $H_s$, the deviations in floater surge and mooring forces

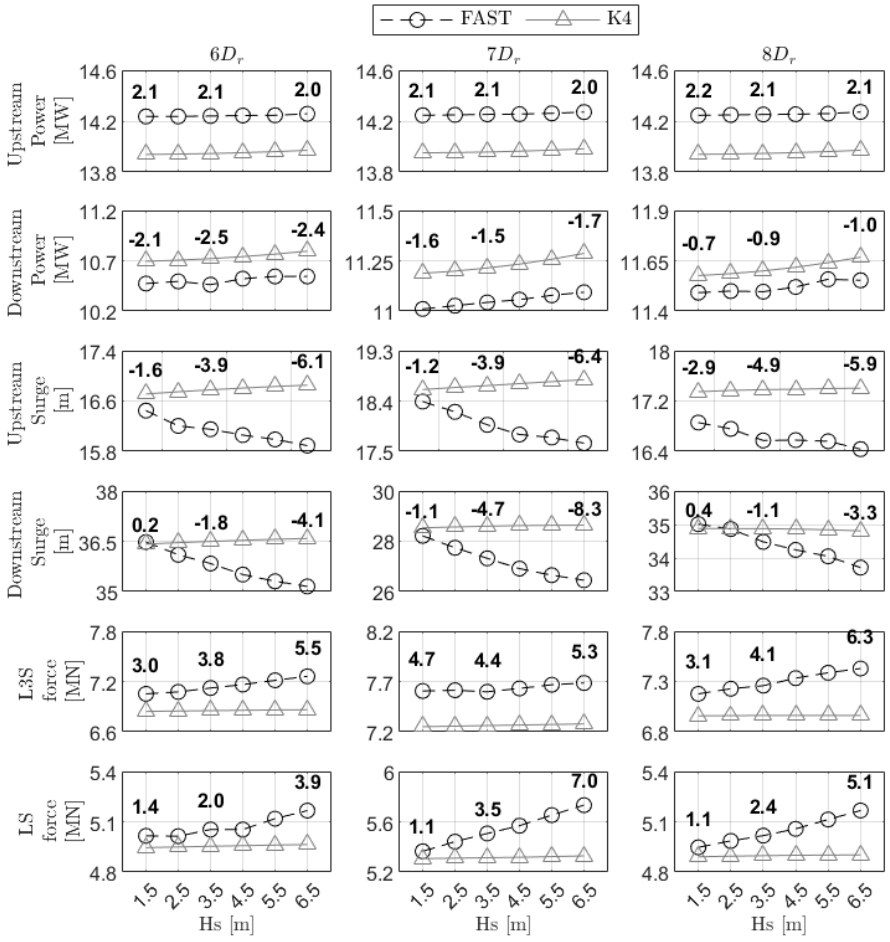


Figure 6.16: Comparison of mean power output, maximum floater surge, and maximum mooring forces for the floating array with shared line configurations, under turbulent wind and irregular wave conditions, as predicted by FAST.Farm ("FAST") and the simplified model with $K4$ ("K4"). Deviations are displayed as percentages of the FAST.Farm results at $H_s$ values of 1.5 m, 3.5 m, and 6.5 m.

mainly arise from differences in the hydrodynamic and mooring models used by the two tools. FAST.Farm accounts for wave radiation damping, while the simplified model neglects these forces. The higher damping in FAST.Farm leads to smaller surges compared to the simplified model, as observed in the free decay test of a single FOWT (Figure 6.6), where including radiation damping

reduces surge displacement. FAST.Farm also incorporates dynamic mooring forces, while the simplified model relies on quasi-static mooring analysis. Including these mooring dynamic forces in FAST.Farm further restricts floater motions, contributing to the reduced surge.

Overall, these two sets of turbulent wind and irregular wave tests demonstrate the predictive accuracy of the simplified model compared to FAST.Farm in terms of power production, floater surge, and mooring forces for the floating turbine array with shared line configurations. Although differences in these parameters are observed, the deviations remain within an acceptable range, indicating that the simplified model can produce results comparable to those of the higher-fidelity simulation tool.

## 6.4 Application of the simplified modeling approach

Section 6.3 demonstrates that the simplified modeling approach can effectively capture the dynamic performance of a floating array with three shared line configurations under various environmental conditions, producing results comparable to those from FAST.Farm. This section addresses two challenges associated with shared line designs and introduces a new configuration aimed at reducing surge motion and increasing lay-down length. In addition, the array is expanded from two to four FOWTs to highlight the applicability of the simplified model for large-scale wind farm simulations.

### 6.4.1 Improved shared line design for the two-turbine array

The first challenge associated with shared line configurations is the increased surge motion, which results from the reduced mooring stiffness compared to conventional designs. This effect is evident in turbulent wind tests (Figures 6.12 and 6.13), where the downstream floater exhibits larger surge than the upstream floater. Such increased surge presents challenges for cable design and safety, as excessive motion may lead to cable damage.

The second challenge concerns the lay-down length of the upwind anchor lines, particularly those connected to the upstream floater, which experience the highest loads in a shared line configuration. High mooring forces increase the risk of lifting the dragged embedment anchor from the seabed. Figure 6.17 illustrates the lay-down length of anchor line L3S, which experiences the highest load during turbulent wind tests.

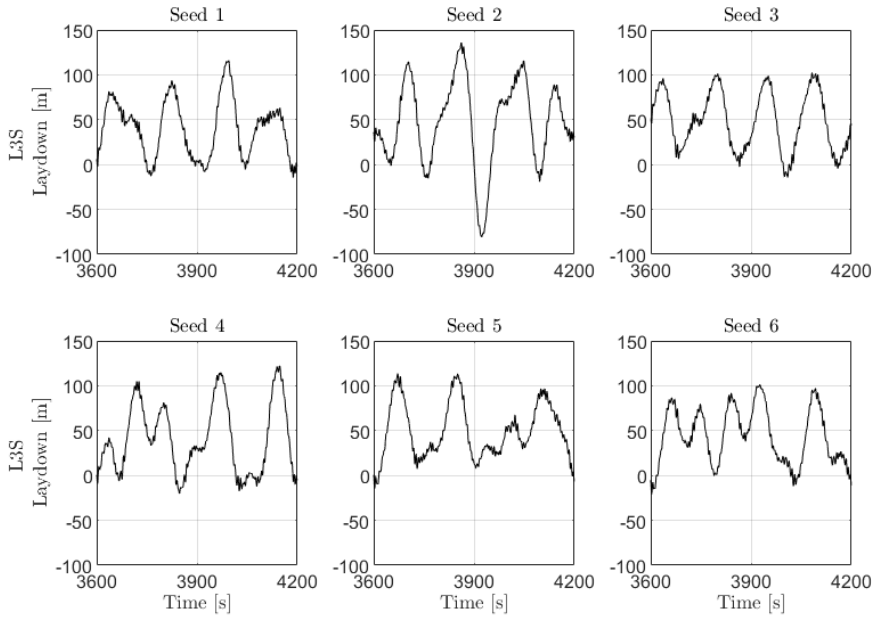


Figure 6.17: The lay-down length of the anchor line L3S in shared line Design 1 under the turbulent wind conditions across six wind seeds.

The tests were conducted with a mean upstream wind speed of 11 m/s, a significant wave height of 6.5 m, and $7D_r$ spacing between the two FOWTs. Negative lay-down lengths are observed, even though the maximum mooring force remains within the allowable range (Figure 6.13). A negative lay-down length indicates that the dragged embedment anchor has lifted off the seabed, posing a significant risk to the mooring integrity of the floating array.

To enhance the dynamic performance of the floating array, a new shared line design (Design 2) is proposed. Compared to Design 1 (Tables 6.2 and 6.3), De-

sign 2 doubles the mooring mass to reduce maximum surge and ensure sufficient minimum lay-down length. The design follows a similar workflow for selecting the line with the smallest chain diameter, as described in Section 6.2.2. The corresponding mooring properties are summarized in Table 6.11 for the anchor lines and Table 6.12 for the shared line.

Table 6.11: Design parameters, constraints, and properties for refined anchor lines.

| | Variable | Range, unit | Design 2 |
|---|---|---|---|
| Parameter | Length ratio | [0.3:0.05:0.7] | 0.3 |
| | Chain diameter | [68:1:205] mm | 177 |
| | Chain grade | [R3, R3S, R4, R4S] | R4S |
| Constraint | Mooring mass per turbine | 4e5 kg | 4e5 |
| | Total unstretched length | [600 1000] m | 967 |
| | Pretension ratio | [0.1 0.3] | 0.30 |
| Property | Mass per unit length in air | kg/m | 623 |
| | Mooring tension stiffness | GN | 5.1 |
| | Anchor radius | m | 981 |
| | Mooring pretension | MN | 8.48 |

Table 6.12: Design parameters, constraints, and properties for the refined shared line.

| | Variable and range | Design 2 | | |
|---|---|---|---|---|
| Parameter | FOWT distance [6, 7, 8] $D_r$ | 6 | 7 | 8 |
| | Length ratio [0.3:0.05:0.7] | 0.3 | 0.35 | 0.55 |
| | Chain diameter [60:1:200] mm | 205 | 195 | 195 |
| | Chain grade [R3, R3S, R4, R4S] | | R3 | |
| Constraint | Mooring mass per turbine 4e5 kg | | 4e5 | |
| | Pretension ratio [0.1 0.3] | 0.26 | 0.30 | 0.30 |
| Property | Total unstretched length m | 1443 | 1658 | 1903 |
| | Mass per unit length in air kg/m | 836 | 757 | 757 |
| | Mooring tension stiffness GN | 6.8 | 6.2 | 6.2 |
| | Mooring pretension MN | 6.60 | 7.18 | 7.18 |

The floating array with Design 2 is simulated using the simplified modeling approach with a wake growth rate of 0.04, under turbulent wind conditions with a mean wind speed of 11 m/s and irregular waves with a significant wave height of 1.5 m. The simulation setup and post-processing procedures follow

those described in Section 6.2.4. Figures 6.18 and 6.19 compares the maximum floater surge and the minimum lay-down length of anchor line L3S between Design 1 and Design 2.

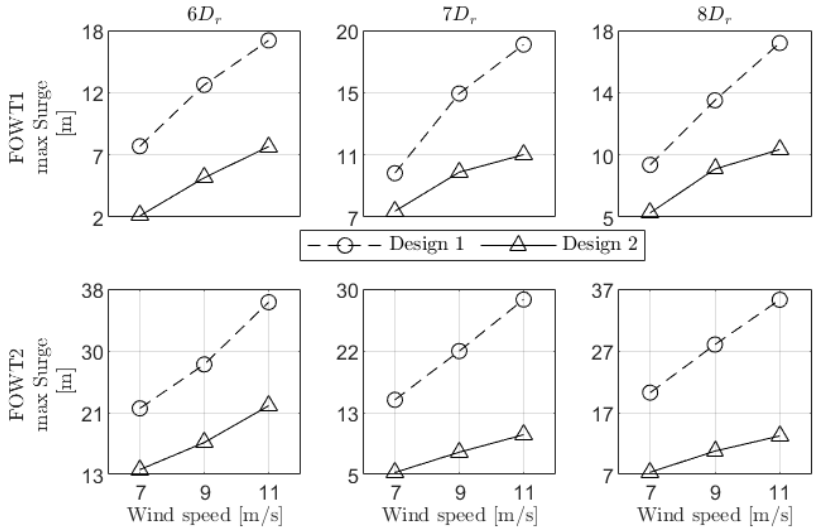


Figure 6.18: Comparison of the maximum floater surge averaged across wind seeds between two shared line designs.

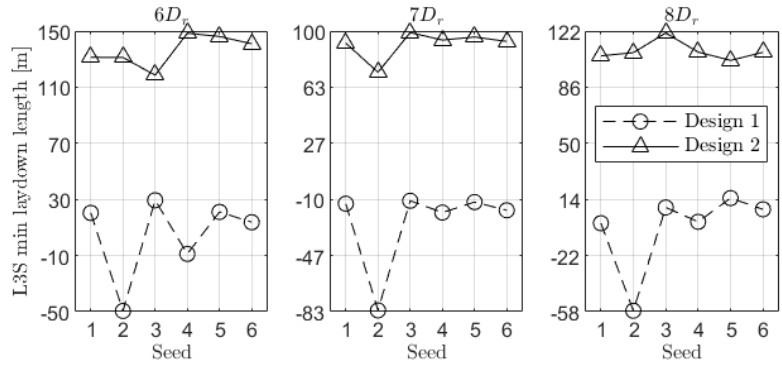


Figure 6.19: Comparison of the minimum lay-down length of the anchor line L3S between two shared line designs.

Design 2 increases the mooring chain diameter and doubles the mooring mass, significantly enhancing the mooring stiffness. As a result, the maximum surge motion is reduced, and the minimum lay-down length across all six simulations

exceeds 60 m, compared to Design 1 under identical environmental conditions. This outcome suggests that while Design 2 provides improved stability, it may be conservative, and further optimization is recommended to avoid over-design of the shared line configurations. Overall, the rapid analysis of the two-turbine array confirm the effectiveness of the simplified modeling approach and establish its strong potential as a practical tool for parametric studies and large-scale floating wind farm simulations.

### 6.4.2 Power prediction of the four-turbine floating array

Figure 6.20 illustrates a four-turbine array. The properties of each FOWT are described in Section 4.3.3, with the principal dimensions summarized in Table 4.1. All four FOWTs have similar structural properties, with a fairlead radius of 42.5 m. The initial angle between each pair of mooring lines is 120°. All anchor lines share similar characteristics listed in Table 6.2. The turbine spacing ($D_s$) is $8D_r$.

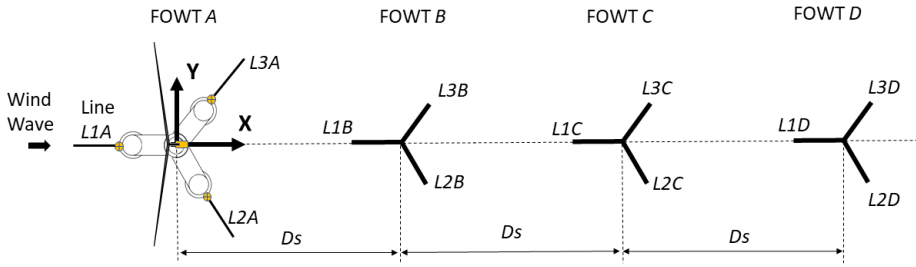


Figure 6.20: A four-turbine array using conventional configurations.

To estimate the disturbed wind speed at a downstream turbine located within multiple wakes, the wake superposition model proposed by [53] is employed to account for the combined effects of upstream turbine wakes, as expressed in Equation 6.1. This wake overlap model is implemented within the wake module of the simplified modeling approach.

$$U = \left( \sum_{i=1}^{n} U_i^2 / n \right)^{1/2} \tag{6.1}$$

where $U$ is the disturbed wind speed at the downstream turbine affected by multiple wakes, and $U_i$ is the reduced wind speed at the turbine due to the wake from a single upstream turbine $i$. $U_i$ can be calculated using the Gaussian wake model (Equation 4.5). The variable $n$ is the number of upstream turbines contributing to the wake. This wake overlap model is not based on the superposition of the wind speed deficits, such as linear or squared deficit superposition models, but combines the reduced downstream wind speeds to ensure that the disturbed wind speed remains positive and physically meaningful [53].

The four-turbine array is evaluated under steady upstream inflow conditions, with a wind speed of 11 m/s. Wake-induced velocity deficits result in different downstream wind speeds and power outputs. Each simulation runs for 4800 s, excluding wave loads, with the mean wind speed and power recorded over the final 600 s. Figure 6.21 compares the power outputs of three downstream turbines as predicted by FAST.Farm and the simplified modeling approach, which uses different wake parameters applied to each downstream FOWT. $KA$, $KB$, $KC$ represent the wake parameters accounting for the contributions from upstream FOWTs A, B, and C, respectively.

The power comparison demonstrates that the simplified model can provide predictions comparable to FAST.Farm for the four-turbine array. This case study highlights the application of the simplified model for wind-farm simulations with conventional mooring configurations. For instance, layout optimizations are often based on static analyses rather than dynamic simulations of the entire floating wind farm, due to high computational demands. However, static analyses may underestimate floater motions and mooring forces. The simplified model overcomes this limitation, enabling efficient evaluation of array dynamics while providing power predictions comparable to those from higher-fidelity simulation tools.

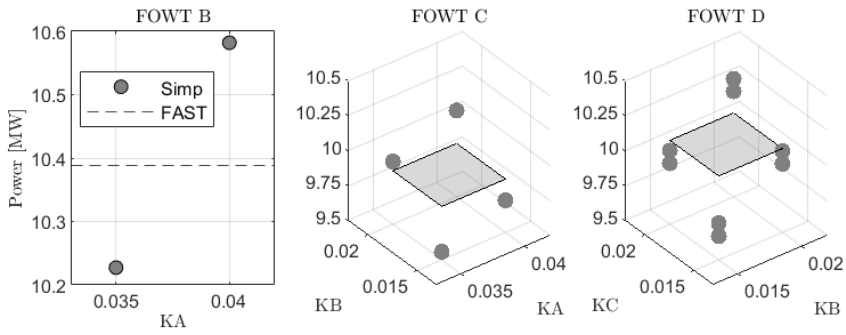


Figure 6.21: Comparison of downstream turbine power outputs predicted by FAST.Farm ("FAST") and the simplified modeling approach ("Simp") with different wake growth rates, accounting for the contributions from upstream FOWTs A, B, and C. The gray shading (FOWTs C and D) indicates the FAST.Farm results.

## 6.5 Summary

This chapter introduces a simplified modeling approach for analyzing the dynamic performance of floating turbine arrays. Verification against FAST.Farm (v3.5.1) demonstrate that this approach significantly enhances the computational efficiency and predicts comparable results of power output, floater surge, and mooring force as those from FAST.Farm under various environmental conditions.

The increased simulation-to-CPU time ratio represents a reduction of more than 75-fold in computational effort. Such an advantage facilitates rapid analysis and enables large-scale simulations of floating wind farms with both conventional and shared mooring designs. Findings from static and decay tests indicate that the simplified model effectively captures the fundamental dynamics of the floating array. It is more suitable than FAST.Farm, which is not designed for simulations that exclude wind loads. Both steady and turbulent wind tests suggest that fine-tuning the wake expansion parameter in the Gaussian-based wake model could improve the accuracy of turbine power predictions.

The limitations of the simplified model are also addressed. The Gaussian-based wake model predicts only the mean deficit, while FAST.Farm accounts for wake dynamics, which leads to differences in power output and mooring line forces for the downstream turbine. Also, the omission of wave radiation damping and mooring dynamics in the simplified model results in higher surge motions and underestimated mooring forces.

In addition, this chapter demonstrates the application of the simplified model for rapid analysis of an improved shared line design for a two-turbine array, as well as power prediction for a four-turbine array accounting for multiple wake effects. These case studies highlight the strong potential of the simplified model for further shared line and wind-farm layout optimization. Overall, the study provides a valuable framework for advancing shared line designs, paving the way toward more cost-effective and sustainable floating wind energy production.

# 7 Shared mooring optimization for floating wind farms

As discussed in Section 2.3.3, mooring optimization studies for individual FOWTs often use frequency-domain analysis [39, 58]. However, time-domain analysis provides higher accuracy in predicting dynamic responses, which is critical for floating wind farms with shared line designs, where coupling and wake effects amplify both floater motions and mooring force fluctuations. Such dynamic flow-structure interactions may be underestimated by frequency-domain analysis, while the high computational demand of time-domain analysis has limited its application in mooring optimization for FOWTs.

Furthermore, as shared line research is still in its early stages, most studies evaluate only a narrow set of configurations, with limited systematic exploration of optimal solutions for floating wind farms. Moreover, existing mooring optimization primarily targets cost reduction under extreme loading conditions, with limited consideration of mooring fatigue. As discussed in Section 5.4.3, however, mooring fatigue is a critical factor in feasibility assessments and should be incorporated into mooring design to ensure structural integrity.

In light of these considerations, this chapter proposes two optimization strategies for shared line designs: cost-driven and cost–fatigue balance. The nonlinear design method (Chapter 5) generates shared line configurations, while the simplified modeling approach (Chapter 6) predicts FOWT responses under both extreme and normal operating conditions. Wake effects are included in dynamic simulations, and mooring fatigue is considered in design evaluations.

Overall, the proposed optimization process provides robust support for comprehensive evaluation and practical implementation of shared line designs in floating wind farms.

## 7.1 Shared mooring optimization strategy

As illustrated in Figure 5.22, the mooring cost comparison between conventional and shared line configurations shows that, although shared line designs exhibit approximately 3% higher cost at the lowest-cost end, they achieve over 30% lower fatigue damage (Table 5.7). This highlights the potential of shared mooring optimization to minimize cost while maintaining a balance between expense and fatigue performance.

### 7.1.1 Cost-driven optimization

The cost-driven optimization aims to identify shared line designs that minimize mooring material costs ($C_m$) for floating wind farms. This strategy, widely adopted in floating structures, follows a routine procedure similar to those in the existing studies for conventional mooring systems [11, 57, 58, 39], where cost reduction is achieved by adjusting the line properties and layout arrangement of mooring lines. The design variables include chain mass and material properties, subject to constraints related to line strength, floater offset, and anchor safety requirements.

Particle Swarm Optimization (PSO) is chosen for this nonlinear single-objective optimization problem, because it is more flexible than the gradient-based methods, especially when the objective function is discontinuous due to the presence of two discrete design variables. Also, PSO has been successfully applied to mooring optimization for a deep-water production structure [61]. The optimization objective, mooring material costs, can be explicitly formulated in terms of the design variables, according to the Equation 5.3. However, a known drawback of PSO is its tendency to converge prematurely to local optima and

its relatively high computational cost compared with deterministic methods, such as Nelder–Mead simplex algorithm used in frequency-domain mooring analyses [39].

### 7.1.2 Cost–fatigue balance optimization

In contrast to the cost-driven strategy, which focuses on a single objective, the optimization for cost–fatigue balance addresses two objectives: minimizing mooring material cost ($C_m$) and minimizing mooring fatigue damage ($D_m$). There is no single solution that simultaneously optimizes both objectives. Designs with lower mooring cost favor lighter mooring lines with smaller chain diameters, while designs with lower mooring fatigue damage require heavier lines with larger diameters, as discussed in Section 5.5. These two objectives conflict, so improving one can worsen the other. Therefore, the optimal solution represents the best trade-off between mooring material cost and fatigue damage.

At the current stage of shared mooring research, it remains challenging to assign weighting factors to balance mooring material cost and fatigue damage in the objective function. This difficulty arises from the lack of cost analyses that quantify the relationship between expenses and fatigue damage for shared mooring applications. Moreover, mooring fatigue damage cannot be directly expressed in terms of the design variables for mooring configurations, adding further complexity to this two-objective optimization.

To address these challenges, the Non-dominated Sorting Genetic Algorithm II (NSGA-II) is selected. This algorithm allows simultaneous consideration of both objectives and searches for a set of Pareto-optimal solutions. Each solution is non-dominated and represents a trade-off between mooring cost and fatigue damage. Unlike genetic algorithm, NSGA-II does not require explicitly defined objective functions [132], making it well-suited for this problem. The algorithm has been applied in [59] to investigate the influence of mooring on platform optimization. However, NSGA-II requires evaluations of a

large population over many generations, which is computationally expensive for time-domain FOWT analyses. In addition, for high-dimensional optimization problems, NSGA-II may converge slowly and prematurely to sub-optimal regions.

## 7.2 Two optimization algorithms for shared line designs

Studies on mooring optimization in the offshore oil and gas industry, as well as platform optimization in the floating wind sector, have demonstrated the effectiveness of using PSO and NSGA-II [61, 125, 59]. Prior to formulating the optimization problems, the working principles of both algorithms are briefly introduced in this section.

### 7.2.1 PSO algorithm

A detailed description of the PSO algorithm and its applications can be found in [133, 134]. PSO is a stochastic search technique inspired by the social behavior of animals and uses a swarm to represent a population of candidate solutions. Each candidate within the swarm is called a particle. In this study, each particle represents a shared line design for floating wind farms.

The algorithm seeks the optimal solution through interactions among particles, with each moving towards its own best position (personal best) and the best positions found by the swarm (global best). Particle positions correspond to the design variables of each shared line configuration, and solutions are evaluated based on both design constraints and the objective function, namely mooring material cost. The workflow of the PSO algorithm is shown in Figure 7.1.

During initialization, a population of particles with random positions and velocities is generated. In this study, Latin hypercube sampling is used to initialize the swarm, ensuring a spread distribution across the design space. Each particle is then evaluated using the objective function based on its position. If

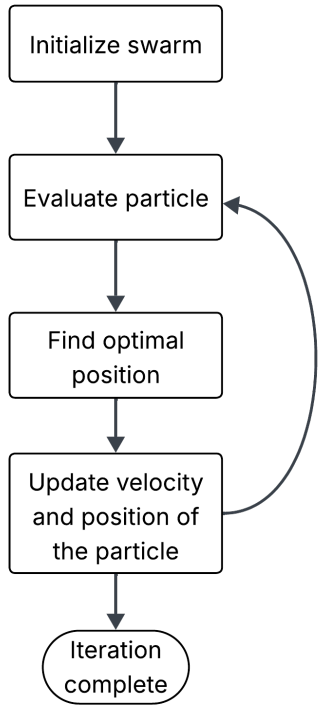


Figure 7.1: The workflow of the PSO algorithm (adapted from [134]).

a candidate particle, or a shared line design, violates any design constraints, a penalty is applied to its objective function value to reduce its likelihood of being selected as the best solution.

At each iteration, the positions, velocities, and corresponding objective function values of the particles are updated. When a particle identifies its personal best fitness or lowest mooring material cost, its position is stored, and the deviation between this best position and its current position is added to its velocity. Simultaneously, the difference between the global best position within the neighborhood and the current position of each particle is also incorporated into its velocity. The velocity update model is presented in Equation 7.1.

$$v_i(t+1) = w \cdot v_i(t) + c_1 \cdot r_1 \cdot (P_i - x_i(t)) + c_2 \cdot r_2 \cdot (G - x_i(t)) \tag{7.1}$$

where $v_i(t)$ is the velocity of particle $i$ at iteration $t$ and $w_x$ controls its impact on the updated velocity. $c_1$ and $c_2$ refer to the cognitive and social factors, respectively for considering the particle and the swarm influence. $r_1$ and $r_2$ are random numbers that uniformly distributed in the range [0, 1]. $P_i$ denotes the best position of particle $i$, while $G$ is the best position found by all particles in the swarm. $x_i(t)$ is the current position of particle $i$ at time $t$, and the updated position of the particle $x_i(t+1)$ is written in Equation 7.2 [135].

$$x_i(t+1) = x_i(t) + v_i(t+1) \tag{7.2}$$

The parameters $w_x$, $c_1$, and $c_2$ in Equation 7.1 are set to 0.7, 1.5, and 1.5, respectively, consistent with the study by [61]. Sensitivity tests are performed using static analysis to investigate the influence of different $w_x$, $c_1$, and $c_2$ on the optimal results, as discussed in Section 7.4.2.

The optimization proceeds for a maximum of 100 iterations, with the global best solution gradually converging toward the optimal configuration. Although the MATLAB PSO solver [135] can perform cost-driven optimization, high memory usage during parallel execution caused premature termination at 20 iterations for a swarm size of 100. The default solver output does not include particle velocity information, preventing continuation even with available position data. This limitation arises because each iteration involves dynamic simulations of floating turbines under both extreme and normal operation conditions, which process 4800-second wind and wave time series and generate corresponding floater motions, line forces, and lay-down lengths. To address this issue, the velocity update in Equation 7.1 was implemented manually in MATLAB Simulink, bypassing the built-in toolbox and enabling error-free completion of all 100 iterations.

### 7.2.2 NSGA-II

In optimization for cost-fatigue balance, a Pareto-optimal solution represents the best trade-off between mooring cost and fatigue damage, such that no objective can be improved without simultaneously worsening the other. To seek such non-dominated solutions, evolutionary algorithms are often used, due to their ability to produce a diverse population of candidate solutions across the search space. Both NSGA [132] and NSGA-II [136] are examples of evolutionary algorithms, which are inspired by the principles of natural selection and evolution, where the most competitive solutions survive and evolve over generations.

Key steps in evolutionary algorithms include selection, crossover, and mutation. Candidate solutions with higher fitness values are selected for reproduction to pass their properties to the next generation. Crossover combines parts of two selected solutions to produce offspring and explore new regions in the search space. Mutation introduces random changes to design variables to ensure diversity and prevent premature convergence.

The main difference between NSGA and a simple genetic algorithm lies in the selection process, while the crossover and mutation operations remain largely the same [132]. Two critical parameters govern these operations: the crossover probability ($p_c$), which specifies the chance that crossover is performed on two selected solutions to generate offspring, and the mutation probability ($p_m$), which defines the chance of updating variables in a solution [137]. In this study, $p_m$ is set to 0.9 to enhance diversity, while $p_c$ is set to 0.1 to reduce the risk of premature convergence.

NSGA-II solves the problems related to high computational complexity of NSGA [136], and avoids the reliance on the user-dependent sharing parameter required by NSGA [132]. NSGA-II also improves efficiency by modifying the non-dominated sorting procedure and assigning a crowd distance comparison mechanism to ensure diversity across the search space. The workflow of NSGA-II is shown in Figure 7.2.

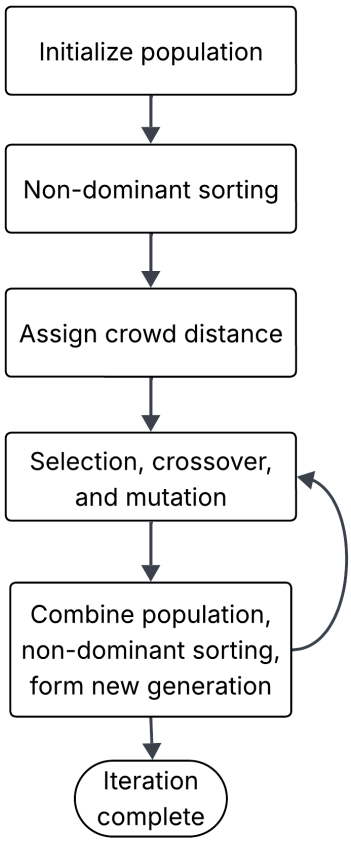


Figure 7.2: The NSGA-II workflow, with key steps adapted from [138].

The NSGA-II procedure is detailed in [136]. First, a random initial population $P_0$ is generated using the Latin hypercube sampling method to ensure a well-distributed spread across the design space. $P_0$ is sorted according to the non-dominant principles, with each candidate assigned a rank based on its non-dominant level and a crowd distance to preserve diversity. An offspring population $Q_0$ is then created from $P_0$ through selection, crossover, and mutation. $P_0$ and $Q_0$ are combined to form population $R_0$.

In the $t$-th generation, the combined population, denoted as $R_t$, is formed by combining the parent population $P_t$ and the offspring population $Q_t$. $R_t$ is then

sorted according to the non-dominant principles, and produce a series of fronts. The first front, $F_1$, contains the best non-dominant solutions, followed by the subsequent fronts $F_2$ and $F_3$, and so on, which are near-optimal solutions chosen after $F_1$. A new parent population $P_{t+1}$ is constructed by selecting solutions from these fronts until the population size is reached. $F_1$ is first chosen, followed by the subsequent fronts $F_2$ and $F_3$, and so on. In case the final front $F_l$ not fully accommodated, the solutions in $F_l$ are sorted in descending order by the crowded-comparison operator, and its best solutions are selected to fill population slots. Then $P_{t+1}$ is used to produce a new offspring population $Q_{t+1}$ through selection, crossover and mutation. The procedure continues until it reaches the maximum generation numbers.

Unlike the single-objective optimization that uses a penalty function to handle the violation of design constraints, the multiple-objective optimization follows the constraint-handling approach proposed by [136]. This approach uses the binary tournament selection, where two solutions are compared based on their feasibility and fitness. For shared mooring optimization problem with two objective targets and 14 design constraints, as detailed in Section 7.3.3, each candidate configuration can be either feasible or infeasible. The compared two configurations can meet three situations, and the strategy for selecting between two solutions in each situation is as follows:

1. For two feasible solutions, select the one with better fitness using the crowd-distance comparison operator;

2. For one feasible and one infeasible solutions, select the feasible one;

3. For two infeasible solutions, select the one with less violations;

In this constrained approach, feasible solutions are assigned higher nondominant ranks than infeasible ones. While among infeasible solutions, those with less constraint violations are ranked more favorably. NSGA-II is implemented manually in MATLAB Simulink, rather than using the embedded solver, to ensure error-free parallel execution of the dynamic simulations, similar as the discussion in Section 7.2.1.

## 7.3 Formulation of the shared mooring optimization problem

### 7.3.1 Objective function

A general objective problem is formulated in Equation 7.3, where $f(x)$ refers to the target determined by design variables $x$, and the optimization algorithm is employed to minimize or maximize $f(x)$. In this study, the cost-driven optimization aims at minimizing mooring cost ($C_m$), while in optimization for cost-fatigue balance, both mooring cost ($C_m$) and fatigue damage ($D_m$) are considered in the objective function.

$$f(x) = f(x_1, x_2, ..., x_n) \tag{7.3}$$

However, neither $C_m$ nor $D_m$ can be expressed in a closed-form mathematical equation. $C_m$ is derived from an empirical model (Equation 5.3), in which $C_m$ depends on chain $MBL$ and total line length ($L_T$). Chain $MBL$ (Equation 5.2) is a function of chain grade ($G_c$) and chain diameter ($D_c$), while the calculation of $L_T$ differs between anchor lines and the shared line.

For anchor lines, $L_T$ is calculated by dividing the line mass ($M_L$), which is the product of the mass ratio ($R_M$) and the floater displaced mass, by the line mass per unit length ($\rho_c$, Equation 5.1), which depends on $D_c$. In contrast, the shared line length ($L_T$) is determined from force equilibrium (Figure 5.2), where pretensions are balanced between the anchor lines and the shared line, such that its characteristic length ($L_a$) and suspended length ($L_S$) are obtained from elastic catenary equations (Equation 4.1).

Pretensions in each anchor line is determined by its suspended length ($L_S$) based on elastic catenary equations, and its $L_S$ is a function of the total length ($L_T$) and the static length ratios ($R_L$). The complete design workflow is presented in Section 5.1.5. Since shared line profiles are derived from nonlinear

catenary equations, the shared line mooring cost ($C_m$) cannot be expressed mathematically in closed form.

As a result, the objective function for mooring material cost, denoted as $f(C_m)$, is written in Equation 7.4, where the subscripts 1 and 2 in the design variables correspond to the anchor line and the shared line, respectively.

$$f(C_m) = f(D_{c1}, D_{c2}, R_L, R_M, G_{c1}, G_{c2}) \tag{7.4}$$

Similarly, the objective function for the cost-fatigue balance optimization is given in Equation 7.5.

$$f(C_m, D_m) = f(D_{c1}, D_{c2}, R_L, R_M, G_{c1}, G_{c2}) \tag{7.5}$$

where $D_m$ represents the maximum mooring line fatigue damage (Equations 4.3 and 4.4) across the anchor lines and the shared line within each shared line configuration under the given loading condition. Although these design variables ($D_{c1}$,$D_{c2}$,$R_L$,$R_M$,$G_{c1}$,$G_{c2}$) define the shared line configuration, there is no direct analytical expression to quantify fatigue damage across all mooring lines and loading conditions. These dependencies are interrelated and must be resolved through dynamic simulation rather than analytical formulations.

Nevertheless, this expression issue does not affect the use of PSO or NSGA-II, since both are population-based, derivative-free algorithms that evaluate objective functions directly from static analyses and dynamic simulations, without requiring explicit analytical expressions.

### 7.3.2 Design variables

The design of the shared mooring line configurations follows the workflow of the nonlinear design method (Figure 5.2). The design parameters used in the shared mooring optimization are summarized in Table 7.1. The site has a

water depth of 200 m. The mooring lines are composed of steel chains, and drag embedment anchors are selected across all shared line designs.

The four input variables in Equations 7.4 and 7.5, including chain diameter ($D_{c1}$), static length ratio ($R_L$), chain grade ($G_{c1}$), and mass ratio ($R_M$), are used to define the anchor lines. The remaining two variables, chain diameter ($D_{c2}$) and chain grade ($G_{c2}$), are used for generating the shared line based on the anchor line profile and the distance between two FOWTs. The bounds for these variables are based on the static investigation of shared line designs presented in Chapter 5. In the shared line designs, all anchor lines have similar properties.

Table 7.1: Design parameters.

| Parameter | Input data |
|---|---|
| Water depth | 200 m |
| Mooring line material | Steel chain |
| Mooring anchor type | Drag embedment anchor |
| Distance between two FOWTs | $6D_r$ |
| Chain diameter $D_{c1}$ | [70 220] mm |
| Static anchor line length ratio $R_L$ | [0.3 1.5] |
| Chain grade $G_{c1}$ | [R3, R3S, R4, R4S] |
| Anchor line mass ratio $R_M$ | [1/3 5/3]% |
| Chain diameter $D_{c2}$ | [70 220] mm |
| Chain grade $G_{c2}$ | [R3, R3S, R4, R4S] |

To define the position of a sample solution in the design space, the variable bounds are first scaled using the normalized values. Specific rounding is then applied to the continuous variables, allowing $D_{c1}$ and $D_{c2}$ rounded to one decimal place, while $R_L$ and $R_M$ rounded to two decimal places. As for discrete variables ($G_{c1}$ and $G_{c2}$), the sampling method detects the closest predefined values from the set of possible properties.

### 7.3.3 Design constraints

In the optimization process, design constraints are used to filter feasible solutions, and can be formulated as either equality constraints ($h_i(x)$) or inequality constraints ($g_j(x)$), as shown in Equation 7.6. For the shared mooring optimization problem, only $g_j(x)$ are applied.

$$\begin{aligned} h_i(x) &= 0 \quad \text{for} \quad i = 1, 2, ..., m \\ g_j(x) &\leq 0 \quad \text{for} \quad j = 1, 2, ..., n \end{aligned} \tag{7.6}$$

For each shared line configuration, design constraints ensure static equilibrium between the anchor lines and the shared line, maintain structural safety under extreme loading conditions, and provide fatigue resistance to dynamic cyclic loads under normal operation conditions. Table 5.3 lists the constraints applied for both static and dynamic feasibility checks. As discussed in Section 5.1.4, a safety factor of 10 accounts for steel chain lifetime fatigue, using a quasi-static mooring model for analyzing non-redundant mooring configurations, to provide an additional reliability margin. This approach, including the safety factor of 10, has also been applied in frequency-domain optimization study [58]. The design constraints are summarized in Table 7.2 as part of the mooring optimization problem formulation.

### 7.3.4 Penalty function

Penalty functions are incorporated into the objective function, indicating the violation of design constraints in the candidate samples. A general objective function including penalty terms is written as Equation 7.7. In this study, the penalty formulation includes only contributions from inequality constraints.

$$f_{\text{pen}}(x) = f(x) + \sum_{j=1}^{p} \mu_j \max(0, g_j(x)) \tag{7.7}$$

Table 7.2: Design constraints.

| Category | Constraint | Formulation |
|---|---|---|
| No-wind | Anchor line length | $600 \leq g_1(x) \leq 1000$ |
| | Pretension ratio | $0.1 \leq g_2(x) \leq 0.2$ |
| | Shared line mass ratio | $0.5 \leq g_3(x) \leq 1.5$ |
| | Shared line static length ratio | $g_4(x) \geq 0.3$ |
| Static wind | Maximum force ratio | $g_5(x) \leq 0.5$ |
| | Minimum lay-down length ratio | $g_6(x) \geq 0.1$ |
| | Maximum horizontal offset | $g_7(x) \leq 60$ |
| Extreme | Maximum force ratio | $g_8(x) \leq 0.5$ |
| | Minimum lay-down length ratio | $g_9(x) \geq 0.0$ |
| | Maximum horizontal offset | $g_{10}(x) \leq 60$ |
| Operation | Maximum force ratio | $g_{11}(x) \leq 0.5$ |
| | Minimum lay-down length ratio | $g_{12}(x) \geq 0.0$ |
| | Maximum horizontal offset | $g_{13}(x) \leq 60$ |
| | Maximum Lifetime fatigue damage | $g_{14}(x) \leq 0.1$ |

where $f(x)$ is the objective function without any penalty. $g_j(x)$ represents the inequality constraints, and $\mu_j$ is a weighting factor that indicates the consequence of violation of design constraints.

The penalty function is only used in the cost-driven optimization problem. To avoid the complexity of tuning individual weight factors for each inequality constraint, the feasibility of a candidate shared mooring design is checked with all design constraints. If a candidate design violates any design constraint during the four evaluations (two static and two dynamic checks), a fixed penalty of $3 \times 10^6$ USD is added to $f(x)$. This value is selected based on the distribution of mooring costs, as shown in Figure 5.22, where the upper bound falls at the order of $3 \times 10^6$ USD.

## 7.4 Case study: two-turbine floating array

A case study of a two-FOWT array (Figure 5.1), which is the smallest unit for shared line designs, is considered in shared mooring optimization prob-

lems. The array uses the FOWT models described in Section 4.3.3, with key dimensions in Table 4.1. The two FOWTs have similar dimensions, with the upstream floater rotated 180° relative to the downstream floater. The fairlead radius is 42.5 m, with an initial angle of 120° between mooring lines. Four similar anchor lines are secured to the seabed, while the shared line connects the two floaters without anchors.

### 7.4.1 Load cases for shared mooring optimization

Sensitivity tests (Figure 5.6) show that a wind direction of 30° results in the largest floater offset and maximum mooring force ratio in anchor line L2S, while a direction of 0° produces the maximum mooring force ratio in anchor line L3S and in the shared line, among directions from 0° to 90°. Therefore, the optimization study considers load cases at both 0° and 30°, as summarized in Table 7.3. The environmental parameters include mean upstream wind speed ($V_m$), wind direction ($\theta$), significant wave height ($H_s$), and peak wave period ($T_p$). The wind direction $\theta$ is defined relative to the positive X-axis, and the array layout is rotated so that inflow aligns with 0°, as illustrated in Figure 5.4. No ocean current is included, as explained in Section 4.2.4, because the current reduces relative fluid velocity and decreases hydrodynamic forces on the floater and mooring lines.

Table 7.3: Environmental conditions for shared mooring optimization.

| Load case | $V_m$ [m/s] | $\theta$ [°] | $H_s$ [m] | $T_p$ [s] |
|---|---|---|---|---|
| Static, without wind | - | [0,30] | - | - |
| Static, rated-wind force | - | [0,30] | - | - |
| Dynamic, extreme | 11 | [0,30] | 5.1 | 9 |
| Dynamic, operation | 11 | [0,30] | 1.5 | 7 |

The static no-wind test ensures force equilibrium between the anchor lines and the shared line, while the static wind test applies a constant force of 2.2 MN to the FOWTs to determine static offset, mooring force, and lay-down length. At

0°, the wake effect is included in analysis, by reducing the force on the downstream FOWT to 1.8 MN, following Section 5.2.4. In dynamic simulations, the Kaimal model generates synthetic wind fields, using the Normal Turbulent Model for the IEC turbulence type with Class C turbulence intensity. Irregular waves are modeled using the Pierson–Moskowitz (PM) spectrum, consistent with the single FOWT study [120]. The rationale for the selected sea states is similar to that described in Section 5.4.1.

The simplified modeling approach (Chapter 6) is used to perform dynamic simulations of the floating array with shared line configurations under both extreme and normal operational loading conditions. This model has been verified against the higher-fidelity simulation tool FAST.Farm (v3.5.1) for the same array (Section 6.2). The simulation set-up follows Section 6.2.4. Each simulation runs for 4800 s, with the final 1-hour of data used to extract the maximum floater offset, maximum mooring line force, minimum lay-down length, and stress cycles for mooring fatigue calculations. For studless mooring chains, the fatigue damage (Equations 4.3 and 4.4) is calculated from all stress cycles following the procedure in Section 4.1.4. Hourly mooring fatigue damage is then extrapolated assuming that sea states near the rated wind speed occur approximately 18% of the time (Figure 6.2) over the 25-year design life [121].

### 7.4.2 Sensitivity tests on the PSO velocity factors

To investigate the influence of control factors ($w_x$) in the velocity update model (Equation 7.1), three values of $w_x$ are examined, with constant cognitive ($c_1$) and social ($c_2$) factors of 1.5. Figure 7.3 illustrates the evolution of the global best solution and corresponding configuration parameters (Equation 7.4) for three $w_x$ values under static optimization with a sample size of 100.

Tuning $w_x$ is critical for the PSO algorithm, as it controls the balance between global exploration and local exploitation. A higher value guides a broader search across the design space, while a lower value guides convergence toward local regions. The results show that $w_x = 0.9$ causes the highest mooring

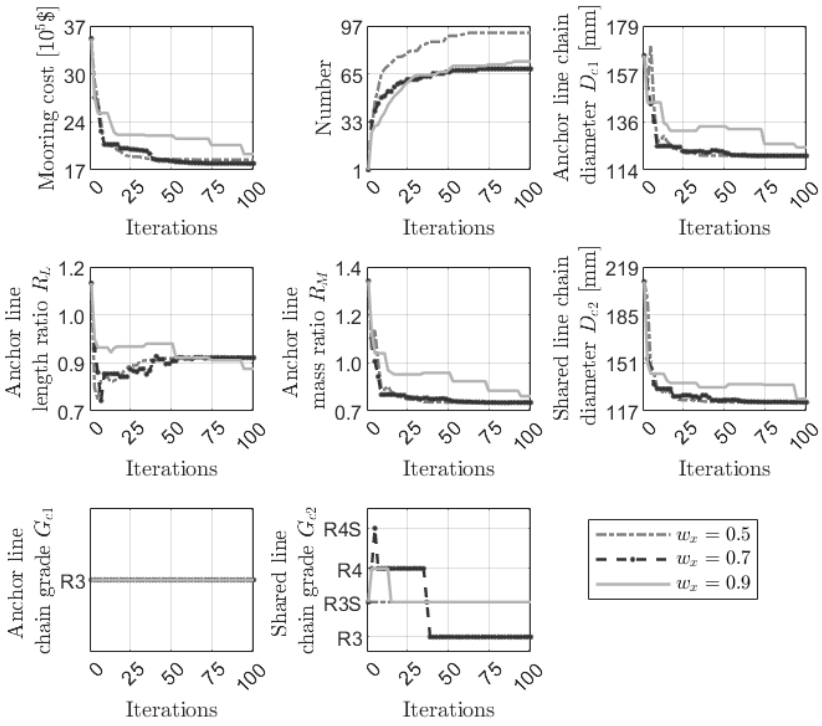


Figure 7.3: Evolution of the global best solution and configuration parameters for three $w_x$ values under static optimization, with cognitive ($c_1$) and social ($c_2$) factors of 1.5.

cost, while $w_x = 0.7$ produces the lowest. For feasible configurations out of 100 samples, $w_x = 0.5$ generates the largest count after 100 iterations, while $w_x = 0.7$ gives the least count. For line properties, $w_x = 0.9$ leads to higher chain diameters and mass ratios, while the remaining $w_x$ values produce relatively similar properties. Although only static analysis is considered, Figure 5.6 demonstrates that it effectively captures trends in FOWT performance for different shared line configurations, allowing meaningful comparisons. Overall, $w_x = 0.7$ is acceptable for controlling the PSO algorithm, and achieves the lowest mooring cost with sufficient exploration.

The second test evaluates the cognitive ($c_1$) and social ($c_2$) factors in the velocity update model (Equation 7.1), with $w_x = 0.7$ during static optimization.

Figure 7.4 shows the evolution of the global best solution and configuration parameters (Equation 7.4) for three values of $c_1$ and $c_2$.

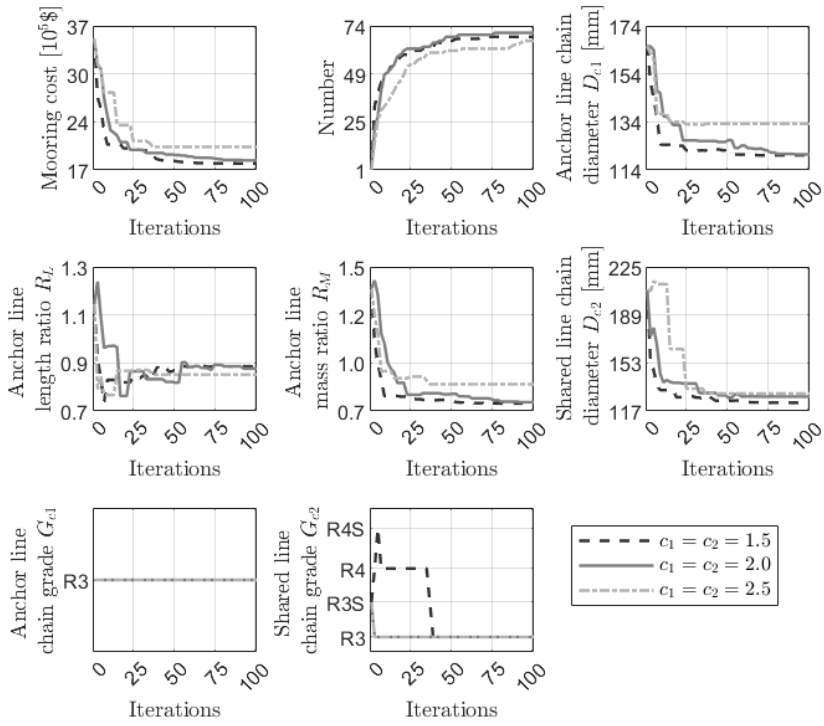


Figure 7.4: Evolution of the global best solution and configuration parameters for three values of cognitive ($c_1$) and social ($c_2$) under static optimization, with $w_x = 0.7$.

$c_1$ controls the influence of a particle own best position (local best), while $c_2$ controls the influence of the swarm best position (global best) on the updated velocity. Setting $c_1 = c_2$ ensures balanced exploration of both local region and global search space. The results indicate that $c_1 = c_2 = 1.5$ produces the lowest mooring cost ($C_m$) and smaller design variables for chain diameter and mooring mass ratio, while the number of feasible configurations out of the 100 samples is comparable to $c_1 = c_2 = 2.0$ after 100 iterations. Therefore, $c_1 = c_2 = 1.5$ is acceptable for the PSO algorithm, as it offers an effective compromise between local and global search.

### 7.4.3 Cost-driven optimization of shared line configurations

The PSO algorithm is applied to the cost-driven optimization using a swarm of 100 particles, in which each particle represents a possible shared line design defined by specific properties of both the anchor lines and the shared line. The particle positions are initialized using Latin hypercube sampling within the defined range of each design variable. Figure 7.5 shows these initialized particle positions along with the corresponding anchor line chain diameters.

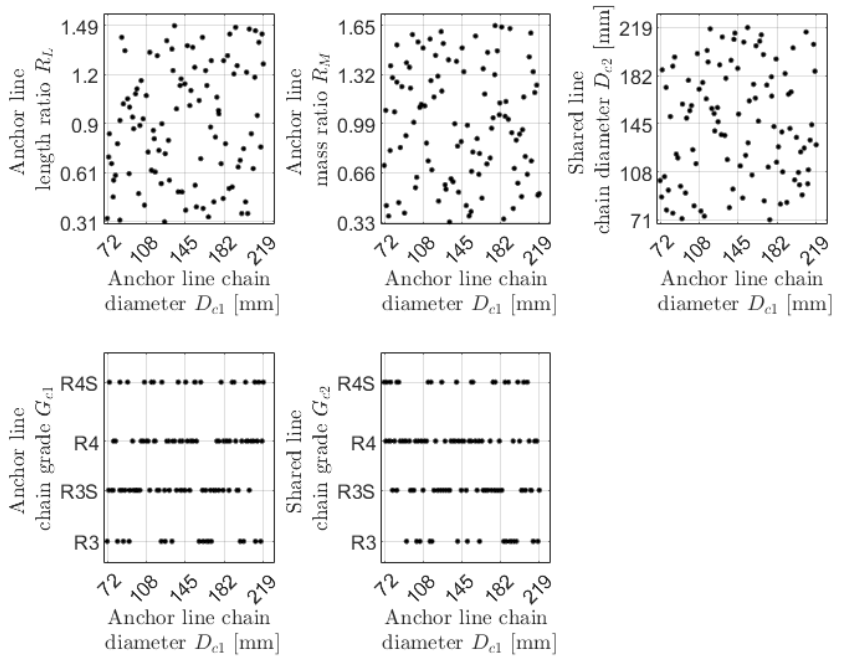


Figure 7.5: Initialized particle positions of the swarm in the PSO algorithm.

The particles are widely distributed across the bounds of each continuous variable. For the discrete chain grade, the mapping method identifies the closet predefined values within the bounds from the initialized options, resulting in a relatively higher distribution around the middle two grades (R3S and R4). This diversity in the swarm positions is important to promote exploration and avoid clustering.

Figure 7.6 illustrates the evolution of the global best solutions (mooring costs) and the corresponding global best positions (configuration properties) over 100 iterations.

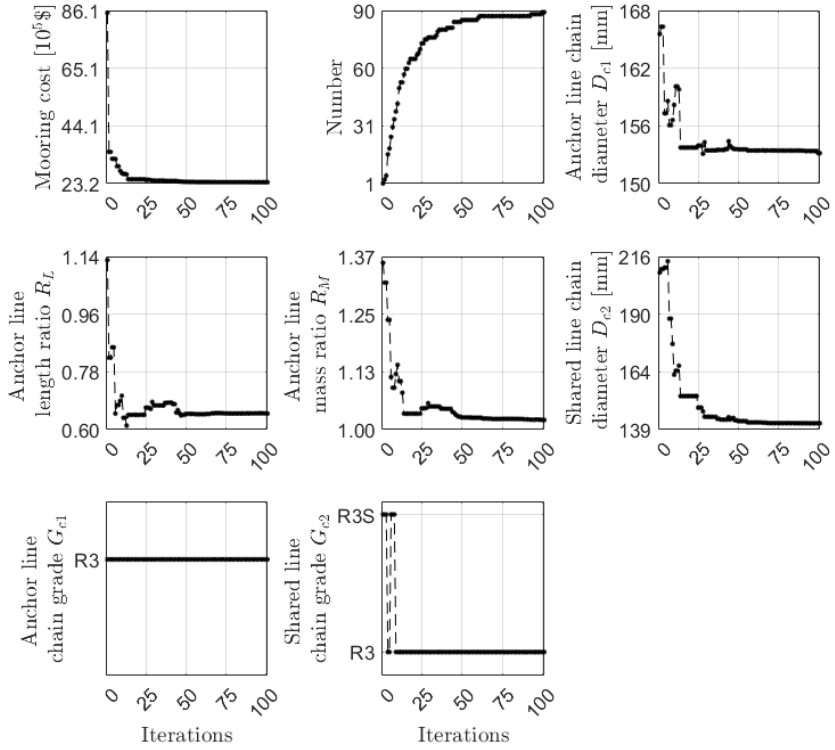


Figure 7.6: Evolution of the global best solutions and corresponding positions.

At each iteration, the objective function (mooring cost) is evaluated for each particle, and its feasibility is checked against the 14 design constraints described in Section 7.3.3. For infeasible candidates that violate any constraints, a penalty is added to their mooring costs to discourage infeasible solutions during the optimization process. The global best solution found in the initial swarm reaches $86 \times 10^5$ USD, as it violates design requirements, so penalties are added to its mooring cost.

The consistent reduction in mooring cost throughout the optimization process indicates the convergence of the PSO algorithm. The global best solution progressively approaches the optimal mooring cost of $24 \times 10^5$ USD and reaches convergence after 75 iterations. Within the first 25 iterations, the global best solution decreases by 71%, down to $25 \times 10^5$ USD. Between the 25th and 50th iterations, the improvement in mooring cost slows, with a modest 4% drop, bringing the mooring cost to $24 \times 10^5$ USD at the 40th iteration. Slight improvements continue with a decrease of less than 2%, and by the 75th iteration the global best solution reaches the optimal mooring cost. This indicates that the swarm has effectively converged without further improvement.

The feasibility rate is measured as the ratio of the number of feasible solutions to the swarm of 100 particles. Although the initial swarm consists entirely of infeasible solutions, this rate exceeds 50% after 10 iterations and 60% by the 25th iteration. This consistent increase in feasibility rate demonstrates that the penalty function guides particles toward the feasible region, with less constraint violations over iterations.

The positions of global best solutions, including chain properties and length ratios, display fluctuation over 100 iterations. For instance, the chain diameter of the anchor lines shows a local maximum within the first 25 iterations, and then remains relatively stable, with a decrease of less than 1%, until it converges to 153 mm around the 75th generation. The temporary rise does not increase mooring cost, as the corresponding mooring mass follows a decreasing trend, which shortens the total length and offsets the cost impact.

Chain grades for the anchor lines remain at the lowest grade throughout 100 iterations, as these four lines dominate the total mooring cost in shared line configurations. Using the lowest chain grade minimizes the chain $MBL$ and mooring costs, which depend on the chain $MBL$ for both anchor and mooring line costs (Equation 5.3). In contrast, the shared line grade fluctuates between R3S and R3 during the first 12 iterations, following changes in the remaining configuration properties, before settling at the lowest grade to minimize mooring cost.

Figures 7.7 to 7.9 show the personal best positions of the particles and the global best positions of the swarm at the 25th, 75th, and 100th iterations, respectively. These figures illustrate the variability and convergence of the swarm after initialization.

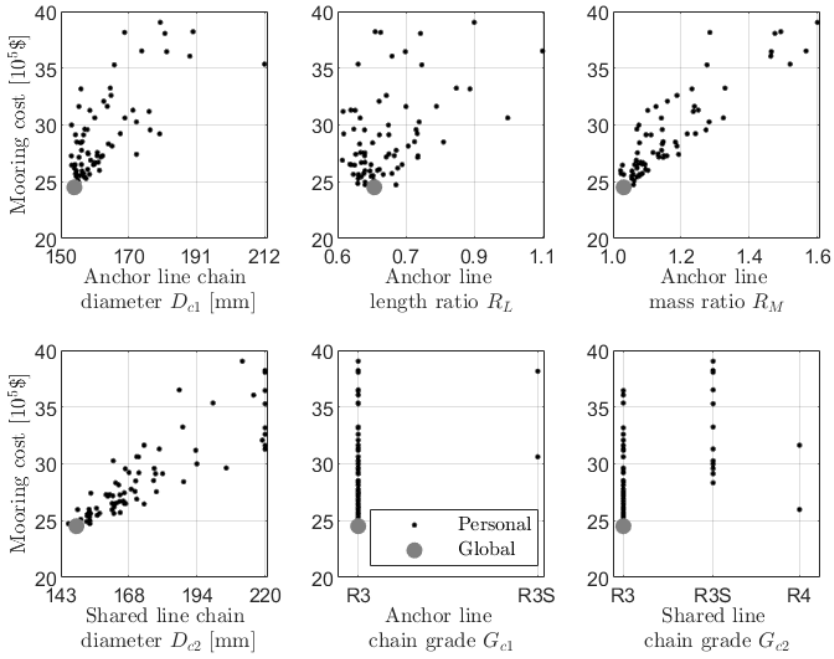


Figure 7.7: Personal and global best positions at the 25th iteration.

By the 25th iteration (Figure 7.6), the PSO algorithm produces more than 60 feasible solutions out of 100 particles. The personal best positions maintain a spread distribution across the design space, showing high diversity in configuration properties. By the 75th iteration, the feasibility rate approaches 90%, but the personal best positions of these feasible solutions become concentrated around the global best, indicating strong convergence of the swarm. This concentration is most pronounced at 100th iteration, where most feasible solutions cluster within a small region near the global best. These trends demonstrate that the PSO algorithm effectively guides particles toward the optimal solution.

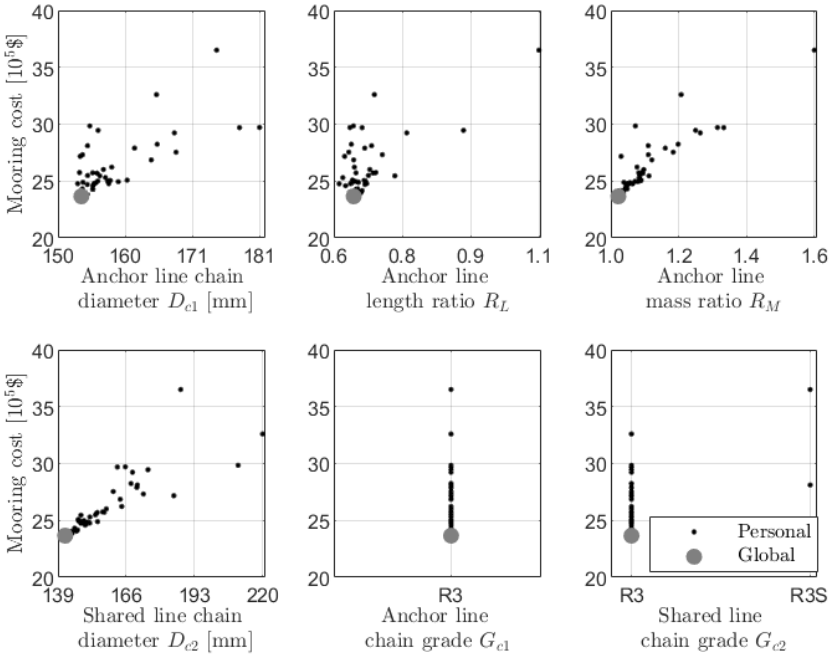


Figure 7.8: Personal and global best positions at the 75th iteration.

The evolution of the global best solutions demonstrates convergence within 100 iterations. The mooring cost stabilizes after 75 iterations, with negligible improvements in subsequent iterations. The number of feasible solutions reaches 88, and design variables for shared line configurations show minor changes, indicating effective stabilization of particle positions. This confirms that 100 iterations are sufficient for the cost-driven shared mooring optimal solutions.

### 7.4.4 Cost-fatigue balance optimization of shared line configurations

NSGA-II is applied to the cost–fatigue balance optimization, with the goals to minimize both mooring cost and fatigue damage. Solutions are ranked into Pareto fronts based on the non-domination levels, with crowding distance

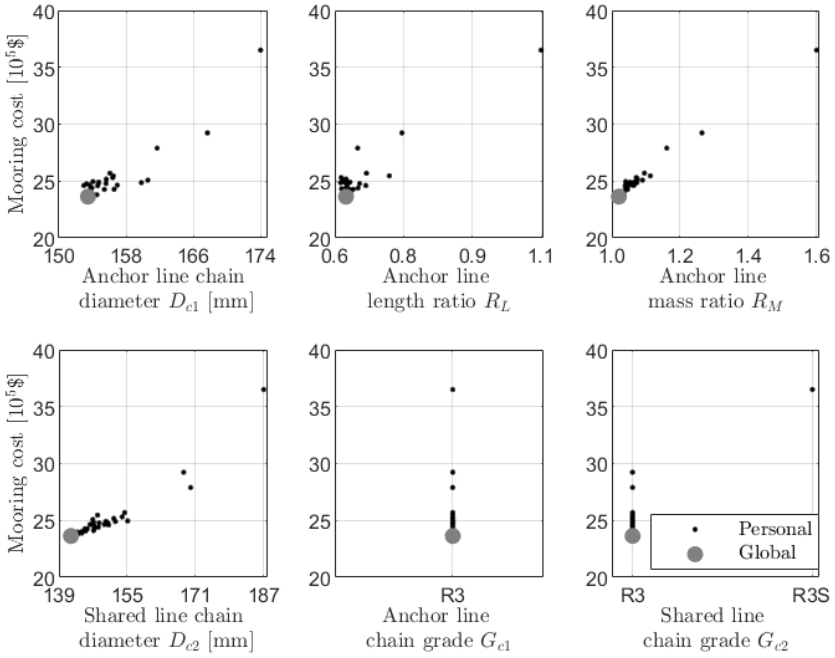


Figure 7.9: Personal and global best positions at the 100th iteration.

introduced to maintain diversity. The next generation is selected by elitism (best individuals) and diversity preservation. The initial 100 candidates (Figure 7.5) fail to meet the design constraints, leading to null offspring and premature termination of the optimization.

To address this, a constrained initialization approach is employed. A total population of 3000 samples is generated using Latin hypercube sampling method and evaluated against the design constraints. From these, 20 feasible solutions are obtained and combined with 80 randomly chosen samples to form the new population. The properties of these 100 samples are shown in Figure 7.10.

The constrained initialization ensures a broad distribution of 100 samples across the design space, which promotes exploration and helps to prevent premature clustering. While this initialization provides diversity, the occurrence probabilities of these samples differ from those of the initial swarm positions shown in

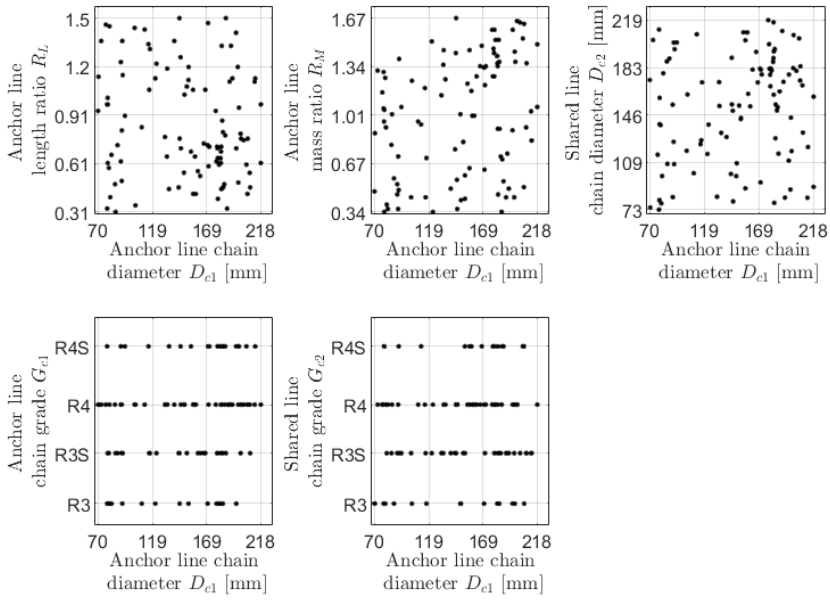


Figure 7.10: Properties of the initial population in NSGA-II.

Figure 7.5. For discrete chain grades, the mapping method assigns the closest predefined values within the bounds of the initialized options, resulting in a denser distribution around R4.

NSGA-II is performed over a population size of 100 over 100 generations. Figure 7.11 illustrates the evolution of Pareto fronts, showing progressive convergence toward the optimal trade-off solutions. A grayscale gradient indicates the progress, with darker shades representing earlier generations. The Pareto fronts exhibit noticeable clustering during the first 50 generations, after that improvements slow with only slight refinements observed.

As explained in Section 7.1.2, no single solution can simultaneously minimize both mooring cost and fatigue damage. Designs with lower mooring cost favor lighter lines with smaller chain diameters that induce higher fatigue, while designs with lower fatigue require heavier lines with larger diameters that increase mooring cost, as discussed in Section 5.5. These two objectives conflict,

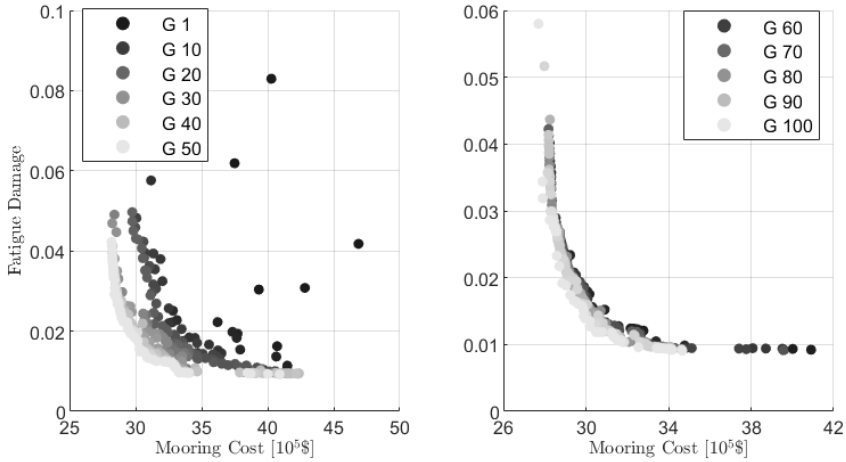


Figure 7.11: Evolution of Pareto fronts.

so improving one can worsen the other. Pareto fronts represent the trade-off between mooring material cost and fatigue damage.

Pareto fronts in the first 10 generations are sparse, with relatively high mooring costs and large fatigue damage compared to subsequent generations. This dispersion results from the constrained initialization, which promotes wide exploration of the objective space. As the optimization progresses, Pareto fronts gradually shift from the upper-right region (high cost and large fatigue) toward the lower-left region (lower cost and small fatigue). Rapid convergence occurs between the 10th and 40th generations, after that improvements slow and the Pareto fronts become more compact. After 50 generations, reductions in mooring cost are still noticeable, while improvements in fatigue resistance are minimal.

The Pareto fronts maintain a diverse set of trade-off solutions throughout the optimization process. This progression demonstrates the effectiveness of NSGA-II in guiding the population toward optimal, non-dominated solutions for the two conflicting objectives. To further illustrate this evolution, Figure 7.12 shows the feasible solutions and corresponding Pareto fronts at selected generations.

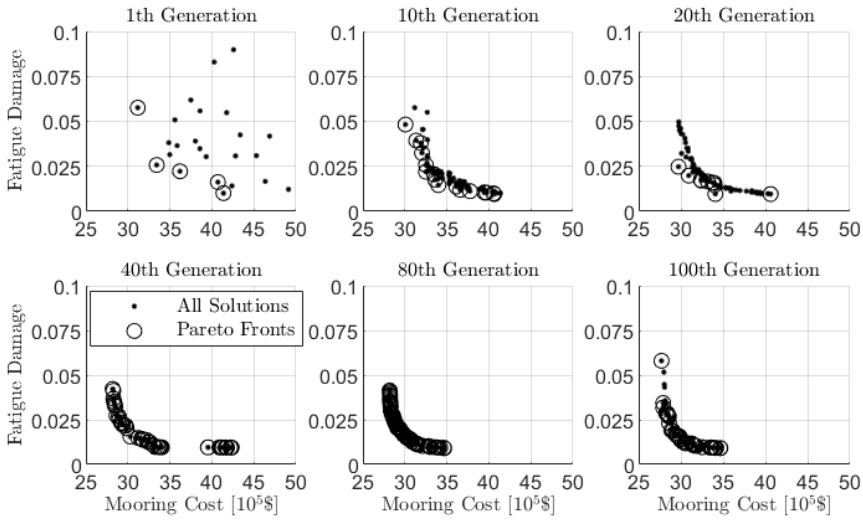


Figure 7.12: All feasible solutions and their Pareto fronts at selected generations.

In the first generation, feasible solutions are sparsely distributed, while some located near the lower-left edge, featuring low mooring cost or low fatigue damage, are not sorted in the Pareto front. This occurs because Pareto dominance is determined by relative trade-offs, not absolute values. Each solution is compared against all others, when no other solution has lower cost and fatigue, then it is sorted into the first front. During the first 20 generations, feasible solutions and their corresponding Pareto fronts distribute differently, with many solutions scattered across regions featuring relatively high mooring costs and fatigue damage.

As the evolution progresses, by the 40th generation, more Pareto fronts are identified, and feasible solutions gradually cluster around the advancing fronts. After that, the alignment between Pareto fronts and feasible solutions becomes increasingly consistent. By the 80th generation, nearly all feasible solutions are recognized as Pareto fronts, with significant reductions in mooring cost achieved. At the 100th generation, the Pareto fronts maintain a similar upper cost bound as at the 80th generation, but shift slightly toward lower costs accompanied by higher fatigue damage.

Figure 7.13 presents configuration characteristics of the Pareto fronts at the 100th generation using a dual-axis format. The x-axis represents key configuration parameters, the left y-axis shows mooring cost, and the right y-axis indicates mooring fatigue.

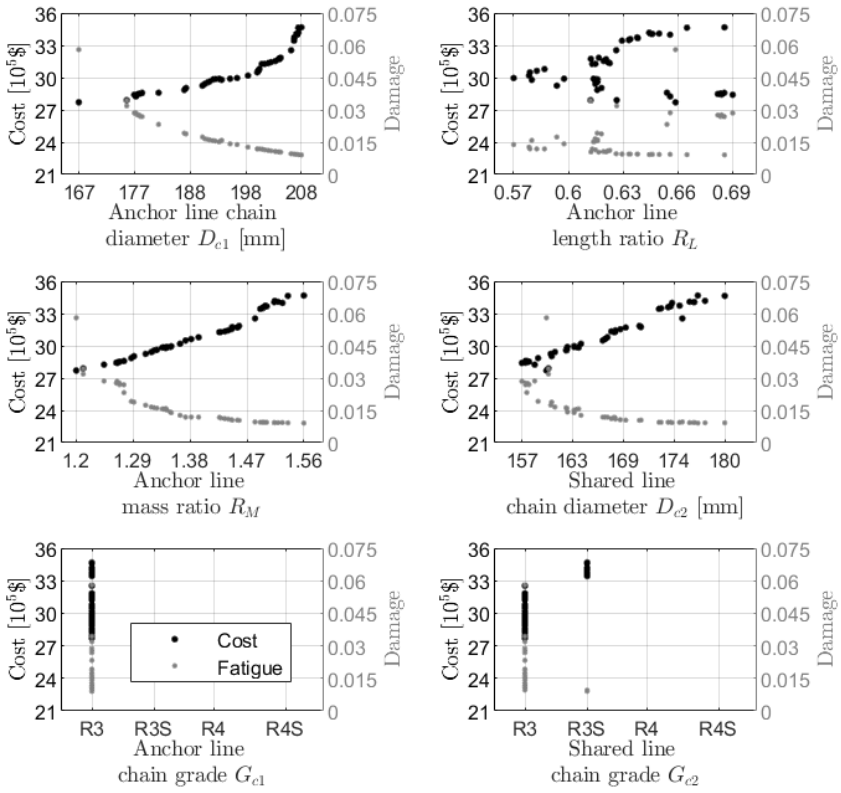


Figure 7.13: Configuration properties of Pareto fronts at the 100th generation.

For design variables such as anchor line chain diameter, line mass, and shared line chain diameter, reductions in mooring cost are achieved at the expense of increased fatigue damage. In contrast, the anchor line length ratio is strongly constrained by pretension requirements, leading to a less consistent trade-off between mooring cost and fatigue performance. All solutions use the lowest chain grade (R3) for the anchor lines, while shared lines select either R3 or

R3S, with the majority using R3. The distribution of the Pareto front also indicates that no single optimal solution is identified by NSGA-II for this cost-fatigue balance optimization problem. Instead, the algorithm identifies a set of non-dominated solutions that represent the best trade-offs between mooring cost ($C_m$) and fatigue damage ($D_m$).

The evolution of the population reveals a distinct relationship: reductions in $C_m$ are accompanied by greater $D_m$. Equation 7.8 quantifies this trade-off relationship based on the Pareto fronts at the 100th generation. Since the relative weighting between mooring cost and fatigue damage is uncertain, this trade-off relationship allows informed-decisions and highlights the limitations of the single-objective optimization. The unit of $C_m$ is $1 \times 10^5$ USD.

$$D_m = -0.0004 \times C_m^3 + 0.0373 \times C_m^2 - 1.1998 \times C_m + 12.8752 \tag{7.8}$$

The trade-off relationship is formulated by fitting a polynomial to the Pareto front data at the 100th generation (Figure 7.12). The coefficient of determination $R^2$ is 0.9203, indicating a good overall fit. The polynomial predicts well in the middle region of mooring costs, while its accuracy decreases near the two ends of Pareto fronts. The knee point is the solution with the most balanced trade-off between $C_m$ and $D_m$, which is located at the region of highest curvature, where an improvement in one objective causes a relatively high deterioration in the other. Using the cubic polynomial (Equation 7.8) to calculate the maximum curvature, the knee-point solution has a mooring cost of $27.7 \times 10^5$ USD and a corresponding mooring fatigue damage of 0.058. This knee-point solution is further used for comparison with the optimal solution generated from the PSO algorithm.

### 7.4.5 Comparison

The global best solution obtained from the PSO algorithm at the 100th iteration, and the knee-point solution on the Pareto fronts at the 100th generation

identified by NSGA-II are compared in terms of mooring cost, fatigue damage, and configuration properties. This comparison highlights the differences between cost-driven and cost-fatigue balance optimization approaches, as summarized in Table 7.4.

Table 7.4: Comparison of the optimal solutions obtained from the PSO algorithm and NSGA-II.

| Parameter | PSO | NSGA-II |
|---|---|---|
| Mooring cost $C_m$ [$10^5$ USD] | 23.6 | 27.7 |
| Mooring fatigue damage $D_m$ | 0.09 | 0.06 |
| Anchor line chain diameter $D_{c1}$ [mm] | 153.2 | 167.1 |
| Anchor line length ratio $R_L$ | 0.65 | 0.66 |
| Anchor line mass ratio $R_M$ [%] | 1.02 | 1.20 |
| Shared line chain diameter $D_{c2}$ [mm] | 141.5 | 160.1 |
| Anchor line chain grade $G_{c1}$ | R3 | R3 |
| Shared line chain grade $G_{c2}$ | R3 | R3 |

The optimal design obtained from the cost-driven PSO optimization minimizes mooring material cost but results in relatively high fatigue damage. This configuration features smaller chain diameters and lighter mooring mass compared to the solution obtained from the cost–fatigue balance optimization using NSGA-II, which is the knee point on the Pareto fronts at the 100th generation. The NSGA-II solution balances the trade-off between mooring cost and fatigue damage. While its mooring cost is slightly higher than the PSO solution, it maintains better fatigue resistance. This represents a compromise design, where improvements in fatigue resistance inevitably lead to increased mooring costs.

## 7.5 Summary

This chapter presents two optimization strategies for floating turbine arrays using shared mooring line configurations. The cost-driven strategy focuses on minimizing mooring material cost and employs the PSO algorithm to identify

the lowest-cost design. In contrast, the cost–fatigue balance strategy aims to minimize both mooring cost and fatigue damage. NSGA-II is applied to solve this multi-objective optimization problem.

A case study of a two-turbine array is conducted to investigate shared mooring optimization, addressing the research gaps that few studies optimize shared mooring in time-domain analysis while accounting for wake effects and mooring fatigue. Using a simplified modeling approach, the shared line design is developed following a nonlinear design method, and the resulting optimal solutions are compared in terms of mooring cost, fatigue, and configuration properties. The PSO algorithm produces the global best solution with the lowest mooring cost, while NSGA-II generates the Pareto-optimal solution that balances mooring cost and fatigue damage.

# 8 Conclusion

## 8.1 Summary of findings

This study addresses key technical challenges in the design, simulation, and optimization of shared line mooring configurations to comprehensively evaluate their performance and promote the sustainable development of floating wind farms. A nonlinear design method is first introduced to generate practical and cost-effective mooring configurations. Compared with stiffness-linearized approaches, this method produces more robust shared line designs. A simplified modeling framework is then developed to simulate dynamic responses of entire floating wind farms. Its computational efficiency and predictive accuracy are verified against FAST.Farm, demonstrating its applicability for early-stage assessments of floating turbine arrays. Finally, the PSO and NSGA-II algorithms are applied to investigate cost-driven and cost-fatigue balance optimization problems, respectively. Supported by the simplified modeling framework, the optimization study evaluates shared line designs under both extreme and normal operating conditions, incorporating wake effects and mooring fatigue.

### 8.1.1 Nonlinear design method for shared line configurations

Sensitivity tests show that the shared line mass ratio has a monotonic influence on the dynamic responses of FOWTs. Using five uniformly distributed ratios across the full range can effectively capture these effects for given anchor line profiles. Moreover, shared line and conventional mooring configurations exhibit different critical wind directions, which should be considered in mooring design.

To support more reliable designs, static analyses should also incorporate key parameters such as floater pitch, wake effects, and mooring axial stiffness.

Comparisons between static and dynamic analyses highlight the strengths and limitations of static approaches. While static analysis serves as an effective lower-bound screening tool, relying solely on it can underestimate floater offsets and misidentify critical parameters such as wind direction. Similarly, comparing nonlinear versus stiffness-linearized methods for given anchor line profiles demonstrates that, although the linearized approach is simpler, neglecting mooring elasticity and configuration properties can lead to unrealistic shared line designs that exceed the limits of available chain diameters and line masses.

Using the nonlinear design method, over 2000 conventional and more than 500 shared line designs are generated for a two-turbine array, all satisfying design requirements under both extreme and operation conditions. For conventional moorings, heavier line masses allow larger chain diameters, longer lay-down lengths, lower mooring force ratios, and smaller floater offsets. For shared line configurations, heavier anchor lines provide similar benefits, however, the floater maximum offsets and mooring force ratios are strongly influenced by the ratio of shared line mass to anchor line mass. Incorporating mooring fatigue into design evaluations reduces the number of feasible configurations from 5604 to 5016, and including wake effects in dynamic simulations further reduces the number to 2206. These considerations are critical for mooring design, as they shift designs toward larger chain diameters and heavier mooring masses, and induce larger extreme floater offsets.

Comparative studies of 2206 conventional and 510 shared line mooring configurations for the two-turbine array show that, although shared line designs exhibit slightly higher costs (around 3%) at the extremes due to heavier masses needed to withstand larger offsets, their most frequent cost achieves a 15% reduction compared to conventional moorings. At both extreme costs, shared line designs demonstrate higher fatigue resistance, with over a 30% decrease in mooring fatigue damage, highlighting their advantages in maintaining long-term mooring integrity.

### 8.1.2 Simplified modeling of the floating wind farm

The simplified modeling approach significantly improves the computational efficiency. The simulation-to-CPU time ratio is increased from less than 0.2 (using FAST.Farm) to over 15 (using the simplified model), when simulating a two-turbine array with various shared line moorings under similar loading conditions. This increased time ratio represents a reduction of more than 75-fold in computational effort, which enables rapid analysis and large-scale simulations of entire floating wind farms with shared mooring designs.

Results from static and decay tests show that the simplified model effectively captures the fundamental dynamics of the floating array, and deliver floater motions and mooring forces comparable to those from FAST.Farm. Its flexible wind modeling makes it more suitable for such wind-free tests, in contrast to FAST.Farm v3.5.1, which is not designed for no-wind simulations and requires artificially low wind speeds to avoid simulation errors.

Comparisons under both steady wind with regular waves and turbulent wind with irregular waves demonstrate that the simplified model provides reasonable accuracy in predicting power output, floater motions, and mooring forces. However, as the Gaussian wake model uses a constant wake expansion parameter across different wind speeds, results from both tests suggest that fine-tuning this wake parameter could improve the accuracy of turbine power predictions.

The quasi-static mooring model and Gaussian wake model used in the simplified approach overlook mooring and wake dynamics, respectively. In contrast, FAST.Farm accounts for these dynamic effects, resulting in different power output, floater surge, and mooring line forces for the downstream turbine. Also, the absence of wave radiation damping and dynamic mooring modeling in the simplified framework leads to higher surge motions and underestimated mooring forces.

The simplified modeling approach is demonstrated in two applications: refining shared line designs to mitigate surge motions and ensure adequate laydown lengths, and verifying power predictions for a four-turbine array against

FAST.Farm results. These examples highlight its broad applicability for shared mooring and wind-farm layout optimization, which overcomes the high computational costs typically associated with dynamic simulations needed to capture critical FOWT responses.

### 8.1.3 Shared mooring optimization framework

Two strategies are proposed for shared mooring optimization to address different design priorities. The cost-driven strategy, widely used in floating structures, focuses on minimizing mooring costs and is well-suited for early-stage planning and cost evaluation. In contrast, the cost–fatigue trade-off strategy seeks solutions that balance two conflicting objectives: reducing mooring cost and lowering fatigue damage. Comparative studies show that no single design can optimize both objectives simultaneously. By balancing cost and fatigue, the trade-off strategy is appropriate for detailed design stages, with considerations of long-term mooring fatigue resistance alongside mooring cost.

Although design variables such as chain diameter, chain grade, mass ratio, and length ratio define the shared line configuration, there is no direct analytical expression to quantify mooring cost and fatigue damage. These dependencies are highly interrelated and can only be resolved through dynamic simulations rather than analytical formulations. This limitation does not affect the application of PSO or NSGA-II, as both are population-based, derivative-free algorithms that evaluate objective functions directly from static analyses and dynamic simulations, without requiring explicit analytical expressions.

A case study of a two-turbine array is conducted to investigate shared mooring optimization. Sensitivity tests through static optimization indicate that setting the PSO control factor to 0.7 provides an effective compromise between global search and convergence, while equal cognitive and social coefficients of 1.5 balance local and global search. Using the simplified modeling approach, both cost-driven and cost–fatigue balance optimizations are performed in time-domain analyses, accounting for wake effects and mooring fatigue.

The cost-driven PSO optimization produces a design that minimizes mooring cost but exhibits relatively high fatigue damage, with smaller chain diameters and lighter mooring mass. In contrast, the NSGA-II optimization identifies a knee-point solution on the Pareto front at the 100th generation, balancing mooring cost and fatigue damage. Although its mooring cost is slightly higher than the PSO optimal solution, it achieves improved fatigue resistance, representing a compromise design where enhanced fatigue resistance comes at the expense of increased cost.

## 8.2 Contribution to the community

**Reliable shared line mooring designs** This study advances shared line design by introducing a nonlinear design method that integrates realistic configuration characteristics and practical design constraints. Unlike existing approaches that focus solely on floater offset, this method incorporates mooring line strength and geometric properties to ensure structural integrity and avoid impractical configurations. A case study highlights the limitations of the stiffness-linearized method, which results in chain diameters and masses exceeding current market availability, while the proposed method generates more robust configurations that remain within allowable limits.

In addition, the nonlinear design method incorporates mooring cost and enables a comprehensive evaluation of cost-saving potential across various shared line configurations. Dynamic analyses reveal the limitations of static-only assessments and refine previous conclusions regarding the cost benefits of shared line designs. Contrary to claims that shared moorings always induce lower costs than conventional designs, the study shows that at cost extremes, conventional moorings may be more economical, while the most frequent mooring cost for shared lines achieves up to a 15% saving. Collectively, these findings provide a more reliable, scalable, and economically informed design framework for the floating wind community.

**Efficient simulations of floating wind farms** This study contributes to the floating wind community by developing the simplified modeling approach, which enables efficient and accurate dynamic analysis of floating wind farms. The approach comprises three main modules: a low-order multi-body simulation module, a quasi-static mooring model, and a Gaussian-based wake model. This integrated approach captures more accurate dynamic responses of arrayed FOWTs, compared to some of the existing studies that neglect wake effects.

In addition, compared to FAST.Farm, which provides higher fidelity in modeling, the simplified model significantly reduces computational effort while capturing the comparable fundamental dynamics. Its flexible wind modeling capability makes it more suitable than tools like FAST.Farm, which cannot handle wind-free scenarios. Moreover, its simple architecture and high computational efficiency enable large-scale dynamic simulations, such as shared mooring and layout optimization for extensive wind farms, which remain challenging for current higher-fidelity simulation tools, further enhancing its utility for floating wind farm design and research.

**Tailored shared mooring optimization** This study presents the first time-domain shared mooring optimization that incorporates wake effects and mooring fatigue, in contrast to existing optimization studies in floating wind sector that rely on frequency-domain analysis, which may overlook the dynamic performance of arrayed FOWTs, as well as the optimization studies in other floating structures that pay insufficient to mooring fatigue. Methodologically, the study enhances optimization robustness through tailored initialization and constraint handling techniques.

In addition, this study proposes two optimization strategies to advance floating wind exploration by addressing both mooring costs and the trade-off between mooring cost and fatigue performance. The single-objective, cost-driven strategy minimizes mooring-related expenses and employs the PSO algorithm to identify the most cost-effective design. This approach is valuable for early-stage project planning and economic evaluation. In contrast, the multi-objective

cost–fatigue balance strategy uses NSGA-II to explore trade-offs between long-term mooring fatigue and material costs. This strategy identifies compromise solutions that enable more sustainable and maintainable designs.

## 8.3 Three challenges in shared mooring design and analysis

### 8.3.1 Mooring cost estimation

The first challenge in the design and analysis of shared line configurations lies in the accurate estimation of cost savings compared to conventional moorings. The cost model used in this study is based on empirical analyses for steel chains and drag embedment anchors. Although its relevance to current prices is supported by comparisons with an actual floating wind project, this model is inadequate to evaluate alternative mooring configurations that use different line materials and anchor types, which limits the exploration of cost-saving potentials offered by shared mooring systems.

Moreover, there is a lack of comprehensive cost analyses that consider both mooring fatigue and material costs. Cost evaluations in this study shows that shared line designs improve mooring fatigue performance but slightly increase material costs at the extremes of cost spectrum compared to conventional configurations. Similarly, non-redundant mooring configurations is acceptable in floating wind applications, while redundant configurations increase mooring material costs but offer larger safety margins for long-term mooring fatigue performance. Without a detailed assessment of both mooring-related cost and fatigue performance, it is difficult to determine appropriate weighting factors in shared mooring evaluations.

### 8.3.2 FOWT performance prediction

Experimental validation of shared line configurations for floating turbine arrays remains limited. Existing studies often rely on middle-fidelity or simplified simulations, which may underestimate dynamic responses. For example, the damping factor, which is typically prescribed from literature or experience, strongly influences slow-drift forces. These forces are expected to bring a more pronounced impact on shared mooring designs, which tend to exhibit lower surge and sway eigenfrequencies than conventional moorings. Tuning such key parameters in simulations requires more validations through experiments.

In addition, the multi-disciplinary nature of FOWTs leads to complex interactions among the turbine, tower, floater, and mooring lines under varying environmental conditions. Middle-fidelity or simplified models can efficiently simulate shared moorings but may not fully capture coupled dynamics, such as wake effects and higher-order hydrodynamic forces. High-fidelity tools provide higher accuracy but at higher computational cost. As turbines and farm sizes scale up, to balance accuracy and efficiency becomes essential for the practical design and analysis of shared mooring systems.

### 8.3.3 Mooring integrity maintenance

Compared to conventional moorings, the shared line design introduces additional complexity to the multi-body systems of floating turbine arrays. Coupling effects between the connected FOWTs, combined with altered mooring stiffness, can result in higher floater offsets and increased mooring forces in the upwind lines. These responses, in turn, affect the long-term mooring integrity and FOWT operational safety. Improvement can be achieved, for instance, by increasing mooring mass. However, given the cost-driven design philosophy utilized for floating wind projects, it is crucial to strike a balance between mooring cost and structural performance.

In addition, shared mooring designs influence dynamic cable performance. However, few studies have addressed this interaction, as mooring analyses are typically decoupled from cable responses. Floater offset limits are applied in shared mooring designs to ensure cable safety, but allowable offset ranges that impact cable curvature and operational performance remain largely unexplored. Moreover, shared mooring layouts alter floater orientation, which significantly affects cable alignment and dynamics. This lack of mooring design constraints and cable-mooring interaction poses challenges on mooring integrity of shared line designs and structural safety of dynamic cables.

## 8.4 Recommendation for future researches

### 8.4.1 Mooring-related cost model extension

To improve the accuracy of mooring cost estimates, future studies should explore cost models to reflect the current prices for the growing use of diverse mooring materials and anchor types in floating wind projects. Existing cost models should be expanded to include alternatives beyond steel chains and drag embedment anchors. Examples include combined mooring configuration using both chains and fiber ropes, or the use of suction pile anchors. Such updates can accommodate a broader range of shared mooring options.

In addition, comprehensive analyses of life-cycle mooring-related costs, considering material costs and mooring performance are recommended. The cost-fatigue balance optimization shows that reductions in mooring material costs are often accompanied by increased mooring fatigue. This highlights the need for strategic balance between these competing objectives. Future studies could explore how reduced fatigue can lower maintenance costs or how optimized material costs can contribute to the overall savings, supporting informed decision-making to achieve the overall cost efficiency.

Potential innovations may involve the development of a sophisticated life-cycle cost model that incorporates current prices for diverse mooring line materi-

als and anchor types, and accounts for both upfront mooring material costs and long-term maintenance activities in relation to mooring fatigue. This cost model could further integrate factors such as material degradation (e.g., friction during operation at pad-eye and fairlead positions), environmental impacts (e.g., marine growth and sediment movement), and maintenance schedules (e.g., tension adjustment and corrosion protection), to provide a more realistic mooring cost estimation.

### 8.4.2 Improved predictions of FOWT responses

Simplifications in floating farm dynamics, such as neglecting wake effects and mooring dynamics, can underestimate floater motions and mooring forces. In the absence of physical experiments or prototypes, future studies are encouraged to adopt a hybrid approach that integrates high- and low-fidelity tools, using key parameters to calibrate lower-order models. For example, wake-deficit correction factors derived from CFD simulations can improve wake modeling in the lower-order tools such as simplified modeling approach. This integration enhances the reliability of system-level assessments with manageable computational demands.

Future FOWT design should explicitly consider interactions between inter-array cables and mooring lines. This is particularly important in shared mooring layouts, where mooring arrangements can significantly influence cable configurations and dynamic responses, such as through floater orientation. Conversely, mooring design is affected by cable operational requirements, including allowable floater offsets. Despite these interactions, no clear design limits or best practices exist. To address this gap, fully coupled simulations integrating both cables and mooring lines are recommended. Such studies could provide insights into constraints and dependencies between these two systems, and help to define the design space for more robust cable and shared line designs.

Potential innovations such as scaled-down experiments, can advance floating wind farm simulations by replicating floater motions and truncated mooring

lines or cables to capture realistic dynamics. Hybrid approaches combining physical tests and numerical simulations can also overcome aerodynamic and hydrodynamic scaling challenges. For instance, wave-tank models of floating turbine arrays can incorporate aerodynamic forces from simulations, with parameters such as damping coefficients and slow-drift forces used to calibrate numerical tools, improving prediction accuracy of floating wind farm performance.

### 8.4.3 Performance enhancement for floating wind farms

Floating wind projects often use non-redundant mooring configurations, unlike oil & gas applications. Shared line designs use one line to support two floaters and amplify failure consequences of non-redundant configurations. Future studies should assess the need for redundancy and the cost–performance trade-off. Cluster-spread configurations with multiple lines per cluster offer a potential solution to mitigate failure risk. Analyses of these redundant designs under single-line breakage scenarios can help define appropriate safety factors for the design, analysis, and optimization of shared mooring systems.

Shared line mooring designs can increase floater offsets and amplify surge, sway, and yaw motions compared to conventional moorings. These increased motions affect wake dynamics, influencing power output, blade loading, and mooring forces of downstream FOWTs. These effects, particularly the roll–yaw coupling, remain unclear. Future studies should investigate the influence of shared line designs on downstream turbine performance and explore different turbine control strategies to optimize power output and FOWT performance.

Future work could leverage artificial intelligence, data-driven methods, and surrogate models for long-term monitoring and advanced control of floating wind farms. Given the limited experimental or measured data, machine learning or surrogate models trained on high-fidelity simulations may effectively predict mooring fatigue and turbine performance. Adaptive yaw control in shared line configurations could steer wakes, enhance power output, and mitigate fatigue

damage. In addition, co-design of shared mooring layouts with adaptive controllers, using hybrid optimization techniques that combine evolutionary and gradient-based methods, offers a pathway to balance competing objectives such as maximizing energy production and minimizing structural degradation.

# A Static design using the stiffness-linearized method

Figure A.1 illustrates the mooring forces and the wind force acting on two FOWTs along the X-axis. At a wind direction of 0°, the symmetric shared line mooring configuration minimizes the sway offsets of the two FOWTs, as the mooring forces in each line are balanced by the adjacent lines along the Y-axis. In the stiffness-linearized design method, only surge and sway motions are considered, and each mooring line is modeled as a linear spring. Assuming small offsets, the total force on each line is the sum of its pretension and the increased force, which is calculated as the product of its linearized stiffness and the floater's offset.

In the case study, the upwind anchor lines (L2S, L3S) have similar line properties, as do the downwind lines (L5S, L6S). Consequently, the mooring forces within each anchor line pair are identical when the floater moves along the X-axis. It is assumed that small surge displacements have a negligible effect on the spacing angles between adjacent lines. Therefore, the fairlead forces are summed for each anchor line pair along the X-axis. The static equilibrium between the wind force and the mooring forces along the X-axis is expressed for each FOWT in Equation A.1.

$$\begin{aligned} (MF_{3s} + K_{3s} \times X_1) \times 2 &= WF_1 + MF_s + K_s \times (X_2 - X_1), \\ MF_s + K_s \times (X_2 - X_1) &= WF_2 + (MF_{6s} + K_{6s} \times X_2) \times 2. \end{aligned} \tag{A.1}$$

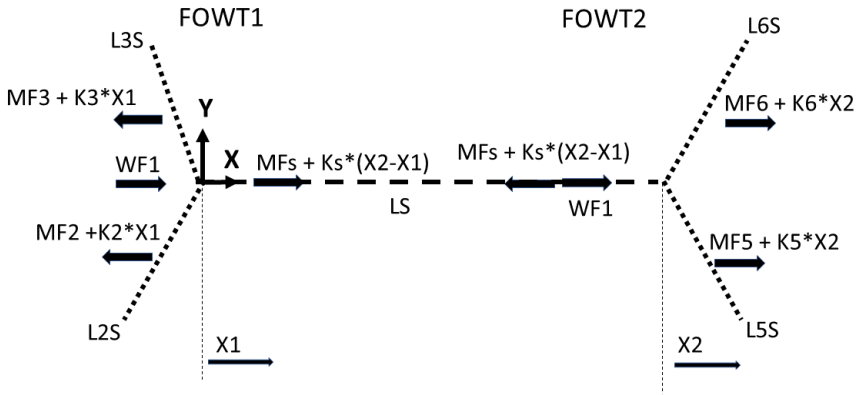


Figure A.1: Wind and mooring forces on each FOWT at a wind direction of 0°.

where $MF$ represents the mooring fairlead pretension, and $K$ denotes the linearized mooring stiffness, with the subscription number indicating the anchor line number. $MF_s$ and $K_s$ correspond to the pretension and stiffness of the shared line LS. In this case study, both $MF$ and $K$ only consider the X-axis component. $X_1$ and $X_2$ refer to the floater offset of the upstream FOWT1 and downstream FOWT2, respectively, measured from its static equilibrium positions. $WF_1$ denote the wind force acting on the turbines, since no wake effect is considered in the stiffness-linearized method. The properties of the upwind lines (L2S, L3S) and the shared line (LS) are unknown, whereas the downwind lines have properties similar to the anchor lines in shared line baseline configurations, as listed in Table 5.4.

# Bibliography


[1] U. Nations, "For a livable climate: Net-zero commitments must be backed by credible action," https://www.un.org/en/climatechange/net-zero-coalition, 2025, accessed: 2025-01-20.

[2] S. Boehm, L. Jeffery, J. Hecke, C. Schumer, J. Jaeger, C. Fyson, K. Levin, A. Nilsson, S. Naimoli, E. Daly *et al.*, "State of climate action 2023," Berlin and Cologne, Germany, San Francisco, CA, and Washington, DC: Bezos Earth Fund, Climate Action Tracker, Climate Analytics, ClimateWorks Foundation, NewClimate Institute, the United Nations Climate Change High-Level Champions, and World Resources Institute., Tech. Rep., 2023.

[3] J. Lee, F. Zhao *et al.*, "Global wind report 2024," Global Wind Energy Council, Belgium, Tech. Rep., 2024.

[4] C. Maienza, A. Avossa, F. Ricciardelli, D. Coiro, G. Troise, and C. T. Georgakis, "A life cycle cost model for floating offshore wind farms," *Applied Energy*, vol. 266, p. 114716, 2020.

[5] V. Sykes, M. Collu, and A. Coraddu, "A review and analysis of the uncertainty within cost models for floating offshore wind farms," *Renewable and Sustainable Energy Reviews*, vol. 186, p. 113634, 2023.

[6] BVG Associates Limited, "Guide to a Floating Offshore Wind Farm," https://guidetofloatingoffshorewind.com/wind-farm-costs/, accessed: 2025-08-30.

[7] Bowie Malcolm, "Development Specification and Layout Plan - Kincardine Offshore Wind Farm," Kincardine Offshore Windfarm Ltd, Tech. Rep., March 2018, https://marine.gov.scot/sites/default/files/kowl-pl-0004-011_-_development_specification_and_layout_plan_rev_c3_redacted_0.pdf Accessed: 2025-01-21.

[8] Equinor, "Hywind scotland brochure," https://www.equinor.com/content/dam/statoil/documents/newsroom-additional-documents/news-attachments/brochure-hywind-a4.pdf, 2014, last accessed on 2025-01-21.

[9] Equinor, "Hywind Tampen," 2023, https://www.equinor.com/energy/hywind-tampen, Last accessed on 2024-01-15.

[10] DOF Subsea, "Hywind tampen: Floating wind farm installation," sut.org/Hywind-Tampen-Installation, 2023, accessed: 2025-01-15.

[11] K.-T. Ma, Y. Luo, C.-T. T. Kwan, and Y. Wu, *Mooring System Engineering for Offshore Structures*. Gulf Professional Publishing, 2019.

[12] DNVGL, "Offshore standard DNVGL-OS-E301 Position mooring," *Høvik, DNV GL AS.*, 2021.

[13] Atkins Ltd, "Kincardine Floating Offshore Wind Demonstrator Project Habitats Regulations Appraisal Appropriate Assessment," March 2016, https://marine.gov.scot/sites/default/files/00498907_0.pdf, Last accessed on2025-01-22.

[14] H. Kim, J. Choung, and G.-Y. Jeon, "Design of mooring lines of floating offshore wind turbine in jeju offshore area," in *International Conference on Offshore Mechanics and Arctic Engineering*, vol. 45530. American Society of Mechanical Engineers, 2014.

[15] Q. Pan, M. Y. Mahfouz, and F. Lemmer, "Assessment of mooring configurations for the iea 15mw floating offshore wind turbine," in *Journal of Physics: Conference Series*, vol. 2018. IOP Publishing, 2021, p. 012030.

[16] Q. Pan and P. W. Cheng, "Cost-based mooring designs and a parametric study of bridles for a 15 mw spar-type floating offshore wind turbine," in *Journal of Physics: Conference Series*, vol. 2265. IOP Publishing, 2022, p. 042013.

[17] S. Quallen, T. Xing, P. Carrica, Y. Li, and J. Xu, "Cfd simulation of a floating offshore wind turbine system using a quasi-static crowfoot mooring-line model," in *ISOPE International Ocean and Polar Engineering Conference*. ISOPE, 2013, pp. ISOPE–I.

[18] F. Borisade, C. Koch, F. Lemmer, P. W. Cheng, F. Campagnolo, and D. Matha, "Validation of innwind. eu scaled model tests of a semisubmersible floating wind turbine," *International Journal of Offshore and Polar Engineering*, vol. 28, no. 01, pp. 54–64, 2018.

[19] C. Barrera, R. Guanche, Á. Rodríguez, J. A. Armesto, and I. J. Losada, "On the importance of mooring system parametrisation for accurate floating structure designs," *Marine Structures*, vol. 72, p. 102765, 2020.

[20] M. Hall and A. Goupee, "Validation of a lumped-mass mooring line model with deepcwind semisubmersible model test data," *Ocean Engineering*, vol. 104, pp. 590–603, 2015.

[21] J. Azcona and F. Vittori, "Mooring system design for the 10mw triple spar floating wind turbine at a 180 m sea depth location," in *Journal of Physics: Conference Series*, vol. 1356, no. 1. IOP Publishing, 2019, p. 012003.

[22] K. Xu, K. Larsen, Y. Shao, M. Zhang, Z. Gao, and T. Moan, "Design and comparative analysis of alternative mooring systems for floating wind turbines in shallow water with emphasis on ultimate limit state design," *Ocean Engineering*, vol. 219, p. 108377, 2021.

[23] S. H. Sørum, N. Fonseca, M. Kent, and R. P. Faria, "Assessment of nylon versus polyester ropes for mooring of floating wind turbines," *Ocean Engineering*, vol. 278, p. 114339, 2023.

[24] BW Ideol, "Bw ideol's first floater in operation," 2018, https://www.bw-ideol.com/en/floatgen-demonstrator, Last accessed on 2025-01-25.

[25] T. Utsunomiya, I. Sato, and K. Tanaka, "At-sea experiment on durability and residual strength of polyester rope for mooring of floating wind turbine," in *International Conference on Offshore Mechanics and Arctic Engineering*, vol. 58882. American Society of Mechanical Engineers, 2019, p. V009T13A017.

[26] S. H. Sørum, N. Fonseca, M. Kent, and R. P. Faria, "Modelling of synthetic fibre rope mooring for floating offshore wind turbines," *Journal of Marine Science and Engineering*, vol. 11, no. 1, p. 193, 2023.

[27] D. W. Fredriksson, J. DeCew, M. R. Swift, I. Tsukrov, M. D. Chambers, and B. Celikkol, "The design and analysis of a four-cage grid mooring

for open ocean aquaculture," *Aquacultural engineering*, vol. 32, no. 1, pp. 77–94, 2004.

[28] Z. Gao and T. Moan, "Mooring system analysis of multiple wave energy converters in a farm configuration," in *Proceedings of the 8th European Wave and Tidal Energy Conference, Uppsala, Sweden*, 2009, pp. 7–10.

[29] M. Goldschmidt and M. Muskulus, "Coupled mooring systems for floating wind farms," *Energy Procedia*, vol. 80, pp. 255–262, 2015.

[30] L. Xie, C. Li, M. Yue, H. He, W. Jia, Q. Liu, Z. Xu, L. Fan, M. Bashir, and Y. Yan, "Dynamic analysis of an improved shared moorings for floating offshore wind farm," *Renewable Energy*, vol. 232, p. 120963, 2024.

[31] P. Beiter, W. Musial, A. Smith, L. Kilcher, R. Damiani, M. Maness, S. Sirnivas, T. Stehly, V. Gevorgian, M. Mooney *et al.*, "A spatial-economic cost-reduction pathway analysis for us offshore wind energy development from 2015–2030," National Renewable Energy Lab.(NREL), Golden, CO (United States), Tech. Rep., 2016.

[32] P. Connolly and M. Hall, "Comparison of pilot-scale floating offshore wind farms with shared moorings," *Ocean Engineering*, vol. 171, pp. 172–180, 2019.

[33] S. Wilson, M. Hall, S. Housner, and S. Sirnivas, "Linearized modeling and optimization of shared mooring systems," *Ocean Engineering*, vol. 241, p. 110009, 2021.

[34] M. Hall, E. Lozon, S. Housner, and S. Sirnivas, "Design and analysis of a ten-turbine floating wind farm with shared mooring lines," in *Journal of Physics: Conference Series*, vol. 2362, no. 1. IOP Publishing, 2022, p. 012016.

[35] E. Lozon and M. Hall, "Coupled loads analysis of a novel shared-mooring floating wind farm," *Applied Energy*, vol. 332, p. 120513, 2023.

[36] M. U. Rentschler, F. Adam, and P. Chainho, "Design optimization of dynamic inter-array cable systems for floating offshore wind turbines," *Renewable and Sustainable Energy Reviews*, vol. 111, pp. 622–635, 2019.

[37] R. Taninoki, K. Abe, T. Sukegawa, D. Azuma, and M. Nishikawa, "Dynamic cable system for floating offshore wind power generation," *SEI Technical review*, vol. 84, no. 53-58, p. 146, 2017.

[38] G. Benassai, A. Campanile, V. Piscopo, and A. Scamardella, "Ultimate and accidental limit state design for mooring systems of floating offshore wind turbines," *Ocean Engineering*, vol. 92, pp. 64–74, 2014.

[39] M. Brommundt, L. Krause, K. Merz, and M. Muskulus, "Mooring system optimization for floating wind turbines using frequency domain analysis," *Energy Procedia*, vol. 24, pp. 289–296, 2012.

[40] T. Sant, D. Bonnici, R. Farrugia, and D. Micallef, "Measurements and modelling of the power performance of a model floating wind turbine under controlled conditions," *Wind Energy*, vol. 18, no. 5, pp. 811–834, 2015.

[41] Y. Liu, Q. Xiao, A. Incecik, C. Peyrard, and D. Wan, "Establishing a fully coupled cfd analysis tool for floating offshore wind turbines," *Renewable Energy*, vol. 112, pp. 280–301, 2017.

[42] P. Cheng, Y. Huang, and D. Wan, "A numerical model for fully coupled aero-hydrodynamic analysis of floating offshore wind turbine," *Ocean Engineering*, vol. 173, pp. 183–196, 2019.

[43] NREL, " OpenFAST Documentation, National Renewable Energy Lab." https://raf-openfast.readthedocs.io/en/latest/, 2023, online; Accessed: 2023-06-06.

[44] E. Branlard, J. Jonkman, C. Brown, and J. Zhang, "A digital twin solution for floating offshore wind turbines validated using a full-scale prototype," *Wind Energy Science*, vol. 9, no. 1, pp. 1–24, 2024.

[45] W. Yu, F. Lemmer, and P. W. Cheng, "Modeling and validation of a tuned liquid multi-column damper stabilized floating offshore wind turbine coupled system," *Ocean Engineering*, vol. 280, p. 114442, 2023.

[46] Y. Zhang and H. Liu, "Coupled dynamic analysis on floating wind farms with shared mooring under complex conditions," *Ocean Engineering*, vol. 267, p. 113323, 2023.

[47] Q. Pan, F. Guo, and F. D. Lüdecke, "Nonlinear modelling of shared mooring concepts for floating offshore wind turbines," in *Journal of Physics: Conference Series*, vol. 2626. IOP Publishing, 2023, p. 012037.

[48] O. Gözcü, S. Kontos, and H. Bredmose, "Dynamics of two floating wind turbines with shared anchor and mooring lines," in *Journal of Physics: Conference Series*, vol. 2265, no. 4. IOP Publishing, 2022, p. 042026.

[49] G. Liang, Z. Jiang, and K. Merz, "Dynamic analysis of a dual-spar floating offshore wind farm with shared moorings in extreme environmental conditions," *Marine Structures*, vol. 90, p. 103441, 2023.

[50] A. S. Wise and E. E. Bachynski, "Wake meandering effects on floating wind turbines," *Wind Energy*, vol. 23, no. 5, pp. 1266–1285, 2020.

[51] A. Jacobsen and M. Godvik, "Influence of wakes and atmospheric stability on the floater responses of the hywind scotland wind turbines," *Wind Energy*, vol. 24, no. 2, pp. 149–161, 2021.

[52] C. L. Archer, A. Vasel-Be-Hagh, C. Yan, S. Wu, Y. Pan, J. F. Brodie, and A. E. Maguire, "Review and evaluation of wake loss models for wind energy applications," *Applied Energy*, vol. 226, pp. 1187–1207, 2018.

[53] Y. Ma, C. L. Archer, and A. Vasel-Be-Hagh, "The jensen wind farm parameterization," *Wind Energy Science*, vol. 7, no. 6, pp. 2407–2431, 2022.

[54] J. M. Jonkman and K. Shaler, "Fast. farm user's guide and theory manual," National Renewable Energy Laboratory Golden, CO, USA, Tech. Rep., 2021.

[55] A. Chehouri, R. Younes, A. Ilinca, and J. Perron, "Review of performance optimization techniques applied to wind turbines," *Applied Energy*, vol. 142, pp. 361–388, 2015.

[56] E. C. Edwards, A. Holcombe, S. Brown, E. Ransley, M. Hann, and D. Greaves, "Evolution of floating offshore wind platforms: A review of at-sea devices," *Renewable and Sustainable Energy Reviews*, vol. 183, p. 113416, 2023.

[57] I. A. Ja'e, M. O. A. Ali, A. Yenduri, Z. Nizamani, and A. Nakayama, "Optimisation of mooring line parameters for offshore floating structures: A review paper," *Ocean Engineering*, vol. 247, p. 110644, 2022.

[58] I. Fylling and P. A. Berthelsen, "Windopt: an optimization tool for floating support structures for deep water wind turbines," in *International conference on offshore mechanics and arctic engineering*, vol. 44373, 2011, pp. 767–776.

[59] S. Zhou, F. Lemmer, W. Yu, P. W. Cheng, C. Li, and Y. Xiao, "Optimization of the dynamic response of semi-submersibles: influence of

the mooring system," in *International Conference on Offshore Mechanics and Arctic Engineering*, vol. 59353. American Society of Mechanical Engineers, 2019, p. V001T01A027.

[60] L. Li, Z. Jiang, M. C. Ong, and W. Hu, "Design optimization of mooring system: An application to a vessel-shaped offshore fish farm," *Engineering Structures*, vol. 197, p. 109363, 2019.

[61] B. d. F. Monteiro, J. S. Baioco, C. H. Albrecht, B. S. L. P. de Lima, and B. P. Jacob, "Optimization of mooring systems in the context of an integrated design methodology," *Marine Structures*, vol. 75, p. 102874, 2021.

[62] EnBW Energie Baden-Württemberg AG, "Floating wind turbine: Nezzy$^2$," enbw.com/Nezzy2, accessed: 2025-08-30.

[63] Norwegian Offshore Wind, "Hywind Demo - Zephyros," norwegianoffshorewind.no/Zephyros, 2025, last accessed on 2025-01-15.

[64] Equinor, "StatoilHydro - Hywind Presentation," https://www.equinor.com/news/archive/2008/05/22/downloads/StatoilHydro%20Hywind%20English%20presentation.pdf, 2008, last accessed on 2025-01-15.

[65] Principle Power, "Windfloat 1 project," 2011, https://www.principlepower.com/projects/windfloat1, Last accessed on 2025-01-21.

[66] Stiesdal Offshore, "The TetraSpar full-scale demonstration project," stiesdal.com/TetraSpar, 2021, last accessed on 2025-01-28.

[67] Principle Power, "Windfloat atlantic," 2011, https://www.principlepower.com/projects/windfloat-atlantic, Last accessed on 2025-01-21.

[68] M. Lerch, M. De-Prada-Gil, C. Molins, and G. Benveniste, "Sensitivity analysis on the levelized cost of energy for floating offshore wind farms," *Sustainable Energy Technologies and Assessments*, vol. 30, pp. 77–90, 2018.

[69] CRRC, "The Qihang 20MW Floating Offshore Wind Turbine Successfully Installed," https://www.crrcgc.cc/en/2025-02/13/article_2025021317225881058.html., 2025, accessed: 2024-09-30.

[70] Blue H Engineering, "The Blue H historical technology development," https://www.bluehengineering.com/historical-development.html/, accessed: 2025-08-30.

[71] MacGregor, "Mooring systems brochure," 2022, https://www.macgregor.com/globalassets/picturepark/imported-assets/81909.pdf, Last accessed on 2025-01-21.

[72] BW Ideol, "Floatgen's anchors have been delivered," 2016, https://www.bw-ideol.com/en/actualites/floatgens-anchors-have-been-delivered, Last accessed on 2025-03-25.

[73] Delmar Systems, "Windfloat atlantic," delmarsystems.com/windfloat-atlantic, accessed: 2025-08-30.

[74] American Bureau of Shipping, "Design and installation of drag anchors and plate anchors," *Houston, TX 77060 USA*, March, 2017.

[75] E. Steinar, "Hywind scotland pilot park project plan for construction activities 2017," Hywind Scotland, Statoil, Tech. Rep., 2017.

[76] A. Myhr, C. Bjerkseter, A. Ågotnes, and T. A. Nygaard, "Levelised cost of energy for offshore floating wind turbines in a life cycle perspective," *Renewable energy*, vol. 66, pp. 714–728, 2014.

[77] ABC Moorings, "Mooring lines," https://abc-moorings.weebly.com/mooring-lines.html, 2025, last accessed on 2025-02-25.

[78] Z. Jiang, "Mooring design for floating wind turbines: A review," *Renewable and Sustainable Energy Reviews*, vol. 212, p. 115231, 2025.

[79] Orcina, "Chain: Mechanical properties," https://www.orcina.com/webhelp/OrcaFlex/Content/html/Chain,Mechanicalproperties.htm, 2016, accessed: 2024-01-19.

[80] DNVGL, "Offshore standard DNVGL-OS-E302 Offshore mooring chain," *Høvik, DNV GL AS.*, 2018.

[81] Exxon Mobil Corporation, "Exxonmobil's hoover diana project to be honored at otc 2002," exxonmobil.com/Hoover-Diana-OTC-2002, accessed: 2024-09-30.

[82] T. T. Arthur and J. K. Meier, "Diana/hoover installation: Overview," in *Offshore Technology Conference*. OTC, 2001, pp. OTC–13 085.

[83] Equinor, "Hywind scotland project," 2017, https://www.equinor.com/energy/hywind-scotland, Last accessed on 2025-01-21.

[84] BVG Associates Ltd, "Guide to a Floating Offshore Wind Farm," BVG Associates Ltd, Tech. Rep., May 2023, https://guidetofloatingoffshorewind.com/wp-content/uploads/2023/10/BVGA-16444-Floating-Guide-r2.pdf Accessed: 2024-02-14.

[85] J.-K. Haukeland, "Marine operations and logistics lessons learned from hywind tampen," https://www.sintef.no/globalassets/project/eera-deepwind-2024/presentasjoner/closing_jan-kristian-haukeland.pdf, 2025, accessed: 2025-01-20.

[86] G. Liang, K. Merz, and Z. Jiang, "Modeling of a shared mooring system for a dual-spar configuration," in *International Conference on Offshore Mechanics and Arctic Engineering*, vol. 84416. American Society of Mechanical Engineers, 2020, p. V009T09A057.

[87] T. Lopez-Olocco, G. Liang, A. Medina-Manuel, L. S. Ynocente, Z. Jiang, and A. Souto-Iglesias, "Experimental comparison of a dual-spar floating wind farm with shared mooring against a single floating wind turbine under wave conditions," *Engineering Structures*, vol. 292, p. 116475, 2023.

[88] T. Burton, N. Jenkins, D. Sharpe, and E. Bossanyi, *Wind energy handbook*. John Wiley & Sons, 2011.

[89] R. J. Barthelmie, S. T. Frandsen, M. Nielsen, S. Pryor, P.-E. Rethore, and H. E. Jørgensen, "Modelling and measurements of power losses and turbulence intensity in wind turbine wakes at middelgrunden offshore wind farm," *Wind Energy: An International Journal for Progress and Applications in Wind Power Conversion Technology*, vol. 10, no. 6, pp. 517–528, 2007.

[90] N. Angelou, J. Mann, and C. Dubreuil-Boisclair, "Revealing inflow and wake conditions of a 6mw floating turbine," *Wind Energy Science Discussions*, vol. 2023, pp. 1–35, 2023.

[91] P. R. Pinet, *Essential invitation to oceanography*. Jones & Bartlett Publishers, 2014.

[92] S. Elias and D. Alderton, *Encyclopedia of geology*. Academic Press, 2020.

[93] T. I. Fossen, *Handbook of marine craft hydrodynamics and motion control*. John Wiley & Sons, 2011.

[94] R. Marsh and E. Van Sebille, *Ocean currents: physical drivers in a changing world*. Elsevier, 2021.

[95] U. Özinan, D. Liu, R. Adam, T. Choisnet, and P. W. Cheng, "Power curve measurement of a floating offshore wind turbine with a nacelle-based lidar," in *Journal of Physics: Conference Series*, vol. 2265. IOP Publishing, 2022, p. 042016.

[96] C. Chen, Y. Ma, and T. Fan, "Review of model experimental methods focusing on aerodynamic simulation of floating offshore wind turbines," *Renewable and Sustainable Energy Reviews*, vol. 157, p. 112036, 2022.

[97] D. Roddier, C. Cermelli, A. Aubault, and A. Weinstein, "Windfloat: A floating foundation for offshore wind turbines," *Journal of renewable and sustainable energy*, vol. 2, no. 3, 2010.

[98] H. Shin, P. T. Dam, K. J. Jung, J. Song, C. Rim, and T. Chung, "Model test of new floating offshore wind turbine platforms," *International Journal of Naval Architecture and Ocean Engineering*, vol. 5, no. 2, pp. 199–209, 2013.

[99] F. Adam, C. Steinke, F. Dahlhaus, and J. Großmann, "Gicon®-tlp for wind turbines–validation of calculated results," in *ISOPE International Ocean and Polar Engineering Conference*. ISOPE, 2013, pp. ISOPE–I.

[100] E. Oguz, D. Clelland, A. H. Day, A. Incecik, J. A. López, G. Sánchez, and G. G. Almeria, "Experimental and numerical analysis of a tlp floating offshore wind turbine," *Ocean Engineering*, vol. 147, pp. 591–605, 2018.

[101] I. Bayati, A. Facchinetti, A. Fontanella, F. Taruffi, and M. Belloli, "Analysis of fowt dynamics in 2-dof hybrid hil wind tunnel experiments," *Ocean Engineering*, vol. 195, p. 106717, 2020.

[102] W. Du, Y. Zhao, Y. He, and Y. Liu, "Design, analysis and test of a model turbine blade for a wave basin test of floating wind turbines," *Renewable Energy*, vol. 97, pp. 414–421, 2016.

[103] A. C. Young, A. J. Goupee, H. J. Dagher, and A. M. Viselli, "Methodology for optimizing composite towers for use on floating wind turbines," *Journal of renewable and sustainable energy*, vol. 9, no. 3, 2017.

[104] N. Pollini, A. Pegalajar-Jurado, and H. Bredmose, "Design optimization of a tetraspar-type floater and tower for the iea wind 15 mw reference wind turbine," *Marine Structures*, vol. 90, p. 103437, 2023.

[105] L. Arany and S. Bhattacharya, "Simplified load estimation and sizing of suction anchors for spar buoy type floating offshore wind turbines," *Ocean Engineering*, vol. 159, pp. 348–357, 2018.

[106] H. Li, Z. Hu, J. Wang, and X. Meng, "Short-term fatigue analysis for tower base of a spar-type wind turbine under stochastic wind-wave loads," *International Journal of Naval Architecture and Ocean Engineering*, vol. 10, no. 1, pp. 9–20, 2018.

[107] H. Namik and K. Stol, "Individual blade pitch control of a spar-buoy floating wind turbine," *IEEE transactions on control systems technology*, vol. 22, no. 1, pp. 214–223, 2013.

[108] S. Quallen and T. Xing, "Cfd simulation of a floating offshore wind turbine system using a variable-speed generator-torque controller," *Renewable Energy*, vol. 97, pp. 230–242, 2016.

[109] A. Subbulakshmi, M. Verma, M. Keerthana, S. Sasmal, P. Harikrishna, and S. Kapuria, "Recent advances in experimental and numerical methods for dynamic analysis of floating offshore wind turbines—an integrated review," *Renewable and Sustainable Energy Reviews*, vol. 164, p. 112525, 2022.

[110] DTU Wind Energy, "HAWC2: An aeroelastic code," https://www.hawc2.dk/, 2019, accessed: 2025-03-26.

[111] F. Lemmer, "Low-order modeling, controller design and optimization of floating offshore wind turbines," Ph.D. dissertation, University of Stuttgart, 2018.

[112] NREL, "FLORIS Wake Modeling Wind Farm Controls," https://nrel.github.io/floris/index.html, 2023, accessed: 2025-03-26.

[113] J. J. Bertin and R. M. Cummings, *Aerodynamics for engineers*. Cambridge University Press, 2021.

[114] O. Faltinsen, *Sea loads on ships and offshore structures*. Cambridge university press, 1993, vol. 1.

[115] M. Hansen, *Aerodynamics of wind turbines*. Routledge, 2015.

[116] M. Hall, "Moordyn user's guide," *Orono, ME: Department of Mechanical Engineering, University of Maine*, 2015.

[117] L. Vermeer, J. N. Sørensen, and A. Crespo, "Wind turbine wake aerodynamics," *Progress in aerospace sciences*, vol. 39, no. 6-7, pp. 467–510, 2003.

[118] G. C. Larsen, H. Aagaard Madsen, and F. Bingöl, "Dynamic wake meandering modeling," Risoe National Laboratory. Denmark. Forskningscenter Risoe, Tech. Rep., 2007.

[119] M. Bastankhah and F. Porté-Agel, "A new analytical model for wind-turbine wakes," *Renewable energy*, vol. 70, pp. 116–123, 2014.

[120] M. Y. Mahfouz, M. Salari, S. Hernandez, F. Vigara, C. Molins, and P. Trubat, "Public design and fast models of the two 15mw floater-turbine concepts," corewind.eu/15MW-floater-turbine, 2020, accessed: 2024-09-30.

[121] F. Vigara, L. Cerdán, R. Durán, S. Muñoz, M. Lynch, S. Doole, C. Molins, P. Trubat, and R. Guanche, "D1.2 Design Basis," ESTEYCO, COBRA, INNOSEA, JDR, UPC, FIHAC, Tech. Rep., 2019.

[122] F. Lemmer, W. Yu, P. W. Cheng, A. Pegalajar-Jurado, M. Borg, R. F. Mikkelsen, and H. Bredmose, "The triplespar campaign: Validation of a reduced-order simulation model for floating wind turbines," in *International Conference on Offshore Mechanics and Arctic Engineering*, vol. 51319. American Society of Mechanical Engineers, 2018, p. V010T09A086.

[123] NREL, "TurbSim Module," https://github.com/OpenFAST/openfast/tree/main/modules/turbsim, 2016, accessed: 2024-10-03.

[124] E. Gaertner, J. Rinker, L. Sethuraman, F. Zahle, B. Anderson, G. E. Barter, N. J. Abbas, F. Meng, P. Bortolotti, W. Skrzypinski *et al.*, "IEA Wind TCP Task 37: Definition of the IEA 15-MW Offshore Reference Wind Turbine," National Renewable Energy Lab.(NREL), Golden, CO (United States), Tech. Rep., 2020.

[125] A. Ojo, M. Collu, and A. Coraddu, "Multidisciplinary design analysis and optimization of floating offshore wind turbine substructures: A review," *Ocean Engineering*, vol. 266, p. 112727, 2022.

[126] H. M. Irvine, *Cable Structures*. Gulf Professional Publishing, 2019.

[127] K. Shaler, "Python scripts for InflowWind set up," https://github.com/kshaler/FFarmTools, 2020, accessed: 2024-09-30.

[128] Q. Pan, W. Yu, and P. W. Cheng, "Simplified modeling of floating offshore wind farms with shared mooring line configurations," *Ocean Engineering*, vol. 327, p. 121018, 2025.

[129] R. J. Barthelmie, K. Hansen, S. T. Frandsen, O. Rathmann, J. Schepers, W. Schlez, J. Phillips, K. Rados, A. Zervos, E. Politis *et al.*, "Modelling and measuring flow and wind turbine wakes in large wind farms offshore," *Wind Energy: An International Journal for Progress and Applications in Wind Power Conversion Technology*, vol. 12, no. 5, pp. 431–444, 2009.

[130] L. Parada, C. Herrera, P. Flores, and V. Parada, "Wind farm layout optimization using a gaussian-based wake model," *Renewable energy*, vol. 107, pp. 531–541, 2017.

[131] M. Golbazi and C. L. Archer, "Surface roughness for offshore wind energy," in *Journal of Physics: Conference Series*, vol. 1452, no. 1. IOP Publishing, 2020, p. 012024.

[132] N. Srinivas and K. Deb, "Muiltiobjective optimization using nondominated sorting in genetic algorithms," *Evolutionary computation*, vol. 2, no. 3, pp. 221–248, 1994.

[133] M. Clerc and J. Kennedy, "The particle swarm-explosion, stability, and convergence in a multidimensional complex space," *IEEE transactions on Evolutionary Computation*, vol. 6, no. 1, pp. 58–73, 2002.

[134] D. Wang, D. Tan, and L. Liu, "Particle swarm optimization algorithm: an overview," *Soft computing*, vol. 22, no. 2, pp. 387–408, 2018.

[135] MathWorks, "Particle Swarm Optimization Algorithm," https://www.mathworks.com/help/gads/particle-swarm-optimization-algorithm.html, 2024, accessed: 2025-01-21.

[136] K. Deb, A. Pratap, S. Agarwal, and T. Meyarivan, "A fast and elitist multiobjective genetic algorithm: Nsga-ii," *IEEE transactions on evolutionary computation*, vol. 6, no. 2, pp. 182–197, 2002.

[137] M. Mitchell, *An introduction to genetic algorithms*. MIT press, 1998.

[138] Y. Yusoff, M. S. Ngadiman, and A. M. Zain, "Overview of nsga-ii for optimizing machining process parameters," *Procedia Engineering*, vol. 15, pp. 3978–3983, 2011.